The role of the mTOR pathway and amino acid availability for pre- and postnatal cardiac development, growth and function

Dissertation

zur Erlangung des akademischen Grades
doctor rerum naturalium
(Dr. rer. nat.)
im Fach Biologie

eingereicht an der
Lebenswissenschaftlichen Fakultät
der Humboldt-Universität zu Berlin
von
M.Sc. Maria Hennig

Präsident der Humboldt-Universität zu Berlin
Prof. Dr. Jan-Hendrik Olbertz

Dekan der Lebenswissenschaftlichen Fakultät
Prof. Dr. Richard Lucius

Gutachter/-innen:
1. Prof. Dr. Harald Saumweber
2. Prof. Dr. Ludwig Thierfelder
3. Prof. Dr. Silke Rickert-Sperling

Tag der mündlichen Prüfung: 26.06.2015

TABLE OF CONTENTS

ABBREVIATIONS ..... **VI**

LIST OF TABLES ..... **X**

LIST OF FIGURES ..... **XI**

1 SUMMARY **1**

2 ZUSAMMENFASSUNG **3**

3 INTRODUCTION **6**

3.1 The heart of the matter 6

3.2 Developmental programming of adulthood disease 7

3.2.1 The developmental programming concept (“thrifty phenotype” hypothesis) 7

3.2.2 Animal models of intrauterine growth restriction and implications for the heart 9

3.3 Growth and organ size control of the mammalian heart 11

3.3.1 Prenatal cardiac development and growth 11

3.3.2 Growth mechanisms and metabolic changes in the perinatal mammalian heart 14

3.3.3 Postnatal cardiac growth: Pathological and physiological cardiac hypertrophy 15

3.3.4 The mechanistic target of rapamycin pathway and its role in cardiac growth 16

3.3.4.1 Regulation and function of the mTOR pathway with emphasis on mTORC1 18

3.3.4.2 The role of the mTOR pathway in the mammalian heart 21

3.4 The heart conditional *holocytochrome c synthase* KO mouse model: A novel model for impaired intrauterine cardiac development 23

3.5 Aims and Hypotheses 25

4 MATERIAL **27**

4.1 Laboratory equipment 27

4.2 Consumables 28

4.3 Chemicals and reagents 28

4.4 Size standards 30

4.5 Enzymes and enzyme kits 30

4.6 Inhibitors 30

4.7 Buffers and solutions 30

4.8 Consumable kits 31

4.9 PCR Primers 31

4.10 Antibodies 33

4.11 Other substances for immunohistochemistry 34

4.12 Software 34

4.13 Online tools 35

5 METHODS 36

5.1 Animal experiments 36

5.1.1 Mouse strains 36

5.1.1.1 “Floxed” Hccs mice 36

5.1.1.2 Nkx2-5Cre mice 36

5.1.1.3 “Floxed” Raptor mice 37

5.1.2 Breeding strategies 37

5.1.2.1 Generation of heart conditional Hccs KO mice 37

5.1.2.2 Generation of heart conditional Raptor KO mice 38

5.1.3 Mouse embryo and organ preparations 39

5.1.3.1 Preparation of embryonic hearts 39

5.1.3.2 Preparation of hearts and organs from newborn mice 40

5.1.3.3 Preparation of hearts and organs from 3 week and 11 week old mice 40

5.1.4 Rapamycin injection 41

5.1.5 Low protein diet 41

5.1.6 Evaluation of food intake 41

5.1.7 Echocardiography 42

5.2 Bioinformatical methods 43

5.3 Molecular biological methods 43

5.3.1 Mouse genotyping 43

5.3.1.1 Isolation of genomic DNA from murine tissue 43

5.3.1.2 DNA concentration measurement 44

5.3.1.3 Genotyping by polymerase chain reaction 44

5.3.1.4 Agarose gel electrophoresis 45

5.3.2 RNA expression analyses 45

5.3.2.1 RNA isolation 45

5.3.2.2 RNA concentration measurement and quality control by RNA gel electrophoresis 46

5.3.2.3 cDNA synthesis 46

5.3.2.4 Quantitative real-time PCR 47

5.3.2.4.1 Primer design and determination of optimal annealing temperature by gradient PCR 47

5.3.2.4.2 Determination of optimal primer concentrations 47

5.3.2.4.3 Gene expression analyses 48

5.3.3 Western blot analyses 49

5.3.3.1 Protein isolation 49

5.3.3.2 Protein concentration measurement 49

5.3.3.3 SDS-polyacrylamide gel electrophoresis 50

5.3.3.4 Western blot analyses 51

5.3.4 Histology 52

5.3.4.1 Paraffin embedding and sectioning 52

5.3.4.2 Histological stainings 52

5.3.4.2.1 Hematoxylin and eosin staining 52

5.3.4.2.2 Sirius red staining 53

5.3.4.3 Fluorescent and immunofluorescent stainings 53

5.3.4.3.1 Fluorescent wheat germ agglutinin staining 53

5.3.4.3.2 Fluorescent terminal dUTP nick end labeling 54

5.3.4.3.3 Immunofluorescent KI67 staining 54

5.3.4.3.4 Immunofluorescent phospho-histone H3 staining 55

5.3.4.4 Histological analyses 55

5.3.4.4.1 Evaluation of H&E-stained embryonic, P1 and adult hearts 55

5.3.4.4.2 Quantification of fibrosis in adult hearts 56

5.3.4.4.3 Measurement of cardiomyocyte cross sectional area in P1 and adult hearts 56

5.3.4.4.4 Quantification of apoptosis rates in embryonic 13.5 dpc and P1 hearts 56

5.3.4.4.5 Quantification of proliferation rates in neonatal hearts 57

5.3.4.4.6 Quantification of proliferation rates in embryonic 13.5 dpc hearts 57

5.4 Statistical analysis 58

6 RESULTS 59

6.1 Gene clusters involved in cellular metabolism and amino acid homeostasis are enriched in neonatal c*Hccs*$^{+/-}$ hearts 59

6.2 Enhanced mTOR pathway activity in neonatal c*Hccs*$^{+/-}$ hearts 60

6.3 Consequences of prenatal mTORC1 inhibition by rapamycin on cardiac development, growth and function 61

6.3.1 Prenatal mTORC1 inhibition by rapamycin treatment of pregnant mice 61

6.3.2 Prenatal mTORC1 inhibition neither affects litter size nor genotype distribution 64

6.3.3 Consequences of prenatal mTORC1 inhibition for neonatal hearts 65

6.3.3.1 Prenatal mTORC1 inhibition causes intrauterine growth restriction and cardiac developmental delay in neonatal mice 65

6.3.3.2 Prenatal mTORC1 inhibition reduces cardiomyocyte size, induces apoptosis but does not affect proliferation in neonatal hearts 67

6.3.3.3 Cardiac function in neonatal mice is largely unaffected by prenatal mTORC1 inhibition 70

6.3.4 Consequences of prenatal mTORC1 inhibition for adult hearts 71

6.3.4.1 Prenatal mTORC1 inhibition does not affect cardiac morphology and size of adult hearts 71

6.3.4.2 Prenatal mTORC1 inhibition increases cardiomyocyte size but does not induce pathological remodeling or left ventricular dysfunction in adult hearts 74

6.4 Consequences of cardiac-specific *Raptor* ablation on heart development and survival 76

6.4.1 Cardiac-specific *Raptor* ablation causes embryonic lethality 77

6.4.2 Cardiac-specific *Raptor* ablation results in hypoplastic embryonic hearts 77

6.4.3 Cardiac-specific *Raptor* ablation blocks mTORC1 activity in embryonic hearts 78

6.5 Consequences of pre- and postnatal amino acid restriction on cardiac development, growth and function 79

6.5.1 Mice on LPD do not compensate for the reduced protein content by increased food intake 79
6.5.2 Prenatal amino acid restriction neither affects litter size nor genotype distribution 80
6.5.3 Consequences of prenatal amino acid restriction for neonatal hearts 81

6.5.3.1 Prenatal amino acid restriction does not change cardiac morphology but reduces HW/BW ratio in neonatal cHccs$^{+/-}$ mice 81
6.5.3.2 Prenatal amino acid restriction increases cardiomyocyte CSA but does not affect proliferation rates in neonatal hearts 82

6.5.4 Consequences of prenatal amino acid restriction for embryonic 13.5 dpc hearts 84

6.5.4.1 Prenatal amino acid restriction does not affect mTOR pathway activity and does not change cardiac morphology in 13.5 dpc embryonic hearts 85
6.5.4.2 Prenatal amino acid restriction neither affects apoptosis nor proliferation rates but does alter the expression of cell cycle regulating genes in 13.5 dpc embryonic hearts 86

6.5.5 Consequences of combined pre- and postnatal amino acid restriction for adult hearts 91

6.5.5.1 Pre- and postnatal amino acid restriction does neither affect mTOR pathway activity nor cardiac morphology and size of adult hearts 91
6.5.5.2 Pre- and postnatal amino acid restriction reduces cardiomyocyte size without inducing fibrosis in adult hearts 93
6.5.5.3 Pre- and postnatal amino acid restriction does not cause cardiac dysfunction 95

7 DISCUSSION 98

7.1 The role of the mTOR pathway during heart development and consequences of prenatal mTOR pathway inhibition for postnatal health 98

7.1.1 Rapamycin injection in pregnant dams specifically inhibits mTORC1 but not mTORC2 in the offspring heart 98
7.1.2 Prenatal mTORC1 inhibition by rapamycin is a new model for IUGR in mice 99
7.1.3 Reduced cardiomyocyte size and increased apoptosis rates are responsible for cardiac growth retardation in neonates after prenatal mTORC1 inhibition 101
7.1.4 Prenatal mTORC1 inhibition does not affect cardiac regeneration of c*Hccs*$^{+/-}$ mice but alters apoptosis and cell growth in the neonatal c*Hccs*$^{+/-}$ myocardium 103
7.1.5 Prenatal mTORC1 inhibition by rapamycin does not severely impair heart function in neonates 105
7.1.6 Limitations of the rapamycin approach and suggestions for improvement 106
7.1.7 Cardiac-specific *Raptor* ablation revealed that the mTOR pathway is essential during early embryonic cardiac development 108
7.1.8 Adult mice after prenatal mTORC1 inhibition by rapamycin treatment demonstrate postnatal catch-up growth but no signs of cardiac dysfunction 111

7.2 Consequences of pre- and postnatal amino acid restriction 113

7.2.1 Prenatal amino acid restriction does not induce IUGR in neonatal mice 114
7.2.2 Consequences of prenatal amino acid restriction for neonatal cardiac organ size 115

7.2.3 Cellular and functional consequences in the heart after pre- and postnatal amino acid restriction 116

7.2.3.1 Consequences in neonatal hearts 116

7.2.3.2 Consequences in 13.5 dpc embryonic hearts 117

7.2.3.3 Consequences in adult hearts 118

7.2.4 Consequences of pre- and postnatal amino acid restriction on mTOR pathway activity 119

7.3 Conclusions and perspectives 121

SUPPLEMENTAL INFORMATION XII

BIBLIOGRAPHY XXI

ERKLÄRUNG XXXII

ABBREVIATIONS

♀	female
♂	male
Δ	delta
1°	primary
2°	secondary
4E-BP1	eukaryotic translation initiation factor 4E binding protein 1
A	adenine
AA	aortic arch
AB	antibody
ACC	acetyl-Coenzyme A carboxylase
ADP	adenosine diphosphate
AMP	adenosine monophosphate
AMPK	5´-adenosine monophosphate-activated protein kinase
ANOVA	analysis of variance
Ao	Aorta
APS	ammonium persulfate
Atg13	mammalian autophagy-related gene 13
ATP	adenosine triphosphate
AU	arbitrary units
AVCu	atrioventricular cushions
AW	abdominal wall
B-mode	brightness-mode
bp	base pair
BSA	bovine serum albumin
BW	body weight
c	cardiac
C	cytosine
Ca	caudal
CA	common atrium
cact*Akt*	cardiac-specific constitutively active Akt
Ccn	cyclin
Cdk	cyclin-dependent kinase
Cdkn	cyclin-dependent kinase inhibitor
cDNA	complementary deoxyribonucleic acid
c*Hccs*$^{/-}$	cardiac-specific hemizygous holocytochrome *c* synthase knockout
c*Hccs*$^{+/-}$	cardiac-specific heterozygous holocytochrome *c* synthase knockout
CHD	coronary heart disease
Chop	C/EBP-homologous protein 10
ckid*Akt*	cardiac-specific kinase-deficient Akt
c*Mtor*-KO	cardiac-specific Mtor knockout
Col1a1/2	collagen, type I, alpha 1/2
Col3a1	collagen, type III, alpha 1
CoM	compact myocardium
Cr	Cranial
Cre	Cre recombinase
c*Rheb*-KO	cardiac-specific Rheb knockout
CSA	cross sectional area
C_T	threshold cycle
CV	common ventricle
CVD	cardiovascular disease
CYT *c*	cytochrome c
DAPI	death-associated protein 1 or 4´,6-Diamidino-2-phenylindol
DAVID	database for annotation, visualization, and integrated discovery
ddH_2O	double distilled water
Deptor	DEP domain containing mTOR-interacting protein
dia	diastole
DMA	Dimethylacetamide
DNA	deoxyribonucleic acid
dNTP	deoxyribonucleotide
dpc	days post coitum
dUTP	deoxynucleotide triphosphate

ECL	enhanced chemiluminescence
ECM	extracellular matrix
EDTA	ethylenediaminetetraacetic acid
EF	ejection fraction
e.g.	*exempli grati* (for example)
EIF4B	eukaryotic translation initiation factor 4B
EIF4E	eukaryotic translation initiation factor 4E
EnC	endocardium
EpC	epicardium
et al.	*et alii* (and others)
EtBr	ethidium bromide
ETC	electron transport chain
EtOH	ethanol
F1/F2	first/second filial generation
FIP200	focal adhesion kinase family-interacting protein of 200 kDa
Fn	fibronectin
FP	forward primer
FRB	FKBP12-rapamycin-binding
FS	fractional shortening
g	g-force (gravitational acceleration)
G	guanine
Gapdh	glyceraldehyde 3-phosphate dehydrogenase
H$_2$O	water
H_2O_2	hydrogen peroxide
Hccs	holocytochrome *c* synthase
Hccs$^{+/Y}$	hemizygous wildtype holocytochrome *c* synthase gene
Hccs$^{+/+}$	homozygous wildtype holocytochrome *c* synthase gene
HCl	hydrochloride
H&E	hematoxylin and eosin
HH3	histone H3
HIF1α	hypoxia inducible factor 1, alpha subunit
HRP	horseradish peroxidase
HW	heart weight
HW/BW	heart weight to body weight
IGF	insulin-like growth factor
IgG	Immunoglobulin G
i.p.	intraperitoneal
IRS1	insulin receptor substrate 1
IUGR	intrauterine growth restriction
IVC	inferior vena cava
IVS	interventricular septum
KCl	potassium chloride
kDa	kilodalton
KH_2PO_4	monopotassium phosphate
KO	knockout
KW	kidney weight
KW/BW	kidney weight to body weight
L	left
LA	left atrium
LKB1	serine/threonine kinase LKB1
loxP	locus of X-over P1
LPD	low protein diet
LV	left ventricle
LVID	left ventricular internal diameter
LVNC	left ventricular noncompaction
LVPW	left ventricular posterior wall
LW	liver weight
LW/BW	liver weight to body weight
MeOH	methanol
MLST8	mammalian lethal with sec-13 protein 8
M-mode	motion mode
mRNA	messenger ribonucleic acid
MSIN1	mammalian stress-activated map kinase-interacting protein

Mtor	mechanistic target of rapamycin
mTORC1/2	mechanistic target of rapamycin complex 1/2
Myh7	β-myosin heavy chain
n	number
n/a	not applicable
Na_2HPO_4	disodium hydrogen phosphate
NaCl	sodium chloride
NaOH	sodium hydroxide
NCBI	National Center for Biotechnology Information
NGS	normal goat serum
Nkx2-5	NK2 homeobox 5 gene
Nkx2-5Cre	NK2 homeobox 5 gene with *Cre* recombinase sequence in 3´ untranslated region
NP-40	Nonyl phenoxypolyethoxylethanol
Nppa/b	natriuretic peptide type A/B
OD	optical density
OFT	outflow tract
o/n	over night
p	phosphor
P1/P2/P3	postnatal day 1/2/3
PBS	phosphate buffered saline
PCR	polymerase chain reaction
PDK1	phosphoinositide-dependent kinase 1
PEG300	polyethylene glycol 300
PFA	paraformaldehyde
pH	*potentia hydrogenii* (power of water)
p-HH3	phospho-histone H3
PI3K	phosphoinositide 3-kinase
POI	protein of interest
PRAS40	proline-rich Akt substrate 40 kDa
PROTOR1/2	protein observed with rictor 1 and 2
PT	pulmonary trunk
PV	pulmonary vein
p-value	probability value
qPCR	quantitative real-time PCR
R	right
RA	right atrium
Raptor	regulatory-associated protein of mTOR
RAG	RAS-related GTP-binding protein
RAS	renin-angiotensin system
Rheb	Ras homolog enriched in brain
Rictor	rapamycin-insensitive companion of mTOR
RIPA	radioimmunoprecipitation assay
RNA	ribonucleic acid
RNase	ribonuclease
RP	reverse primer
Rpm	rotations per minute
rRNA	ribosomal ribonucleic acid
RT	room temperature
RV	right ventricle
S6	S6 ribosomal protein
S6K1	S6 kinase 1
s.c.	subcutaneous
SDS	sodium dodecyl sulfate
SDS-PAGE	sodium dodecyl sulfate polyacrylamid gel electrophoresis
SEM	standard error of the mean
Ser	serine
SGK1	serum- and glucocorticoid-induced protein kinase 1
SPD	standard protein diet
SPSS	Statistical Package for the Social Sciences
Sry	sex determining region of chromosome Y gene
SVC	superior vena cava
SW	spleen weight
SW/BW	spleen weight to body weight
sys	systole

T	thymine
T_A	annealing temperature
TAC	transverse aortic constriction
TBS	tris buffered saline
TBS-T	tris buffered saline with Tween 20
TdT	terminal deoxynucleotidyl transferase
TEMED	tetramethylethylenediamine
Tgfβ1/3	transforming growth factor, beta 1/3
Thr	threonine
TM	trademark
Tr	trabeculae
Tris	tris(hydroxymethyl)aminomethane
Tris-HCl	Tris-hydrochloride
TrM	trabeculated myocardium
tRNA	transfer ribonucleic acid
TSC1/2	tuberous sclerosis 1/2
TTE	tris-taurin-EDTA
TUNEL	terminal deoxynucleotidyl transferase dUTP nick end labeling
Tyr	tyrosine
ULK1	unc-51-like kinase 1
UPR	unfolded protein response
USA	United States of America
UV	ultraviolet
Vim	vimentin
vs.	versus
v/v	volume per volume
w/v	weight per volume
WGA	wheat germ agglutinin
WHO	world health organization
WT	wildtype
Yap1	yes-associated protein 1

Measurement units were used according to the SI (Le Système international d'unités, International System of Units).

Gene and protein names were used according to “The National Center for Biotechnology Information” (NCBI). Murine gene and protein nomenclature was applied according to the guidelines of the “International Committee on Standardized Genetic Nomenclature for Mice”. Murine gene symbols are italicised, with only the first letter in uppercase and the remaining letters in lowercase (e.g. *Mtor*). Murine protein designations are not italicised and all letters are upper case (e.g. MTOR).

LIST OF TABLES

Table 1. Protein components of the two mTOR complexes and their known functions 17
Table 2. Laboratory equipment 27
Table 3. Consumables 28
Table 4. Chemicals and reagents 28
Table 5. Size standards 30
Table 6. Enzymes and enzyme kits 30
Table 7. Inhibitors 30
Table 8. Formulation of buffers and solutions 30
Table 9. Consumable kits 31
Table 10. PCR Primers 32
Table 11. Antibodies for western blot 33
Table 12. Antibodies for immunohistochemistry 34
Table 13. Other substances for immunohistochemistry 34
Table 14. Software 34
Table 15. Online tools 35
Table 16. Genotyping PCR setup 44
Table 17. Gel composition for SDS-PAGE 50
Table 18. Neonatal c*Hccs*$^{+/-}$ hearts display significant enrichment of genes involved in amino acid homeostatic and metabolism 59

Supplementary Table S1. Differentially regulated genes in neonatal c*Hccs*$^{+/-}$ hearts XII
Supplementary Table S2. Neonatal c*Hccs*$^{+/-}$ hearts display enrichment of genes involved in amino acid metabolism XVI
Supplementary Table S3. Neonatal c*Hccs*$^{+/-}$ hearts display enrichment of genes involved in amino acid transport XVI
Supplementary Table S4. Neonatal c*Hccs*$^{+/-}$ hearts display enrichment of genes involved in cellular metabolism XVI
Supplementary Table S5. Echocardiographic measurements in neonatal mice after prenatal mTORC1 inhibition XVII
Supplementary Table S6. Echocardiographic measurements in 11 week old adult mice after prenatal mTORC1 inhibition XVII
Supplementary Table S7. Echocardiographic measurements in 11 week old adult mice after pre- and postnatal amino acid restriction XVII

LIST OF FIGURES

Figure 1. Schematic drawing of the mammalian heart. 6
Figure 2. The “thrifty phenotype” hypothesis. 8
Figure 3. Morphogenesis of the mouse heart during the second half of gestation. 12
Figure 4. mTORC1 and mTORC2 have distinct cellular functions. 17
Figure 5. Simplified schematic drawing of the mTOR signaling network in mammalian cells. 20
Figure 6. Breeding strategy to generate heart conditional *Hccs* KO mice. 38
Figure 7. Breeding strategy to generate heart conditional *Raptor* KO mice. 39
Figure 8. Elevated mTORC1 activity in neonatal c*Hccs*$^{+/-}$ hearts. 61
Figure 9. Successful mTORC1 inhibition in neonatal hearts. 64
Figure 10. Prenatal mTORC1 inhibition neither changes litter size nor genotype distribution. 65
Figure 11. Prenatal mTORC1 inhibition induces overall growth restriction and reduces heart size in neonatal mice. 67
Figure 12. Prenatal mTORC1 inhibition does not affect cardiomyocyte proliferation rates but induces apoptosis and reduces cardiomyocyte size in neonatal hearts. 69
Figure 13. Echocardiographic measurements in neonatal mice after prenatal mTORC1 inhibition revealed largely normal cardiac function. 71
Figure 14. Adult mice after prenatal mTORC1 inhibition demonstrate partial normalization of body and heart weight. 73
Figure 15. Prenatal mTORC1 inhibition increases cardiomyocyte CSA but does not cause pathological remodeling or impaired cardiac function in 11 week old adult hearts. 75
Figure 16. Cardiac-restricted *Raptor* KO mice (c*Raptor*$^{-/-}$) die in utero. 78
Figure 17. Food intake of non-pregnant and pregnant adult females on SPD and LPD does not differ. 80
Figure 18. Intrauterine amino acid restriction neither affects litter size nor genotype distribution. 81
Figure 19. Prenatal LPD exposure does not change cardiac morphology of neonatal hearts but reduces HW/BW ratio in c*Hccs*$^{+/-}$ newborns compared to *Hccs*$^{+/+}$ controls. 82
Figure 20. Intrauterine LPD exposure does not alter proliferation rates but increases cardiomyocyte CSA in the LV myocardium of *Hccs*$^{+/+}$ and c*Hccs*$^{+/-}$ neonatal hearts. 84
Figure 21. LPD 13.5 dpc hearts demonstrate normal mTOR pathway activity and resemble SPD 13.5 dpc hearts in morphology. 86
Figure 22. Prenatal amino acid restriction neither induces apoptosis nor reduces proliferation but does affect the expression of cell cycle regulating genes in 13.5 dpc embryonic hearts. 89
Figure 23. Pre- and postnatal amino acid restriction neither alters mTOR pathway activity nor causes overall growth retardation or heart size reduction in 11 week old adult mice. 92
Figure 24. Pre- and postnatal amino acid restriction results in reduced cardiomyocyte size but does not induce compensatory fibrosis in 11 week old adult hearts. 94
Figure 25. Pre- and postnatal amino acid restriction neither induces the expression of genes associated with cardiac stress nor alters cardiac function in 11 week old adult LPD mice. 97

Supplementary Figure 1. Protein levels and phosphorylation status of mTORC1 and mTORC2 core components are unchanged in c*Hccs*$^{+/-}$ neonatal hearts. XVIII
Supplementary Figure 2. Phosphorylation status of mTORC1 downstream targets S6K1 and S6 is unchanged in 3 day and 3 week old c*Hccs*$^{+/-}$ hearts compared to hearts from *Hccs*$^{+/+}$ littermate controls. XVIII
Supplementary Figure 3. Prenatal rapamycin treatment of pregnant mice results in mTORC1 inhibition in neonatal kidney and lung tissue as well as reduced neonatal kidney weight. XIX
Supplementary Figure 4. Prenatal mTORC1 inhibition from 11.5 dpc onwards results in preterm birth and fetal lethality. XIX
Supplementary Figure 5. Organ weights of liver, kidney and spleen in 11 week old adult mice upon intrauterine mTORC1 inhibition are not significantly different compared to those of vehicle treated animals. XX

1 SUMMARY

Intrauterine development influences the susceptibility to cardiovascular disease in adulthood, although the underlying molecular mechanisms are vastly unknown. Our group has previously demonstrated that the murine prenatal heart has a substantial regenerative capacity in response to tissue mosaicism for mitochondrial dysfunction caused by heart-specific inactivation of the X-linked holocytochrome *c* synthase (*Hccs*) gene. In heterozygous heart conditional *Hccs* knockout (c*Hccs*$^{+/-}$) embryos, hyperproliferation of healthy cardiomyocytes compensates for the effective loss of 50 % cardiac cells, ensuring formation of a normally contracting heart at birth. However, it was assumed that embryonic heart regeneration alters peri- and postnatal cardiac growth. Indeed, neonatal c*Hccs*$^{+/-}$ hearts are hypoplastic and contain a reduced number of cardiomyocytes. Thereby, c*Hccs*$^{+/-}$ mice resemble many findings of classical intrauterine growth restriction (IUGR) models, which also demonstrate hypoplastic hearts and a reduced complement of cardiomyocytes at birth. Interestingly, in adult c*Hccs*$^{+/-}$ hearts, compensatory increase in cell size (hypertrophy) normalizes morphology and organ size.

The PhD project presented here aims at identifying pre- and postnatal adaptive growth mechanisms utilized by the hypoplastic c*Hccs*$^{+/-}$ heart to restore organ size and allow normal heart function throughout lifetime. Unbiased functional annotation of genes differentially expressed in neonatal c*Hccs*$^{+/-}$ hearts (identified in a genome wide RNA microarray screen) revealed numerous gene clusters involved in amino acid metabolism and protein homeostasis. The mechanistic target of rapamycin (mTOR) pathway is a master regulator of postnatal cardiac metabolism and growth that is sensitive to amino acid availability. We hypothesized that both normal amino acid homeostasis as well as mTOR pathway activation are crucial to sustain regeneration and compensatory growth of c*Hccs*$^{+/-}$ hearts to build a regularly sized organ and allow normal postnatal function.

Indeed, we revealed increased mTOR pathway activity in neonatal c*Hccs*$^{+/-}$ hearts compared to littermate controls. To elucidate the role of the mTOR pathway for c*Hccs*$^{+/-}$ heart development, growth and function, we inhibited mTOR complex 1 (mTORC1) in fetal and neonatal mice by rapamycin treatment of pregnant dams. Rapamycin treated neonates were characterized by overall growth restriction (reduction of whole body size and organ weights) and developmental delay, where cardiac development was especially affected with most severe consequences in c*Hccs*$^{+/-}$ hearts (reduction of heart size, weight and heart weight to body weight ratio, severe thinning and noncompaction of the ventricular myocardium as well as immature myocardial morphology). While proliferation rates in neonatal rapamycin treated hearts were unaffected, the reduced neonatal heart size was attributed to decreased cardiomyocyte size and increased apoptosis compared to vehicle treated neonates, both were again more pronounced in rapamycin c*Hccs*$^{+/-}$ hearts than in rapamycin *Hccs*$^{+/+}$ hearts.

This indicates not only the importance of the mTOR pathway for cardiac development in general, but furthermore suggests that its enhanced activation is of particular importance for the developmentally impaired c*Hccs*$^{+/-}$ heart. Surprisingly, prenatal mTORC1 inhibition only marginally affects heart function in newborn mice as determined by echocardiography. Moreover, reduced neonatal body and heart size was mostly normalized during postnatal life in both genotypes until the age of 11 weeks. Postnatal normalization of heart size was achieved by increased cardiomyocyte size, while extracellular matrix deposition was not affected. Furthermore, no indications for pathological conditions or myocardial tissue remodeling were observed in adult hearts after prenatal mTORC1 inhibition and cardiac function in adulthood was normal. In conclusion, we propose that prenatal mTORC1 inhibition by rapamycin treatment of pregnant dams represents a new model of IUGR in the mouse, which allows the investigation of developmental programming mechanisms particularly in the fetal and neonatal phase of development.

Given the induction of genes involved in amino acid metabolism in neonatal c*Hccs*$^{+/-}$ hearts, we studied the effect of pre- and postnatal amino acid restriction on cardiac development, growth and function by feeding dams a low protein diet (LPD) throughout pregnancy and keeping the offspring on LPD until adulthood. Even though we did not find major effects of prenatal amino acid restriction on body and heart weight of neonatal *Hccs*$^{+/+}$ and c*Hccs*$^{+/-}$ mice, we observed increased cardiomyocyte size at birth in both LPD genotypes compared to their corresponding standard protein diet (SPD) controls. To investigate the underlying mechanisms that allow normal heart size despite increased cardiomyocyte size, we focused on proliferation rates. Importantly, proliferation in neonatal hearts was found to be unaffected by prenatal LPD exposure. Hence, we speculated that intrauterine LPD treatment might reduce proliferation rates in prenatal hearts, potentially resulting in a reduction of the cardiomyocyte number at birth. However, proliferation was unaffected in 13.5 days post coitum (dpc) LPD embryonic hearts as well. Still, proliferation rates in fetal LPD hearts remain to be investigated. In adulthood, heart size and function of unstressed LPD animals were normal. Even though amino acid restriction did not affect postnatal heart growth on the organ level, cardiomyocyte size in LPD adults was surprisingly reduced compared to adult SPD mice, whereas extracellular matrix deposition was normal. These data point toward other cardiac cell types that might compensate for the decreased cardiomyocyte size in adulthood resulting in normal heart size of adult LPD animals. Taken together, the embryonic murine heart appears to be surprisingly resistant to intrauterine amino acid restriction. These findings suggest that the late fetal period might be the more vulnerable phase during development and is especially sensitive for maternal malnutrition, which might have major implications in the context of IUGR, developmental programming and disease prevention in humans.

2 ZUSAMMENFASSUNG

Die Entwicklung eines Embryos und Fetus im Uterus beeinflusst die Anfälligkeit für kardiovaskuläre Erkrankungen im weiteren Verlauf des Lebens entscheidend. Die zugrundeliegenden molekularen und zellulären Mechanismen sind jedoch weitestgehend unbekannt. Das pränatale Mausherz weist eine beachtliche Regenerationsfähigkeit auf. So resultiert die Herz-spezifische Inaktivierung des X-chromosomalen „*holocytochrome c synthase*“ (*Hccs*) Gens in einem Zellmosaik für mitochondriale Dysfunktion. In Embryonen, welche heterozygot für den kardialen *Hccs* Knockout (c*Hccs*$^{+/-}$) sind, kompensieren die gesunden Kardiomyozyten den Verlust der 50 % dysfunktionalen *Hccs*-defizienten Zellen durch vermehrte Proliferation. Dadurch wird bis zur Geburt ein funktionsfähiges Herz gebildet. Möglicherweise beeinflusst diese embryonale Herzregeneration jedoch das peri- und postnatale Herzwachstum. Tatsächlich sind neugeborene c*Hccs*$^{+/-}$ Herzen hypoplastisch und beinhalten eine reduzierte Kardiomyozytenzahl. Damit ähnelt das c*Hccs*$^{+/-}$ Modell klassischen Tiermodellen für intrauterine Wachstumseinschränkung („*intrauterine growth restriction*“, IUGR), welche bei der Geburt ebenfalls hypoplastische Herzen mit einer verminderten Anzahl an Kardiomyozyten haben. Interessanterweise konnte in Herzen ausgewachsener c*Hccs*$^{+/-}$ Mäuse gezeigt werden, dass ein verstärktes Größenwachstum der Kardiomyozyten zur Normalisierung der Herzgröße führt.

Die vorliegende Doktorarbeit zielt auf die Identifikation prä- und postnataler adaptiver Wachstumsmechanismen ab, welche dem hypoplastische c*Hccs*$^{+/-}$ Herz die Anpassung der Organgröße und die Aufrechterhaltung einer normalen Herzfunktion im Verlauf des Lebens ermöglichen. Funktionelle Annotationsanalysen differenziell exprimierter Gene in neugeborenen c*Hccs*$^{+/-}$ Herzen identifizierten viele Gencluster, welche im Aminosäuremetabolismus und in der Proteinhomeostase eine Rolle spielen. Die „*mechanistic target of rapamycin*“ (mTOR) Signalkaskade ist ein zentraler Regulator des postnatalen kardialen Metabolismus und Wachstums und ist außerdem sensitiv gegenüber der Aminosäureverfügbarkeit. Wir vermuteten, dass sowohl eine ausgeglichene Aminosäurehomöostase als auch die Aktivität der mTOR Signalkaskade eine entscheidende Rolle bei der pränatalen Regeneration und dem postnatalen kompensatorischen Wachstum der c*Hccs*$^{+/-}$ Herzen spielen und sind somit am Aufbau der regulären Organgröße und der Aufrechterhaltung der normalen postnatalen Herzfunktion beteiligt sind.

Tatsächlich haben wir eine erhöhte Aktivität der mTOR Signalkaskade in neugeborenen c*Hccs*$^{+/-}$ Herzen im Vergleich zu Wurfkontrollen festgestellt. Um die Rolle der mTOR Signalkaskade hinsichtlich Entwicklung, Wachstum und Funktion der c*Hccs*$^{+/-}$ Herzen zu analysieren, haben wir den mTOR Komplex 1 (mTORC1) in fetalen und neugeborenen Mäusen mittels einer Rapamycin-Behandlung in trächtigen Weibchen inhibiert. Rapamycin-behandelte Neugeborene zeichneten sich durch ein vermindertes Gesamtwachstum sowie

einer Entwicklungsverzögerung aus. Dabei war die kardiale Entwicklung besonders betroffen, was sich mit größter Deutlichkeit in den c*Hccs*$^{+/-}$ Herzen zeigte (z.B. Reduktion von Herzgröße, -gewicht, Verhältnis von Herzgewicht zu Körpergewicht sowie deutliche Verdünnung und mangelnde Kompaktierung des ventrikulären Myokards). Proliferationsraten in Herzen Rapamycin-behandelten Neugeborenen waren nicht verändert. Jedoch konnte die verminderte Herzgröße auf eine verringerte Kardiomyozytengröße sowie auf eine erhöhte Apoptoserate (verglichen mit Vehikel-behandelten Neugeborenen) zurückgeführt werden. Beide zellulären Veränderungen waren erneut besonders deutlich in den Rapamycin-behandelten c*Hccs*$^{+/-}$ Herzen ausgeprägt. Diese Beobachtungen heben einerseits die Bedeutung der mTOR Signalkaskade für das grundlegende perinatale kardiale Wachstum hervor und zeigen andererseits, dass eine erhöhte Aktivität der mTOR Signalkaskade in c*Hccs*$^{+/-}$ Herzen nach gestörter pränataler Entwicklung von besonderer Bedeutung ist. Überraschenderweise führt die pränatale mTORC1 Inhibierung nur zu geringfügigen Veränderungen der Herzfunktion neugeborener Mäuse. Des Weiteren normalisierte sich das reduzierte Körper- und Herzgewicht der neugeborenen Rapamycin-behandelten Mäuse weitestgehend im weiteren Verlauf des Lebens bis zum Alter von 11 Wochen. Die postnatale Normalisierung der Herzgröße wird durch eine erhöhte Kardiomyozytengröße gewährleistet. Vermehrte Ablagerungen extrazellulärer Matrix oder pathologische Fibrose waren dabei nicht zu beobachten. Anhaltspunkte für pathologische Zustände oder myokardialen Gewebeumbau in 11 Wochen alten Mausherzen nach pränataler Rapamycin-Behandlung wurden ebenfalls nicht gefunden. Auch die Herzfunktion war normal. Zusammenfassend schlagen wir die pränatale mTORC1-Inhibierung durch Rapamycin-Behandlung trächtiger Weibchen als ein neues IUGR Modell vor, welches Untersuchungen von Programmierungs-Mechanismen vor allem in der fötalen und perinatalen Entwicklung erlaubt.

Angesichts der Induktion von Aminosäuremetabolismus-relevanten Genen in neonatalen c*Hccs*$^{+/-}$ Herzen, untersuchten wir die Auswirkungen prä- und postnataler Aminosäurerestriktion auf Herzentwicklung, -wachstum und -funktion. Hierfür wurde Mäusen während der gesamten Schwangerschaft eine Niedrigproteindiät („*low protein diet*“, LPD) gefüttert. Die Nachkommen wurden anschließend fortführend auf LPD gehalten. Zwar fanden wir keine weitreichenden Veränderungen hinsichtlich Körper- und Herzgröße neugeborener *Hccs*$^{+/+}$ und c*Hccs*$^{+/-}$ Mäuse, jedoch konnten wir eine deutlich erhöhte Kardiomyozytengröße in beiden LPD Genotypen verglichen mit den jeweiligen Standardproteindiät (SPD) Kontrollgruppen bei der Geburt feststellen. Um zu untersuchen, wodurch die Herzgröße trotz erhöhter Kardiomyozytengröße konstant gehalten wird, fokussierten wir uns auf Proliferationsraten. Kardiale Proliferationsraten in neugeborenen LPD Mäusen waren unverändert verglichen mit neugeborenen SPD Mäusen. Demnach könnte eine pränatale Aminosäurerestriktion jedoch Auswirkungen auf die Proliferationsraten in pränatalen Herzen

haben und somit eventuell zu einer verringerten Zellzahl in neugeborenen Herzen führen. Allerdings waren die Proliferationsraten in 13.5 dpc embryonalen Herzen ebenfalls nicht durch Aminosäurerestriktion verändert. Analysen der Proliferationsraten in fetalen LPD Herzen wurden bisher jedoch nicht durchgeführt. Herzgröße und -funktion in 11 Wochen alten ungestressten LPD Mäusen waren normal obwohl die Kardiomyozytengröße in adulten LPD Herzen verringert war. Diese Daten lassen daher vermuten, dass andere kardiale Zelltypen die verringerte Kardiomyozytengröße kompensieren, was in einem normalen Herzgewicht in 11 Wochen alten LPD Tieren resultiert. Zusammenfassend ist festzuhalten, dass embryonale Mausherzen erstaunlich resistent gegenüber intrauteriner Aminosäurerestriktion sind. Jedoch scheint die späte Fetalphase die entscheidende und am meisten verwundbare Phase während der Entwicklung im Uterus zu sein, welche daher möglicherweise besonders empfindlich für maternale Mangelernährung ist. Perspektivisch könnte dies bedeutende Auswirkungen im Hinblick auf IUGR und der Prävention von Erkrankungen im Erwachsenenalter im Menschen haben.

3 INTRODUCTION

3.1 The heart of the matter

The mature mammalian heart consists of four valves and four chambers (two cranial atria and two caudal ventricles) with the wall of each chamber built up of three tissue layers: endocardium, myocardium and epicardium (Figure 1). As a muscular organ, it constantly pumps blood throughout the blood vessels to all parts of the body by repeated, rhythmic contractions. The human heart beats approximately 60-80 times per minute, which sums up to over 30 billion beats per lifetime with a total volume of 200 million liter blood that is pumped through the body's blood vessels. During each cardiac cycle, the right atrium (RA) relaxes and receives deoxygenated blood from the body periphery via the vena cava. In diastole, the relaxed right ventricle (RV) receives blood through the tricuspid valve from the contracting RA. Subsequent contraction of the RV during systole passes the blood through the pulmonary valve into the pulmonary arteries to the lungs, where carbon dioxide is exchanged for oxygen. Oxygenated blood returns from the lungs through the pulmonary veins into the relaxed left atrium (LA). The latter then contracts and the blood is pushed through the mitral valve into the relaxed left ventricle (LV). Subsequent contraction of the LV during systole ejects the oxygenated blood out of the heart through the aortic valve into the aorta from where it is distributed to the systemic circulation (Figure 1).

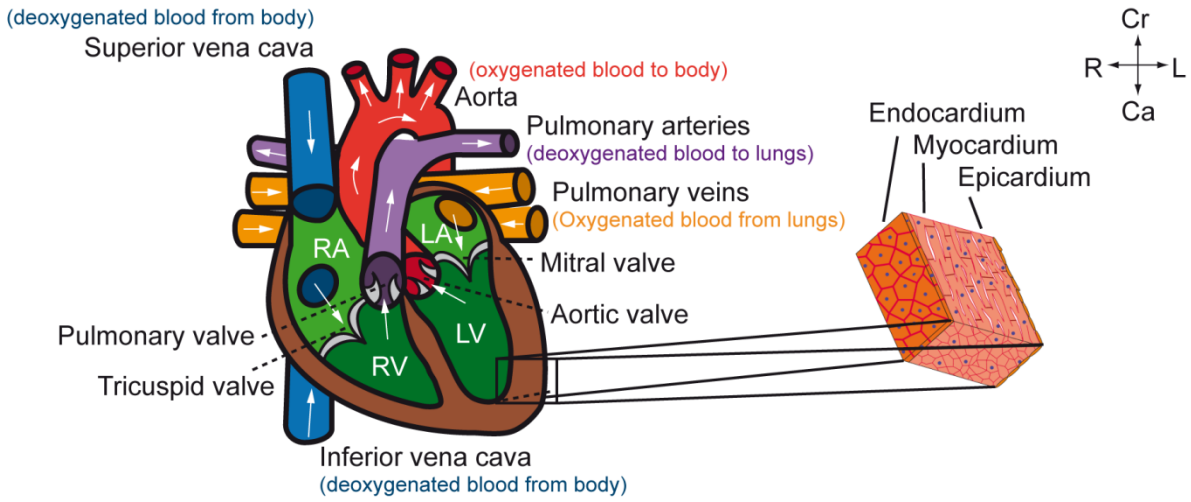

Figure 1. Schematic drawing of the mammalian heart.
The mature mammalian heart consists of four chambers (left (LV) and right (RV) ventricle, left (LA) and right (RA) atrium) and four valves (pulmonary, tricuspid, mitral and aortic valve). The wall of each chamber is built up of three tissue layers: endocardium, myocardium and epicardium. The compass indicates the orientation of the heart in the body (Ca: caudal, Cr: cranial, L: left, R: right). Figure modified from Lin *et al*. 2012[1].

According to the World Health Organization (WHO), cardiovascular diseases (CVD) are the most common cause of death worldwide with 17.5 million people killed in 2012. The numbers are continuously increasing with dramatic costs for health care systems (according to the Federal Statistical Office ("*Statistisches Bundesamt*") 37 Billion Euro only in Germany in

2008). Importantly, causes of CVD can be found in both embryonic development and adulthood. While classical lifestyle-related risk factors, for instance hypertension, smoking, obesity or diabetes, are widely acknowledged to cause CVD, developmental origins of CVD are far less established and are not necessarily part of the public awareness. Thus, investigation and elucidation of mechanisms underlying the latter remain absolutely imperative to allow better disease prevention.

3.2 Developmental programming of adulthood disease

3.2.1 The developmental programming concept ("thrifty phenotype" hypothesis)

Mammalian development *in utero* is a complex and dynamic process. It depends on the interaction of the mother with the embryo or fetus, respectively, to sustain optimal growth and survival throughout pregnancy. The supply of the growing embryo and fetus with nutrients, oxygen and endocrine signals impacts not only the growth of the unborn itself but also the health of the offspring in adulthood (Figure 2). In this context, low birth weight in newborns was suggested to be inversely related to the susceptibility for CVD, cardiovascular mortality and insulin resistance in adulthood[2-6]. Based on these initial observations, Hales and Barker proposed the "thrifty phenotype" hypothesis, which states that fetuses exposed to unfavorable intrauterine growth conditions induce various permanent physiological cellular, molecular and metabolic adaptations in anticipation of similar suboptimal conditions in postnatal life[7] (Figure 2). This programming might slow down embryonic and fetal growth, ultimately resulting in lower birth weight[7]. In case of nutritionally rich postnatal conditions and resources, as provided in the Western culture, the adaptive changes could become maladaptive and the trade-off for overcoming the challenge during intrauterine development might be an increased susceptibility to suffer from chronic diseases in later life[7]. Supporting evidence for the developmental programming concept comes from human epidemiology. Studies with monozygotic twins revealed that the twin with Type 2 diabetes mellitus in adulthood had a significantly lower birth weight compared to its euglycaemic co-twin[8]. Periods of famine also provide important insights regarding the effects of global nutrient restriction during pregnancy. The Second World War Dutch famine was provoked by a Nazi blockade of the western part of Holland from 1944 to 1945. Caloric intake was severely reduced to a daily dose of 450-750 kcal. Individuals born from pregnancies during the famine suffered from maternal undernutrition, had lower birth weights and displayed increased occurrence of coronary heart disease and elevated atherogenic blood lipids in adulthood[9-11].

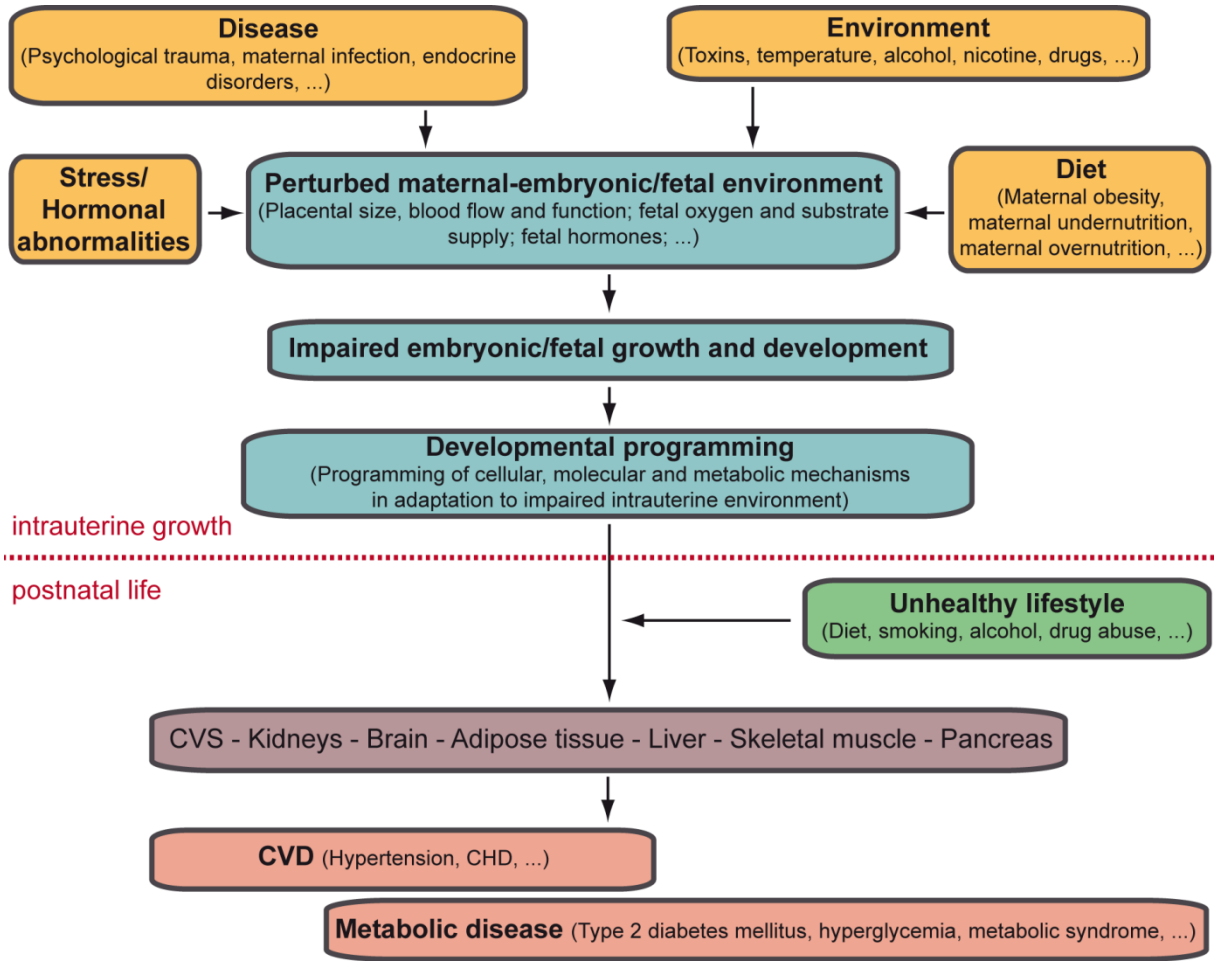

Figure 2. The "thrifty phenotype" hypothesis.
Adverse environmental cues from the mother (yellow) cause unfavorable intrauterine growth conditions for the developing embryo and fetus (blue). Subsequently, permanent physiological adaptations in the unborn are induced, a process known as developmental programming. This programming in combination with an unhealthy lifestyle later in life (green) systemically affects a variety of different organ systems (purple) and consequently predisposes the entire organism for chronic diseases in adulthood (red). Figure modified from Fowden *et al.*[12] and Langley-Evans and McMullen[13]. (CHD: coronary heart disease, CVD: cardiovascular disease, CVS: cardiovascular system)

Importantly, intrauterine growth restriction (IUGR) is not the only determinant of long-term health. Various lifestyle-related risk factors (e.g. drug abuse, alcohol and nicotine consumption) as well as accelerated postnatal growth (also referred to as "catch-up growth", e.g. due to obesity) additionally promote the manifestation of adulthood disease following IUGR and developmental programming[14-17] (Figure 2). For example, the Dutch famine studies demonstrated that individuals with the worst glucose tolerance were those who had a low birth weight and became obese as adults[9]. Thus, suboptimal intrauterine conditions cause a predisposition for adulthood diseases that is manifested if additional stress occurs later in life (Figure 2). This combination of developmental programming and unhealthy lifestyle is a major risk factor of the world wide epidemic of the most common chronic adulthood diseases, such as stroke, hypertension, coronary heart disease, Type 2 diabetes mellitus, hyperglycemia or metabolic syndrome[18,19] (Figure 2). Furthermore, developmental programming is at least partially responsible for the increasing incidence of diabetes in low-

and middle-income countries, where the combination of poor nutrition *in utero* and overnutrition in later life is common[20].

Unfortunately, due to the long time span between the impairment of development *in utero* and the observable consequences later in life, very little mechanistic knowledge can be retrieved from these few human epidemiology studies. However, there is accumulating experimental data from a variety of animal models, which try to shed light on this problem (see Chapter 3.2.2).

3.2.2 Animal models of intrauterine growth restriction and implications for the heart

Intrauterine growth restriction (IUGR) is the most commonly used model in various animal species to identify basic molecular and cellular mechanisms of developmental programming. To date, consequences of IUGR on cardiac development and growth are best described in studies manipulating maternal nutrition during gestation. Fetal nutrient supply is one of the most important environmental determinants affecting pregnancy outcome, where amino acids are assigned a key role[21]. The original rodent model of maternal protein and thus amino acid restriction involves feeding pregnant rats a isochaloric low protein diet (LPD) (8-10 % protein versus 20-22 % protein in standard protein diet (SPD))[22]. Body (BW) and heart weight (HW) of LPD newborns are significantly lower compared to pups from dams on SPD[23]. Although HW to BW (HW/BW) ratio is not different between the diet groups, hearts of LPD newborn rats have significantly less cardiomyocytes[23]. Consistently, a suppressed replicative potential of neonatal cardiomyocytes correlates with prenatal LPD[24]. Notably, changes in HW and cardiomyocyte number in LPD neonatal rats often normalize within the first few weeks of life if the diet is changed to SPD after birth, indicating postnatal compensatory growth[25]. Interestingly, prenatal amino acid restriction provokes significant changes in heart morphology and function later in life, as obvious by increased deposition of extracellular matrix (ECM)[26], cardiac hypertrophy[27] and increased stiffening[28] of the LV in young adults under baseline conditions. Consistently, spontaneous cardiac dysfunction[27], impaired recovery after ischemia-reperfusion injury[28-30], and altered cellular stress response[31] were observed in adult rat hearts upon intrauterine amino acid restriction, suggesting significant consequences of LPD-induced IUGR for the health of the cardiovascular system in adulthood.

In humans, placental insufficiency (e.g. due to abnormalities in placental development or maternal nicotine abuse) is one of the most common causes of IUGR in Western societies and results in low birth weight offspring that are predisposed to adulthood disease[32]. Placental insufficiency, induced by uterine artery ligation in pregnant rats, resembles many observations seen after LPD, such as HW reduction and decreased cardiomyocyte number in neonates[33]. In line with the LPD studies, these impairments can be restored if postnatal nutrition is normalized[33]. Although the underlying cellular mechanisms (i.e. proliferative or hypertrophic

growth) are poorly understood, these findings also indicate postnatal restoration of cardiac organ size after IUGR.

In addition, IUGR can result from maternal chronic hypoxia. Experimental studies in pregnant rats exposed to low oxygen conditions (10.5 % low oxygen compared to 21 % normal oxygen) for a defined period of time during gestation demonstrated increased HW/BW ratios in neonates and in fetuses prior to birth[34,35]. Furthermore, apoptosis rates in fetal hearts are increased and cardiomyocytes are prematurely terminally differentiated and hypertrophic[34]. In mice, maternal hypoxia during pregnancy causes ventricular dilation, myocardial hypoplasia (thinner ventricular myocardium) as well as heart failure in mid-gestation embryos[36]. Importantly, prenatal hypoxia leads to LV hypertrophy and increased cardiomyocyte size in adult rat hearts[35,37]. Furthermore, intrauterine hypoxia has significant adverse consequences for cardioprotection in the adult rat myocardium, resulting in pathological cardiac remodeling[28], cardiac fibrosis[28] and LV diastolic dysfunction[35] under baseline conditions as well as increased susceptibility to ischemia-reperfusion injury[28,38]. Notably, maternal nutritional intake is reduced by hypoxia[28], suggesting that there might be an overlap in the consequences observed after IUGR induced by maternal hypoxia or maternal undernutrition.

All these IUGR models agree that perturbations of intrauterine environment affect cardiomyocyte morphology and number as well as heart size at birth. Moreover, even though the results are not always consistent (perhaps reflecting differences in methodology, the animal species or strains), most of these studies demonstrate that postnatal restoration of cardiac organ size after IUGR occurs and, importantly, is associated with adverse consequences for heart morphology and function later in life. In human studies (see Chapter 3.2.1), accelerated postnatal growth was also correlated with an increased risk for CVD in adulthood[14-17]. These observations strongly support the concept of developmental programming. However, studies identifying precise molecular mechanisms and targets are rare. The most widely discussed mechanism how such programming might happen are epigenetic modifications of certain gene promoters resulting in aberrant gene expression[39]. Even though the epigenetic code is heritable, it is thought not to be fixed throughout the entire lifetime. Instead, it is known to be vulnerable to alterations during several life stages: embryogenesis, fetal and neonatal development, puberty as well as old age[40,41]. During gestation, the developing embryo and fetus is subject to both demethylation and remethylation[42]. Thus, the process of methylation is a good candidate for disturbances by environmental interference and hence provides a potential mechanism for developmental programming. Even if such changes have rarely been experimentally proven yet, epigenetic modifications of renin-angiotensin system (RAS) components have been suggested to be affected by intrauterine LPD in rats[43]. In this context, the expression of the murine AT_{1b}

angiotensin receptor gene in the adrenal gland was upregulated by the first week of life, which was accompanied by significant undermethylation of the proximal promoter of the AT_{1b} gene[43]. Importantly, these changes were suggested to provoke adulthood hypertension in the LPD rat model[43]. However, the precise molecular mechanisms that underlie such an alteration in methylation pattern as a result of developmental programming remain to be determined. Consequently, the actual programming mechanisms that enhance disease susceptibility in adulthood after impaired intrauterine development remain mostly obscure. Due to the short life span and reproduction time of most animal models, long-term consequences of developmental programming, which would be more relevant for human subjects, are difficult to analyze. Besides, because IUGR affects the entire organism, dissecting developmental programming mechanisms in one particular organ and differentiating between primary and secondary causes and effects imposed by systemic alterations remains difficult. Nevertheless, only if these challenges are successfully solved and basic processes of developmental programming in the heart are uncovered, focus can be directed toward therapeutic or preventive strategies for adulthood CVD induced during prenatal development.

3.3 Growth and organ size control of the mammalian heart

IUGR affects hearts size and cardiomyocyte number and thereby impacts on postnatal cardiovascular health. But how does the heart grow after all? Between the early heart tube stage and adulthood, the murine heart increases more than 300-fold in mass[44]. While fetal cardiac growth mainly occurs through cardiomyocyte proliferation, postnatal heart growth primarily involves increased cardiomyocyte size. Importantly, both the early patterning events of the embryonic heart and growth as well as maturation of the various cardiac structures during embryonic, fetal and postnatal life are essential for survival of the entire organism.

3.3.1 Prenatal cardiac development and growth

Mammalian heart development from a simple tube-like vessel into a mature complex four-chambered organ has been examined extensively over the past decades, whit the mouse being the best studied model[45-47]. In the murine embryo, at about 8 days post coitum (dpc), a primitive linear heart tube composed of a myocardial and endocardial cell layer has formed, which shortly after begins to contract. Between 8.5 dpc and 10.5 dpc, the heart tube undergoes rightward looping to align the atria as well as inflow and outflow tract cranial to the ventricles. Furthermore, the future ventricles become distinct and balloon outwards. Meanwhile, a third tissue layer is added to the outer surface of the heart, called epicardium. At the same time, myocardial cells of the ventricular chambers proliferate, differentiate and protrude into the lumen to develop trabeculation of endocardium-covered myocardium. The trabeculae formed at the inner curvature of the ventricular chambers are especially important

for proper and powerful cardiac contraction. Moreover, the inner surface area increases and the nutritional requirements of the growing myocardium can be met from the luminal blood even in the absence of a mature coronary circulatory system. To fulfill these requirements in the early phases of cardiac development, the trabeculated layer is much thicker than the outer layer of compact myocardium (Figure 3A). Importantly, between trabeculated and compact layer a gradient regarding cardiomyocyte differentiation as well as proliferation rate exists. Cardiomyocytes within the trabeculated layer are further differentiated and appear elongated with mature sarcomere organization but proliferate only slowly[48-50]. In contrast, cells in the outer compact myocardium appear round and small with less mature sarcomere structures but high proliferative capacity[48-50]. Thus, proliferative growth of the embryonic myocardium is mainly accomplished by cell apposition from the periphery. At 10.5 dpc, looping is completed and the heart has acquired well-defined chambers, all now composed of an endothelial, myocardial and epicardial layer (Figure 3A). Since inflow and outflow tract (OFT) are now in close proximity and the chambers (common atrium and common ventricle) are specified and functional, cardiac septation can begin from 11.0 dpc onwards. The atrial and ventricular chambers are divided into two atria and two ventricles, forming a pre-stage four-chamber heart (Figure 3B). Meanwhile, mitral and tricuspid orifices are formed and the OFT divides into the left and the right ventricular outlets. By these septation events, systemic and pulmonary circulations become separate. At 13.5 dpc LV and RV are almost completely separated by the interventricular septum (IVS) (Figure 3B).

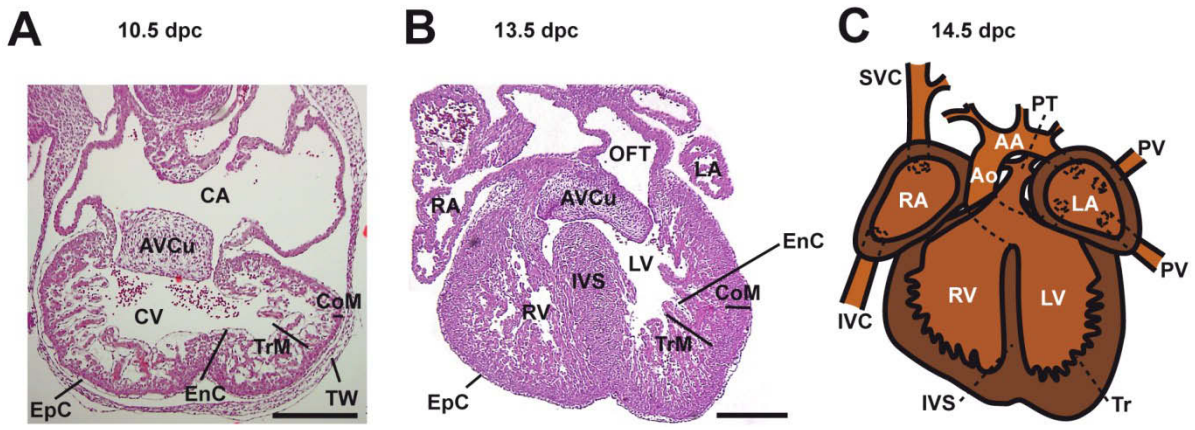

Figure 3. Morphogenesis of the mouse heart during the second half of gestation.
A) Ventral view of an H&E-stained longitudinal heart section at 10.5 dpc. At this stage, looping is complete and one common ventricle (CV) and one common atrium (CA) are obvious. The wall of each chamber is made up of all three tissue layers: endocardium (EnC), epicardium (EpC) and myocardium. Note that the trabeculated myocardial layer (TrM) is much thicker than the outer compact myocardium (CoM) (scale bar = 300 µm). **B)** Ventral view of an H&E-stained longitudinal heart section at 13.5 dpc reveals almost complete septation (scale bar = 300 µm). **C)** Ventral view of a schematic longitudinal heart section at 14.5 dpc. The pulmonary trunk (PT) and the aorta (Ao) connect to the chambers and ensure the separation of pulmonary and systemic circulation. (AA: aortic arch, AVCu: atrioventricular cushions, H&E: hematoxylin and eosin, IVC: inferior vena cava, IVS: interventricular septum, LA: left atrium, LV: left ventricle, OFT: outflow tract, PV: pulmonary vein, RA right atrium, RV: right ventricle, SVC: superior vena cava, Tr: trabeculae, TW: thoracic wall).)

After septation is completed at 14.5 dpc (Figure 3C), the ventricular myocardium undergoes further remodeling, primarily as a result of proliferative growth and thickening of the compact

myocardial layer accompanied by compaction of the trabeculae. At the same time, the coronary system is established to meet the increasing nutritional requirements of the mature myocardium. The last step of heart development is the formation of the valve leaflets based on sculpting of the endocardial cushions (OFT cushions and atrioventricular cushions (AVCu)), a process that continues until birth. On the way to a mature adult heart, the proportion of the compact myocardium increases even more (especially in the LV), while trabeculation only remains as a thin layer of honeycomb-like relief on the luminal surface of both ventricles.

In fact, growth of the heart is tightly regulated so that the heart reaches a predetermined final size in adulthood. Thus, impairments of growth regulatory pathways potentially result in congenital heart malformations, the leading form of major birth defects in humans. For instance, failure of the process of myocardial compaction can lead to a disease termed left ventricular noncompaction (LVNC). LVNC is characterized by prominent and excessive trabeculation with deep recesses in the ventricular wall and subsequent thinning of the compact myocardium[51]. This can cause heart failure, stroke, arrhythmias and sudden cardiac death in adulthood[52]. Even though LVNC was shown to be caused by mutations in genes encoding sarcomeric[53], cytoskeletal[54], nuclear-membrane[55] and chaperone proteins[56], the precise underlying molecular and cellular mechanisms are unknown. In addition, research suggests that LVNC is caused by proliferation defects during heart development[57]. In this context, the Hippo kinase cascade is an important regulator of cardiac organ growth[58]. In mice, fetal cardiomyocyte-restricted inactivation of the *yes-associated protein 1* (*Yap1*) gene (YAP1 is normally inhibited by Hippo kinase activity) causes decreased cardiomyocyte proliferation leading to myocardial hypoplasia and embryonic lethality after 16.5 dpc[59]. In contrast, fetal activation of *Yap1* stimulates cardiomyocyte proliferation particularly within the trabeculated myocardium, which normally exhibit low cell cycle activity[59]. This causes marked expansion of the trabeculated myocardium, resulting in chamber obliteration and fetal death after 15.5 dpc[59]. Furthermore, cardiac-specific inactivation of the mitochondrial apoptosis inhibitor *Survivin* results in decreased proliferation of cardiomyocytes within the compact myocardium during murine development[60]. Consequently, cardiac *Survivin* knockout (KO) mice have less cardiomyocytes at birth, resulting in smaller hearts[60]. These mice die prematurely after 8 month due to progressive heart failure associated with pathological hypertrophy and fibrosis[60]. The *Survivin* model resembles many phenotypic abnormalities found in animal models of IUGR, such as reduced heart size and cardiomyocyte number at birth and development of heart disease in adulthood (see Chapter 3.2.2). However, its potential to serve as model for the investigation of developmental programming mechanisms specifically within the heart is limited. In contrast to the concept of developmental programming, the genetic alteration persists throughout the entire postnatal

life and is not released after birth, as normally the case for unfavourable intrauterine growth conditions. In summary, even though few animal models for impaired prenatal heart development exist, they have limited potential to study molecular and cellular mechanisms of cardiac developmental programming; either because they die *in utero* or, if they survive until adulthood and indeed develop postnatal heart disease, because the insult is not restricted to prenatal development.

3.3.2 Growth mechanisms and metabolic changes in the perinatal mammalian heart

Cardiomyocytes in the pre- and postnatal mammalian heart demonstrate significant differences regarding their growth patterns. Embryonic and fetal cardiac cells are highly proliferative[61,62]. Thus, prenatal increase in cardiac mass is primarily achieved by proliferation of mononucleated contractile cardiomyocytes and non-cardiomyocytes, leading to an increase in cell number (hyperplasia)[61,62]. This proliferative potential, however, decreases in late gestation and soon after birth cardiomyocytes lose their capability of dividing[63]. Consequently, a rapid switch from hyperplastic to hypertrophic (increase in size) cardiomyocyte growth occurs[64]. In rodents, this transition occurs within the first postnatal week[65]; whereas it takes place almost immediately after birth in larger mammals[64,66]. At a morphological level, the switch from pre- to postnatal growth patterns coincides with terminal differentiation of cardiomyocytes, characterized by a marked increase in myofibril density, appearance of mature intercellular junctional complexes (intercalated discs) and binucleation[65,67,68]. In rodents, the latter is achieved since cardiomyocytes undergo a final round of deoxyribonucleic acid (DNA) synthesis and nuclear mitosis (karyokinesis) without cell division (cytokinesis)[69]. In humans, karyokinesis is rare so that adult human cardiomyocytes are polyploid but not necessarily multinucleated. After terminal differentiation, cardiomyocytes withdraw from the cell cycle without permitting further cell division. For a long time it was widely believed that from now on cytokinesis is blocked and continuous increase in heart muscle mass and thus organ size is accomplished exclusively by the enlargement of individual pre-existing cardiac cells in the absence of cell division[68-71]. However, this strict paradigm of terminal differentiation is currently under debate. In mice, a brief but intense proliferative burst of predominantly binucleated cardiomyocytes during preadolescence was revealed[72]. Anyway, cardiomyocyte hypertrophy is the predominant postnatal growth mechanism. Especially from the neonatal period until early adulthood it facilitates the rapid increase of heart size to accommodate the increasing demands of the fast growing animal[73].

Even though the molecular and cellular mechanisms, which regulate cardiomyocyte cell cycle exit, binucleation and terminal differentiation accompanying the switch from proliferative to hypertrophic cardiac growth are not well understood, changes in the expression pattern of cell cycle regulating genes have a significant impact. Cell cycle

activating genes, such as cyclin-dependent kinases (Cdk) (e.g. *Cdk 2*, *4* and *6*) and cyclins (Ccn) (e.g. *Ccnd1*, *Ccnd2*, *Ccnd3*, *Ccna*, *Ccnb* and *Ccne*) are highly expressed in the prenatal heart but demonstrate decreased expression in neonates and are almost undetectable in adult hearts[70,74-79]. In contrast, genes coding for cyclin-dependent kinase inhibitors (Cdkn) (e.g. *Cdkn1a* and *Cdkn1b*) display a higher expression in adult hearts than in prenatal stages[80,81]. Importantly, in the context of elucidating underlying mechanisms responsible for the switch from proliferative to hypertrophic cardiac growth, transition to the oxygen-rich postnatal environment, accompanied by the switch to an oxidative metabolism, was recently identified as an essential factor that facilitates postnatal cardiomyocyte cell cycle exit[82]. The transition from hyperplastic to hypertrophic growth is furthermore accompanied by major changes in cardiac metabolism. *In utero* and in early neonates the mammalian heart performs mainly glycolysis, using carbohydrates, such as lactate and glucose, as primary substrates for adenosine triphosphate (ATP) production[83-87]. In contrast, the rates of mitochondrial glucose and fatty acid oxidation in the fetal heart are low due to low oxygen concentrations[88,89]. However, the rate of both processes, glucose and fatty acid oxidation, increases immediately after birth, while glycolytic rates decrease[90,91]. Consistently, in the adult heart, fatty acids are the preferred energy substrates and most of the required ATP comes from mitochondrial oxidative phosphorylation as well as glucose oxidation[92]. The perinatal metabolic transition is associated with changes in the activity of key enzymes involved in the regulation of fatty acid as well as glucose metabolism. Increased 5´-adenosine monophosphate-activated protein kinase (AMPK) activity results in inhibition of acetyl-Coenzyme A carboxylase (ACC) and consequently in a drop in cardiac malonyl Coenzyme A levels[93-96]. These metabolic changes are considered to be the key event responsible for the increase in myocardial fatty acid oxidation rates in the postnatal heart[96,97]. Taken together, the determination of final cardiac organ size is a highly coordinated and complex process relying on a precise regulation of cell number established during embryonic and fetal development as well as cell size achieved by postnatal cardiac hypertrophic growth. In this context, metabolic changes accompanying the transition from prenatal to postnatal cardiac growth play an important role.

3.3.3 Postnatal cardiac growth: Pathological and physiological cardiac hypertrophy

Physiological cardiac hypertrophy not only drives the normal growth of the heart from birth to early adulthood but also the growth of the maternal heart during pregnancy[98]. It furthermore occurs as response to physiological stimuli, such as isotonic exercise (running, walking, cycling, swimming) as well as isometric/static exercise (wrestling, weight lifting)[99]. In contrast, pathological cardiac hypertrophy serves the heart to overcome pathological conditions and maintain cardiac function[100,101]. It develops in response to pressure overload (e.g. due to hypertension or aortic stenosis) or volume overload (e.g. due to aortic regurgitation or

arteriovenous fistulas or shunts) as well as in response to valve disease, myocardial infarction, ischemia and genetic mutations[100,101]. Dependent on the initiating stimulus, both (pathological and physiological hypertrophy) can be subclassified as concentric (hearts with thick walls and relatively small cavities) and eccentric (hearts with large dilated cavities and relatively thin walls), respectively[102,103]. While isotonic exercise[103] and volume overload[102] cause eccentric hypertrophy; isometric exercise[103] and pressure overload[102] provoke concentric hypertrophy. Even though physiological and pathological hypertrophic cardiac growth both result in an increase in cell mass due to increased cardiomyocyte size, they induce distinct histological and molecular changes[104-108]. The enlargement of cardiomyocytes and the formation of new sarcomeres during pathological hypertrophy initially allows compensatory growth, ensuring normalization of wall stress and permitting normal cardiovascular function at rest[100]. However, if the pathological insult persists, cardiac fibroblasts and ECM proteins accumulate disproportionately and excessively[109]. This causes cardiac fibrosis and mechanical stiffness of the ventricular wall, which contributes to diastolic dysfunction (i.e. insufficient filling of the ventricles upon relaxation) and can progress to systolic dysfunction (i.e. reduced contractility and insufficient output)[109]. Cardiac function in the pathologically hypertrophied heart may eventually decompensate, leading to LV dilation, potentially resulting in heart failure, arrhythmia and sudden death[110]. Furthermore, pathological cardiac hypertrophy is often associated with upregulation of fetal genes, including *natriuretic peptide type A* (*Nppa*), *natriuretic peptide type B* (*Nppb*) and genes for fetal isoforms of contractile proteins, such as *skeletal α-actin* and *β-myosin heavy chain* (*Myh7*)[111-114]. In contrast, increase of interstitial fibrosis and upregulation of the fetal gene program are not associated with physiological hypertrophy, and decompensation into dilated cardiomyopathy or heart failure does not occur[103,115]. Finally and most importantly, physiological hypertrophy is reversible, while pathological hypertrophy, especially after establishment of fibrosis and tissue remodeling, is irreversible[116]. Interestingly, the mechanistic target of rapamycin (mTOR) pathway was shown to be of particular importance in the regulation of cardiomyocyte size and hypertrophic growth in adult murine hearts; both under physiological as well as pathological conditions[117] (see Chapter 3.3.4).

3.3.4 The mechanistic target of rapamycin pathway and its role in cardiac growth

Even though progress has been made in elucidating the structural and molecular characteristics of cardiac hypertrophy, our understanding of the precise molecular signaling pathways defining “physiological” versus “pathological” postnatal cardiac growth is incomplete. In this context, the mechanistic target of rapamycin (mTOR) pathway has been implicated in controlling cardiac organ size and regulating both types of hypertrophy within the heart (reviewed by Csibi and Blenis[58]) (see Chapter 3.3.4.2). It is not only a master regulator of cell growth, metabolism, proliferation and survival but also acts as a key sensor

of cell nutrition and energy status[118]. The MTOR protein itself is an evolutionary conserved 289 kDa serine-threonine kinase that belongs to the phosphoinositide 3-kinase (PI3K)-related kinase family. It forms the catalytic subunit of two distinct multiprotein complexes, mTOR complex 1 (mTORC1) and 2 (mTORC2), which differ in their functions and complex components (Table 1, Figure 4 and see 3.3.4.1, Figure 5)[118]. Importantly, mTOR pathway activity depends on sufficient amino acid availability[119]. Given that the mTOR signaling cascade plays a major role in the regulation of heart growth (see Chapter 3.3.4.2), it might even be involved in IUGR-induced cardiac hypoplasia (e.g. reduced heart size after prenatal amino acid restriction).

Table 1. Protein components of the two mTOR complexes and their known functions

mTORC1		mTORC2	
MTOR	serine/threonine kinase	**MTOR**	serine/threonine kinase
RAPTOR	scaffold protein regulating assembly, localization and substrate binding of mTORC1[120,121]	***RICTOR***	scaffold protein regulating assembly and substrate binding of mTORC2[122]
PRAS40	mTORC1 inhibitor[123-126]	***MSIN1***	scaffold protein regulating assembly of mTORC2 and its interaction with SGK1[127,128]
DEPTOR	MTOR inhibitor[129]	*PROTOR 1/2*	increases mTORC2-mediated activation of SGK1[124,130-132]
MLST8	function unknown (loss does not affect mTORC1 activity toward known substrates)[133]	DEPTOR	MTOR inhibitor[129]
TTI1/TEL2 complex	scaffold proteins regulating assembly and stability of mTORC1[134]	**MLST8**	function unknown (but essential for mTORC2 activity)[133]
		TTI1/TEL2 complex	scaffold proteins regulating assembly and stability of mTORC2[134]

Listed are complex components of mTORC1 and mTORC2. Italic components are specific for mTORC1 or mTORC2, respectively. Bold components are core components essential for complex function. Table adapted from Laplante and Sabatini[135]. (DEPTOR: DEP domain containing mTOR-interacting protein, MLST8: mammalian lethal with sec-13 protein 8, MSIN1: mammalian stress-activated map kinase-interacting protein, MTOR: mechanistic target of rapamycin, mTORC1/2: mTOR complex 1/2, RAPTOR: regulatory-associated protein of mTOR, RICTOR: rapamycin-insensitive companion of mTOR, PRAS40: proline-rich Akt substrate 40 kDa, PROTOR1/2: protein observed with rictor 1 and 2, SGK1: serum- and glucocorticoid-induced protein kinase 1)

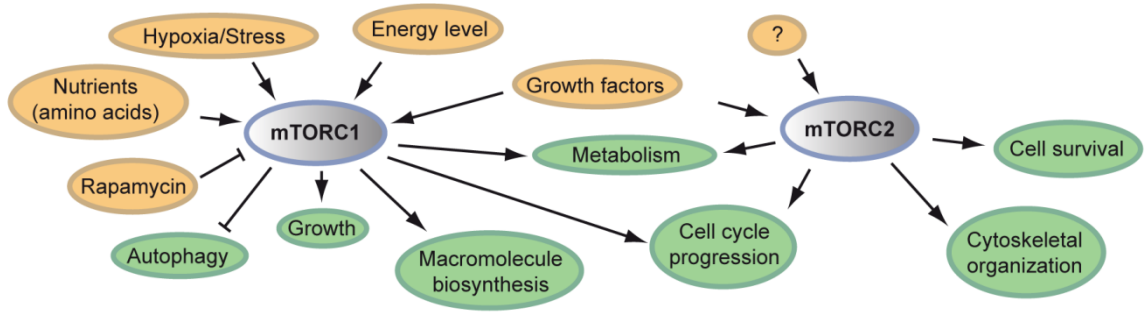

Figure 4. mTORC1 and mTORC2 have distinct cellular functions.
The mechanistic target of rapamycin (mTOR) kinase functions as the catalytic subunit of two different multiprotein complexes termed mTOR complex 1 (mTORC1) and 2 (mTORC2). mTORC1 integrates various upstream signals such as amino acids, stress, oxygen, energy and growth factors. It regulates multiple anabolic and catabolic processes, respectively, and promotes cell cycle progression. In contrast, mTORC2 responds to growth factors and is subsequently involved in the control of cell survival, metabolism, cell cycle progression and cytoskeletal organization. While mTORC1 is inhibited by rapamycin, mTORC2 is not. Figure modified from Laplante and Sabatini[135].

3.3.4.1 Regulation and function of the mTOR pathway with emphasis on mTORC1

mTORC1 is activated by three major upstream signals: growth factors, high cellular energy status and nutrients (amino acids)[135]. Growth factors stimulate mTORC1 through the PI3K-phosphoinositide-dependent kinase 1 (PDK1)-AKT pathway (Figure 5a). AKT phosphorylates and thus inactivates the mTORC1 inhibitor complex tuberous sclerosis ½ (TSC1/2) at serine 939 and threonine 1462[136-140]. On the other hand, growth factor activated AKT phosphorylates the non-essential mTORC1 inhibitory component proline-rich Akt substrate 40 kDa (PRAS40), which in turn dissociates from regulatory-associated protein of mTOR (RAPTOR), resulting in mTORC1 activation[123-126]. Moreover, phosphorylation of AKT at serine 473 links upstream mTORC2 activity to mTORC1[141]. The energy status of the cell is signaled to mTORC1 through AMPK, which is a master sensor of intracellular ATP levels (Figure 5b)[142,143]. In response to energy starvation (low ATP/adenosine diphosphate (ADP) or ATP/adenosine monophosphate (AMP) ratio), AMPK is activated and phosphorylates TSC2 on at least two residues (threonine 1271 and serine 1387) as well as RAPTOR at serine 792[144,145]. Consequently, mTORC1 becomes inactivated. Even in the presence of additional upstream stimuli (e.g. growth factors), amino acids must be available to activate mTORC1 (Figure 5c)[119,146]. Although it has long been known that amino acids signal independently of TSC1/2[147], the precise molecular mechanisms by which intracellular amino acids activate mTORC1 are currently under debate. Several modes of actions have recently been proposed, as reviewed in Jewell *et al*., 2013[148] and Shimobayashi and Hall, 2014[149]. In this context, it was shown that in the presence of amino acids, mTORC1 translocates from a poorly characterized cytoplasmic location to the lysosomal surface to get in proximity to its main activator RHEB [150-156]. Moreover, mTORC1 is a physiological target of rapamycin, also named sirolimus, a macrolipid produced in *Streptomyces hygroscopius* that is known to inactivate mTORC1 (Figure 5d)[157-159]. Rapamycin works through a gain-of-function mechanism in which it binds to the intracellular FKBP12 protein, which in turn binds to and inhibits the kinase activity of mTORC1[158,159].

Downstream, mTORC1 promotes cell growth and proliferation by activating various anabolic processes (e.g. protein and lipid biosynthesis (Figure 5e), mitochondrial metabolism and biogenesis (Figure 5f)) and by limiting catabolic processes such as autophagy (Figure 5g)[160]. Among those downstream effects of mTORC1, protein biosynthesis is by far the best characterized process (Figure 5h). mTORC1 directly phosphorylates two important translational regulators: eukaryotic translation initiation factor 4E binding protein 1 (4E-BP1) and S6 kinase 1 (S6K1)[161]. Phosphorylation of 4E-BP1 prevents it from binding to and thereby interfering with the cap-binding protein eukaryotic translation initiation factor 4E (EIF4E). Instead, after 4E-BP1 dissociation, EIF4E forms a complex that is required for initiation of cap-dependent translation[162]. Phosphorylation and activation of S6K1 leads,

through a number of effectors (e.g. eukaryotic translation initiation factor 4E (EIF4B) and S6 ribosomal protein (S6)), to increased messenger ribonucleic acid (mRNA) biogenesis, translational initiation and elongation[161]. In the context of positive regulation of anabolic processes, mTORC1 furthermore controls cellular metabolism and ATP production (Figure 5f). It does so by increasing the glycolytic flux by activating transcription and translation of hypoxia inducible factor 1, alpha subunit (HIF1α), a positive regulator of many glycolytic genes[163,164]. Moreover, mTORC1 is involved in mitochondrial biogenesis and oxidative metabolism by increasing the mitochondrial DNA content, mitochondrial membrane potential and mitochondrial oxygen consumption[165].

Inhibition of catabolic processes by mTORC1 occurs via inhibition of autophagy (Figure 5g), the central cellular degradation process important for protein turn-over, recycling of damaged organelles and consequently organismal and cellular adaptation to nutrient starvation (reviewed by Baehrecke[166] and Mizushima and Komatsu[167]). In mammals, mTORC1 directly phosphorylates and thereby suppresses a protein complex consisting of unc-51-like kinase 1 (ULK1), mammalian autophagy-related gene 13 (ATG13) and focal adhesion kinase family-interacting protein of 200 kDa (FIP200), which is required to initiate autophagy[168-171]. Besides, mTORC1 impacts autophagy by additional mechanisms, for instance by regulation of the autophagy suppressor death-associated protein 1 (DAP1)[172]. Furthermore, mTORC1 inhibits the biogenesis of lysosomes, which are important cellular components required for autophagy[173-175].

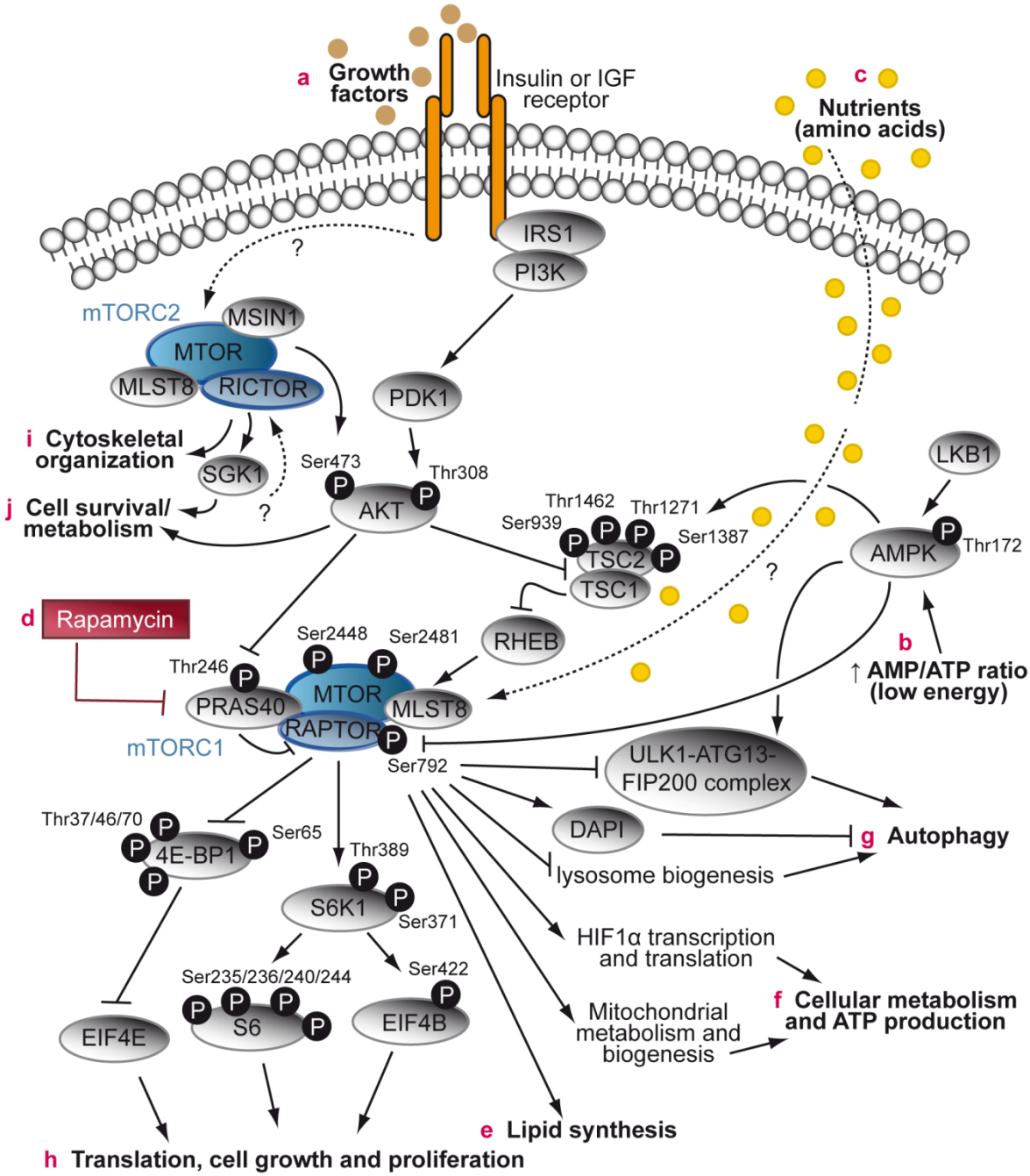

Figure 5. Simplified schematic drawing of the mTOR signaling network in mammalian cells.
Figure shows major upstream and downstream cascades of mTOR signaling. Critical inputs regulating mTORC1activity include **a)** growth factors such as insulin and insulin-like growth factors (IGFs), **b)** energy signals that act through adenosine monophosphate-activated protein kinase (AMPK), **c)** nutrient signals that are generated by amino acids and **d)** inhibition through rapamycin. When active, mTORC1 promotes **e)** lipogenesis, **f)** cellular energy metabolism, **g)** autophagy inhibition and **h)** mRNA translation and protein synthesis. In contrast, mTORC2 is activated by **a)** growth factors and regulates **i)** cytoskalatal organization and **j)** cell survival and metabolism. Note that not all complex components of mTORC1 and mTORC2 are shown. Only selected phosphorylation sites and cascade components are depicted. Arrows represent activation, whereas bars represent inhibition. Dashed lines indicate connections that have not been fully elucidated yet. (4E-BP1: eukaryotic translation initiation factor 4E binding protein 1, AKT: serine/threonine protein kinase Akt, AMP: adenosine monophosphate, AMPK: adenosine monophosphate-activated protein kinase, ATP: adenosine trihosphate, ATG13: autophagy-related gene 13, DAPI: death-associated protein 1, EIF4B: eukaryotic translation initiation factor 4B, EIF4E: eukaryotic translation initiation factor 4E, FIP200: focal adhesion kinase family-interacting protein of 200 kDa, HIF1α: hypoxia inducible factor 1, alpha subunit, IRS1: insulin receptor substrate 1, LKB1: serine/threonine kinase LKB1, MLST8: mammalian lethal with sec-13 protein 8, MSIN1: mammalian stress-activated map kinase-interacting protein, MTOR: mechanistic target of rapamycin, mTORC1/2: mTOR complex 1/2, PDK1: phosphoinositide-dependent kinase 1, PIK3: phosphatidylinositol 3-kinase, PRAS40: proline-rich Akt substrate 40 kDa, RAPTOR: regulatory-associated protein of TOR, RHEB: Ras homolog enriched in brain, RICTOR: rapamycin-insensitive companion of mTOR, S6: ribosomal protein S6, S6K1: S6 kinase 1, Ser: serine, SGK1: serum- and glucocorticoid-induced protein kinase 1, Thr: threonine, TSC1/2: tuberous sclerosis 1/2, Tyr: tyrosine, ULK1: unc-51-like kinase 1)

3.3.4.2 The role of the mTOR pathway in the mammalian heart

A growing number of publications within the last couple of years revealed that the mTOR pathway is of particular importance in the heart and acts as a key regulator of postnatal cardiac metabolism and growth[176]. While conventional *Mtor*, *Rictor*, *Raptor* and *Rheb* KO mice die early during embryonic development[122,177-181], tamoxifen-inducible cardiac-specific *Mtor* and *Raptor* deletion in adult mice both lead to cardiac dysfunction and heart failure, with chamber dilation and wall thinning[182,183]. This goes in line with massive apoptosis, fibrosis, induction of autophagy, mitochondrial abnormalities and dysfunction, sarcomere disarray and death within less than eight weeks after tamoxifen-induced gene deletion under baseline conditions[182,183].

Furthermore, the mTOR signaling cascade was shown to play a key role in the development of both types of postnatal cardiac hypertrophy (physiological and pathological, see Chapter 3.3.3), either relying on increased protein turnover required for cardiomyocyte growth[176]. In this context, mTOR pathway activity has been demonstrated to be increased in the physiologically hypertrophied heart after prolonged exercise[117]. In contrast, pressure overload upon transverse aortic constriction (TAC) was associated with decreased mTOR pathway activity[117]. Additionally, pharmacological inhibition of mTORC1 by rapamycin in adulthood inhibits pathological cardiac hypertrophy in response to pressure overload and reduces heart size[184,185]. Rapamycin administration also blunts both established compensated and decompensated cardiac hypertrophy induced by TAC[186]. Interestingly, neither constitutively active nor wildtype (WT) *Mtor* overexpression induced significant increase in cardiac mass in mice[187,188]. In contrast, adult mice with inducible cardiac-specific *Mtor* or *Raptor* deletion do not develop compensatory cardiac hypertrophy after TAC-induced pressure overload, but rapidly demonstrate signs of ventricular dilation and cardiac dysfunction already 1 to 2 weeks after the TAC procedure[182,183]. In conclusion, changes in opposite directions of the myocardial mTOR pathway appear to distinguish between physiological and pathological hypertrophies.

Even though there is a constantly growing body of evidence emphasizing the role of the mTOR signaling cascade in the healthy as well as challenged adult heart, studies on its role during prenatal cardiac development as well as in the perinatal period are scarce. Recently, Tamai *et al*. showed that mice with a cardiac-specific deficiency for *Rheb* (c*Rheb*-KO), the most important upstream regulator of mTORC1, die from postnatal day 8 to 10[189]. Surprisingly, analysis in 3 and 5 day old c*Rheb*-KO mice revealed no differences regarding heart size and function compared to controls[189]. However, at day 8, c*Rheb*-KO mice presented signs of dilated cardiomyopathy, such as significantly lower HW/BW ratios and reduced cardiomyocyte cross sectional area (CSA) as well as cardiac dysfunction compared to controls[189]. Why this phenotypic abnormalities become obvious only from postnatal day 8

onwards remains elusive. In conclusion, Tamai *et al*. suggested that RHEB-dependent mTORC1 activation is not required for embryonic as well as neonatal heart development immediately after birth[189]. However, RHEB becomes essential for postnatal cardiomyocyte hypertrophic growth and normal heart development after the early postnatal period[189]. Importantly, as stated by the authors, a suggested RHEB-independent mTORC1 signaling pathway in the neonatal period until day 8 remains unknown and requires further investigation.

Another study focusing on components of the mTOR signaling pathway within the heart examined the role of the mTORC1 upstream kinase AKT in the regulation of organ size[190]. Shioi *et al*. generated and characterized transgenic mice expressing constitutively active *Akt* (cact*Akt*) and kinase-deficient *Akt* (ckid*Akt*) specifically within the heart[190]. They observed a significant increase in cardiomyocyte size and HW in 3 to 4 month old adult cact*Akt* mice compared to non-transgenic controls. This coincided with increased S6K1 activity, as determined by immune complex kinase assays[190]. Interestingly, the cardiomyocyte and heart overgrowth could be attenuated by rapamycin treatment[190]. These observations suggest that MTOR or effectors of MTOR mediate cact*Akt*-induced heart growth[190]. However, cardiomyocyte and heart size in adult ckid*Akt* mice were not different compared to non-transgenic controls, even though ckid*Akt* mice effectively attenuated PI3K-induced overgrowth of the heart[190]. Unfortunately, mTOR pathway activity was not analyzed in ckid*Akt* mice at any developmental stage[190], leaving open questions regarding the role of MTOR in the prenatal, perinatal and neonatal heart.

To the best of our knowledge, there is only one published study that characterized mice harboring a heart conditional KO of one of the mTORC1 core components (namely *Mtor* itself) during prenatal development[191]. This heart-specific, embryonic *Mtor*-KO mouse model (c*Mtor*-KO) suggests an essential role of mTOR signaling during heart development[191]. Hearts of embryonic c*Mtor*-KO mice demonstrated increased apoptosis rates, reduced cardiomyocyte proliferation, decreased heart size and cardiac dysfunction compared to controls[191]. Thus, c*Mtor*-KO mice are embryonically lethal and died from 13.5 dpc onwards[191]. However, since no complete cardiac *Mtor* inactivation was achieved[191], substantial parts of the data are not conclusive and show a high variability between the animals analyzed, such that the true significance of this study awaits further confirmation.

Taken together, the studies discussed above underscore the complexity associated with mTOR signaling in the heart, such that pharmacologic inhibition with rapamycin can blunt physiological hypertrophy, but deletion of *Mtor* or other pathway regulators induces cardiac dilatation and pathology. Thus, many aspects of the pathophysiology of mTOR signaling are still unclear and further studies are required to complete the entire picture of mTOR pathway regulation and function within the heart. Importantly, the precise role of MTOR in pre- and

perinatal heart development also remains obscure. Moreover, the involvement of mTOR signaling in IUGR and developmental programming has not been addressed to date.

3.4 The heart conditional *holocytochrome c synthase* KO mouse model: A novel model for impaired intrauterine cardiac development

According to the concept of developmental programming, the entire organism undergoes adaptations in response to IUGR, as demonstrated by the variety of organs affected (see Chapter 3.2). Consequently, dissecting the precise cause and effect of molecular changes in one particular organ is still an ongoing challenge. To this end, apart from the traditional models for developmental programming and IUGR, studies on organ-specific embryonic and fetal growth disturbances might prove useful. In this context, our group has generated a new mouse model for impaired prenatal cardiac development[192].

The model is based on heart-specific inactivation of the highly conserved holocytochrome *c* synthase (*Hccs*) gene[192]. The *Hccs* gene product is a mitochondrial heme lyase that is responsible for the activation of two related electron transporters, which are crucial components of the electron transport chain (ETC): cytochrome (CYT) *c* and *c*1[193,194]. In mammals, the ETC can be found in the inner mitochondrial membrane where it serves as the site of oxidative phosphorylation through the ATP synthase complex[195]. Coordinated transport of electrons and protons along a series of carrier molecules leads to the production of energy in form of ATP. This makes mitochondria the most important energy producers in animal cells[196]. Hence, in cardiomyocytes, mitochondria are present in large amount to cover the high energy demand for constant contraction. The HCCS enzyme is located within the mitochondrial intermembrane space and catalyzes the transfer of a prosthetic heme moiety to the precursor apo-CYT *c* and *c*1, which in turn become functionally active holo-cytochromes[197,198]. Active CYT *c*1 integrates into complex III of the ETC and delivers electrons from ubiquinol to CYT *c*, which in turn shuttles the electrons between complex III and complex IV[195,196,199].

In mice and humans, the *Hccs* gene is located on the X chromosome. Consequently, its allelic expression is subjected to X chromosome inactivation, a highly conserved process that occurs exclusively in mammals[200]. It leads to random transcriptional silencing of one of the two X chromosomes in all female somatic cells during early embryonic development. Thus, differences in dosage of X-linked genes between the sexes are compensated. The silencing pattern is maintained through successive cell divisions in the arising daughter cells such that females can be considered cellular mosaics, which determines the phenotypic outcome in females heterozygous for X-linked mutations[201].

In the heart conditional *Hccs* KO model, parts of the *Hccs* gene are specifically knocked out in cardiomyocytes from 7.5 dpc onwards applying *Cre/locus of X-over P1* (*loxP*)

recombination[192] (see Chapter 5.1.2.1). In affected cells, the HCCS enzyme is inactive. Consequently, no active CYT *c* and *c*1 can be built, complex III assembly and the electron shuttle to complex IV within the ETC is disturbed and mitochondrial energy production does not function properly[192]. Subsequently, loss of HCCS enzymatic activity results in mitochondrial dysfunction, causing disturbed cardiomyocyte differentiation as well as reduced cell cycle activity[192].

Our breeding strategy allows the generation of healthy control males (*Hccs*$^{+/Y}$) and females (*Hccs*$^{+/+}$), as well as cardiac-specific hemizygous KO males (c*Hccs*$^{-/Y}$) and heterozygous KO females (c*Hccs*$^{+/-}$) (see Chapter 5.1.2.1, Figure 6). c*Hccs*$^{-/Y}$ males exhibit dysfunction of the ETC in all cardiomyocytes and die at midgestation[192]. In contrast, in heterozygous c*Hccs*$^{+/-}$ females, 50 % of cardiac cells have the defective X chromosome silenced and remain healthy, while 50 % of cardiomyocytes keep the defective X chromosome active and consequently demonstrate disturbed ETC function[192]. Thus, in c*Hccs*$^{+/-}$ offspring, a cardiac mosaic for mitochondrial dysfunction develops at midgestation[192]. However, *Hccs*-deficient cardiac cells are not actively eliminated and are still detectable in adult c*Hccs*$^{+/-}$ hearts[192] Interestingly, increased proliferation of the healthy cardiac cell population during the second half of gestation compensates for the functional loss of 50 % cardiac tissue[192]. Thereby, the contribution of *Hccs*-deficient cardiac cells to the cardiac tissue decreases from 50 % at midgestation to 10 % at birth, which in turn implies that 90 % of the neonatal heart is built of the healthy cardiac cell population[192]. Importantly, in spite of the functional inactivation of roughly half of the cardiomyocytes at 7.5 dpc, c*Hccs*$^{+/-}$ mice have a functional heart at birth and survive to adulthood, indicating an impressive regenerative potential of the embryonic mammalian heart[192].

However, formation of the heart from just 50 % of embryonic cardiomyocytes is not sufficient to generate a mature organ until birth. Despite normal function, hearts of neonatal c*Hccs*$^{+/-}$ mice reveal a hypoplastic phenotype. They have a reduced HW/BW ratio, thinner LV walls, significant reduction in cardiomyocyte number by 25 % and LV noncompaction (e.g. thin myocardial compact layer accompanied by hypertrabeculation) (unpublished data). Surprisingly, the reduction in heart size as well as LV wall dimensions was no longer evident in adult c*Hccs*$^{+/-}$ hearts, suggesting postnatal compensatory growth. While no alterations in cardiomyocyte proliferation rates were observed at any postnatal stage, cardiomyocyte hypertrophy was revealed to account for this catch-up growth of the hypoplastic myocardium (unpublished data). Important to note, c*Hccs*$^{+/-}$ mice sustain lifelong normal cardiac function under baseline conditions[192]. Nevertheless, adult c*Hccs*$^{+/-}$ mice demonstrate significant cellular and molecular alterations in response to cardiac stress and ageing. This indicates that the reduced set of cardiomyocytes in combination with compensatory

adaptations cause different alterations in c*Hccs*$^{+/-}$ hearts in response to stress compared to healthy *Hccs*$^{+/+}$ hearts (unpublished data).

Importantly, the heart conditional *Hccs* KO model resembles many observations found in classical IUGR models (see Chapter 3.2.2), such as reduced heart size at birth, altered stress response in adulthood and postnatal cardiac catch-up growth. According to the developmental programming concept (see Chapter 3.2.1), the latter contributes to increased disease susceptibility in adulthood rather than being beneficial[15,16]. However, in contrast to the well-established developmental programming models, no systemic insult is applied in c*Hccs*$^{+/-}$ mice. Nevertheless, formation of the heart from a mosaic of healthy and defective cardiomyocytes can be considered as an insult affecting cardiac development and growth. Thereby, our model provides an organ specific developmental impairment and consequently might serve as a new model for impaired prenatal cardiac growth and developmental programming in the heart.

3.5 Aims and Hypotheses

Impaired embryonic and fetal growth has various effects on postnatal health in humans because unfavorable intrauterine growth conditions induce permanent physiological adaptations in the unborn organism, which are supposed to provoke increased disease susceptibility in adulthood[2,3,7]. Elucidation of key processes and factors essential for the pre- and even postnatal heart to cope with the molecular, cellular and organ-wide consequences of IUGR might reveal new strategies for the prevention of congenital and postnatal heart diseases. In this context, the heart conditional *Hccs* KO model resembles many observations identified in classical animal models for IUGR, such as smaller hearts, thinner left ventricular walls and reduced cardiomyocyte number at birth as well as postnatal cardiac catch-up growth and altered stress response in adulthood[15,16,23,192]. Thus, we propose that our model is suitable to study basic mechanisms of pre- and postnatal adaption of the myocardium in response to impaired intrauterine development and that it might help to identify molecular mechanisms of cardiac developmental programming.

Results from previously performed genome-wide microarray analysis and preliminary data suggest that adaptations employed by embryonic and neonatal c*Hccs*$^{+/-}$ hearts in response to disturbed cardiac development are predominantly involved in amino acid metabolism and protein homeostasis (unpublished data). Moreover, in the well-established LPD rat model, neonatal hearts were shown to be hypoplastic, as evident by a reduced HW and a significant reduction in the cardiomyocyte number[23]. Given that our neonatal c*Hccs*$^{+/-}$ mice resemble those findings and considering that the mTOR signaling cascade is a master regulator of postnatal cardiac metabolism and growth that is sensitive to amino acid availability, we

hypothesize that amino acid availability as well as mTOR pathway activation are crucial to sustain regeneration and compensatory growth of c*Hccs*$^{+/-}$ hearts. To test this hypothesis and to investigate the importance of amino acids and mTOR for development and growth of c*Hccs*$^{+/-}$ hearts, this PhD project aims at interfering with these metabolic switches that were identified during impaired intrauterine cardiac development. We aspire to achieve this interference by prenatally inhibiting the mTOR pathway and by applying a dietary protein restriction model. To this end, pregnant dams will be treated with the pharmacological mTORC1 inhibitor rapamycin. In a second approach, a protein-restricted diet will be fed during pre- and postnatal development to limit the amino acid availability. We hypothesize that interfering with these key mechanisms will inhibit cardiac adaptation and reduce heart size, resulting in impaired cardiac function in adulthood and eventually causing postnatal heart disease. To test this, consequences of the two experimental strategies (mTOR inhibition and amino acid restriction) will be studied in the c*Hccs*$^{+/-}$ model with regard to heart development and growth as well as long-term consequences and cardiac function in adulthood. Because organ size is mainly determined by the combination of cell number and size, main emphasis will be put on processes like apoptosis and proliferation as well as on cardiomyocyte size.

Importantly, the consequences of both interventions (mTOR inhibition and amino acid restriction) are not only going to be analyzed with respect to the c*Hccs*$^{+/-}$ model. Data about the general role of the mTOR pathway during heart development are limited and insufficient. Due to its crucial role in cardiac metabolism and growth, we hypothesize that prenatal impairment of the mTOR signaling cascade will also alter cardiac development in general, independent of the c*Hccs*$^{+/-}$ model. In line, consequences of prenatal amino acid restriction in the mouse are vastly unknown and pre- and postnatal impairment of the amino acid availability might also have important implications for the murine heart. Thus, another important aim of this thesis is to elucidate the role of the amino acid availability and mTOR signaling during heart development.

In summary, this PhD project aims to answer the following two central questions:

1. What are the consequences of prenatal mTORC1 inhibition and pre- as well as postnatal amino acid restriction on heart development, growth and function in general?
2. Are amino acid availability and mTOR pathway activation essential for embryonic regeneration and postnatal compensatory growth of c*Hccs*$^{+/-}$ hearts?

By answering these crucial questions and by using our c*Hccs*$^{+/-}$ model as new tool to resemble IUGR in the heart, we aim at investigating mechanisms of cardiac growth and organ size control, which in the end might also be key players in developmental programming.

4 MATERIAL

4.1 Laboratory equipment

Table 2. Laboratory equipment

Equipment	Company
Agarose electrophoresis unit HE99X max horizontal	Hoefer, Holliston, USA
Centrifuge 5402 with 18-place kit rotor F-45-18-11	Eppendorf, Hamburg, Germany
Centrifuge 5425 with 24-place aerosol-tight fixed-angle rotor FA-45-24-11	Eppendorf, Hamburg, Germany
Centrifuge 5810R with swing-bucket rotor A-4-62	Eppendorf, Hamburg, Germany
Confocal laser scanning microscope TSC SPE	Leica Microsystems, Wetzlar, Germany
Cryolys® Precellys® 24 cooling unit	peqLab Biotechnology, Wilmingon, USA
Film developing machine Curix 60	Agfa, Mortsel, Belgium
Digital camera EOS 400D	Canon, Tokyo, Japan
Digital camera for microscope IC80 HD	Leica Microsystems, Wetzlar, Germany
Fluorescence microscope Biozero BZ-8100	Keyence, Osaka, Japan
Gel documentation system GelDoc2000	Bio-Rad Laboratories, Hercules, USA
Glass ware	Schott, Mainz, Germany
Homogenizer Precellys® 24	peqLab Biotechnology, Wilmingon, USA
Hybridization oven OV1	Biometra, Göttingen, Germany
Imaging system Odyssey® Fc	LI-COR® Biosciences, Lincoln, USA
Light microscope DM IL	Leica Microsystems, Wetzlar, Germany
Light microscope M205 C	Leica Microsystems, Wetzlar, Germany
Magnetic stirrer	neoLab Migge, Heidelberg, Germany
Microcentrifuge Galaxy mini	VWR, Radnor, USA
Microcentrifuge MiniStar silverline	VWR, Radnor, USA
Micropestle	Carl Roth, Karlsruhe, Germany
Microtome RM 2155	Leica Microsystems, Wetzlar, Germany
Microwave oven 0749730M	Privileg, Stuttgart, Germany
Mini-PROTEAN® combs (1.0 mm, 10 well and 15 well)	Bio-Rad Laboratories, Hercules, USA
Mini-PROTEAN® tetra handcast system	Bio-Rad Laboratories, Hercules, USA
Mini-PROTEAN® tetra cell	Bio-Rad Laboratories, Hercules, USA
Mini Trans-Blot® cell	Bio-Rad Laboratories, Hercules, USA
MiniTwist nutating mixer	Select BioProducts, Edison, USA
Orbital shaker 3017	GFL, Burgwedel, Germany
Paraffin embedding center EC 350	Leica Microsystems, Wetzlar, Germany
pH meter 766	Knick Eleketronische Messgeräte, Berlin, Germany
Pipette filler Pipetus®	Hirschmann Laborgeräte, Eberstadt, Germany
Pipettes (2 µl, 10 µl, 20 µl, 100 µl, 200 µl, 1000 µl)	Gilson, Middleton, USA
PowerPac™ basic power supply	Bio-Rad Laboratories, Hercules, USA
Precision scale AB104	Mettler-Toledo, Greifensee, Switzerland
Scale 440-47N	Kern&Sohn, Balingen, Germany
Sonifier® cell disruptor 450	Branson Ultrasonics, Danbury, USA
Spacer plates with 1.0 mm integrated spacers	Bio-Rad Laboratories, Hercules, USA
Spectrophotometer nanoDrop ND-1000	peqLab Biotechnology, Wilmingon, USA
Spectrophotometer SmartSpec™ 3000	Bio-Rad Laboratories, Hercules, USA
Staining boxes Rotilabo®	Carl Roth, Karlsruhe, Germany
Staining cuvettes	Carl Roth, Karlsruhe, Germany
Stain Tray™	Carl Roth, Karlsruhe, Germany
Surgical instruments	Fine Science Tools, Heidelberg, Germany
Thermasonic® gel warmer	Parker Laboratories, Fairfield, USA
Thermocycler PTC-200	Bio-Rad Laboratories, Hercules, USA
Thermocycler Tetrad® 2	Bio-Rad Laboratories, Hercules, USA
Thermomixer® comfort	Eppendorf, Hamburg, Germany
Vevo® 2100 ultrasound system	FUJIFILM VisualSonics, Toronto, Canada
Vevo® compact dual anesthesia system	FUJIFILM VisualSonics, Toronto, Canada
Vevo® imaging station	FUJIFILM VisualSonics, Toronto, Canada
Vevo® MicroScan™ transducer MS400	FUJIFILM VisualSonics, Toronto, Canada

Equipment	Company *continued*
Vevo® MicroScan™ transducer MS700	FUJIFILM VisualSonics, Toronto, Canada
Vortex mixer VortexGenie® 2	Scientific Industries, Bohemia, USA
ViiA™ 7 real-time PCR system	Applied Biosystems, Foster City, USA
Water bath HI1210	Leica Microsystems, Wetzlar, Germany
X-ray cassettes	Dr. Goos-Suprema, Heidelberg, Germany

4.2 Consumables

Table 3. Consumables

Consumable	Company
Ceramic beads (1.4 mm and 2.8 mm)	peqLab Biotechnology, Wilmingon, USA
CL-XPosure™ films	Thermo Fischer Scientific, Waltham, USA
Histology embedding cassettes	Carl Roth, Karlsruhe, Germany
Falcon tubes (15 ml and 50 ml)	Greiner Bio-One, Kremsmünster, Austria
Filter papers	Macherey-Nagel, Düren, Germany
Glass cover slips	Gerhard Menzel, Braunschweig, Germany
Homogenization tubes	peqLab Biotechnology, Wilmingon, USA
MicroAmp® optical 384-well reaction plates	Applied Biosystems, Foster City, USA
MicroAmp® optical adhesive films	Applied Biosystems, Foster City, USA
Microtome blades R35	FEATHER Safety Razor, Osaka, Japan
Nitrocellulose blotting membrane Amersham Hybond ECL (pore size 0.45 µm)	GE Healthcare, Fairfield, USA
PCR disposable strips of 8 tubes with caps	BRAND, Wertheim, Germany
Petri dishes	Greiner Bio-One, Kremsmünster, Austria
Pipette tips (2 µl, 10 µl, 20 µl, 100 µl, 200 µl, 1000 µl)	Biozym Scientific, Hessisch Oldendorf, Germany
Serological pipettes (2 ml, 5 ml, 10 ml, 25 ml)	Sarstedt, Nümbrecht, Germany
Spectrophotometer cuvettes	BRAND, Wertheim, Germany
Superfrost® plus microscope slides	Gerhard Menzel, Braunschweig, Germany
Surgical disposable scalpels	B. Braun Melsungen, Melsungen, Germany
Reaction tubes (1.5 ml and 2.0 ml)	BRAND, Wertheim, Germany
Reagent and centrifuge tubes (5 ml)	Sarstedt, Nümbrecht, Germany
Weighing dishes	Greiner Bio-One, Kremsmünster, Austria
Whatman® gel blotting paper	GE Healthcare, Fairfield, Germany

4.3 Chemicals and reagents

Table 4. Chemicals and reagents

Chemical/Reagent	Company
2-Mercaptoethanol	Carl Roth, Karlsruhe, Germany
2-Propanol	Carl Roth, Karlsruhe, Germany
Acetic acid	Carl Roth, Karlsruhe, Germany
Agarose	Biozym Scientific, Hessisch Oldendorf, Germany
Ammonium persulfate (APS)	Carl Roth, Karlsruhe, Germany
Bovine serum albumin (BSA)	Carl Roth, Karlsruhe, Germany
Bromophenol blue	Carl Roth, Karlsruhe, Germany
Chlorophorm	Carl Roth, Karlsruhe, Germany
Coumaric acid	Sigma-Aldrich, St. Louis, USA
Deoxyribonucleotides (dNTPs)	Fermentas, Burlington, Canada
Developer type E	Christiansen und Linhardt, Planegg, Germany
Dimethylacetamide (DMA)	Sigma-Aldrich, St. Louis, USA
Direct red 80	Sigma-Aldrich, St. Louis, USA
Disodium hydrogen phosphate (Na_2HPO_4)	Carl Roth, Karlsruhe, Germany
DNA loading dye (6×)	Fermentas, Burlington, Canada

Chemical/Reagent	**Company** *continued*
Electrode gel	GE Medical Systems Information Technologies, Freiburg, Germany
Eosin G solution (0.5 %)	Carl Roth, Karlsruhe, Germany
Ethanol (EtOH)	Carl Roth, Karlsruhe, Germany
Ethidium bromide (EtBr)	Carl Roth, Karlsruhe, Germany
Ethylenediaminetetraacetic acid (EDTA)	Sigma-Aldrich, St. Louis, USA
Eukitt® quick hardening mounting medium	Sigma-Aldrich, St. Louis, USA
Fixer type F	Christiansen und Linhardt, Planegg, Germany
Glycerol	Carl Roth, Karlsruhe, Germany
Glycine	Serva, Heidelberg, Germany
Hematoxylin solution according to Harris	Carl Roth, Karlsruhe, Germany
Heematoxylin solution according to Weigert	Carl Roth, Karlsruhe, Germany
Hydrochloride (HCl) (37 %)	Carl Roth, Karlsruhe, Germany
Hydrogen peroxide (H_2O_2) (30 %)	Carl Roth, Karlsruhe, Germany
Isoflurane (Forene®)	Abbott Laboratories, North Chicago, USA
Luminol	Sigma-Aldrich, St. Louis, USA
Methanol (MeOH)	Carl Roth, Karlsruhe, Germany
Monopotassium phosphate (KH_2PO_4)	Carl Roth, Karlsruhe, Germany
Nitrogen (N_2)	Linde, Munich, Germany
Nonyl phenoxypolyethoxylethanol (NP-40) (Igepal®)	Sigma-Aldrich, St. Louis, USA
Normal goat serum (NGS)	Jackson ImmunoResearch Laboratories, West Grove, USA
Paraffin (Paraplast®)	Carl Roth, Karlsruhe, Germany
Paraformaldehyde (PFA)	Carl Roth, Karlsruhe, Germany
Picric acid solution (1.3 % in H_2O (saturated))	Sigma-Aldrich, St. Louis, USA
Polyethylene glycol 300 (PEG300)	Sigma-Aldrich, St. Louis, USA
Potassium chloride (KCl)	Carl Roth, Karlsruhe, Germany
Powdered milk	Carl Roth, Karlsruhe, Germany
Rapamycin	Cayman chemical, Ann Arbor, USA
RNA loading dye (2×)	Fermentas, Burlington, Canada
RNase AWAY®	Thermo Fisher Scientific, Waltham, USA
Rotiphorese® gel 30 (acrylamide/bisacrylamide 37.5:1)	Carl Roth, Karlsruhe, Germany
Sodium chloride (NaCl)	Carl Roth, Karlsruhe, Germany
Sodium chloride (NaCl) solution (0.9 %)	B. Braun Melsungen, Melsungen, Germany
Sodium citrate	Carl Roth, Karlsruhe, Germany
Sodium deoxycholate	Sigma-Aldrich, St. Louis, USA
Sodium dodecyl sulfate (SDS)	Carl Roth, Karlsruhe, Germany
Sodium hydroxide (NaOH)	Carl Roth, Karlsruhe, Germany
Taurine	Carl Roth, Karlsruhe, Germany
Tetramethylethylenediamine (TEMED)	Carl Roth, Karlsruhe, Germany
Toluol	Carl Roth, Karlsruhe, Germany
Tris-hydrochloride	Carl Roth, Karlsruhe, Germany
Tris(hydroxymethyl)aminomethane (Tris)	Carl Roth, Karlsruhe, Germany
Triton® X 100	Carl Roth, Karlsruhe, Germany
TRIzol® reagent	Invitrogen, Carlsbad, USA
Tween® 20	Carl Roth, Karlsruhe, Germany
Tween® 80	Sigma-Aldrich, St. Louis, USA
Ultrasound transmission gel Aquasonic® 100	Parker Laboratories, Fairfield, USA
Xylol	Carl Roth, Karlsruhe, Germany

4.4 Size standards

Table 5. Size standards

Size standard	Company
Generuler™ 100 bp DNA ladder	Fermentas, Burlington, Canada
HiMark™ prestained high molecular weight protein standard	Invitrogen, Carlsbad, USA
PageRuler™ prestained protein ladder	Fermentas, Burlington, Canada
RiboRuler™ low range RNA ladder	Fermentas, Burlington, Canada

4.5 Enzymes and enzyme kits

Table 6. Enzymes and enzyme kits

Enzyme (kit)	Further required kit components	Company
M-MuLV reverse transcriptase (200 U/µl)	10× reverse transcriptase reaction buffer	New England Biolabs, Beverly, USA
Power SYBR®Green PCR master mix	n/a	Applied Biosystems, Foster City, USA
Proteinase K (30 U/mg) (lyophilized)	n/a	Carl Roth, Karlsruhe, Germany
Taq DNA polymerase (5 U/µl)	10× PCR buffer	Qiagen, Hilden, Germany
RNase-free DNase set (lyophilized) (1500 Kunitz units)	RNase-free water RDD buffer	Qiagen, Hilden, Germany

(n/a: not applicable)

4.6 Inhibitors

Table 7. Inhibitors

Inhibitor	Company
COmplete mini EDTA-free protease inhibitor cocktail tablets	Roche Diagnostics, Mannheim, Germany
PhosSTOP phosphatase inhibitor cocktail tablets	Roche Diagnostics, Mannheim, Germany
RiboLock® ribonuclease inhibitor (40 U/µl)	Fermentas, Burlington, Canada

4.7 Buffers and solutions

Table 8. Formulation of buffers and solutions

Buffer/Solution	Formulation
Acidified water	1 % (v/v) acetic acid in ddH_2O
Antibody solution	0.1 % (v/v) Triton® X 100, 0.05 % (v/v) Tween® 20, 1 % (w/v) BSA in 1× TBS
10 % APS	10 % (w/v) APS in ddH_2O
Blocking solution	5 % (v/v) NGS in antibody solution
ECL solution A	0.4 mM coumaric acid, 2.5 mM luminol in 1× ECL stock solution
ECL solution B	0.018 % (v/v) H_2O_2 (30 %) in 1× ECL stock solution
1× ECL stock solution	100 mM Tris-HCl in ddH_2O (pH 8.8)
70 %, 80 %, 90 %, 96 %, 99 % EtOH	x % (v/v) EtOH in ddH_2O
1× Lysis buffer	100 mM Tris-HCl, 200 mM NaCl, 5 mM EDTA, 0.2 % (w/v) SDS in ddH_2O (pH 8.5), before use add 0.02 % (w/v) proteinase K
5 % milk in 1× TBS-T	5 % (w/v) milk in 1× TBS-T
10 N NaOH	10 N NaOH in ddH_2O

Buffer/Solution	Formulation *continued*
1× PBS	1.8 mM KH_2PO_4 in 8.1 mM Na_2HPO_4, 140 mM NaCl, 2.9 mM KCl in ddH_2O (pH 7.4)
4 % PFA solution	4 % (w/v) PFA in 1× PBS
Proteinase K solution	0.02 % (w/v) proteinase K in 1× TBS
1× RIPA buffer	0.1% (w/v) SDS, 1 % (v/v) NP-40, 0.5 % (w/v) sodium deoxycholate, 1mM EDTA in 1× TBS For 10 ml 1× RIPA buffer: 1 PhosSTOP phosphatase inhibitor and 1 cOmplete mini EDTA-free protease inhibitor cocktail tablet
10 % SDS	10 % (w/v) SDS in ddH_2O
1× SDS running buffer	2.5 mM Tris, 19.2 mM glycine, 0.1% (w/v) SDS in ddH_2O
5× SDS sample buffer	15 % (v/v) 2-marcaptoethanol, 15 % (w/v) SDS, 1.5 % (w/v) bromophenol blue, 50 % (v/v) glycerol in 1× TBS
Sirius red solution	0.1 % (w/v) Direct red 80 in picric acid solution
1× Sodium citrate buffer	10 mM sodium citrate in ddH_2O (pH 6.0)
1× TBS	50 mM Tris, 150 mM NaCl in ddH_2O (pH 7.6)
1× TBS-T	1 % (v/v) Tween® 20 in 1× TBS
1× Transfer buffer (for large proteins)	10 mM Tris, 19.2 mM glycine, 0.01 % (w/v) SDS, 10 % (v/v) MeOH in ddH_2O
1× Transfer buffer (for normal proteins)	10 mM Tris, 19.2 mM glycine, 0.01 % (w/v) SDS, 20 % (v/v) MeOH in ddH_2O
1 M Tris	1 M Tris in ddH_2O (pH 6.8 or pH 8.8)
1× TTE buffer	90 mM Tris, 30 mM taurine, 1 mM EDTA in ddH_2O

4.8 Consumable kits

Table 9. Consumable kits

Kit	Company
ApopTag® fluorescein *in situ* apoptosis detection kit	Millipore, Billerica, USA
DC™ protein assay	Bio-Rad Laboratories, Hercules, USA
RNeasy® mini kit	Qiagen, Hilden, Germany

4.9 PCR Primers

All primers (including random hexamer primer for cDNA synthesis) were ordered from BioTeZ, Berlin, Germany. Primers were delivered in lyophilized form and were dissolved in double distilled water (ddH_2O) to a stock concentration of 50 µM.

Table 10. PCR Primers

Primer pairs for genotyping

Amplification product	Primer name	Sequence (5´ → 3´)	Product size	T_A
WT and "floxed" *Hccs* allele	mHccs_FP	GTTACGGAAAGGGTGAGTGA	380 bp (*Hccs* WT allele), 450 bp ("floxed" *Hccs* allele)	60 °C
	mHccs_RP	TCATTCAGGCCAGGACTTCT		
Nkx2-5 WT allele and *Nkx2-5Cre* knockin allele	mNkx2-5_FP	GCCCTGTCCCTCAGATTTCACACC	265 bp (*Nkx2-5* WT allele)	60 °C
	mNkx2-5_RP	GCGCACTCACTTTAATGGGAAGAG		
	mNkx2-5Cre_FP	GATGACTCTGGTCAGAGATACCTG	Together with mNkx2-5_RP: 583 bp (*Nkx2-5Cre* knockin allele)	60 °C
WT and "floxed" *Raptor* allele	mRaptor_FP	CTCAGTAGTGGTATGTGCTCAG	141 bp (*Raptor* WT allele), 180 bp ("floxed" *Raptor* allele)	60 °C
	mRaptor_RP	GGGTACAGTATGTCAGCACAG		
Sry (Sex determination)	mSRY_FP	AGAGATCAGCAAGCAGCTGG	249 bp (for males)	60 °C
	mSRY_RP	TCTTGCCTGTATGTGATGGC		

Primer pairs for quantitative real-time PCR

Primer name	Sequence (5´ → 3´)	Concentration	Product size	T_A
mNppa cDNA_FP	CAGCATGGGCTCCTTCTCCAT	5 µM	89 bp	60 °C
mNppa cDNA_RP	TGTACACAGGATTTGCTCCAATATG			
mNppb cDNA_FP	AGGACCAAGGCCTCACAAAA	10 µM	108 bp	58 °C
mNppb cDNA_RP	TTGAGATATGTGTCACCTTGGAATTT			
mCol1a1 cDNA_FP	CATGTTCAGCTTTGTGGACCT	10 µM	153 bp	57 °C
mCol1a1 cDNA_RP	ATCAAGCATACCTCGGGTTTC			
mCol1a2 cDNA_FP	TGTTGGCCCATCTGGTAAAGA	5 µM	113 bp	57 °C
mCol1a2 cDNA_RP	CAGGGAATCCGATGTTGCC			
mCol3a1 cDNA_FP	GGAACCTGGTTTCTTCTCACC	5 µM	176 bp	57 °C
mCol3a1 cDNA_RP	ATGTCATCGCAAAGGACAGAT			
mCcnb1 cDNA_FP	GCTGACCCAAACCTCTGTAG	1 µM	132 bp	60 °C
mCcnb1 cDNA_RP	GAGGATAGCTCTCATGTTTCC			
mCcnd1_2 cDNA_FP	GAAGTTGTGCATCTACACTGA C	5 µM	132 bp	60 °C
mCcnd1_2 cDNA_RP	GAGAGGAAGTGTTCGATGAAATC			
mCcng1_2 cDNA_FP	GGCCTCAGAATGACTGCAAG	5 µM	158 bp	60 °C
mCcng1_2 cDNA_RP	CACCCAAGATGCTTCGCCTG			
mFn_2 cDNA_FP	GGCAGTGGTCATTTCAGATGCG	5 µM	139 bp	58 °C
mFn_2 cDNA_RP	CTCCCTTTCCATTCCCGAGG			
mGapdh cDNA_FP	AGGTTGTCTCCTGCGACTTCA	1 µM	101 bp	56 – 60 °C
mGapdh cDNA_RP	CCAGGAAATGAGCTTGACAAAGTT			
mMyh7 cDNA_FP	CTAGAGTCAAAGTGGGCAACG	5 µM	120 bp	60 °C
mMyh7 cDNA_RP	GTGTCACCATCCAGTTGAACA			
mCdkn1a _2 cDNA_FP	CAGCTCCGGAGGACCACGTGGCC	5 µM	150 bp	60 °C
mCdkn1a _2 cDNA_RP	CCAATCTGCGCTTGGAGTGATAG			
mCdkn1b cDNA_FP	GACTCGTCAGACAATCCGG	1 µM	155 bp	60 °C
mCdkn1b cDNA_RP	GTCTGCTCCACAGTGCCAG			
mTgfβ1 cDNA_FP	TGGAGCAACATGTGGAACTC	5 µM	101 bp	56 °C
mTgfβ1 cDNA_RP	AGACAGCCACTCAGGCGTAT			
mTgfβ3 cDNA_FP	CTGGAAATCAGCATCCACTGT	5 µM	119 bp	57 °C
mTgfβ3 cDNA_RP	CCATGGTCATCTTCATTGTCC			
mVim cDNA_FP	GTTTCCAAGCCTGACCTCACT	5 µM	188 bp	57 °C
mVim cDNA_RP	TGTCTCCGGTACTCGTTTGAC			

(FP: forward primer, m: murine, RP: reverse primer, T_A: annealing temperature, WT: wildtype)

4.10 Antibodies

Table 11. Antibodies for western blot

Antibody	Product number	Source	Dilution	Company
Primary antibody (1° AB)				
Anti-α-ACTININ	A 7811	mouse	1:500 in 5 % milk in 1× TBS-T	Sigma-Aldrich, St. Louis, USA
Anti-α-TUBULIN	T 9026	mouse	1:10,000 in 5 % milk in 1× TBS-T	Sigma-Aldrich, St. Louis, USA
Anti-p-4E-BP1 (Ser65)	9451	rabbit	1:1,000 in 5 % BSA in 1× TBS-T	Cell Signaling Technology, Danvers, USA
Anti-p-4E-BP1 (Thr37/46)	2855	rabbit	1:1,000 in 5 % BSA in 1× TBS-T	Cell Signaling Technology, Danvers, USA
Anti-p62	5114	rabbit	1:1,000 in 5 % BSA in 1× TBS-T	Cell Signaling Technology, Danvers, USA
Anti-p-AKT (Ser473)	4060	rabbit	1:2,000 in 5 % BSA in 1× TBS-T	Cell Signaling Technology, Danvers, USA
Anti-p-MTOR (Ser2448)	2971	rabbit	1:2,000 in 5 % BSA in 1× TBS-T	Cell Signaling Technology, Danvers, USA
Anti-p-MTOR (Ser2481)	2974	rabbit	1:2,000 in 5 % BSA in 1× TBS-T	Cell Signaling Technology, Danvers, USA
Anti-p-S6 (Ser235/236)	4858	rabbit	1:2,000 in 5 % BSA in 1× TBS-T	Cell Signaling Technology, Danvers, USA
Anti-p-S6 (Ser240/244)	4838	rabbit	1:1,000 in 5 % BSA in 1× TBS-T	Cell Signaling Technology, Danvers, USA
Anti-p-S6K1 (Thr389)	9234	rabbit	1:1,000 in 5 % BSA in 1× TBS-T	Cell Signaling Technology, Danvers, USA
Anti-GAPDH	MA1-22670	mouse	1:40,000 in 5 % milk in 1× TBS-T	Thermo Fisher Scientific, Waltham, USA
Anti-RAPTOR	2280	rabbit	1:1,000 in 5 % BSA in 1× TBS-T	Cell Signaling Technology, Danvers, USA
Anti-RICTOR	2114	rabbit	1:1,000 in 5 % BSA in 1× TBS-T	Cell Signaling Technology, Danvers, USA
Anti-4E-BP1	9644	rabbit	1:1,000 in 5 % BSA in 1× TBS-T	Cell Signaling Technology, Danvers, USA
Anti-AKT	4691	rabbit	1:1,000 in 5 % BSA in 1× TBS-T	Cell Signaling Technology, Danvers, USA
Anti-MTOR	2983	rabbit	1:1,000 in 5 % BSA in 1× TBS-T	Cell Signaling Technology, Danvers, USA
Anti-S6	2217	rabbit	1:1,000 in 5 % BSA in 1× TBS-T	Cell Signaling Technology, Danvers, USA
Anti-S6K1	2708	rabbit	1:1,000 in 5 % BSA in 1× TBS-T	Cell Signaling Technology, Danvers, USA
Secondary antibody (2° AB)				
Anti-mouse IgG HRP-linked	7076	horse	1:2,000 in 5 % milk in 1× TBS-T	Cell Signaling Technology, Danvers, USA
Anti-rabbit IgG HRP-linked	7074	goat	1:2,000 in 5 % milk in 1× TBS-T	Cell Signaling Technology, Danvers, USA

Table 12. Antibodies for immunohistochemistry

Antibody	Product number	Source	Dilution	Company
1° AB				
Anti-CYT *c*	sc-13156	mouse	1:50 in antibody solution	Santa Cruz Biotechnology, Dallas, Texas
Anti-KI67	MA1-90584	rabbit	1:100 in antibody solution	Thermo Fisher Scientific, Waltham, USA
Anti-p-HH3 (Ser10)	9701	rabbit	1:200 in antibody solution	Cell Signaling Technology, Danvers, USA
2° AB				
Anti-mouse IgG Alexa Fluor® 488-linked	A11001	goat	1:500 in antibody solution	Invitrogen, Carlsbad, USA
Anti-rabbit IgG Alexa Fluor® 555-linked	A21428	goat	1:500 in antibody solution	Invitrogen, Carlsbad, USA

4.11 Other substances for immunohistochemistry

Table 13. Other substances for immunohistochemistry

Substance	Product number	Dilution	Company
Alexa Fluor® 555-conjugated WGA	W32464	1:500 in antibody solution	Invitrogen, Carlsbad, USA
ProLong® Gold antifade mountant	P36934	n/a	Invitrogen, Carlsbad, USA
ProLong® Gold antifade mountant with DAPI	P36941	n/a	Invitrogen, Carlsbad, USA
TO-PRO®-3	T3605	1:1,000 in antibody solution	Invitrogen, Carlsbad, USA

(n/a: not applicable)

4.12 Software

Table 14. Software

Software	Company
Adobe Illustrator CS4	Adobe Systems, San Jose, USA
Adobe Photoshop CS4	Adobe Systems, San Jose, USA
BZ-8100 observation application (Biozero BZ-8100 fluorescence microscope)	Keyence, Osaka, Japan
BZ image analysis application (Biozero BZ-8100 fluorescence microscope)	Keyence, Osaka, Japan
FireCam control (Gel documentation system GelDoc2000)	Leica Microsystems, Wetzlar, Germany
ImageJ	Open source
Image Studio Ver2.0 (Imaging system Odyssey® Fc)	LI-COR® Biosciences, Lincoln, USA
Leica application suite advanced fluorescence (Confocal laser scanning microscope TSC SPE)	Leica Microsystems, Wetzlar, Germany
Leica application suite (Digital camera for microscope IC80 HD)	Leica Microsystems, Wetzlar, Germany
ND-1000 V3.8.1 (Spectrophotometer nanoDrop ND-1000)	peqLab Biotechnology, Wilmingon, USA
Office 2010	Microsoft, Redmond, USA
PASWStatistics18 (SPSS)	IBM, Armonk, USA
Vevo® 2100 analysis software 1.5.0 (Vevo® 2100 System)	FUJIFILM VisualSonics, Toronto, Canada
Viia™ 7 (ViiA™ 7 real-time PCR system)	Applied Biosystems, Foster City, USA

4.13 Online tools

Table 15. Online tools

Tool	URL	Last use
DAVID	http://david.abcc.ncifcrf.gov/	11th October 2014
NCBI PrimerBlast	http://www.ncbi.nlm.nih.gov/tools/primer-blast/	11th October 2014

5 METHODS

5.1 Animal experiments

Animal experiments were carried out in strict accordance to the institutional guidelines of the Max Delbrück Center for Molecular Medicine in Berlin, Germany and had previously been approved by the responsible authority (State Office of Health and Social Affairs Berlin, Germany ("Landesamt für Gesundheit und Soziales" (LAGeSo)) (approval numbers G0027/10 and T0113/07)). All efforts were made to minimize suffering of the mice according to the ARRIVE guidelines[202].

Mice were kept in the animal facility of the Max Delbrück Center for Molecular Medicine in Berlin, Germany with a 12 h day and night cycle at 24±2 °C. If not stated differently, a commercially available dry food diet purchased from ssniff® (ssniff® M-Z autoclavable complete feed for mice - breeding, V1124-3) was fed. In any case, mice had unrestricted access to food and water.

5.1.1 Mouse strains

5.1.1.1 "Floxed" Hccs mice

The "floxed" Hccs mouse strain carries two locus of X-over P1 (*loxP*) sites (a site on the bacteriophage P1 consisting of 34 bp) flanking the catalytic domain of the X-chromosomal *holocytochrome c synthase* (*Hccs*) gene (exon 5 to 7[193]). Mice were generated as previously described and are viable, fertile, normal in size and do not display any gross physical or behavioral abnormalities[192]. In this study, females homozygous for the "floxed" *Hccs* allele (♀ $Hccs^{loxP/loxP}$) were used to generate heart conditional *Hccs* knockout (KO) mice (see Chapter 5.1.2.1, Figure 6).

5.1.1.2 Nkx2-5Cre mice

Nkx2-5Cre mice were kindly provided by Professor Richard Harvey from the Victor Chang Cardiac Research Institute in Darlinghurst, Australia[203]. The Nkx2-5Cre strain carries a nuclear-localizing *Cre* recombinase sequence in the 3' untranslated region of the NK2 homeobox 5 gene (*Nkx2-5*) on chromosome 17[203]. The cardiac homeobox transcription factor *Nkx2-5* is a cardiac lineage marker activated in heart progenitors at early cardiac crescent stages[204]. Thus, Nkx2-5Cre mice express *Cre* recombinase in cardiac progenitor cells from 7.5 days post coitum (dpc) onwards[205]. These mice are viable, fertile, normal in size and do not display any gross physical or behavioral abnormalities[203]. In this study, Nkx2-5Cre males heterozygous for the *Nkx2-5Cre* knockin allele (♂ $Nkx2\text{-}5^{WT/Cre}$) were used to generate heart conditional *Hccs* KO mice (see Chapter 5.1.2.1, Figure 6). Nkx2-5Cre males

homozygous for the *Nkx2-5Cre* knockin allele (♂ *Nkx2-5*$^{Cre/Cre}$) were used to generate heart conditional *Raptor* KO mice (see Chapter 5.1.2.2, Figure 7).

5.1.1.3 "Floxed" Raptor mice

The "floxed" Raptor mouse strain carries two *loxP* sites flanking exon 6 of the *Raptor* gene. Mice were generated as previously described and are viable, fertile, normal in size and do not display any gross physical or behavioral abnormalities[206]. Homozygous "floxed" Raptor mice (*Raptor*$^{loxP/loxP}$), which were ordered from The Jackson Laboratory, Bar Harbor, USA (stock number: 013188), were used to generate heart conditional *Raptor* KO mice (see Chapter 5.1.2.2, Figure 7).

5.1.2 Breeding strategies

5.1.2.1 Generation of heart conditional Hccs KO mice

Generation and characterization of heart conditional *Hccs* KO mice were described previously[192]. Briefly, *Hccs*$^{loxP/loxP}$ females (see Chapter 5.1.1.1) were bred with *Nkx2-5*$^{WT/Cre}$ males (see Chapter 5.1.1.2) to allow cardiac-specific *Cre*/*loxP* recombination. This results in *Cre*-mediated excision of the *loxP*-flanked *Hccs* sequence (catalytic domain) in the offspring from 7.5 dpc onwards specifically in cardiomyocytes and some endocardial cells[192]. Thereby, healthy control female (♀ *Hccs*$^{+/+}$) and male (♂ *Hccs*$^{+/Y}$) offspring, which are heterozygous or hemizygous, respectively, for the "floxed" *Hccs* allele but do not express the *Cre* recombinase sequence, are generated (Figure 6). Besides, because the *Hccs* gene is subjected to X chromosome inactivation, outcomes in males and females carrying both, the "floxed" *Hccs* gene on the maternal X chromosome and the *Cre* recombinase gene on the paternal chromosome 17, differ (Figure 6). Heart conditional hemizygous *Hccs* KO males (c*Hccs*$^{-/Y}$) exhibit *Hccs* inactivation in the entire heart and die at midgestation due to dysfunction of the electron transport chain (ETC)[192] (Figure 6). In contrast, females are considered heart conditional heterozygous *Hccs* KOs (c*Hccs*$^{+/-}$) (Figure 6). In these mice, 50 % of cardiac cells have the "floxed" X chromosome silenced and remain healthy, while 50 % of cardiomyocytes keep the "floxed" X chromosome active and consequently display disturbed ETC function[192]. At birth, control *Hccs*$^{+/Y}$ males and *Hccs*$^{+/+}$ females as well as c*Hccs*$^{+/-}$ females are born in equal ratios[192]. All experiments in this study were performed in c*Hccs*$^{+/-}$ females and *Hccs*$^{+/+}$ female littermate controls.

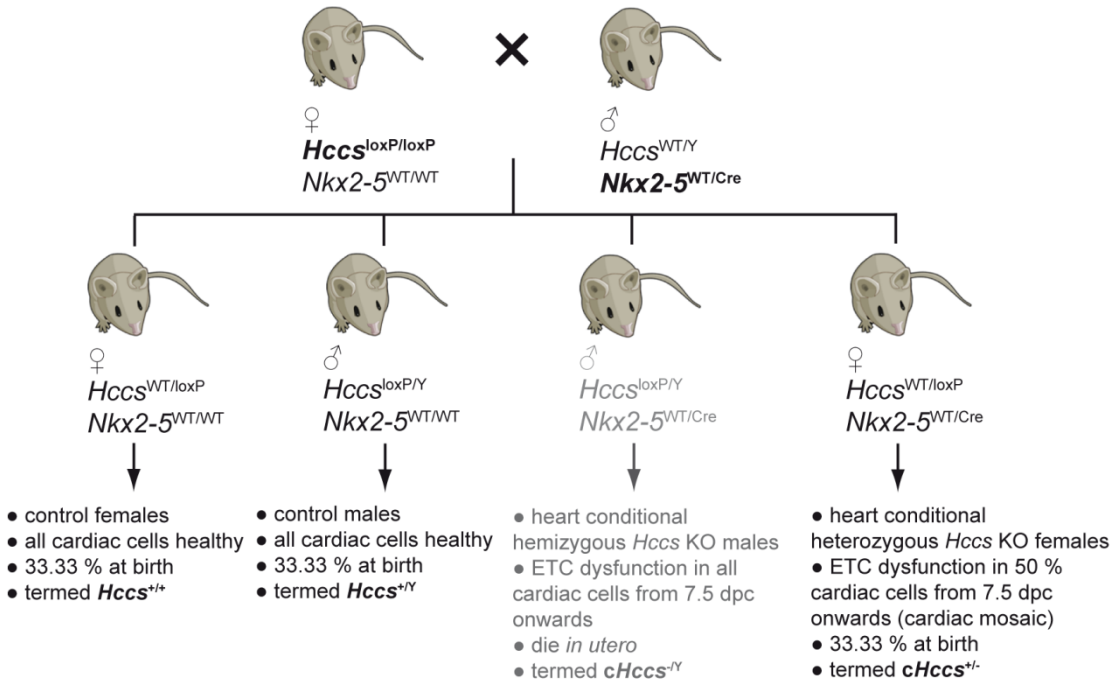

Figure 6. Breeding strategy to generate heart conditional *Hccs* KO mice.
Breeding of *Hccs*$^{loxP/loxP}$ females with *Nkx2-5*$^{WT/Cre}$ males allowed cardiac-specific *Cre*/*loxP* recombination in offspring carrying both, the "floxed" *Hccs* gene on the X chromosome and the *Cre* recombinase gene on chromosome 17, from 7.5 dpc onwards. c*Hccs*$^{-/Y}$ males die *in utero*, while c*Hccs*$^{+/-}$ females develop a cardiac mosaic for the "floxed" *Hccs* allele. Female *Hccs*$^{+/+}$ littermates were used as controls in all experiments in this study. (Cre: *Cre* recombinase sequence, dpc: days post coitum, ETC: electron transport chain, *Hccs*: gene for holocytochrome *c* synthase, KO: knockout, loxP: two locus of X-over P1, *Nkx2-5*: NK2 homeobox 5 gene, WT: wildtype, Y: Y chromosome)

5.1.2.2 Generation of heart conditional Raptor KO mice

Breeding of *Raptor*$^{loxP/loxP}$ females (see Chapter 5.1.1.3) with Nkx2-*5*$^{Cre/Cre}$ males (see Chapter 5.1.1.2) allowed cardiac-specific *Cre*-mediated excision of the *loxP*-flanked *Raptor* sequence in the offspring from 7.5 dpc onwards specifically in cardiac progenitor cells. All offspring in the first filial (F1) generation were heterozygous for the *Nkx2-5-Cre* knock-in and for the "floxed" *Raptor* allele, resulting in heterozygous cardiac-specific *Raptor* KOs (♂/♀ c*Raptor*$^{+/-}$) (Figure 7). Breeding of F1 offspring among each other generated control males and females (♂/♀ *Raptor*$^{+/+}$, 43.75 %) as well as heart conditional heterozygous (♂/♀ c*Raptor*$^{+/-}$, 37.5 %) and homozygous *Raptor* KOs (♂/♀ c*Raptor*$^{-/-}$, 18.75 %) in the second filial (F2) generation (Figure 7). All experiments in this study were performed in c*Raptor*$^{-/-}$ and c*Raptor*$^{+/-}$ females and their respective *Raptor*$^{+/+}$ female littermate controls.

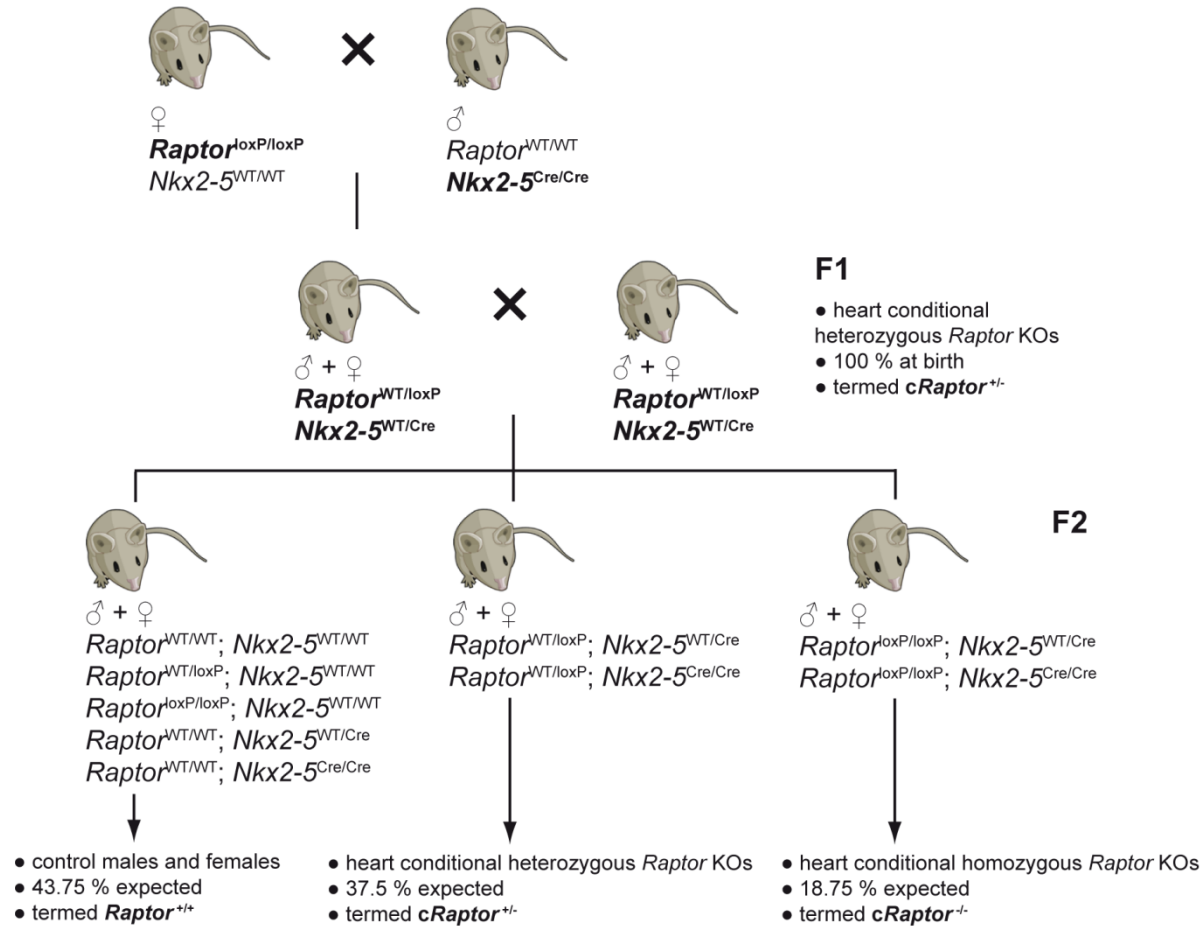

Figure 7. Breeding strategy to generate heart conditional *Raptor* KO mice.
Breeding of *Raptor*$^{loxP/loxP}$ females with *Nkx2-5*$^{Cre/Cre}$ males allowed cardiac-specific *Cre*/*loxP* recombination in all offspring from 7.5 dpc onwards, generating heterozygous heart-specific *Raptor* KOs (♂/♀ c*Raptor*$^{+/-}$) in the F1 generation. Breeding of the F1 offspring generated control males and females (♂/♀ *Raptor*$^{+/+}$) as well as heart conditional heterozygous (♂/♀ c*Raptor*$^{+/-}$) and homozygous *Raptor* KOs (♂/♀ c*Raptor*$^{-/-}$) in the F2 generation. *Cre*-positive female littermates without "floxed" *Raptor* gene (*Raptor*$^{+/+}$) were used as controls in all experiments in this study. (Cre: *Cre* recombinase sequence, F1/F2: first/second filial generation, KO: knockout, loxP: two locus of X-over P1, *Nkx2-5*: NK2 homeobox 5 gene, *Raptor*: gene for regulatory-associated protein of mTOR, WT: wildtype)

5.1.3 Mouse embryo and organ preparations

5.1.3.1 Preparation of embryonic hearts

Mating of mice was performed over night (o/n) and female mice were checked the next morning for vaginal plugs. Females positive for a vaginal plug were considered to be pregnant at 0.5 dpc. Plug-positive dams that exhibited obvious abdominal growth on the appropriate day of pregnancy were sacrificed by cervical dislocation. Mice were placed in a dorsal position and the abdominal wall as well as the abdominal cavity was opened to expose the uterus. The uterine wall was cut open longitudinally and the embryos, each still inside the amnion attached to the placenta, were removed from the left and the right uterus and placed in ice-cold 1× PBS. The amnion was opened and the umbilical cord, connecting the embryo to its placenta, was cut through. The developmental stage of the embryos was confirmed according to Theiler's criteria[207]. If the embryo was required for histological analyses, the heart remained *in situ*. The head and the posterior part of the

embryo (including the tail and the hind limbs) were chopped off and the torso was fixed in 4 % PFA solution and processed for histology. If the heart was designated for RNA or protein isolation, the embryo was placed in a dorsal position, the thorax was opened with precision tweezers and the whole heart (including ventricles and atria) was removed from the thoracic cavity by cutting through the outflow tract (OFT). The heart was cleaned from non-cardiac tissue, snap-frozen in liquid nitrogen and stored at -80 °C. The posterior part of the embryos was used for DNA isolation and subsequent genotyping.

5.1.3.2 Preparation of hearts and organs from newborn mice

Newborn mice prepared within the first 24 h after birth were considered neonatal mice, also referred to as postnatal day 1 (P1). P2 or P3 (postnatal day 2 or 3) relates to pups dissected within the first 48 h or 72 h after birth, respectively. Preparations always took place around noon of the appropriate day. After the body weight (BW) was measured on a precision scale, mice were killed by decapitation. The thorax was opened and the costal arches were forced apart. The heart was removed from the thoracic cavity by cutting through the OFT and washed in ice-cold 1× PBS to remove blood. Non-cardiac tissue was detached, hearts were dried on a paper towel and the heart weight (HW) was measured using a precision scale. The heart was snap-frozen in liquid nitrogen and stored at -80 °C or fixed in 4 % PFA solution for histological analyses. For kidney and lung explantation, the abdominal cavity of P1 mice was opened further sidewards to the spine. Both kidneys were removed from the retroperitoneum by transsecting the ureter and the renal artery and vein. Kidneys were dried on a paper towel and the combined weight of both kidneys was measured on a precision scale. Lung tissue was removed by cutting off half of the right lung. Kidney and lung tissue was washed in 1× PBS, snap-frozen in liquid nitrogen and stored at -80 °C. Tail tips of the pups were clipped and used for DNA isolation as well as subsequent genotyping.

5.1.3.3 Preparation of hearts and organs from 3 week and 11 week old mice

3 and 11 week old mice were killed by cervical dislocation and the BW was determined. Mice were placed in a dorsal position, the abdominal wall was opened and the costal arches were cut through along the lateral wall with dissecting scissors. To remove the heart from the thoracic cavity, the diaphragm was opened and the exposed heart was disconnected at the OFT and in the region of the ascending aorta. The explanted heart was washed in ice-cold 1× PBS to remove remaining blood. Adherent lung and thymus tissue was removed, the heart was dried on paper towel and the HW was measured using a precision scale. The apex of the heart was cut off, bisected (one part for RNA isolation, one for protein isolation) and snap-frozen in liquid nitrogen. The remaining heart tissue was fixed in 4 % PFA solution for histological analyses. A part of the ear of 3 week and 11 week old mice was clipped and used for DNA isolation and subsequent genotyping.

In 11 week old adult mice, not only the heart but also other organs were prepared. After opening the abdominal cavity and the thorax, all organs were evaluated with respect to pathological phenotypes. All six liver lobes were removed in one piece by cutting the ligaments, the portal vein and the hepatic artery. The liver was transferred into ice-cold 1× PBS and the gallbladder was removed. For explanting the spleen from the abdominal cavity, the mesenteries, the splenic artery and the splenic vein were carefully cut through and the spleen was also transferred into ice-cold 1× PBS. Both kidneys were explanted by removing the renal capsule and transsecting the ureter and the renal artery and vein. Subsequently, kidneys were washed in ice-cold 1× PBS. After drying all organs on paper towel, organ weights were measured using a precision scale and organs were snap-frozen in liquid nitrogen and stored at -80 °C.

5.1.4 Rapamycin injection

Rapamycin (Cayman chemical) was dissolved in a stock solution at 20 mg/ml in DMA and stored up to six months at -20 °C. Pregnant dams were treated with rapamycin by subcutaneous (s.c.) injections every 12 h during pregnancy from 11.5 dpc or 15.5 dpc until term. Each injection contained 5 mg rapamycin/kg BW diluted in 200 µl vehicle (10 % PEG 300 and 17 % Tween® 80 in 0.9 % NaCl solution). As controls, pregnant dams were injected with DMA-containing vehicle as described above. BW of pregnant dams was measured daily to constantly adjust rapamycin concentrations during the injection period. S.c. injections were administered alternating in the nuchal fold as well as in the right and the left leg fold. After birth, rapamycin injections ended and offspring were prepared immediately or were weaned after 3 weeks and prepared at the age of 11 weeks.

5.1.5 Low protein diet

Low protein-containing food with 8.8 % crude protein was purchased from ssniff® (ssniff® EF R/M Protein deficient experimental diet, E15202-24). Female and male mice were put on a low protein diet (LPD) two weeks prior to mating. Dams were kept on LPD during pregnancy and, depending on the experimental setup, hearts from offspring were prepared at 13.5 dpc or at P1. Alternatively, after birth mother and offspring were kept on LPD, offspring were weaned after 3 weeks, remained on LPD and were prepared at the age of 11 weeks. As controls, mice were treated the same way using the appropriate sniff® standard protein diet (SPD) containing 22 % crude protein (ssniff® M-Z autoclavable complete feed for mice - breeding, V1124-3).

5.1.6 Evaluation of food intake

To measure the food intake of adult mice, 5 months old non-pregnant females were kept isolated in separate cages. A defined amount of food was weighed and provided to the mice.

The remaining food as well as the BW were measured daily at the same time of day over a period of two weeks. To measure the food intake of pregnant mice, 5 months old pregnant dams were kept isolated in separate cages. A defined amount of food was provided at 13.5 dpc. The remaining food as well as the BW was measured daily at the same time of day until the end of pregnancy. The food intake was calculated from the daily decline in food weight and is given in gram food per day per mouse per kilogram BW.

5.1.7 Echocardiography

Echocardiography is an ultrasound-based diagnostic imaging technique, which allows noninvasive visualization and analysis of the heart morphology and its functional parameters. The echocardiographic measurements and analyses in this study were performed in collaboration with Martin Taube and Stefanie Schelenz from the Technology Platform “Pathophysiology” at the Max Delbrück Center for Molecular Medicine in Berlin, Germany. Operators were blinded for mouse genotypes and groups during echocardiographic measurements as well as data analyses.

11 week old adult mice were anesthetized by a 2.5 %-isofluran-oxygen-mixture using the Vevo® compact dual anesthesia system (FUJIFILM VisualSonics). Measurements on neonates were performed on awake pups. Mice were placed in a dorsal position on the heated (37 °C) stage of the Vevo® imaging station (FUJIFILM VisualSonics) and fixed with their paws on electrode gel-covered electrodes to monitor heart and respiratory rate. Body temperature of adult mice was controlled using a rectal temperature probe and was kept constant at 36 °C to 37 °C using a heat lamp. Body temperature of neonatal mice cannot be directly controlled, but the heat lamp was continuously directed to the pups to maintain the body temperature. To allow optimal imaging, chest fur of adult mice was removed with an electric razor and both, adult and neonatal mice were covered ventrally with preheated (37 °C) ultrasound transmission gel. Echocardiography was recorded using the Vevo® 2100 high frequency ultrasound system (FUJIFILM VisualSonics) with a MicroScan™ transducer MS400 (FUJIFILM VisualSonics) set to 30 MHz for adult mice or MS700 (FUJIFILM VisualSonics) set to 50 MHz for neonatal mice. Recorded echocardiographies were analyzed and evaluated with respect to heart morphology and function using the Vevo® 2100 analysis software. Brightness (B)-mode images were taken to display the two-dimensional parasternal long axis view of the heart. The fraction of blood ejected by the left ventricle (LV) during one contraction (ejection fraction (EF)) was measured by tracing the LV cavity in end-diastole and end-systole. Assessment of LV dimensions (LV internal diameter (LVID) in end-systole and end-diastole) and wall thickness (LV posterior wall (LVPW) thickness in end-systole and end-diastole, interventricular septum (IVS) thickness in end-systole and end-diastole) took place in motion (M)-mode images. From the measured parameters fractional shortening (FS) (fraction of LV dimension in end-diastole

that is shortened in end-systole) was calculated. Hearts of neonatal mice were prepared immediately after echocardiography.

5.2 Bioinformatical methods

Functional annotation of differentially regulated genes in neonatal c*Hccs*$^{+/-}$ mice was done using the online database for annotation, visualization, and integrated discovery (DAVID)[208]. To identify differentially regulated genes, genome-wide microarray analysis using neonatal whole-heart RNA from c*Hccs*$^{+/-}$ mice in comparison to female *Hccs*$^{+/+}$ controls had been performed in the run-up to this study by Manuela Magarin during her PhD project at the Max Delbrück Center for Molecular Medicine in Berlin, Germany. Briefly, for these microarray expression analyses a total of eight Affymetrix GeneChip Mouse Genome 430 2.0 arrays was used. Three neonatal (P1) hearts of the same genotype were pooled and four pooled samples per genotype (*Hccs*$^{+/+}$ and c*Hccs*$^{+/-}$) were analyzed. For unbiased functional group classification, only those genes were selected that were found to be differentially regulated in neonatal c*Hccs*$^{+/-}$ hearts compared to neonatal c*Hccs*$^{+/-}$ littermate control hearts with a fold change higher than +1.5 or lower than -1.5 in combination with a highly significant *p*-value ($p<0.01$) (Supplementary Table S1). The resulting gene list was uploaded to DAVID using the gene functional annotation tool that is based on a novel biological module-centric algorithm to functionally analyze large gene lists[208-210]. The DAVID output was evaluated with regard to the enrichment score of the functional groups and only those gene clusters with a fold enrichment larger than 1.5 in combination with a significant *p*-value ($p<0.05$) were considered for further analyses.

5.3 Molecular biological methods

5.3.1 Mouse genotyping

5.3.1.1 Isolation of genomic DNA from murine tissue

Genomic DNA from murine tissue was isolated for subsequent genotyping. For embryonic samples, the posterior part of the body including the tail was used. For P1, P2 and P3 mice, DNA was isolated from the tail only. For 3 week and 11 week old mice, ear biopsies were used. The tissue was proteinase K (Carl Roth) digested in 200 µl 1× lysis buffer by incubation o/n at 55 °C with constant shaking at 11,000 rpm in a thermomixer (Eppendorf). The next day, the lysate was vortexed and centrifuged for 10 min at 16,000 × *g* at room temperature (RT) to remove undigested cell debris. 100 µl supernatant were diluted with 100 µl 2-propanol, followed by immediate inversion to precipitate the DNA. After 5 min incubation at RT, the mixture was centrifuged for 5 min at 18,400 × *g* at RT and the supernatant was discarded. The DNA pellet was washed with 100 µl 70 % ethanol (EtOH)

followed by a second centrifugation step for 5 min at 18,400 × *g* at RT. The supernatant was again discarded and the pellet was air dried at 37 °C with constant shaking at 11,000 rpm using a thermomixer (Eppendorf) until no EtOH was left. Subsequently, the DNA pellet was resuspended in 100 µl double distilled water (ddH_2O) at 50 °C with constant shaking at 11,000 rpm for 1 h in a thermomixer (Eppendorf).

5.3.1.2 DNA concentration measurement

DNA concentration was measured at 260 nm using a nanoDrop spectrophotometer (peqLab Biotechnology) according to the manufacturer's instructions. Then, 1.5 µl of isolated DNA was applied directly onto the measurement pedestal. The optical density (OD) was determined and the DNA concentration was automatically calculated with ddH_2O serving as blank value. DNA quality was evaluated depending on the OD_{260}/OD_{280} ratio. Only DNA samples with OD_{260}/OD_{280} = 2.0±0.1 were used for genotyping.

5.3.1.3 Genotyping by polymerase chain reaction

Genotyping and sexing of embryos and mice was performed by polymerase chain reaction (PCR), which allows specific amplification of target DNA sequences[211]. Isolated genomic DNA was used as template after dilution to a final concentration of 50 ng/µl. The wildtype (WT) and the "floxed" *Hccs* allele as well as the *Nkx2-5* WT allele and the *Nkx2-5Cre* knockin allele were detected and differentiated according to their size (see Chapter 4.9, Table 10). Raptor animals were genotyped for the WT and the "floxed" *Raptor* allele as well as for the *Nkx2-5* WT and *Nkx2-5Cre* knockin allele, respectively (see Chapter 4.9, Table 10). Sex was determined in embryos and neonates by detection of the *sex determining region of chromosome Y* gene (*Sry*), which identifies males but not females. The PCR reaction mixtures were pipetted on ice into 8-well PCR strips and the PCR program was performed in a thermocycler (Bio-Rad Laboratories). Primer pairs (see Chapter 4.9, Table 10) as well as PCR reaction and protocol (Table 16) were already well-established for all genotyping reaction in the run-up to this study. After the PCR run was completed, PCR products were stored at 4 °C or immediately loaded on an agarose gel.

Table 16. Genotyping PCR setup

PCR reaction mixture		**PCR program**			
Component	**Volume**	**Step**	**Temperature**	**Time**	**Cycles**
10× PCR buffer	2.5 µl	Initialization	95 °C	3 min	1
10 µM forward primer	0.5 µl	Denaturation	95 °C	30 s	40
10 µM reverse primer	0.5 µl	Primer annealing	60 °C	45 s	
2.5 mM dNTPs	1 µl	Elongation	72 °C	1 min	
5 U/µl *Taq* polymerase	0.1 µl	Final elongation	72 °C	8 min	1
50 ng/µl genomic DNA	1 µl	Final hold	4 °C	∞	
ddH_2O	19.4 µl				
Total volume	25 µl				

5.3.1.4 Agarose gel electrophoresis

To analyze the genotyping PCR reactions, the PCR products were separated according to their size in a horizontal 2 % (w/v) agarose gel. The agarose was dissolved in 1× TTE buffer by heating in a microwave. Ethidium bromide (EtBr) was added to the liquid gel solution with a final concentration of 0.2 µg/ml. After cooling down to 55 °C, the agarose-TTE-EtBr-solution was poured into a gel cast and a comb was inserted. Following final gellation, 10 µl of the PCR reaction were loaded. The Generuler^{TM} 100 bp DNA ladder (Fermentas) served as size standard. The gel run was performed in an horizontal agarose electrophoresis unit at 100 V – 130 V in 0.5 µg/ml EtBr-containing 1× TEE buffer. Electrophoresis was terminated when the orange running front of the PCR buffer reached the bottom of the gel. Separated PCR products were visualized under ultraviolet (UV) light (320 nm) in a gel documentation system (Bio-Rad Laboratories).

5.3.2 RNA expression analyses

5.3.2.1 RNA isolation

Isolation of total RNA (including messenger (mRNA), ribosomal (rRNA) and transfer (tRNA) RNA) from murine myocardial tissue was performed under ribonuclease (RNase)-free conditions following the TRIzol® reagent (Invitrogen) method. Snap frozen whole embryonic hearts or approximately 20 mg of apical heart tissue from 11 week old mice were used. Adult heart tissue was transferred to an RNase-free 2-ml homogenization tube that contained a mixture of twelve 1.4 mm and five 2.8 mm ceramic beads (peqLab Biotechnology). Then, 500 µl pre-cooled TRIzol® (Invitrogen) were added and tubes were arranged in the homogenizer system Precellys® 24 (peqLab Biotechnology), which was cooled down to 4 °C beforehand. The tissue was shredded twice with 5000 rpm for 20 s with a 20 s break. Whole embryonic hearts were homogenized on ice in 500 µl pre-cooled TRIzol® using a motorized micropestle (Carl Roth) for 30 s. The TRIzol® reagent is a mono-phasic solution of phenol and guanidine isothiocyanate (a protein denaturant that inactivates RNases) that promotes the release of nucleic acids. It maintains the integrity of the RNA during homogenization, while at the same time it disrupts cells and dissolves cell components. After homogenization, the tissue lysate was transferred into a new RNase-free 1.5-ml tube and incubated at RT for 5 min. Following addition of 100 µl chloroform, the mixture was immediately inverted for 15 s and incubated for 3 min at RT. During subsequent centrifugation for 15 min at 16,500 × *g* and at 4 °C, the acidic phenol-chloroform-solution got separated into three phases: a lower red, phenol-chloroform organic phase containing cell fragments and proteins, a white viscous interphase containing DNA and on top a transparent aqueous RNA-containing phase. The upper transparent phase was transferred into a new RNase-free 2.0-ml tube and the RNA was further purified at RT following the RNeasy® Mini handbook (Qiagen) according to the

manufacturer's instructions. An RNase-free deoxyribonuclease (DNAse) set (Qiagen) was used to digest genomic DNA contaminations directly on the RNA purification columns during a 15 min incubation step at RT. The RNA was eluted from the spin columns using 30 µl RNase-free water for embryonic samples, and 60 µl RNase-free water for adult samples. After RNA concentration measurement and quality control, the samples were stored at -80 °C or immediately processed for complementary DNA (cDNA) synthesis.

5.3.2.2 RNA concentration measurement and quality control by RNA gel electrophoresis

RNA concentration was measured at 260 nm using a nanoDrop spectrophotometer (peqLab Biotechnology) according to the manufacturer's instructions. Thereby, 1.5 µl isolated RNA was applied directly onto the measurement pedestal. The OD was determined and the RNA concentration was automatically calculated. RNase-free water served as blank value. RNA quality was evaluated depending on the OD_{260}/OD_{280} as well as on the OD_{260}/OD_{230} ratios. Only high quality RNA samples with OD_{260}/OD_{280} = 2.0±0.1 and OD_{260}/OD_{230} = 2.0±0.1 were used for cDNA synthesis.

Besides, quality was controlled by RNA gel electrophoresis. Isolated RNA was run on a horizontal 2 % (w/v) agarose gel. RNA was diluted with RNase-free water to a final concentration of 0.7 µg in a total volume of 10 µl. RNA was mixed to equal parts with 10 µl 2× RNA loading dye (Fermentas). RNA samples as well as the RiboRuler^{TM} low range RNA ladder (Fermentas), which served as size standard, were denatured for 10 min at 70 °C in a thermocycler (Bio-Rad Laboratories). The entire 20 µl RNA-loading dye-sample was loaded onto the gel. Gel preparation and gel run were performed as described above (see Chapter 5.3.1.4), except the gel was run at 4 °C at low voltage (60 V). Electrophoresis was terminated when the blue running front of the RNA loading dye reached the bottom of the gel. Separated RNA was visualized under UV light (320 nm) in a gel documentation system (Bio-Rad Laboratories). Only RNA samples that revealed clear 28S and 18S rRNA bands and did not display RNA degradation in the RNA gel were used for cDNA synthesis.

5.3.2.3 cDNA synthesis

Isolated cardiac RNA was reversely transcribed into cDNA. RNA was diluted with RNase-free water to a final concentration of 0.9 µg in a total volume of 10 µl. After addition of 2 µl 50 µM random hexamer primer and 4 µl 2.5 mM dNTPs, samples were incubated for 5 min at 70 °C to denature the secondary structures of the RNA. Next, 2 µl 10× reverse transcriptase reaction buffer, 0.5 µl 40 U/µl RibiLock® ribonuclease inhibitor (Fermentas) and 1 µl 200 U/µl M-MuLV reverse transcriptase (NEB) were added such that the final volume of each reverse transcription reaction was 19.5 µl. Samples were incubated for 10 min at 25 °C to allow primer annealing and for 60 min at 42 °C to synthesize the complementary DNA strand. Last,

the enzyme was inactivated for 10 min at 90 °C. All steps were performed in a thermocycler (Bio-Rad Laboratories) using 8-well PCR strips. After successful reverse transcription, cDNA was diluted 1:3 in ddH_2O. cDNA samples were stored at -20 °C or immediately used for quantitative real-time PCR.

5.3.2.4 Quantitative real-time PCR

5.3.2.4.1 Primer design and determination of optimal annealing temperature by gradient PCR

Primer pairs used for quantitative real-time PCR (qPCR) (see Chapter 4.9, Table 10) were designed using the NCBI Primer-BLAST online tool. Primers were designed according to the following criteria: primer size between 18 bp and 26 bp, size of amplified product between 80 bp and 190 bp, primer annealed within coding region of mRNA transcript, primer did not span exon-exon junctions and primer pairs were separated by at least one intron on the corresponding genomic DNA sequence, which was preferentially longer than 1 kb. Primer pairs were controlled for hairpin formation and self-annealing using the NCBI Primer-BLAST online tool. To determine the optimal annealing temperature for each primer pair, different annealing temperatures were tested by performing a gradient PCR. PCR setup was described above (see Chapter 5.3.1.3, Table 16), except applying 12 different annealing temperatures between 54 °C and 65 °C and using 1 µl 1:3 diluted cDNA (see Chapter 5.3.2.3) as well as 1 µl 50 ng/µl genomic DNA (see Chapter 5.3.1.1) and 1 µl ddH_2O as template, respectively. PCR products were separated in a horizontal 2 % (w/v) agarose gel as described before (see Chapter 5.3.1.4). PCR products were visualized and the optimal annealing temperature for subsequent qPCR was chosen, for which only one single PCR product of the predicted size in the cDNA template reaction was identified. Primer pairs resulting in primer dimers when ddH_2O was used as template or primer pairs amplifying products when genomic DNA was used as template were rejected.

5.3.2.4.2 Determination of optimal primer concentrations

The specificity of each primer pair was confirmed by melt curve analyses and optimal primer concentrations were assessed by evaluation of PCR efficiency after performing qPCR using SYBR®Green. SYBR®Green is a cyanine dye that intercalates into newly synthesized PCR products. The resulting DNA-dye-complex absorbs blue light (497 nm) and emits green light (520 nm). The amount of synthesized DNA rises during the qPCR reaction, which results in increased SYBR®Green fluorescence intensity that can be detected after each PCR cycle. The point at which the fluorescent signal exceeds above a defined threshold is termed threshold cycle (C_T), which in turn is a measure for the amount of template cDNA in the sample. The earlier the threshold is reached, the more template cDNA was present in the initial reaction mixture.

Predefined template cDNA dilution series (undiluted, 1:2, 1:4, 1:8 and 1:16 in ddH_2O) were prepared and 1 µl per dilution was pipetted in triplicates into a 384-well reaction plate. Subsequently, 1.4 µl forward and 1.4 µl reverse primer, 10 µl Power SYBR®Green PCR master mix (Applied Biosystems) and 6.2 µl ddH_2O were added per well to obtain a final qPCR reaction volume of 20 µl. Three primer concentrations (stock concentration: 1 µM, 5 µM and 10 µM in ddH_2O) were tested, each with a separate dilution series. The 384-well reaction plate was vortexed for 30 s and centrifuged at RT for 2 min at 3,220 × *g*. The qPCR run was performed using the ViiA™ 7 real-time PCR system (Applied Biosystems) at 95 °C for 10 min, followed by 40 cycles at 95 °C for 15 s, primer-optimized annealing temperature (as revealed by gradient PCR, see Chapter 4.9, Table 10 and Chapter 5.3.2.4.1) for 30 s and elongation at 72 °C for 30 s. The run was completed by a melt curve analysis. The ViiA™ 7 real-time PCR system automatically measures the SYBR®Green fluorescence in each well after every cycle. The C_T threshold levels were set above background fluorescence and in the exponential phase of the PCR amplification curve. qPCR efficiency was determined based on the dilution series to identify the optimal primer concentration. Theoretically, due to the PCR amplification kinetics, doubling of the template amount results in a C_T difference of 1, which gives a PCR efficiency for the dilution series of 100 %. Only primer pairs with a correlation coefficient above 0.99 and efficiency between 90 % and 110 % were used to analyze relative gene expression in qPCR screens. The melt curve was analyzed to confirm primer specificity. Only if one single peak, originating from one specific PCR product dissociating during melting, was visible, primers were used for further analysis.

5.3.2.4.3 Gene expression analyses

After determination of primer-specific annealing temperatures by gradient PCR, assessment of optimal primer concentration by determining qPCR efficiency and confirmation of primer specificity by melt curve analysis, relative gene expression of target genes was performed using SYBR®Green. Each cDNA sample was run in triplicates using the ViiA™ 7 real-time PCR system (Applied Biosystems) as described before (see Chapter 5.3.2.4.2). Target gene expression was normalized against the expression of *glyceraldehyde 3-phosphate dehydrogenase* (*Gapdh*), which was previously shown to be the most stable reference gene in the heart conditional *Hccs* KO model (personal communication). Relative expression differences between groups were determined using the $2^{-\Delta\Delta CT}$ method (reviewed by Livak and Schmittgen[212]). After normalization to *Gapdh* expression (ΔC_T), data were normalized to the vehicle or SPD *Hccs*$^{+/+}$ control group, which was set to equal 1 ($\Delta\Delta C_T$).

5.3.3 Western blot analyses

5.3.3.1 Protein isolation

For isolation of total protein extracts from murine myocardial tissue whole embryonic, P1 and P3 hearts or approximately 20 mg of apical heart tissue from juvenile 3 week and adult 11 week old mice were used. Snap frozen P1, P3, juvenile and adult heart tissue was transferred to a 2-ml homogenization tube that contained a mixture of twelve 1.4 mm and five 2.8 mm ceramic beads (peqLab Biotechnology). 300 µl pre-cooled 1× radioimmunoprecipitation assay (RIPA) buffer supplemented with proteinase (Roche Diagnostics) and phosphatase inhibitors (Roche Diagnostics) were added to P1 and P3 samples, whereas 400 µl were used for juvenile and adult samples. Tubes were arranged in the homogenizer system Precellys® 24 (peqLab Biotechnology), which was cooled down to 4 °C, and the tissue was shredded twice with 5000 rpm for 20 s with a 20 s break. Whole embryonic 10.5 dpc hearts were homogenized in 25 µl pre-cooled inhibitor-containing 1× RIPA buffer by sonification in the Sonifier® cell disruptor 450 (Branson Ultrasonics) three times for 30 s with a 30 s break and an amplitude of 50 % at 4 °C. Whole embryonic 13.5 dpc hearts were homogenized on ice in 80 µl pre-cooled inhibitor-containing 1× RIPA buffer using a motorized micropestle (Carl Roth) for 30 s. Afterwards, all samples were transferred into a new 1.5-ml tube, fixed on a MiniTwist nutating mixer (Select BioProducts) and incubated for 2 h with gentle agitation at 24 rpm at 4 °C to allow dissociation of the proteins out of the tissue. Subsequently, protein lysates were centrifuged at 16,800 × *g* for 5 min at 4 °C to pellet cell debris. The protein-containing supernatant was collected, if applicable aliquoted in 100 µl fractions and stored at -80 °C or immediately used for concentration measurement and SDS-polyacrylamide gel electrophoresis.

5.3.3.2 Protein concentration measurement

Protein concentration was measured based on the Lowry principle[213] using the DC™ protein assay (Bio-Rad Laboratories) according to the manufacturer's protocol. Protein lysates isolated from embryonic, P1 and P3 hearts were diluted 1:5 in ddH_2O. For protein lysates isolated from juvenile and adult hearts an additional 1:10 dilution was prepared. In parallel, a nine-step BSA dilution series (0 mg/ml – 2 mg/ml in ddH_2O) was used for the calculation of a standard curve. All sample and BSA dilutions were prepared in a reaction volume of 25 µl in duplicates and 25 µl ddH_2O served as blank value. Moreover, 25 µl 1:5 and 1:10 diluted inhibitor-containing 1× RIPA buffer were used as "pseudo"-blanks in order to measure the self-absorption of the inhibitor-containing 1× RIPA buffer. To each 25 µl sample (diluted heart lysates, BSA dilution series, blank, and "pseudo"-blanks) 122.5 µl protein assay reagent A (provided) and 2.5 µl protein assay reagent S (provided) were added. Samples were vortexed and reactions were incubated for 5 min at RT. Afterwards, 1 ml protein assay

reagent B (provided) was added. The samples were vortexed again and incubated for 15 min at RT in the dark. Immediately afterwards the absorption was determined photometrically in a spectrophotometer (Bio-Rad Laboratories) at a wavelength of 750 nm. The absorption values of the 1:5 and 1:10 diluted RIPA-"pseudo"-blanks were subtracted from the absorption values of the 1:5 or 1:10 diluted samples, respectively. A standard curve was calculated using the absorption values of the BSA dilution series. Considering the linear equation of the standard curve and the dilution factor of the protein lysates, the final protein concentration for each sample was determined.

5.3.3.3 SDS-polyacrylamide gel electrophoresis

Separation of proteins according to their size was performed under denaturing conditions by SDS-polyacrylamide gel electrophoresis (SDS-PAGE) according to Laemmli[214]. Discontinuous SDS-PAGE using a two-gel-system, consisting of a low-percentage stacking gel and a higher-percentage separating gel, was applied. 1 mm gels with 10 to 15 wells consisting of a 6 % to 12 % separating gel and a 4 % stacking gel (Table 17) were prepared using the Mini-PROTEAN® tetra handcast system (Bio-Rad Laboratories). Percentage of the separating gel was determined depending on the size of the proteins of interest.

Table 17. Gel composition for SDS-PAGE

	Rotiphorese® gel 30 (30 % Acrylamid)	**ddH_2O**	**1 M Tris** (pH 6.8)	**1 M Tris** (pH 8.8)	**10 % SDS**	**10 % APS**	**TEMED**
4 % stacking gel	667 µl	3.63 ml	625 µl	-	50 µl	25 µl	5 µl
6 % separating gel	2 ml	4.10 ml	-	3.75 ml	100 µl	50 µl	10 µl
10 % separating gel	3.33 ml	2.76 ml	-	3.75 ml	100 µl	50 µl	10 µl
12 % separating gel	4 ml	2.10 ml	-	3.75 ml	100 µl	50 µl	10 µl

For all samples on one gel, the same protein amount was loaded and varied between 20 µg to 100 µg depending on the abundance of the protein of interest in myocardial tissue as well as on the sensitivity of the primary (1°) antibody (AB). The volume of the protein lysates loaded was depending on the protein concentration and by addition of ddH_2O the same final volume for all samples was adjusted. Next, 5× SDS sample buffer was added. Its volume was adapted to the sample volume to reach a 1× final concentration. Samples were incubated for 5 min at 95 °C in a thermocycler (Bio-Rad Laboratories) to denature the proteins by unfolding the secondary structure. The denatured proteins were loaded onto the SDS gel. PageRuler™ prestained protein ladder (Fermentas) as well as HiMark™ prestained high molecular weight protein ladder (Invitrogen) served as size standards. The run was performed in a Mini-PROTEAN® tetra cell (Bio-Rad Laboratories) filled with 1× SDS running buffer for 30 min at 50 V at RT. After proteins were focused in a discrete band in the 4 % polyacrylamide stacking gel, the run was continued at 100 V and the proteins were separated

according to their size in the separating gel. The run was terminated once the blue running front had reached the end of the gels.

5.3.3.4 Western blot analyses

The analysis of separated proteins was performed using western blot following standard procedure. The assembly of the western blot sandwich took place in 1× transfer buffer for normal (i.e. containing 20 % methanol (MeOH)) or for large proteins of interest (> 150 kDa) (i.e. containing 10 % MeOH). Separating gel and nitrocellulose membrane (GE Healthcare) were placed between whatman® paper (GE Healthcare) and mounted inside of a Mini Trans-Blot® cell (Bio-Rad Laboratories). Tank blot was performed in the appropriate 1× transfer buffer. Transfer time was depending on the size of the proteins of interest and varied between 1 h and 3 h at 140 mA at 4 °C. Afterwards, the membrane was blocked for 1 h in 5 % milk in 1× TBS-T with gentle agitation at 40 rpm on an orbital shaker (GFL) to avoid unspecific binding of the 1° AB. Next, the membrane was incubated with 1° AB (see Chapter 4.10, Table 11) o/n at 4 °C with gentle agitation at 24 rpm on a MiniTwist nutating mixer (Select BioProducts). After washing the membrane three times for 5 min in 1× TBS-T with gentle agitation at 40 rpm on an orbital shaker (GFL) at RT, it was incubated in horseradish peroxidase (HRP)-linked secondary (2°) AB (see Chapter 4.10, Table 11) for 1 h with gentle agitation at 24 rpm on a MiniTwist nutating mixer (Select BioProducts) at RT. Subsequently, the membrane was washed again as described before. Next, enhanced chemiluminescence (ECL) reaction was performed by incubating the membrane for 1 min in a 1:1-mixture consisting of ECL solution A and B. Light emission was detected with the imaging system Odyssey® Fc (LI-COR® Biosciences) or by exposure of the membrane to chemiluminescence-sensitive CL-XPosure™ films (Thermo Fischer Scientific). ImageJ software was used to perform densitometric analysis by quantifying size and intensity of detected protein bands. Results were used as a measure for total protein levels or the phosphorylation status of proteins of interest. For final quantification, total protein levels of proteins of interest were normalized against the protein levels of an appropriate and well-established loading control, such as α-ACTININ, α-TUBULIN or GAPDH (personal communication). The loading control was chosen depending on the size of the protein of interest. Band intensities for the phosphorylated forms of proteins of interest were normalized against the band intensities for the corresponding total protein. At the end, data were normalized to the vehicle or SPD *Hccs*$^{+/+}$ control group, which was set to equal 1.

5.3.4 Histology

5.3.4.1 Paraffin embedding and sectioning

For histological analyses, explanted P1 and adult hearts as well as embryonic torsos (heart *in situ*) were embedded into paraffin to allow sectioning. Tissue was first fixed in 4 % PFA solution for 48 h at 4 °C in order to cross-link amino groups in proteins through the formation of reversible methylene bridges. By stabilizing the protein structure, tissue was preserved from degradation and the structure of the cells and of sub-cellular components was maintained during histological analyses. At the same time, the tissue remained permeable for macro-molecules. Because hydrophobic paraffin is immiscible with water, tissue samples were afterwards dehydrated in an increasing EtOH series at RT: 70 % EtOH o/n, 80 % EtOH for 2 h, 90 % EtOH for 2 h, 96 % EtOH for 2 h and 99 % EtOH o/n. Subsequently, samples were cleared twice for 45 min each at RT in toluol to remove remaining ethanol. By incubating the tissue in three consecutive molten paraffin wax baths (60 °C) for 2 h, o/n and for 2 h, respectively, paraffin infiltrated the samples and replaced the toluol. Following embedding of the tissue into paraffin blocks using fresh molten paraffin wax and subsequent hardening, serial sections of 5 µm thickness were cut using a microtome (Leica Microsystems). Finally, sections were mounted on positively charged glass slides (Gerhard Menzel) using a 48 °C water bath (Leica Microsystems) and dried o/n at RT.

5.3.4.2 Histological stainings

Prior to histological stainings, paraffin sections were deparaffinized and rehydrated. At first, slides were incubated for 30 min at 60 °C in a hybridization oven (Biometra) to firmly attach the sections to the glass slides. After cooling down, tissue sections were deparaffinized at RT in three consecutive xylol baths for 5 min each; followed by rehydration at RT in a decreasing series of EtOH baths: twice 99 % EtOH for 3 min each, 96 % EtOH for 3 min, 80 % EtOH for 3 min, 70 % EtOH for 3 min and twice ddH_2O for 5 min each.

5.3.4.2.1 Hematoxylin and eosin staining

Heamtoxylin and eaosin (H&E) staining on paraffin sections was performed to assess overall cardiac morphology and tissue composition. Hematein, an oxidative product of hematoxylin, together with aluminum ions forms a complex called hemalum. The basic hemalum complex stains all acidic (basophil) cell structures, especially nuclei due to its content of nucleic acids, blue. The synthetic acidic dye eosin stains basic (acidophil) cell structures, particularly cytoplasmic proteins, pink. H&E staining was performed by incubating deparaffinized and rehydrated sections 30 s in filtered hematoxylin solution according to Harris (Carl Roth) followed by washing for 5 min under running tap water. Afterwards, tissue sections were stained for 8 min in filtered and acidified (two drops acetic acid per 100 ml) eosin G

solution (Carl Roth). Subsequently, sections were dehydrated (70 % EtOH for 1 min, 96 % EtOH for 5 min, twice 99 % EtOH for 5 min each) and cleared twice in xylol for 5 min each. Finally, sections were mounted under glass coverslips with Eukitt® quick-hardening mounting medium (Sigma-Aldrich).

5.3.4.2.2 Sirius red staining

Sirius red staining on paraffin sections was performed to investigate the extent of interstitial extracellular matrix (ECM) within myocardial tissue. By this procedure, collagen fibers (the main components of ECM) are stained red and muscle fibers as well as the cytoplasm are colored yellow. To stain cell nuclei, deparaffinized and rehydrated paraffin sections were stained for 8 min in hematoxylin according to Weigert (Carl Roth) and washed for 5 min under running tap water. Afterwards, slides were incubated in Sirius red solution for 1 h and washed twice in acidified water for 10 s each; followed by dehydration and mounting as described above (see Chapter 5.3.4.2.1).

5.3.4.3 Fluorescent and immunofluorescent stainings

Paraffin sections used for fluorescent and immunofluorescent stainings were deparaffinized and rehydrated as described before (see Chapter 5.3.4.2).

5.3.4.3.1 Fluorescent wheat germ agglutinin staining

To evaluate cardiomyocyte cross sectional area (CSA) in tissue sections, cell membranes were stained with fluorochrome-conjugated wheat germ agglutinin (WGA), which selectively binds to *N*-acetylneuraminic acid residues[215]. Heat-mediated antigen retrieval was performed on deparaffinized and rehydrated paraffin sections using 1× sodium citrate buffer. Slides where repeatedly boiled in a microwave oven for a total of 20 min and subsequently allowed to cool down to RT. Afterwards, slides were washed three times for 5 min with gentle agitation at 40 rpm on an orbital shaker (GFL) in 1× TBS-T followed by a blocking step in blocking solution for 1 h at RT. Next, sections from neonatal hearts were incubated simultaneously with fluorochrome (Alexa Fluor® 555)-conjugated WGA (Invitrogen) and with the monomeric cyanine nucleic acid stain TO-PRO®-3 (Invitrogen) in a humidified opaque Stain Tray™ (Carl Roth) o/n at 4°C. In contrast, sections from adult hearts were stained with Alexa Fluor® 555-conjugated WGA only. Subsequently, sections were washed three times in the dark as described above, followed by mounting under glass cover slips with ProLong® Gold antifade mountant (Invitrogen) (neonatal hearts) or with ProLong® Gold antifade mountant with 4´,6-Diamidino-2-phenylindol (DAPI) (Invitrogen) (adult hearts) and stored in the dark.

5.3.4.3.2 Fluorescent terminal dUTP nick end labeling

To investigate programmed cell death (apoptosis), terminal deoxynucleotidyl transferase dUTP nick end labeling (TUNEL) was conducted, a fluorescence method that detects nuclear DNA fragmentation (a major hallmark of apoptosis)[216]. The ApopTag® fluorescein *in situ* apoptosis detection kit (Millipore), which is based on template-independent identification of "blunt ends" of double stranded DNA breaks, was used according to the manufacturer's instructions. Briefly, the enzyme terminal deoxynucleotidyl transferase (TdT) catalyzes the addition of digoxigenin-labelled deoxynucleotide triphosphates (dUTPs) to the 3´-hydroxyl termini of exposed DNA strand ends after fragmentation. Digoxigenin incorporation can then be recognized by anti-digoxigenin antibodies conjugated to the fluorescent dye fluorescein, which can be detected by fluorescence microscopy. If not stated differently, all steps were carried out at RT. Enzymatic antigen retrieval was performed on deparaffinized and rehydrated paraffin sections by incubation in proteinase K (Carl Roth) solution for 15 min. Slides were then washed twice for 2 min with gentle agitation at 40 rpm on an orbital shaker (GFL) in 1× TBS. A positive control was included, which was treated with RNase-free DNAse solution (Qiagen) (DNase 1:100 in RDD buffer) for 10 min to enzymatically digest the nuclear DNA and thus provoke DNA breaks. Afterwards, the positive control was washed three times for 5 min as described above. All samples were incubated in equilibration buffer (provided) for 10 s. Labelled dUTPs were added by incubating the samples with working strength TdT enzyme (provided) in reaction buffer (provided) at 37 °C for 1 h. The reaction was terminated by 10 min incubation in stop/wash buffer (provided). Next, slides were washed three times for 1 min as described above. Afterwards, working strength anti-digoxigenin AB conjugate in blocking solution (provided) was added for 30 min in the dark. Slides were again washed three times for 2 min, followed by mounting under glass cover slips with ProLong® Gold antifade mountant with DAPI (Invitrogen) and light-protected storage.

5.3.4.3.3 Immunofluorescent KI67 staining

To assess proliferation rates in neonatal hearts, immunofluorescence staining for KI67 was performed. The KI67 antigen is a nuclear protein that is expressed during all active phases of the cell cycle but is absent in resting cells (reviewed by Scholzen and Gerdes[217]). Heat-mediated antigen retrieval was performed on deparaffinized and rehydrated paraffin sections as described before (see Chapter 5.3.4.3.1). After washing and blocking (for details see Chapter 5.3.4.3.1), sections were incubated o/n with a rabbit anti-KI67 AB (see Chapter 4.10, Table 12) in a humidified Stain Tray™ (Carl Roth) at 4°C. The next day, sections were washed three times as described above and incubated with anti-rabbit IgG fluorochrome (Alexa Fluor® 555)-conjugated 2° AB (see Chapter 4.10,Table 12) for 1h at RT

in the dark. Sections were again washed three times, followed by mounting under glass cover slips with ProLong® Gold antifade mountant with DAPI (Invitrogen) and light-protected storage.

5.3.4.3.4 Immunofluorescent phospho-histone H3 staining

To assess proliferation rates in embryonic hearts, immunofluorescence staining for histone H3 (HH3) phosphorylation at serine 10 was performed. Phosphorylation of HH3 at serine 10 (p-HH3) is restricted to specific stages of mitosis and the late G2 phase of the cell cycle and is essential for cell passage from metaphase to anaphase[218]. Thus, p-HH3 is a commonly used mitosis specific marker in proliferating cells. Heat-mediated antigen retrieval was performed on deparaffinized and rehydrated paraffin sections as described before (see Chapter 5.3.4.3.1). After washing and blocking (see Chapter 5.3.4.3.1), sections were incubated simultaneously with a rabbit anti-p-HH3 AB (to detect proliferating cells) (see Chapter 4.10, Table 12), a mouse anti-CYT *c* AB to differentiate between *Hccs*-deficient and healthy myocardial cells (see Chapter 4.10, Table 12) and TO-PRO®3 (Invitrogen) to label nuclei in a humidified Stain Tray™ (Carl Roth) o/n at 4°C. The next day, sections were washed three times as described above and simultaneously incubated with anti-rabbit IgG Alexa Fluor® 555-conjugated 2° AB and anti-mouse IgG Alexa Fluor® 488-conjugated 2° AB (see Chapter 4.10, Table 12) for 1h at RT in the dark. Again, sections were washed three times, followed by mounting under glass cover slips with ProLong® Gold antifade mountant (Invitrogen) and light-protected storage.

5.3.4.4 Histological analyses

5.3.4.4.1 Evaluation of H&E-stained embryonic, P1 and adult hearts

To assess overall cardiac morphology and tissue composition, light microscopy images of H&E-stained hearts (see Chapter 5.3.4.2.1) were taken using the Biozero BZ-8100 microscope (Keyence). For 10.5 dpc embryonic hearts 5-fold optical magnification, for 13.5 dpc embryonic hearts 4-fold optical magnification and for P1 hearts 2-fold optical magnification was applied. Hearts of 11 week old adult mice were imaged with 2-fold optical magnification. Due to the size of the adult heart, however, four overlapping picture excerpts were taken, which were subsequently merged into a single image using the BZ image analysis application software (Keyence). Pictures of at least two non-adjacent longitudinal (embryonic and P1 hearts) or cross (adult) H&E-stained heart sections were imaged.

5.3.4.4.2 Quantification of fibrosis in adult hearts

Light microscopy images of Sirius red-stained hearts (see Chapter 5.3.4.2.2) from 11 week old adult mice were taken using the Biozero BZ-8100 microscope (Keyence). By applying 5-fold optical magnification, 6 random fields of the left ventricular (LV) myocardium, including free wall and interventricular septum (IVS), were imaged, thereby covering the entire LV tissue. Two non-adjacent Sirius red-stained cross-sections per heart were used. The percentage of interstitial LV fibrotic tissue was quantified using the color-threshold-plugin of the ImageJ software, which measures the red stained area in relation to the total LV myocardial area. Fibrosis of all 12 images was averaged to give a mean estimate of fibrotic tissue for each heart. Perivascular fibrosis was excluded and was cut-out in the images before analysis. Imaging measurements as well as analyses took place in a blinded fashion, such that investigators were unaware of mouse genotypes or treatment groups.

5.3.4.4.3 Measurement of cardiomyocyte cross sectional area in P1 and adult hearts

To measure cardiomyocyte cross sectional area (CSA), WGA-stained P1 longitudinal or 11 week old adult heart cross-sections were used (see Chapter 5.3.4.3.1). For P1, pictures were taken with the confocal laser scanning microscope TSC SPE (Leica Microsystems) applying 120-fold optical magnification. For adult hearts, pictures were taken with the Biozero BZ-8100 fluorescence microscope (Keyence) applying 20-fold optical magnification. For P1 as well as adult hearts, 15 random fields of the LV myocardium, including free wall and IVS, were imaged and two non-adjacent WGA-stained sections per heart were used. At least 200 cardiomyocytes per heart were measured using the area measurement tool of the Biozero BZ image analysis application software (Keyence). Only CSA of cardiomyocytes which were cut along their transverse axis and matched the following selection criteria was measured: visible central nucleus, cell shape close to circular, clear borders of cell discernible and visible cytoplasm. CSA of all cardiomyocytes analyzed were averaged to give a mean estimate of cardiomyocyte CSA for each heart. All measurements as well as analyses took place in a blinded fashion, such that investigators were unaware of mouse genotypes or treatment groups.

5.3.4.4.4 Quantification of apoptosis rates in embryonic 13.5 dpc and P1 hearts

To quantify the number of apoptotic cells, TUNEL-stained 13.5 dpc or P1 hearts were analyzed (see Chapter 5.3.4.3.2). Two longitudinal non-adjacent sections per heart were imaged and pictures of 6 random fields per heart section (entire LV and RV myocardium for 13.5 dpc, LV myocardium for P1) were taken using the Biozero BZ-8100 fluorescence microscope (Keyence) with 15-fold optical magnification. Cells which exhibited nuclear colocalization of TUNEL and DAPI staining were considered apoptotic. Nuclei with positive

TUNEL staining as well as the total number of DAPI-stained nuclei were manually counted using the cell-counter-plugin of the ImageJ software. A total number of approximately 7,000 cells per embryonic heart and 15,000 cells per P1 heart was analyzed. Apoptosis rates (given in percent) were calculated by relating the number of TUNEL-positive nuclei to the total number of nuclei as mean from all images per heart. All measurements as well as analyses took place in a blinded fashion, such that investigators were unaware of mouse genotypes or treatment groups.

5.3.4.4.5 Quantification of proliferation rates in neonatal hearts

To quantify the number of proliferating cells in P1 hearts, KI67-stained longitudinal sections (see Chapter 5.3.4.3.3) were imaged with 40-fold optical magnification using the Biozero BZ-8100 fluorescence microscope (Keyence). Pictures of 10 random fields of one heart section were taken within the LV myocardium, including the free wall and IVS. Cells that exhibited nuclear colocalization of KI67 and DAPI were considered as cycling. KI67-positive nuclei and the total number of DAPI-stained nuclei were manually quantified using the cell-counter-plugin of the ImageJ software. A total number of approximately 5,000 cells per heart was evaluated with respect to their resting or proliferating stage. The proliferation rate per heart was calculated as the percentage of KI67-positive cells related to the total number of DAPI-stained nuclei. All measurements as well as analyses took place in a blinded fashion, such that investigators were unaware of mouse genotypes or treatment groups.

5.3.4.4.6 Quantification of proliferation rates in embryonic 13.5 dpc hearts

To quantify the number of proliferating cells in embryonic 13.5 dpc hearts, p-HH3-stained longitudinal sections (see Chapter 5.3.4.3.4) were imaged with 30-fold optical magnification using the confocal laser scanning microscope TSC SPE (Leica Microsystems). Pictures of 6 to 11 random fields of two non-adjacent heart sections were taken within the LV and RV myocardium. Cells which exhibited nuclear colocalization of p-HH3 and TO-PRO®-3 were considered as cycling. P-HH3-positive nuclei and total number of TO-PRO®-3-stained nuclei was manually quantified using the cell-counter-plugin of the ImageJ software. The number of cells in mitosis was taken as the total p-HH3-positive cells over the total TO-PRO®-3-labeled nuclei of each cell population analyzed. Within c*Hccs*$^{+/-}$ hearts, CYT *c* staining was used to differentiate between the healthy and *Hccs*-deficient myocardial cell population. The proliferation rate of healthy myocardial cells was calculated as the percentage of p-HH3-positive cells related to the total number of TO-PRO®-3-stained nuclei within CYT *c*-positive cells. The proliferation rate of *Hccs*-deficient myocardial cells was calculated as the percentage of p-HH3-positive cells related to the total number of TO-PRO®-3-stained nuclei within CYT *c*-negative cells. In *Hccs*$^{+/+}$ hearts, all cardiomyocytes were CYT *c*-positive and

the proliferation rate per heart was calculated as the percentage of p-HH3-positive cells related to the total number of TO-PRO®-3-stained nuclei. A total number of approximately 5,000 cells per heart was evaluated with respect to their resting or proliferating stage. All measurements as well as analyses took place in a blinded fashion, such that investigators were unaware of mouse genotypes or treatment groups.

5.4 Statistical analysis

All results are presented as mean±standard error of the mean (SEM). All data sets were tested for normal distribution by Kolmogorov-Smirnov test and the homogeneity of variances was assessed by Levene's test with Statistical Package for the Social Sciences (SPSS) (IBM). Given equal variances, differences between two groups were evaluated with unpaired, two-sided student's *t*-test using excel 2010 (Microsoft) and those among multiple groups with one-way analysis of variance (ANOVA) followed by Bonferroni post-hoc test using SPSS (IBM). Differences between multiple groups with unequal variances were evaluated with non-parametric Kruskal-Wallis one-way analysis of variance followed by Mann-Whitney post-hoc test using SPSS (IBM). Genotype distributions were compared to expected Mendelian distribution by *Chi*-square test using Microsoft excel software. A probability (*p*) value less than 0.05 was considered to indicate statistical significance (*$p<0.05$, **$p<0.01$ and ***$p<0.001$).

6 RESULTS

6.1 Gene clusters involved in cellular metabolism and amino acid homeostasis are enriched in neonatal c*Hccs*$^{+/-}$ hearts

Impaired embryonic and fetal growth has various effects on the postnatal health in humans[2,3,7]. In this study, we used the heart conditional *Hccs* KO model (see Chapter 3.4) to investigate adaptive mechanisms of the myocardium in response to impaired intrauterine cardiac development and to potentially identify molecular mechanisms of developmental programming. Hearts of neonatal c*Hccs*$^{+/-}$ mice were found to be hypoplastic, as evident by a reduced HW/BW ratio, thinner LV walls and a significant reduction of the cardiomyocyte number (unpublished data, see Chapter 3.4). To investigate the response and adaptation of the neonatal c*Hccs*$^{+/-}$ heart to hypoplasia, genome-wide microarray RNA expression analysis using neonatal whole-heart RNA was performed in a previous study by Manuela Magarin, a former PhD student in the Thierfelder lab at the Max Delbrück Center for Molecular Medicine in Berlin, Germany. Affymetrix gene array analysis identified 811 genes as differentially regulated (p<0.05) in neonatal c*Hccs*$^{+/-}$ mice in comparison to female *Hccs*$^{+/+}$ littermate controls. Subsequently, as part of this study, unbiased functional group classification was performed using the online database DAVID[208]. Therefore, only those 213 differentially regulated genes were included that had a fold change higher than +1.5 or lower than -1.5 in combination with a highly significant p-value (p<0.01) (Supplementary Table S1.). DAVID functional annotation of these differentially expressed genes revealed many gene groups involved in unfolded protein response (UPR) and apoptosis as well as metabolism and amino acid homeostasis as significantly enriched in neonatal c*Hccs*$^{+/-}$ mice. While another PhD project focuses on the role of DNA damage repair, apoptosis and UPR, this study concentrates on the enrichment of gene classes involved in transcriptional regulation, metabolism and amino acid homeostasis; a more detailed listing is included in the supplemental information section (Supplementary Table S2-4).

Table 18. Neonatal c*Hccs*$^{+/-}$ hearts display significant enrichment of genes involved in amino acid homeostatic and metabolism

Functional group		Fold enrichment	*p*-value
Positive regulation of transcription		3.84	2.69*10^-03
DNA replication		3.48	2.90*10^-03
DNA damage repair		2.94	1.74*10^-02
Unfolded protein response		2.89	2.59*10^-03
Programmed cell death (apoptosis)		2.26	1.57*10^-02
Amino acid metabolism	(Supplementary Table S2)	2.06	3.09*10^-02
Amino acid transport	(Supplementary Table S3)	1.63	2.85*10^-02
Cellular metabolism	(Supplementary Table S4)	1.55	3.68*10^-02

DAVID functional annotation microarray analysis of gene class changes in neonatal c*Hccs*$^{+/-}$ hearts revealed enrichment of gene groups involved in transcriptional regulation, unfolded protein response and apoptosis as well as cellular metabolism and amino acid homeostasis.

6.2 Enhanced mTOR pathway activity in neonatal c*Hccs*$^{+/-}$ hearts

Postnatal cardiomyocyte hypertrophy is a major hallmark of heart-specific c*Hccs*$^{+/-}$ hearts and accounts for the postnatal catch-up growth of the hypoplastic myocardium to compensate for the reduced set of cardiomyocytes (unpublished data, see Chapter 3.4). Given enrichment of genes involved in transcriptional regulation, amino acid homeostasis and cellular metabolism, it was hypothesized that the mechanistic target of rapamycin (mTOR) pathway, an important regulator of translation and transcription, postnatal cardiac metabolism as well as a key sensor of cellular amino acid availability (see Chapter 3.3.4), is involved in the postnatal compensatory growth of hypoplastic neonatal c*Hccs*$^{+/-}$ hearts. To investigate mTOR pathway activity, western blot analyses focusing on protein levels and phosphorylation status of the essential mTORC1 and mTORC2 components MTOR, RAPTOR and RICTOR (see Chapter 3.3.4, Table 1) were performed with whole heart protein extracts from *Hccs*$^{+/+}$ and c*Hccs*$^{+/-}$ neonates (Supplementary Figure 1A). Quantification of MTOR phosphorylation at serine 2448 and 2481 normalized to total MTOR and of total MTOR, RAPTOR and RICTOR protein levels normalized to α-TUBULIN revealed no significant differences between neonatal *Hccs*$^{+/+}$ and c*Hccs*$^{+/-}$ hearts (Supplementary Figure 1B+C). However, given that mTOR pathway regulation is much more complex and depends on the presence or absence of a number of different activators or inhibitors (see Chapter 3.3.4, Table 1), the phosphorylation status of downstream targets is the most commonly used indicator to evaluate mTOR pathway activity. Thus, western blot analyses were carried out to investigate S6 kinase 1 (S6K1) and S6 ribosomal protein (S6) phosphorylation; again using whole heart protein extracts from *Hccs*$^{+/+}$ and c*Hccs*$^{+/-}$ neonates (Figure 8A). Quantification of S6K1 phosphorylation at threonine 389 normalized to total S6K1 (Figure 8B) and of S6 phosphorylation at serine 235, 236, 240 and 244 normalized to total S6 (Figure 8C) revealed a 2.52±0.45-fold increased S6K1 phosphorylation (p<0.01), a 1.73±0.22-fold increased phosphorylation of S6 at serine 235 and 236 (p<0.05) and a 1.59±0.15-fold increased phosphorylation of S6 at serine 240 and 244 (p<0.05) in neonatal c*Hccs*$^{+/-}$ hearts compared to littermate *Hccs*$^{+/+}$ females. These findings indicate enhanced mTOR pathway activation in neonatal c*Hccs*$^{+/-}$ hearts. Interestingly, when c*Hccs*$^{+/-}$ hearts were analyzed at postnatal day 3 (P3) and at the age of 3 weeks, no increased phosphorylation of S6 was observed (Supplementary Figure 2), suggesting that mTOR pathway activation might be a critical compensatory mechanism in c*Hccs*$^{+/-}$ hearts limited to the perinatal period with a potential importance before birth.

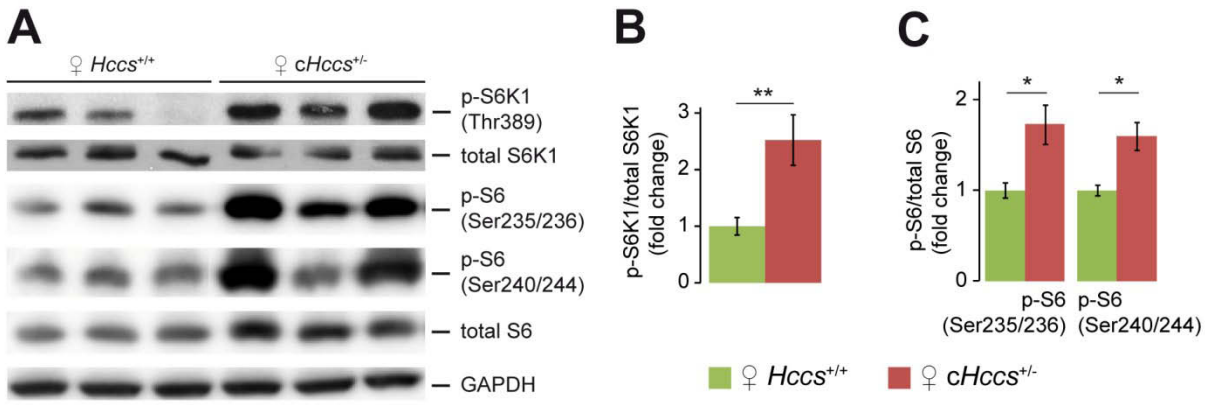

Figure 8. Elevated mTORC1 activity in neonatal c*Hccs*$^{+/-}$ hearts.
A) Western blots of whole heart protein extracts from neonates (P1) illustrating phosphorylation status of S6K1 at threonine 389 and S6 at serine 235, 236, 240 and 244. **B)** Quantification of S6K1 phosphorylation normalized to total S6K1 (n=15 for *Hccs*$^{+/+}$, n=14 for c*Hccs*$^{+/-}$) and **C)** of S6 phosphorylation normalized to total S6 revealed a significant increase in P1 c*Hccs*$^{+/-}$ hearts compared to littermate controls (n=6 per group), indicating enhanced mTORC1 activity. Statistical significance among groups was assessed using unpaired 2-tailed Student *t*-test (**p*<0.05, ***p*<0.01).

6.3 Consequences of prenatal mTORC1 inhibition by rapamycin on cardiac development, growth and function

The mTOR pathway activity was demonstrated to be enhanced in hypoplastic neonatal c*Hccs*$^{+/-}$ hearts (see Chapter 6.2, Figure 8). To investigate if this upregulation is essential for the embryonic regenerative capacity and the peri- and postnatal compensatory growth of c*Hccs*$^{+/-}$ hearts and to study the role of the mTOR signaling cascade during heart development in general, we sought to establish a protocol for pharmacological mTORC1 inhibition in fetal and neonatal mice.

6.3.1 Prenatal mTORC1 inhibition by rapamycin treatment of pregnant mice

To inhibit mTORC1 activity in fetal and neonatal mice, a pharmacological approach using rapamycin was applied. As previously shown, rapamycin is a potent inhibitor of mTORC1[219] that can pass the placental barrier[177]. We established a treatment protocol according to previously published approaches[220] (see Chapter 5.1.4). Briefly, 5 mg rapamycin/kg body weight (BW) was injected subcutaneously in pregnant dams every 12 h from 15.5 days post coitum (dpc) until term. Rapamycin treated *Hccs*$^{+/+}$ as well as c*Hccs*$^{+/-}$ offspring were born alive (see Chapter 6.3.2). As controls, pregnant females were treated with rapamycin-free DMA-containing vehicle (10 % PEG 300 and 17 % Tween® 80 in 0.9 % NaCl solution) (see Chapter 5.1.4). Most of the offspring survived until adulthood (see Chapter 6.3.4); however, a minor percentage died within the first 3 days, independent of the genotype of the pup or the treatment substance. The reason for these occasionally cases of death within the first days after birth was not further investigated; though stressful pregnancy due to frequent injections might have caused rejection of offspring by some mothers.

To confirm mTORC1 inhibition, western blot analyses were performed (Figure 9A). Investigation of the phosphorylation status of the mTORC1 downstream targets S6K1 and S6 revealed a severe reduction at various phosphorylation sites in neonatal rapamycin treated hearts compared to hearts from vehicle treated offspring (Figure 9A), indicating successful mTORC1 inhibition. In contrast, analyses of the phosphorylation status of the mTORC1 downstream target 4E-BP1 at serine 65 and threonine 37 and 46 revealed unchanged phosphorylation in rapamycin treated neonatal hearts compared to their respective vehicle controls (Figure 9A). This suggests that either 4E-BP1 phosphorylation does not exclusively rely on mTORC1 activity or is independent of the mTORC1 activity targeted by rapamycin. Because rapamycin treatment is a systemic pharmacological approach, the entire organism is affected. Inhibition of mTORC1 in neonatal kidney and lung tissue was studied by western blot analyses focusing on the phosphorylation status of S6K1 and S6 (Supplementary Figure 3A+B). A severe reduction of S6K1 and S6 phosphorylation in neonatal rapamycin treated kidney and lung tissue compared to tissue from vehicle treated offspring was observed (Supplementary Figure 3A+B), confirming mTORC1 inhibition in other organs. In some cell types, long-term treatment with rapamycin reduced mTORC2 signaling by suppressing mTORC2 assembly[221,222]. To exclude inhibition of mTORC2 by prenatal rapamycin treatment, western blot analyses focusing on the phosphorylation status of AKT at serine 473, the phosphorylation site targeted by mTORC2 (see Chapter 3.3.4.1, Figure 5), were performed with neonatal whole heart protein extracts (Figure 9A). Quantification of AKT phosphorylation normalized to total AKT revealed no differences between the genotypes or the treatment groups (Figure 9C). Moreover, the mTOR signaling cascade is known to inhibit autophagy, a basic catabolic mechanism during which unnecessary or dysfunctional cellular components (such as proteins or whole organelles) are degraded[168-173,175]. To study the impact of prenatal mTORC1 inhibition on autophagy, western blot analyses of p62 protein levels in neonatal whole heart protein extracts were performed (Figure 9B). The protein p62 is one of the best characterized selective autophagy substrates, which targets proteins for autophagy, gets incorporated into autophagosomes and subsequently degraded[223,224]. Quantification of p62 protein levels normalized to GAPDH identified significantly (p<0.001) decreased p62 levels in hearts from rapamycin treated neonates (0.65±0.03 arbitrary units (AU) for *Hccs*$^{+/+}$, 0.67±0.06 AU for c*Hccs*$^{+/-}$) but no significant differences between the genotypes (1.00±0.08 AU for vehicle *Hccs*$^{+/+}$, 1.20±0.04 AU for vehicle c*Hccs*$^{+/-}$) (Figure 9D). Given that decreased p62 protein levels correlate with induction of autophagy, we conclude that prenatal mTORC1 inhibition results in activation of autophagy in neonatal hearts. All together, these findings indicate that prenatal rapamycin treatment of pregnant mice successfully inhibits mTORC1 in fetal and neonatal mice without affecting mTORC2 activity.

Rapamycin-mediated mTORC1 inhibition should eventually normalize after birth, given that pups are no longer exposed to the treatment. To narrow down the postnatal time window during which mTORC1 remains inhibited and to exclude that postnatal consequences are due to prolonged and irreversible impairment of the mTOR pathway, hearts from offspring of the same rapamycin treated litter were prepared either at postnatal day 1 (P1), 2 (P2) or 3 (P3), respectively. Western blot analyses of whole heart protein extracts examining the phosphorylation status of S6 were performed (Figure 9E). Inhibition of mTORC1 was still evident at P2 but pathway activity was restored by P3 as evident by normal phosphorylation levels of S6 (Figure 9E).

Given that both *Hccs*$^{+/+}$ as well as c*Hccs*$^{+/-}$ mice survived fetal rapamycin treatment starting at 15.5 dpc, we were eager to investigate if mTORC1 inhibition already during embryonic development has differential effects on the survival of *Hccs*$^{+/+}$ and c*Hccs*$^{+/-}$ neonates. Thus, we injected rapamycin in pregnant mice starting at 11.5 dpc. *Hccs*$^{+/+}$ as well as c*Hccs*$^{+/-}$ embryos were subjected to intrauterine lethality, preterm birth at 16.5 dpc and demonstrated severe growth retardation and body malformations due to systemic effects of rapamycin on the entire organism (Supplementary Figure 4). This profound phenotype prevents investigations of the consequences of mTOR pathway inhibition on fetal and perinatal cardiac growth. Hence, these experiments were immediately abandoned as soon as the severe phenotype became apparent. Importantly, for this reason, all of the following results presented in this study are based on rapamycin injections from 15.5 dpc until birth.

In summary, we successfully established a novel protocol to inhibit mTORC1 in hearts, but also other organs, of fetal and neonatal mice by rapamycin treatment of pregnant mice. Moreover, we could demonstrate that after termination of rapamycin treatment at birth, mTORC1 activity is restored by P3, indicating reversible mTORC1 inhibition and normal mTOR pathway activity during postnatal life.

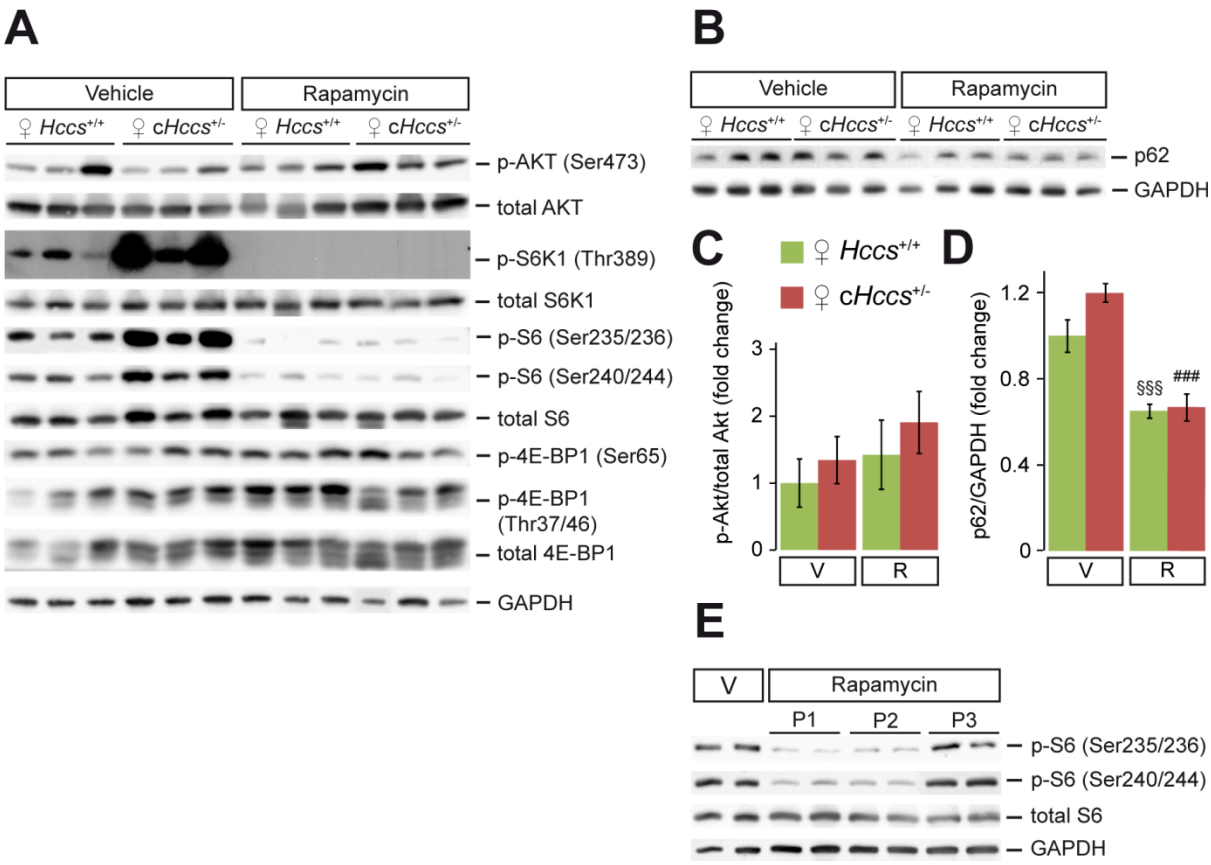

Figure 9. Successful mTORC1 inhibition in neonatal hearts.
A) Western blots of whole heart protein extracts from neonates (P1) after prenatal vehicle or rapamycin treatment illustrating phosphorylation status of AKT, S6K1, S6 and 4E-BP1. Note the severe reduction of S6K1 and S6 phosphorylation in hearts of rapamycin treated neonates compared to vehicle treated offspring, indicating successful mTORC1 inhibition. Phosphorylation of 4E-BP1 was demonstrated to be unaffected by prenatal rapamycin treatment. **B)** Western blots of whole heart protein extracts from neonates (P1) illustrating protein levels of p62 in *Hccs*$^{+/+}$ and c*Hccs*$^{+/-}$ mice after prenatal vehicle or rapamycin treatment. **C)** Quantification of AKT phosphorylation at serine 473 normalized to total AKT revealed no significant differences between the genotypes or the treatment groups, indicating that prenatal rapamycin treatment specifically inhibits mTORC1 but not mTORC2 in P1 hearts (n=5 for vehicle and rapamycin *Hccs*$^{+/+}$, n=6 for vehicle and rapamycin c*Hccs*$^{+/-}$). **D)** Quantification of p62 protein levels normalized to GAPDH revealed no significant differences between the genotypes but a significant decrease in both rapamycin groups compared to vehicle conditions, indicating autophagy activation upon prenatal mTORC1 inhibition (n=6 per group). **E)** Western blots of whole heart protein extracts from vehicle treated neonates at P1 and of rapamycin treated littermates at P1, P2, and P3 illustrating phosphorylation status of S6. Note that mTORC1 inhibition was still evident at P2, while S6 phosphorylation at P3 does not differ compared to P1 vehicle treated offspring, indicating restoration of mTOR pathway activity. For **C)+D)**: Statistical significance among groups was assessed by one-way ANOVA followed by Bonferroni post-hoc test (§§§p<0.001 vs. vehicle *Hccs*$^{+/+}$, ###p<0.001 vs. vehicle c*Hccs*$^{+/-}$). (R: rapamycin, V: vehicle)

6.3.2 Prenatal mTORC1 inhibition neither affects litter size nor genotype distribution

Given the fatal phenotype observed if rapamycin treatment is initiated at 11.5 dpc, we determined if prenatal mTORC1 inhibition from 15.5 dpc onwards also causes intrauterine lethality. For this purpose, litter size as well as genotype distribution within vehicle and rapamycin treated litters were compared at P1 (Figure 10). Pregnant dams treated with vehicle gave birth to 5.4±0.56 offspring per litter, while litter size for rapamycin treated dams was 6.0±0.44 (Figure 10A). The difference was not statistically significant. Besides, the applied breeding strategy theoretically generates 33.33 % *Hccs*$^{+/Y}$ control males, 33.3 % *Hccs*$^{+/+}$ control females and 33.3 % c*Hccs*$^{+/-}$ females, respectively (Figure 10B and see Chapter 5.1.2.1, Figure 6). In vehicle treated litters, 29.92±7.17 % control males, 25.87±5.09 % control females, and 44.21±5.26 % c*Hccs*$^{+/-}$ females were identified (Figure

10B). Rapamycin treated litters split up in 25.24±9.74 % control males, 40.89±10.30 % control females, and 33.87±10.43 % c*Hccs*$^{+/-}$ mice (Figure 10B). Genotype distribution within vehicle as well as rapamycin treated litters compared to the expected genotype distribution was not significantly different as determined with *chi*-square test (Figure 10B). In line, unpaired 2-tailed Student *t*-tests comparing the genotype frequencies of control males, control females and c*Hccs*$^{+/-}$ mice, respectively, between vehicle and rapamycin litters resulted in equal distribution independent of the expected frequencies (Figure 10B). In conclusion, prenatal mTORC1 inhibition does not cause general or genotype-specific intrauterine lethality.

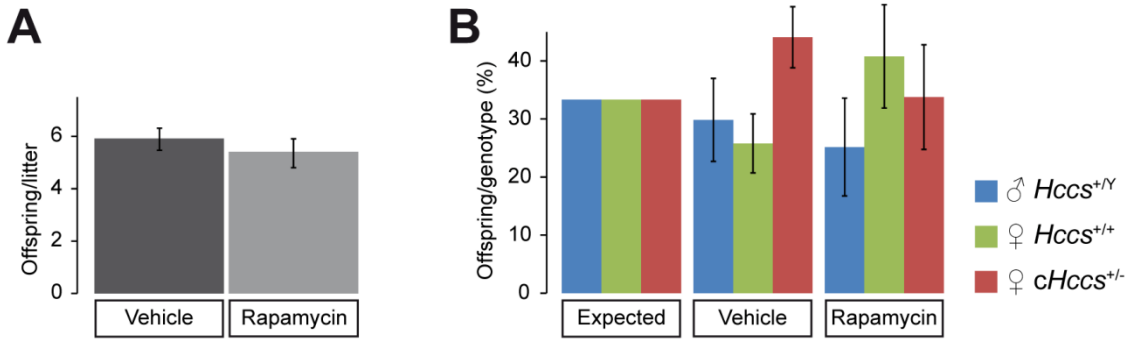

Figure 10. Prenatal mTORC1 inhibition neither changes litter size nor genotype distribution.
A) Average litter size of vehicle and rapamycin treated dams did not differ. Statistical significance among groups was assessed by unpaired 2-tailed Student *t*-tests. **B)** Genotype distribution within vehicle as well as rapamycin treated litters was not significantly different from expected genotype frequencies. Statistical significance between treatment groups and expected genotype distribution was assessed by *chi*-square test. Statistical significance comparing the frequencies of all three genotypes, respectively, between vehicle and rapamycin treated litters independent of expected frequencies was assessed by unpaired 2-tailed Student *t*-tests. For **A)**+**B)**: n=9 litters for both treatment groups.

6.3.3 Consequences of prenatal mTORC1 inhibition for neonatal hearts

Even though mTOR is known to regulate cardiac cell and organ size during postnatal life[58,117,184-186,225], its role during intrauterine growth is less well understood. For this reason, we analyzed organ size, proliferation and apoptosis rates as well as cardiomyocyte size and cardiac function in neonatal hearts after prenatal (15.5 dpc onwards) rapamycin-induced mTORC1 inhibition.

6.3.3.1 Prenatal mTORC1 inhibition causes intrauterine growth restriction and cardiac developmental delay in neonatal mice

To determine the effect of prenatal mTORC1 inhibition on fetal growth and cardiac development, neonatal mice after prenatal rapamycin treatment were analyzed at P1. Investigation of body size (Figure 11A) and weight (Figure 11B) revealed overall growth retardation in rapamycin treated neonates compared to vehicle treated animals. Prenatal rapamycin treatment reduced BW in *Hccs*$^{+/+}$ controls by 16.4 % (p<0.001) and in c*Hccs*$^{+/-}$ neonates by 14.5 % (p<0.01) (Figure 11B). Heart size (Figure 11C+D) and weight (Figure 11E) were also extenuated in rapamycin treated neonates compared to the respective

vehicle treated control groups. Prenatal rapamycin treatment reduced HW in *Hccs*$^{+/+}$ controls by 34.5 % (p<0.001) and in c*Hccs*$^{+/-}$ by 35.3 % (p<0.001) (Figure 11E). Thus, the impact of mTORC1 inhibition on heart weight (HW) is more pronounced than on BW. Consequently, prenatal mTORC1 inhibition results in a significantly (p<0.001) decreased HW to BW (HW/BW) ratio in P1 rapamycin treated animals compared to their respective vehicle control groups (Figure 11F). While HW/BW ratio of vehicle *Hccs*$^{+/+}$ controls was 6.23±0.03 mg/g and of vehicle c*Hccs*$^{+/-}$ animals 5.62±0.06 mg/g, HW/BW ratio of rapamycin *Hccs*$^{+/+}$ controls was 4.87±0.02 mg/g and of rapamycin c*Hccs*$^{+/-}$ animals 4.24±0.03 mg/g. Importantly, the hypoplastic cardiac phenotype (a major hallmark of the heart conditional *Hccs* KO model, reflected by significantly reduced HW and HW/BW ratio in neonatal mice (see Chapter 3.4)) was evident in the vehicle group and was still observed after prenatal mTORC1 inhibition (Figure 11E+F). Histological analyses of neonatal hearts confirmed reduced organ size in both genotypes after prenatal mTORC1 inhibition (Figure 11D). Importantly, however, c*Hccs*$^{+/-}$ hearts demonstrated a more profound phenotype with severe thinning and noncompaction of the ventricular myocardium obvious in the apical regions of both ventricles (Figure 11D, arrowheads). Because rapamycin treatment is a pharmacological approach that affects the entire organisms, consequences of prenatal mTORC1 inhibition on neonatal kidney weight (KW) were analyzed (Supplementary Figure 3C). The accumulated weight of right and left kidney of newborn rapamycin treated *Hccs*$^{+/+}$ controls (7.68±0.09 mg) and c*Hccs*$^{+/-}$ animals (7.80±0.07 mg) was significantly lower compared to their corresponding vehicle control groups (9.56±0.23 mg for *Hccs*$^{+/+}$, 9.45±0.16 mg for c*Hccs*$^{+/-}$), which represents a reduction by 19.7 % in *Hccs*$^{+/+}$ controls (p<0.01) and 17.5 % in c*Hccs*$^{+/-}$ neonates (p<0.05) (Supplementary Figure 3C). Due to the parallel reduction of BW and KW, kidney weight to body weight (KW/BW) ratio in neonates was not significantly different between the genotypes or the treatment groups (Supplementary Figure 3D). Thus, prenatal mTORC1 inhibition reduced BW (Figure 11B) and KW (Supplementary Figure 3C) to a similar extend, while the reduction of HW was much more pronounced (Figure 11E). These data support the hypothesis that the mTOR pathway has an important role during fetal heart development. In summary, prenatal mTORC1 inhibition induces overall growth restriction and developmental delay in neonatal mice, where cardiac development was especially affected and most severe consequences were observed in c*Hccs*$^{+/-}$ hearts.

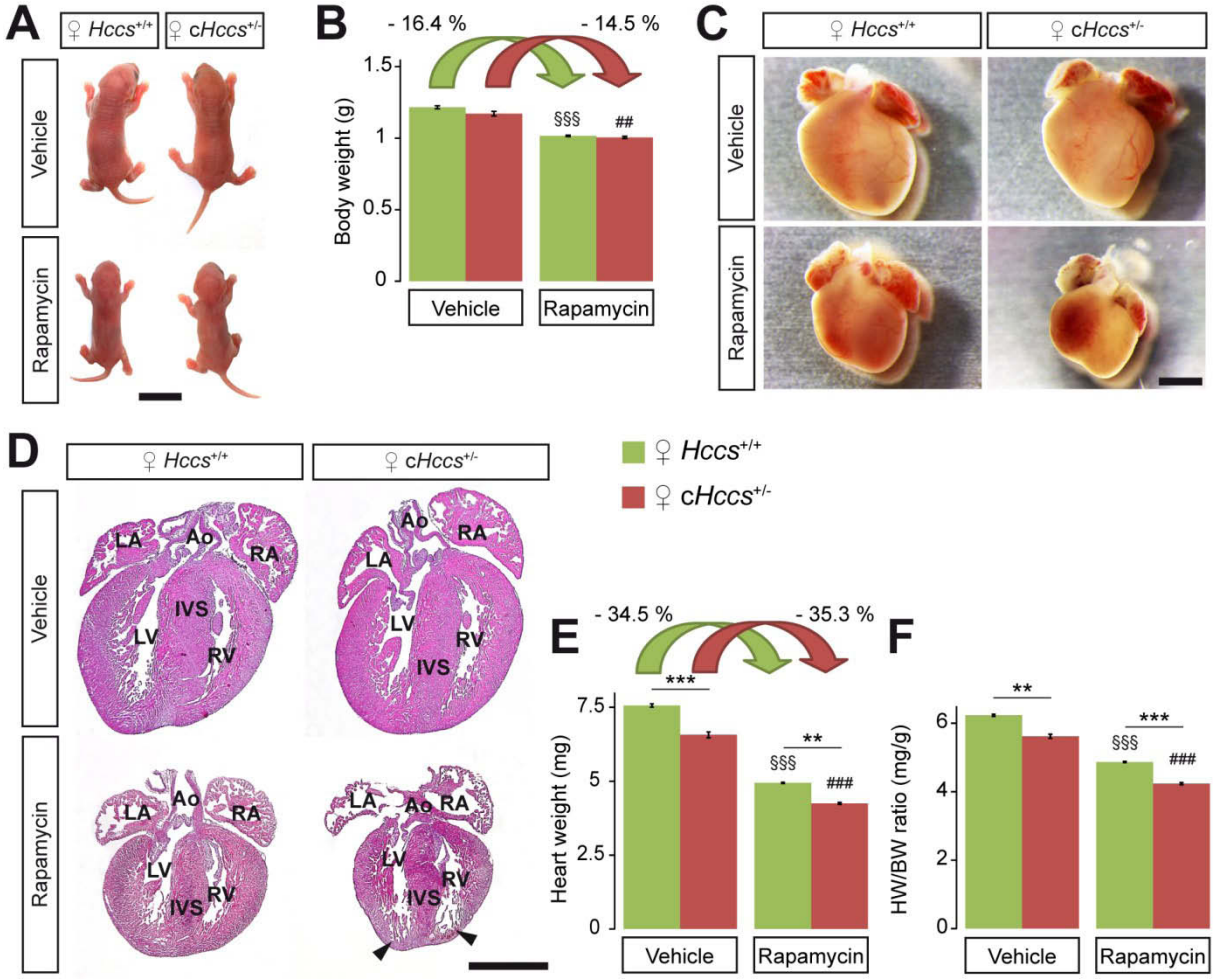

Figure 11. Prenatal mTORC1 inhibition induces overall growth restriction and reduces heart size in neonatal mice.
A) Newborn offspring after prenatal rapamycin treatment were smaller compared to their vehicle treated controls (scale bar = 1 cm). **B)** BW of rapamycin treated neonates was significantly reduced compared to vehicle treated animals. **C)** Neonatal mice after prenatal rapamycin treatment had smaller hearts compared to their vehicle controls (scale bar = 1 mm). **D)** H&E-stained longitudinal heart sections of neonatal mice after prenatal mTORC1 inhibition were morphologically characterized by developmental delay indicated by smaller heart size as well as thinning and noncompaction of the ventricular myocardium, which was most prominent in rapamycin treated c*Hccs*$^{+/-}$ hearts (arrowheads) (scale bar = 1 mm, Ao: aorta, IVS: interventricular septum, LA: left atrium, LV: left ventricle, RA: right atrium, RV: right ventricle). **E)+F)** Rapamycin treated neonates demonstrated significantly lower HW and HW/BW ratio compared to vehicle treated animals. Note that the reduced HW and HW/BW ratio in c*Hccs*$^{+/-}$ compared to *Hccs*$^{+/+}$ newborn females, which is a major hallmark of the heart conditional *Hccs* model, persisted after prenatal mTORC1 inhibition. For **B)+E)+F)**: Statistical significance among groups was assessed by one-way ANOVA followed by Bonferroni post-hoc test (***p*<0.01, ****p*<0.001, §§§*p*<0.001 vs. vehicle *Hccs*$^{+/+}$, ###*p*<0.001 vs. vehicle c*Hccs*$^{+/-}$, n=9 for vehicle *Hccs*$^{+/+}$ and c*Hccs*$^{+/-}$, n=10 for rapamycin *Hccs*$^{+/+}$ and c*Hccs*$^{+/-}$).

6.3.3.2 *Prenatal mTORC1 inhibition reduces cardiomyocyte size, induces apoptosis but does not affect proliferation in neonatal hearts*

We observed significantly reduced heart size in neonatal mice after prenatal mTORC1 inhibition. Theoretically, this reduced heart size can be caused by a decreased cell number or a reduced cell size or a combination of both. To elucidate these options, we investigated proliferation and apoptosis rates as well as cardiomyocyte size in neonatal hearts after prenatal vehicle or rapamycin treatment. Proliferation rates were assessed by immunofluorescence staining for KI67, a marker that labels proliferating cells in all active phases of the cell cycle[217] (Figure 12A). Quantification of KI67-positive nuclei in the LV myocardium revealed no significant differences between the treatment groups or the

genotypes (38.55±2.68 % for vehicle *Hccs*$^{+/+}$, 40.47±1.89 % for vehicle c*Hccs*$^{+/-}$, 35.77±0.85 % for rapamycin *Hccs*$^{+/+}$, 37.27±1.15 % for rapamycin c*Hccs*$^{+/-}$) (Figure 12C). To investigate if prenatal mTORC1 inhibition also provokes apoptosis, terminal deoxynucleotidyl transferase dUTP nick end labeling (TUNEL) stainings were conducted, a fluorescence based method that detects nuclear DNA fragmentation (a major hallmark of apoptosis)[216] (Figure 12B). Quantification of TUNEL-positive nuclei in the LV myocardium of vehicle treated neonates revealed 0.07±0.02 % apoptotic cells in *Hccs*$^{+/+}$ controls and 0.12±0.02 % in c*Hccs*$^{+/-}$ animals (Figure 12D). In contrast, apoptosis rates in rapamycin treated neonates were significantly (p<0.001) increased (0.20±0.01 % for *Hccs*$^{+/+}$, 0.28±0.03 % for c*Hccs*$^{+/-}$) (Figure 12D). Importantly, significantly (p<0.05) more TUNEL-positive cells were identified in rapamycin c*Hccs*$^{+/-}$ neonatal hearts compared to rapamycin *Hccs*$^{+/+}$ controls (Figure 12D). Thus, prenatal mTORC1 inhibition generally induces apoptosis in neonatal hearts with a higher extend in c*Hccs*$^{+/-}$ neonates. To measure cell size, cardiomyocyte cross sectional area (CSA) was studied by wheat germ agglutinin (WGA) fluorescence staining of cell membranes, where WGA selectively binds to *N*-acetylneuraminic acid residues[215] (Figure 12E). Cardiomyocytes within the LV myocardium of hearts from rapamycin treated neonates were significantly (p<0.001) smaller (42.8±0.44 µm^2 for *Hccs*$^{+/+}$, 31.4±1.34 µm^2 for c*Hccs*$^{+/-}$) compared to those of vehicle treated animals (64.7±2.45 µm^2 for *Hccs*$^{+/+}$, 63.3±1.92 µm^2 for c*Hccs*$^{+/-}$) (Figure 12F). Interestingly, within the rapamycin treated group, cardiomyocyte CSA of c*Hccs*$^{+/-}$ hearts was significantly (p<0.05) reduced compared to *Hccs*$^{+/+}$ control hearts (Figure 12F). Hence, mTORC1 inhibition decreases cell size in both genotypes with more pronounced consequences on the compensatory growth of c*Hccs*$^{+/-}$ hearts. In summary, prenatal inhibition of mTORC1 reduces neonatal heart size by affecting cardiomyocyte hypertrophic growth and apoptosis but not proliferation.

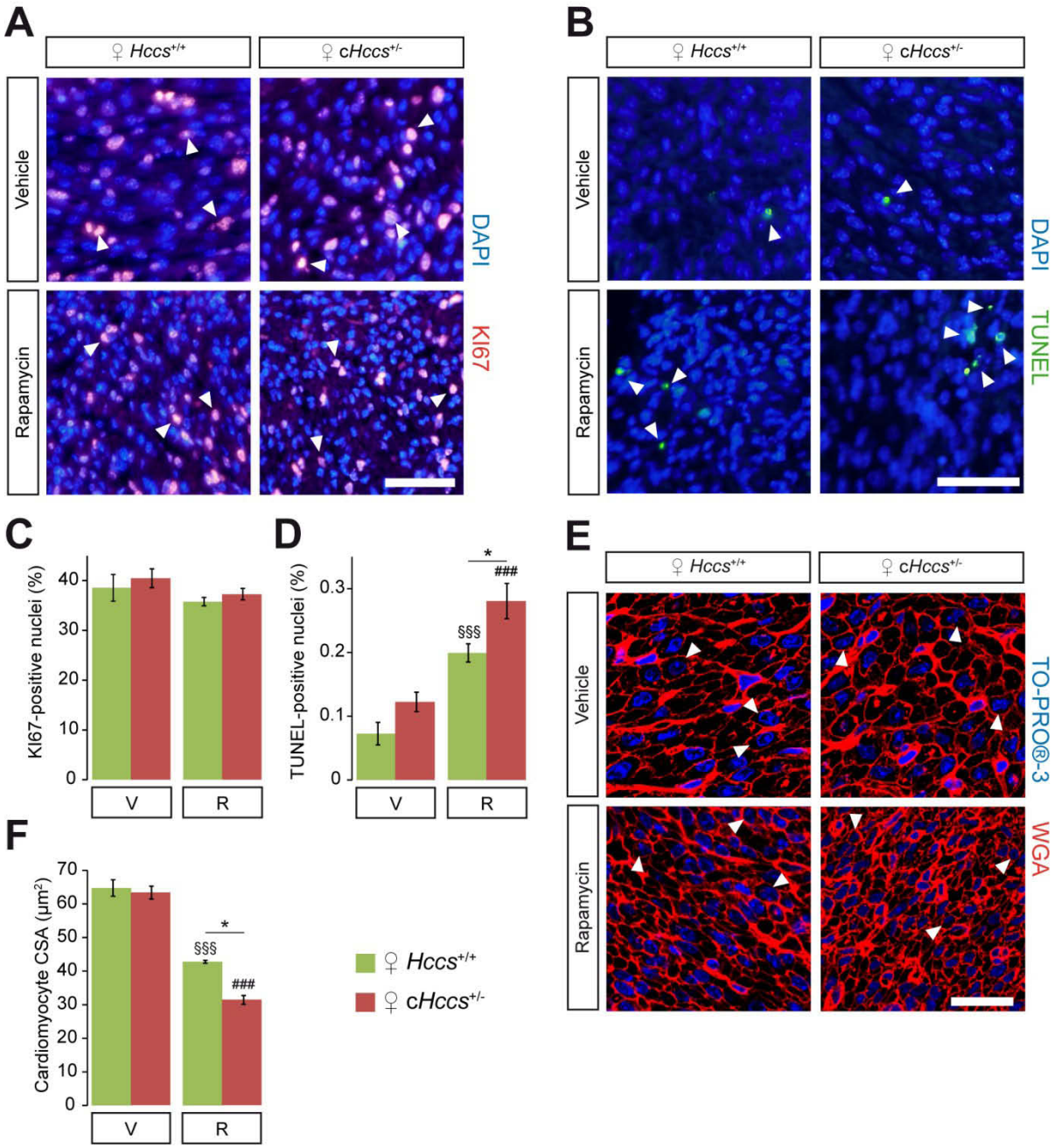

Figure 12. Prenatal mTORC1 inhibition does not affect cardiomyocyte proliferation rates but induces apoptosis and reduces cardiomyocyte size in neonatal hearts.
A) Immunofluorescence images of KI67-labeled nuclei (red) within the left ventricular (LV) myocardium of neonatal hearts. Nuclei were stained in blue with DAPI. Cycling cardiac cells exhibit colocalization of DAPI and KI67 and hence appear pink (arrowheads) (scale bar = 50 µm). **B)** Fluorescence terminal deoxynucleotidyl transferase dUTP nick end labeling (TUNEL) stainings (green) within the LV myocardium of neonatal hearts. Nuclei were stained in blue with DAPI. Cells in apoptosis exhibit colocalization of DAPI and TUNEL (arrowheads) (scale bar = 50 µM). **C)** Quantification of KI67-positive nuclei revealed unchanged proliferation rates within the LV myocardium of vehicle or rapamycin treated hearts and between the genotypes (n=6 for vehicle *Hccs*$^{+/+}$ and c*Hccs*$^{+/-}$, n=12 for rapamycin *Hccs*$^{+/+}$, n=13 for rapamycin c*Hccs*$^{+/-}$). **D)** Quantification of TUNEL-positive nuclei revealed significantly increased programmed cell death in hearts after prenatal mTORC1 inhibition, with apoptosis in rapamycin c*Hccs*$^{+/-}$ hearts being significantly higher than in rapamycin *Hccs*$^{+/+}$ controls. Statistical significance among groups was assessed by one-way ANOVA followed by Bonferroni post-hoc test (*p<0.05, §§§p<0.001 vs. vehicle *Hccs*$^{+/+}$, ###p<0.001 vs. vehicle c*Hccs*$^{+/-}$, n=4 for vehicle *Hccs*$^{+/+}$, n=6 for vehicle c*Hccs*$^{+/-}$ as well as rapamycin *Hccs*$^{+/+}$ and c*Hccs*$^{+/-}$). **E)** Fluorescence images of cross-sectioned cardiomyocytes within the LV myocardium of neonatal hearts. Cardiomyocyte membranes were stained in red with wheat germ agglutinin (WGA) and nuclei in blue with TO-PRO®-3. Only cardiomyocytes that matched the defined measurement criteria were analyzed (arrowheads) (confocal microscopy, scale bar = 25 µm). **F)** Prenatal rapamycin treatment significantly reduced cardiomyocyte cross sectional area (CSA) in both genotypes, and cardiomyocytes in rapamycin c*Hccs*$^{+/-}$ hearts were significantly smaller compared to rapamycin *Hccs*$^{+/+}$ controls (n=5 for vehicle *Hccs*$^{+/+}$ and c*Hccs*$^{+/-}$, n=3 for rapamycin *Hccs*$^{+/+}$ and c*Hccs*$^{+/-}$). For **C)+F)**: Statistical significance among groups was assessed using Kruskal-Wallis one-way analysis of variance followed by Mann-Whitney post-hoc test (*p<0.05, §§§p<0.001 vs. vehicle *Hccs*$^{+/+}$, ###p<0.001 vs. vehicle c*Hccs*$^{+/-}$). (R: rapamycin, V: vehicle)

6.3.3.3 Cardiac function in neonatal mice is largely unaffected by prenatal mTORC1 inhibition

Given the severe phenotype in neonatal hearts after prenatal mTORC1 inhibition, we were eager to investigate if this results in altered cardiac function at birth. Thus, echocardiographic measurements in neonatal *Hccs*$^{+/+}$ and c*Hccs*$^{+/-}$ mice after prenatal vehicle or rapamycin treatment were performed (Figure 13 and Supplementary Table S5). Thickness of the interventricular septum (IVS, 0.27±0.01 mm for vehicle *Hccs*$^{+/+}$, 0.26±0.01 mm for vehicle c*Hccs*$^{+/-}$, 0.24±0.01 mm for rapamycin *Hccs*$^{+/+}$, 0.23±0.02 mm for rapamycin c*Hccs*$^{+/-}$) (Figure 13A) and of the left ventricular posterior wall (LVPW, 0.27±0.02 mm for vehicle *Hccs*$^{+/+}$, 0.27±0.01 mm for vehicle c*Hccs*$^{+/-}$, 0.26±0.01 mm for rapamycin *Hccs*$^{+/+}$, 0.23±0.02 mm for rapamycin c*Hccs*$^{+/-}$) (Figure 13B) in end-diastole were not significantly different between the treatment groups and the genotypes. Left ventricular internal diameter (LVID) in end-diastole was significantly reduced in rapamycin *Hccs*$^{+/+}$ controls (1.27±0.05 mm) compared to vehicle treated *Hccs*$^{+/+}$ mice (1.50±0.04 mm) (p<0.01), but missed statistical significance between the c*Hccs*$^{+/-}$ groups (1.41±0.05 mm for vehicle c*Hccs*$^{+/-}$, 1.27±0.05 mm for rapamycin c*Hccs*$^{+/-}$) (Figure 13C). However, in line with the results obtained from explanted neonatal hearts (see Chapter 6.3.3.1, Figure 11E), a trend toward a reduction in all three parameters (IVS, LVPW, LVID) was obvious for rapamycin treated neonatal hearts compared to their corresponding vehicle control groups (Figure 13A-C). Importantly, histological analyses (see Chapter 6.3.3.1, Figure 11D) as well as the weight data (see Chapter 6.3.3.1, Figure 11E) provided strong indications for reduced chamber dimensions and wall thickness. However, this could only partially be confirmed by echocardiographic measurements and for most parameters the reduction is obvious just as a trend (Figure 13A-C). This deviation might be explained by the exceptionally small rapamycin treated hearts, which pose a resolution challenge for echocardiography, even though a high frequency ultrasound system with a 50 MHz transducer was used. So, clearly determining the epi- and endocardial layers on these images to analyze wall thickness is difficult, resulting in a certain degree of deviation and error.

Surprisingly, analysis of the left ventricular contractile parameters FS (fractional shortening, fraction of LV dimension in end-diastole that is lost in end-systole, 31.86±1.46 % for vehicle *Hccs*$^{+/+}$, 31.98±1.42 % for vehicle c*Hccs*$^{+/-}$, 29.50±1.65 % for rapamycin *Hccs*$^{+/+}$, 27.36±1.53 % for rapamycin c*Hccs*$^{+/-}$) (Figure 13D) and EF (ejection fraction, blood volume ejected by LV during one contraction, 63.05±1.92 % for vehicle *Hccs*$^{+/+}$, 64.06±1.98 % for vehicle c*Hccs*$^{+/-}$, 61.38±3.00 % for rapamycin *Hccs*$^{+/+}$, 55.60±1.77 % for rapamycin c*Hccs*$^{+/-}$) (Figure 13E) revealed only a slight trend (though not significant) regarding FS reduction and a significant reduction of EF (p<0.05) in rapamycin c*Hccs*$^{+/-}$ neonates compared to vehicle c*Hccs*$^{+/-}$ mice. In contrast, in rapamycin *Hccs*$^{+/+}$ neonates, FS and EF

remained normal (Figure 13D+E). These findings suggest that prenatal mTORC1 inhibition slightly reduces cardiac contractility in neonatal c*Hccs*$^{+/-}$ mice, while heart function in rapamycin *Hccs*$^{+/+}$ neonates is mainly unaffected. However, even an EF of 55.60±1.77 % in c*Hccs*$^{+/-}$ neonates can still be considered as being normal and does not indicate severe problems regarding cardiac contractility. Taken together, it rather came as a surprise to us that prenatal mTORC1 inhibition causes a severe phenotype in neonatal hearts but only marginally affects heart function in newborn mice.

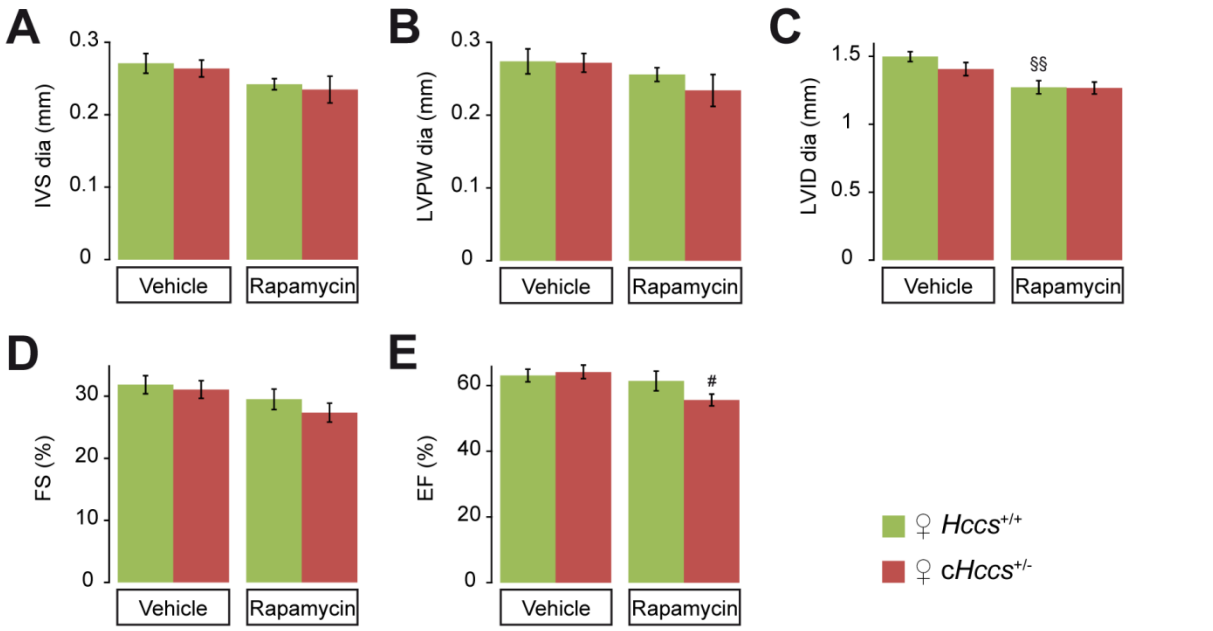

Figure 13. Echocardiographic measurements in neonatal mice after prenatal mTORC1 inhibition revealed largely normal cardiac function.
A) Interventricular septum (IVS) and **B)** left ventricular posterior wall (LVPW) thickness in end-diastole (dia) was slightly reduced after prenatal rapamycin treatment in both genotypes without reaching statistical significance. **C)** End-diastolic left ventricular internal diameter (LVID) was marginally smaller in neonatal c*Hccs*$^{+/-}$ mice and significantly reduced in *Hccs*$^{+/+}$ controls after prenatal mTORC1 inhibition. **D)+E)** Fractional shortening (FS) and ejection fraction (EF) remained unchanged in *Hccs*$^{+/+}$ controls and EF was significantly but not severely reduced in c*Hccs*$^{+/-}$ mice after prenatal rapamycin treatment, indicating largely normal heart function in both genotypes. For **A)**-**E)**: Statistical significance among groups was assessed by one-way ANOVA followed by Bonferroni post-hoc test (§§p<0.01 vs. vehicle *Hccs*$^{+/+}$, #p<0.05 vs. vehicle c*Hccs*$^{+/-}$, n=7 for vehicle *Hccs*$^{+/+}$ and rapamycin c*Hccs*$^{+/-}$, n=6 for vehicle c*Hccs*$^{+/-}$ and rapamycin *Hccs*$^{+/+}$).

6.3.4 Consequences of prenatal mTORC1 inhibition for adult hearts

According to the concept of developmental programming, IUGR can have various consequences on cardiac growth and function in adulthood (see Chapter 3.2). To address the question if prenatal mTORC1 inhibition affects heart morphology, size and function later in life, 11 week old adult animals were analyzed.

6.3.4.1 Prenatal mTORC1 inhibition does not affect cardiac morphology and size of adult hearts

To determine if prenatal mTORC1 inhibition impacts on cardiac morphology and growth later in life, 11 week old adult mice after prenatal vehicle or rapamycin treatment were analyzed with respect to BW and HW as well as cardiac morphology (Figure 14). H&E-stained heart cross-sections revealed no histological, structural or pathological abnormalities between the

genotypes or the treatment groups (Figure 14A). Reduction in BW, as evident in neonatal rapamycin treated animals (see Chapter 6.3.3.1, Figure 11B), remained as trend (p=0.055) in adult *Hccs*$^{+/+}$ control mice (15.26±0.51 g) and was significant (p<0.05) in c*Hccs*$^{+/-}$ adults (15.78±1.08 g) compared to vehicle treated animals (16.91±0.61 g for *Hccs*$^{+/+}$, 18.67±0.57 g for c*Hccs*$^{+/-}$) (Figure 14B). HW was also reduced in neonatal mice after prenatal mTORC1 inhibition (see Chapter 6.3.3.1, Figure 11E). For both genotypes, a slight reduction in HW persists in adulthood (94.47±3.59 mg for vehicle *Hccs*$^{+/+}$, 105.68±8.60 mg for vehicle c*Hccs*$^{+/-}$, 87.53±4.08 mg for rapamycin *Hccs*$^{+/+}$, 89.25±4.81 mg for rapamycin c*Hccs*$^{+/-}$); which, however, missed statistical significance (Figure 14C). In neonatal rapamycin mice, HW/BW ratio was significantly reduced compared to vehicle treated neonates with a higher level of reduction in c*Hccs*$^{+/-}$ neonates (see Chapter 6.3.3.1, Figure 11F). In adult mice, due to the slight reduction of both, BW and HW, HW/BW ratio was unchanged (5.59±0.12 mg/g for vehicle *Hccs*$^{+/+}$, 5.64±0.37 mg/g for vehicle c*Hccs*$^{+/-}$, 5.75±0.22 mg/g for rapamycin *Hccs*$^{+/+}$, 5.69±0.10 mg/g for rapamycin c*Hccs*$^{+/-}$) (Figure 14D). HW/BW ratio was significantly smaller in neonatal rapamycin treated c*Hccs*$^{+/-}$ mice compared to rapamycin treated *Hccs*$^{+/+}$ controls (see Chapter 6.3.3.1, Figure 11F). Importantly, HW and HW/BW ratio was not different between the genotypes in adult mice after prenatal mTORC1 inhibition (Figure 14C+D). This observation suggests that postnatal catch-up growth after prenatal mTORC1 inhibition is enhanced in the c*Hccs*$^{+/-}$ heart compared to the whole body.

To further investigate cardiac size and function, echocardiographic measurements were performed (Figure 14E-G and Supplementary Table S6). End-diastolic IVS (0.74±0.02 mm for vehicle *Hccs*$^{+/+}$, 0.76±0.06 mm for vehicle c*Hccs*$^{+/-}$, 0.62±0.04 mm for rapamycin *Hccs*$^{+/+}$, 0.63±0.04 mm for rapamycin c*Hccs*$^{+/-}$) (Figure 14E) and LVPW thickness (0.75±0.02 mm for vehicle *Hccs*$^{+/+}$, 0.76±0.04 mm for vehicle c*Hccs*$^{+/-}$, 0.61±0.04 mm for rapamycin *Hccs*$^{+/+}$, 0.63±0.04 mm for rapamycin c*Hccs*$^{+/-}$) (Figure 14F) as well as end-diastolic LVID (3.66±0.11 mm for vehicle *Hccs*$^{+/+}$, 3.96±0.18 mm for vehicle c*Hccs*$^{+/-}$, 3.64±0.08 mm for rapamycin *Hccs*$^{+/+}$, 3.91±0.13 mm for rapamycin c*Hccs*$^{+/-}$) (Figure 14G) were not significantly different between the treatment groups and the genotypes. However, in line with the results obtained from explanted adult hearts (Figure 14C) a slight reduction in LV wall thickness was obvious in both genotypes after prenatal mTORC1 inhibition (Figure 14E+F).

Neonatal mice after prenatal mTORC1 inhibition demonstrated reduced KW (see Chapter 6.3.3.1, Supplementary Figure 3C). In adult mice, absolute organ weight as well as organ weight normalized to BW for liver, kidney and spleen were investigated (Supplementary Figure 5). Liver, kidney and spleen weights were slightly reduced in adult rapamycin treated mice of both genotypes; even though the difference was not statistically significant (Supplementary Figure 5A+C+E). When normalized to BW, no significant

differences between the treatment groups or the genotypes were demonstrated for all three organs (Supplementary Figure 5B+D+F).

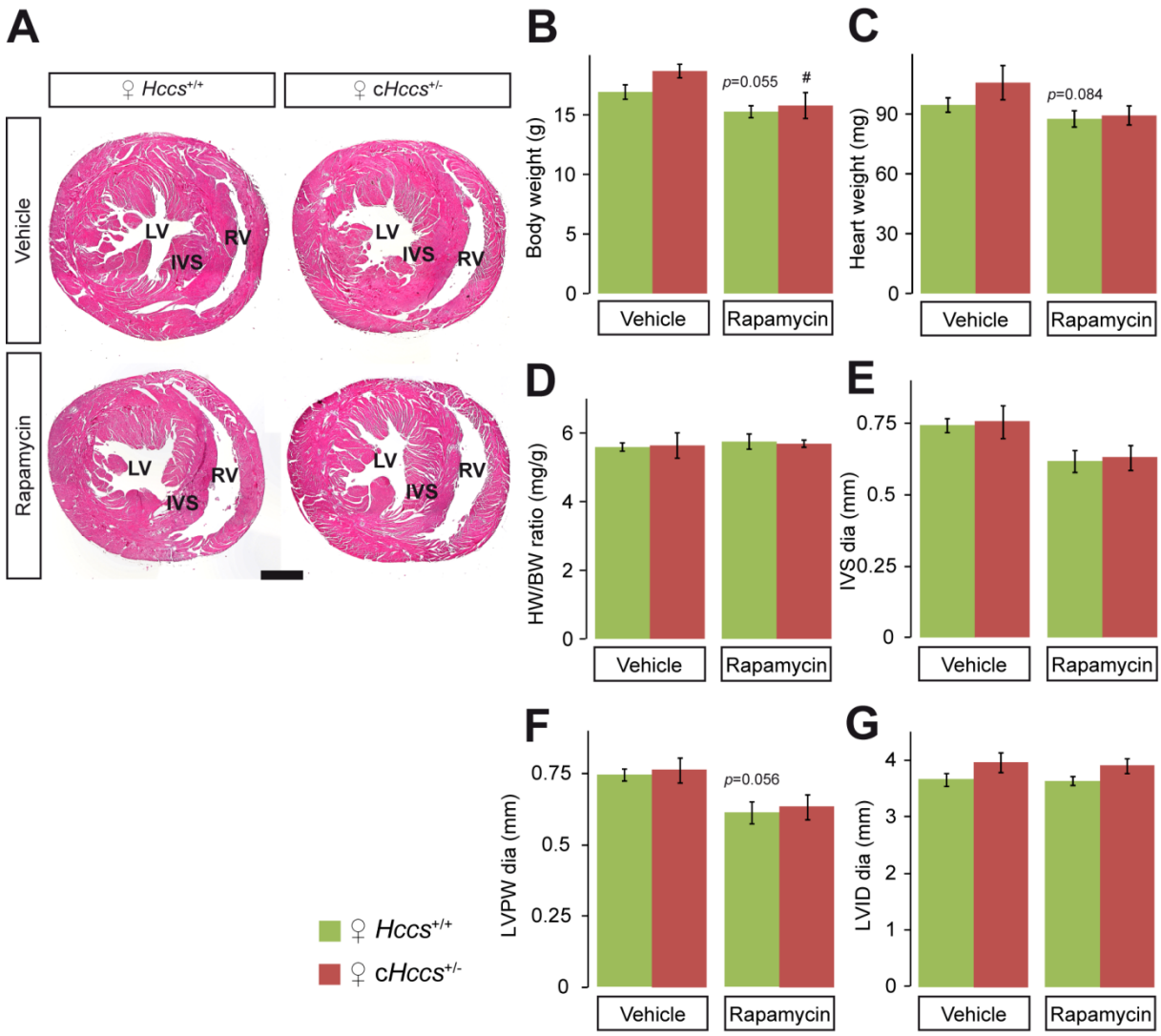

Figure 14. Adult mice after prenatal mTORC1 inhibition demonstrate partial normalization of body and heart weight. **A)** No major morphological changes within the left ventricle (LV), interventricular septum (IVS) or right ventricle (RV) were observed in both genotypes after prenatal mTORC1 inhibition when H&E-stained heart cross-sections were compared with those from adult vehicle treated animals (scale bar = 1 mm). **B)** Body weight (BW) in adult rapamycin c*Hccs*$^{+/-}$ animals was significantly lower compared to the corresponding vehicle group. A similar trend was observed in adult *Hccs*$^{+/+}$ controls, indicating incomplete normalization of BW during postnatal life in both genotypes. **C)** Heart weight (HW) in adult rapamycin treated animals demonstrated a slight reduction in both genotypes compared to the corresponding vehicle groups, again suggesting partial normalization of HW in adulthood. **D)** HW to BW (HW/BW) ratio in adult animals after prenatal mTORC1 inhibition was not different between the treatment groups or the genotypes. Note that the reduced HW/BW ratio observed in neonatal vehicle and rapamycin c*Hccs*$^{+/-}$ mice compared to the corresponding *Hccs*$^{+/+}$ controls is no longer evident in adult animals. **E)** Echocardiographic measurements of the thickness of the interventricular septum (IVS) as well as of **F)** the left ventricular posterior wall (LVPW) in end-diastole in adult mice revealed a slight reduction after prenatal rapamycin treatment in both genotypes without reaching statistical significance. **G)** End-diastolic left ventricular internal diameter (LVID) in adult hearts was not different between the treatment groups and the genotypes. For **B)+D)**: Statistical significance among groups was assessed using Kruskal-Wallis one-way analysis of variance followed by Mann-Whitney post-hoc test (#p<0.05 vs. vehicle c*Hccs*$^{+/-}$). For **C)+E)-G)**: Statistical significance among groups was assessed by one-way ANOVA followed by Bonferroni post-hoc test. For **B)-G)**: n=7 for vehicle *Hccs*$^{+/+}$, n=6 for vehicle and rapamycin c*Hccs*$^{+/-}$, n=9 for rapamycin *Hccs*$^{+/+}$.

In summary, reduction of BW and HW after prenatal mTOR inhibition, as observed in neonatal mice, was mainly normalized during postnatal life in both genotypes; however, it did not completely reach the level of vehicle treated mice by the age of 11 weeks. Importantly, HW/BW ratio was reduced in neonates (see Chapter 6.3.3.1, Figure 11F) but not adult

mice (Figure 14D) after prenatal mTORC1 inhibition. In contrast, KW/BW ratio was neither reduced in rapamycin treated neonates (see Chapter 6.3.3.1, Supplementary Figure 3D) nor in adult mice after prenatal mTORC1 inhibition (Supplementary Figure 5D). These data suggest faster postnatal catch-up growth in the heart as compared to the whole body.

6.3.4.2 Prenatal mTORC1 inhibition increases cardiomyocyte size but does not induce pathological remodeling or left ventricular dysfunction in adult hearts

Even though it was shown that prenatal mTORC1 inhibition results in reduced cardiomyocyte CSA (see Chapter 6.3.3.2, Figure 12F) as well as reduced HW and HW/BW ratio in neonatal hearts (see Chapter 6.3.3.1, Figure 11E+F), HW and HW/BW ratio normalized until adulthood (see Chapter 6.3.4.1, Figure 14C+D). Given that the mTOR pathway plays an important role is postnatal cardiomyocyte growth, we further investigated how cardiomyocyte size develops during postnatal life. To this intend, we measured cardiomyocyte CSA in the LV myocardium of adult hearts after prenatal vehicle or rapamycin treatment on WGA-stained heart sections (Figure 15A). Cardiomyocytes CSA of adult rapamycin hearts was significantly larger (403.35±59.38 µm^2 for *Hccs*$^{+/+}$ (p<0.01), 427.50±89.05 µm^2 for c*Hccs*$^{+/-}$ (p<0.05)) compared to the vehicle control groups (280.03±14.66 µm^2 for *Hccs*$^{+/+}$, 330.11±29.60 µm^2 for c*Hccs*$^{+/-}$) (Figure 15B). Interestingly, compensatory postnatal cardiomyocyte hypertrophy in c*Hccs*$^{+/-}$ hearts (a major hallmark of the heart conditional *Hccs* KO model (see Chapter 3.4)) that was apparent under vehicle conditions, was lost after prenatal rapamycin treatment (Figure 15B). These findings indicate that prenatal mTORC1 inhibition increases adult cardiomyocyte size in both genotypes (thereby allowing normalization of HW/BW ratio until adulthood) but impairs postnatal compensatory hypertrophic growth in c*Hccs*$^{+/-}$ mice.

Although cardiomyocytes make up the bulk of the myocardial volume, the myocardium additionally consists of various nonmyocytes. Cardiac fibroblasts are the most abundant non-myocyte cell type in the heart and synthesize extracellular matrix (ECM), which is mainly built up of collagen fibers. Besides cardiomyocyte enlargement, physiological postnatal heart growth is achieved through ECM synthesis and deposition. However, excessive deposition of ECM by fibroblasts is an indicator of pathological myocardial remodeling (termed fibrosis), and can cause myocardial dysfunction[226,227]. IUGR has been shown to increase ECM deposition in the postnatal heart, thereby potentially contributing to increased disease susceptibility[26,28]. The percentage of interstitial fibrosis was investigated within the LV myocardium of adult mice after prenatal vehicle or rapamycin treatment by Sirius red staining (Figure 15E). Quantification revealed no differences between the genotypes or the treatment groups (1.20±0.17 % for vehicle *Hccs*$^{+/+}$, 1.13±0.26 % for vehicle c*Hccs*$^{+/-}$, 1.05±0.04 % for rapamycin *Hccs*$^{+/+}$, 1.25±0.22 % for rapamycin c*Hccs*$^{+/-}$), indicating normal

collagen deposition (Figure 15C). These results demonstrate that postnatal normalization of heart size after prenatal rapamycin treatment is achieved by increased cell size, but not increased physiological ECM deposition or pathological fibrosis.

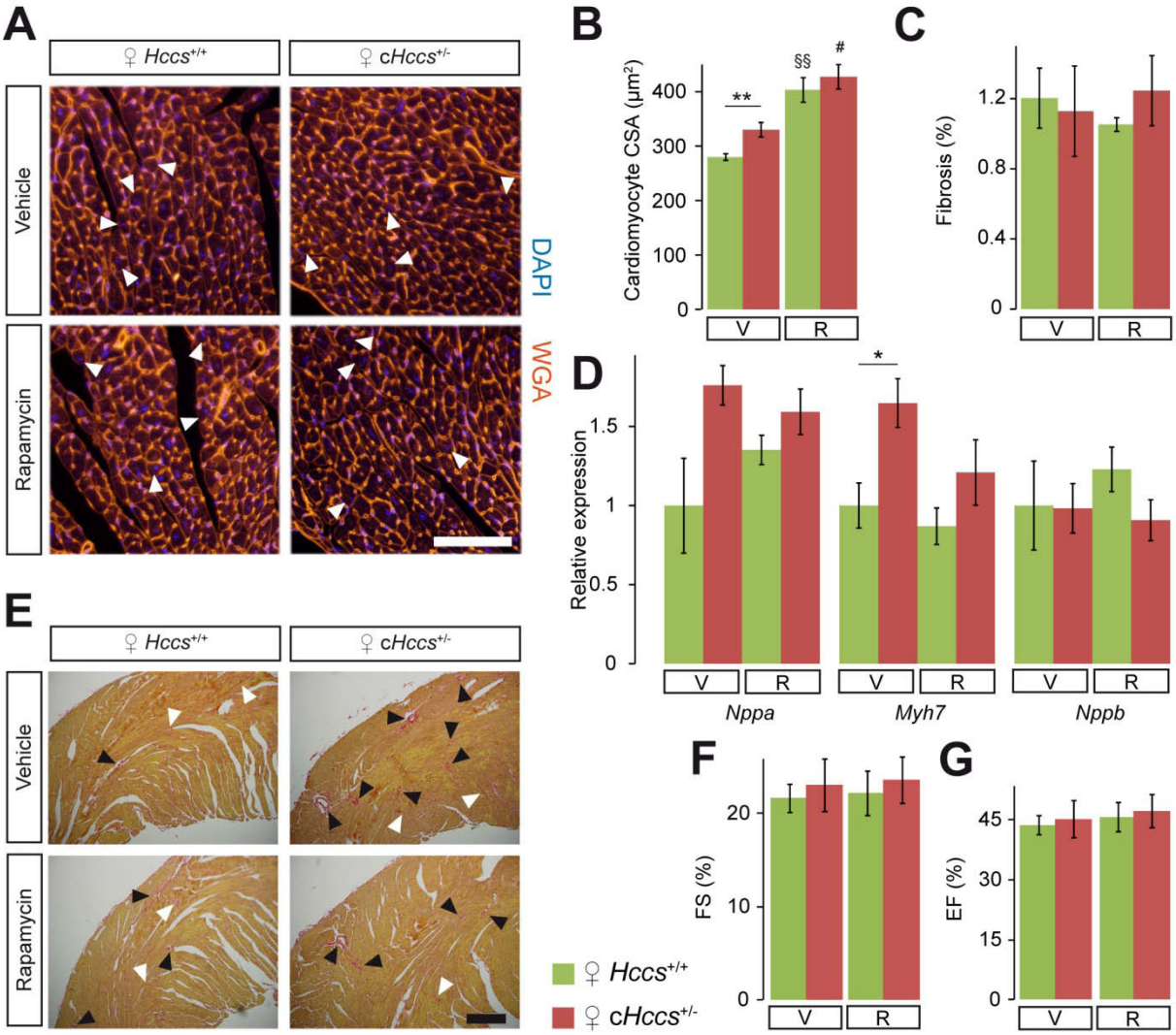

Figure 15. Prenatal mTORC1 inhibition increases cardiomyocyte CSA but does not cause pathological remodeling or impaired cardiac function in 11 week old adult hearts.
A) Fluorescence images of cross-sectioned cardiomyocytes within the left ventricular (LV) myocardium of adult hearts. Cardiomyocyte membranes were stained in orange with wheat germ agglutinin (WGA) and nuclei in blue with DAPI. Only cardiomyocytes that matched the defined measurement criteria were analyzed (arrowheads) (scale bar = 100 µm). **B)** Cardiomyocyte cross sectional area (CSA) was significantly larger in hearts exposed to prenatal rapamycin (R) treatment compared to vehicle (V) treated groups. Note that compensatory cardiomyocyte hypertrophy in c*Hccs*$^{+/-}$ mice, evident in the vehicle group, was lost in adult rapamycin treated hearts (n=6 for vehicle *Hccs*$^{+/+}$, n=5 for vehicle and rapamycin c*Hccs*$^{+/-}$, n=7 for rapamycin *Hccs*$^{+/+}$). **C)** Quantification of fibrotic cardiac tissue within the LV myocardium of adult mice did not reveal differences in collagen accumulation between the treatment groups or the genotypes (n=6 for vehicle and rapamycin *Hccs*$^{+/+}$ and rapamycin c*Hccs*$^{+/-}$, n=8 for vehicle c*Hccs*$^{+/-}$). **D)** Relative *natriuretic peptide type A* (*Nppa*), *β-myosin heavy chain 7* (*Myh7*) and *natriuretic peptide type B gene* (*Nppb*) mRNA levels in adult hearts were determined using qPCR. No significant upregulation of all three heart failure marker genes was observed in rapamycin groups compared to vehicle groups (n=8 for all groups). **E)** Random images of the LV myocardium of Sirius red stained heart cross-sections of adult mice demonstrated only minor collagen deposition in all four groups. White arrowheads highlight the red appearance of fine threads of interstitial collagen. Black arrowheads highlight perivascular fibrosis, which was excluded for quantification (scale bar = 300 µm). **F)** Echocardiographic measurements revealed that left ventricular fractional shortening (FS) and **G)** ejection fraction (EF) in adult mice were neither different between the genotypes nor the treatment groups, indicating that prenatal mTORC1 inhibition did not impair cardiac function in adulthood (n=7 for vehicle *Hccs*$^{+/+}$, n=6 for vehicle and rapamycin c*Hccs*$^{+/-}$, n=9 for rapamycin *Hccs*$^{+/+}$). For **B)+C)**: Statistical significance among groups was assessed using Kruskal-Wallis one-way analysis of variance followed by Mann-Whitney post-hoc test (**p<0.05, §§ p<0.01 vs. vehicle *Hccs*$^{+/+}$, #p<0.05 vs. vehicle c*Hccs*$^{+/-}$). For **D)**, **F)**, **G)**: Statistical significance among groups was assessed by one-way ANOVA followed by Bonferroni post-hoc test (*p<0.05).

To further analyze if prenatal mTORC1 inhibition causes pathological conditions in the heart and eventually leads to impaired cardiac function in adulthood, RNA expression analyses of "heart failure marker genes" were performed (Figure 15D). Moreover, heart function was measured by echocardiography (Figure 15F+G and Supplementary Table S6). As reviewed by McMullen and Jennings, elevated cardiac expression of the fetal genes *natriuretic peptide type A* (*Nppa*), *natriuretic peptide type B* (*Nppb*) and *β-myosin heavy chain* (*Myh7*) is associated with cardiac stress[116]. Hence, the expression of these "heart failure marker genes" is an indication for molecular adaptations of the heart in response to pathological conditions[116]. Relative *Nppa*, *Myh7* and *Nppb* expression in adult hearts after prenatal rapamycin treatment were not significantly different compared to mRNA levels in adult vehicle treated hearts (Figure 15D). Furthermore, the LV contractile parameters FS (21.66±1.53 % for vehicle *Hccs*$^{+/+}$, 23.07±2.81 % for vehicle c*Hccs*$^{+/-}$, 22.21±2.37 % for rapamycin *Hccs*$^{+/+}$, 23.58±2.45 % for rapamycin c*Hccs*$^{+/-}$) and EF (43.64±2.38 % for vehicle *Hccs*$^{+/+}$, 45.18±4.64 % for vehicle c*Hccs*$^{+/-}$, 45.71±3.70 % for rapamycin *Hccs*$^{+/+}$, 47.17±4.12 % for rapamycin c*Hccs*$^{+/-}$) remained unchanged, indicating normal heart function (Figure 15F+G and Supplementary Table S6).

In summary, no indications for pathological conditions or myocardial tissue remodeling were observed in adult hearts after prenatal mTORC1 inhibition. Moreover, cardiac function in adulthood was normal, indicating that the normal heart function in neonatal rapamycin treated mice (see Chapter 6.3.3.3, Figure 13D+E) is maintained during postnatal life and might even improve in rapamycin c*Hccs*$^{+/-}$ females.

6.4 Consequences of cardiac-specific *Raptor* ablation on heart development and survival

Prenatal mTORC1 inhibition by rapamycin treatment is a pharmacological approach that affects the entire fetal as well as maternal organism. Although this certainly resembles the situation of classical IUGR models (see Chapter 3.2.2), direct consequences for the heart are difficult to differentiate from secondary effects caused by rapamycin-induced changes in other organs. Moreover, effects on the maternal metabolism and fetal blood, oxygen and nutritional supply, including proper growth and development of the placenta, are conceivable confounding factors. Despite intriguing findings regarding the consequences of prenatal rapamycin treatment in the neonatal heart, this does not allow a general conclusion about the role of the mTOR pathway during heart development.

Thus, to more precisely analyze the consequences of heart-specific mTORC1 inhibition during development, a genetic approach using a mouse strain that carries two *loxP* sites flanking exon 6 of the *Raptor* gene[206] (see Chapter 5.1.1.3) has been carried out. RAPTOR is an essential component of mTORC1 and regulates its assembly, localization and substrate

binding[120,121]. By analyzing liver protein lysates, Sengupta *et al*. demonstrated that, upon liver-specific *Cre*-mediated excision of the "floxed" *Raptor* sequence, mTORC1 activity was completely eliminated[206]. Importantly, to date, almost nothing is known about mTOR pathway function in the embryonic heart and no conclusive KO approach of any of the mTORC1 components has been published before. In our study, breeding of these "floxed" Raptor mice with mice carrying the *Cre* recombinase sequence under the control of the cardiac *Nkx2-5* promoter allowed tissue specific excision of the *loxP*-flanked *Raptor* sequence in offspring from 7.5 dpc onwards (see Chapter 5.1.2.2, Figure 7).

6.4.1 Cardiac-specific *Raptor* ablation causes embryonic lethality

The conventional KO of both *Mtor* and *Raptor* results in embryonic lethality in mice between 5.5 dpc - 6.5 dpc, shortly after implantation[178-180]. Thus, we were eager to investigate the survival rate of heart-specific *Raptor* KO mice. The applied breeding strategy is assumed to generate 43.75 % WT *Raptor* mice (*Raptor*$^{+/+}$), 37.50 % cardiac-specific heterozygous *Raptor* KOs (c*Raptor*$^{+/-}$) and 18.75 % cardiac-specific homozygous *Raptor* KOs (c*Raptor*$^{-/-}$) (see Figure 16A and Chapter 5.1.2.2, Figure 7). When we analyzed the genotype distribution of alive newborn offspring at birth and of alive 13.5 dpc embryos, we identified *Raptor*$^{+/+}$ and heterozygous c*Raptor*$^{+/-}$ but no homozygous c*Raptor*$^{-/-}$ mice (Figure 16A). Interestingly, during preparation of 13.5 dpc litters, dead pups were observed that were estimated to be arrested in development at approximately 11.5 dpc and were genotyped as being homozygous for the *Raptor* KO. Consequently, genotype distribution of 10.5 dpc litters was investigated. All offspring analyzed were found to be alive and 41.59±8.83 % *Raptor*$^{+/+}$, 35.02±4.93 % c*Raptor*$^{+/-}$ and 23.39±5.03 % c*Raptor*$^{-/-}$ embryos were identified (Figure 16A). In summary, the homozygous cardiac-specific *Raptor* KO results in embryonic lethality between 10.5 dpc and 11.5 dpc, while all heterozygous cardiac-specific *Raptor* KO mice are born alive with no sign of prenatal lethality.

6.4.2 Cardiac-specific *Raptor* ablation results in hypoplastic embryonic hearts

To investigate the cause of embryonic lethality, morphology of 10.5 dpc c*Raptor*$^{+/-}$ and c*Raptor*$^{-/-}$ hearts in comparison to 10.5 dpc WT hearts on H&E-stained sections was analyzed. At this stage, all c*Raptor*$^{-/-}$ mice are alive (see Chapter 6.4.1). Hearts of 10.5 dpc c*Raptor*$^{-/-}$ embryos revealed a severe phenotype with thinning of the compact as well as underdevelopment of the trabeculated myocardium resulting in hypoplastic hearts (Figure 16E). In contrast, 10.5 dpc c*Raptor*$^{+/-}$ hearts did not show any morphological abnormalities (Figure 16E).

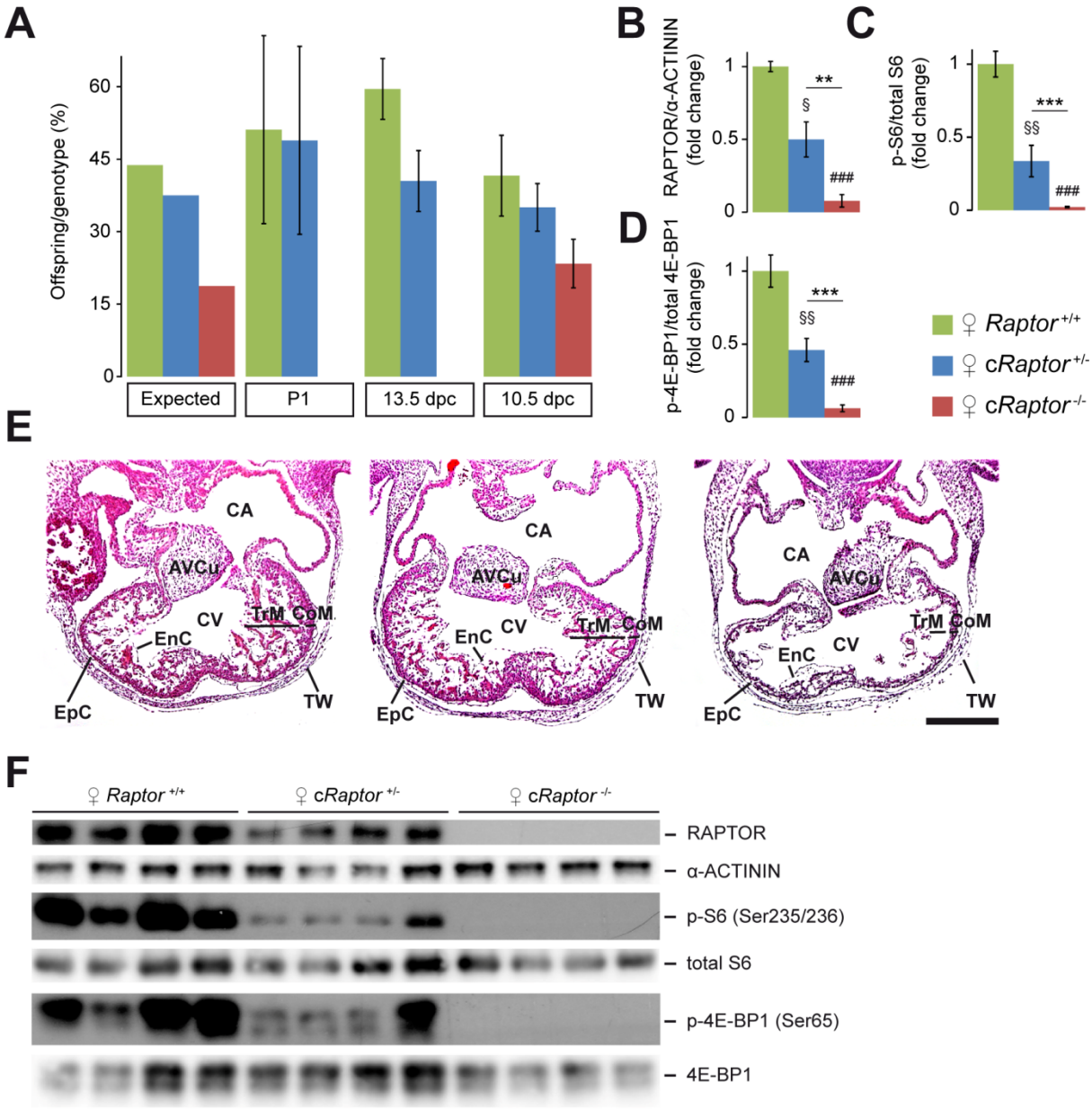

Figure 16. Cardiac-restricted *Raptor* KO mice (c*Raptor*$^{-/-}$) die in utero.
A) Genotype distribution of alive offspring at postnatal day 1 (P1), embryonic day 13.5 dpc and embryonic day 10.5 dpc compared to the expected genotype distribution demonstrated that c*Raptor*$^{-/-}$ mice die *in utero* after 10.5 dpc (n=5 litter for P1, n=3 litter for 13.5 dpc, n=10 litter for 10.5 dpc). **B)** Quantification of total RAPTOR protein levels normalized to α-ACTININ, **C)** S6 phosphorylation at serine 235 and serine 236 normalized to total S6 and **D)** 4E-BP1 phosphorylation at serine 65 normalized to total 4E-BP1 revealed significantly reduced mTORC1 activity in 10.5 dpc c*Raptor*$^{+/-}$ hearts and almost complete impairment of mTORC1 activity in 10.5 dpc c*Raptor*$^{-/-}$ hearts. Statistical significance among groups was assessed by one-way ANOVA followed by Bonferroni post-hoc test (***p*<0.01, ****p*<0.001, §*p*<0.05 vs. *Raptor*$^{+/+}$, §§*p*<0.01 vs. *Raptor*$^{+/+}$, ###*p*<0.001 vs. *Raptor*$^{+/+}$, n=7 per group). **E)** H&E-stained longitudinal heart sections of embryonic 10.5 dpc *Raptor*$^{+/+}$, c*Raptor*$^{+/-}$ and c*Raptor*$^{-/-}$ mice revealed that cardiac-restricted *Raptor* KO causes developmental delay of the heart indicated by thinning of the compact as well as underdevelopment of the trabeculated myocardium resulting in a hypoplastic phenotype, an observation that was not present in 10.5 dpc c*Raptor*$^{+/-}$ hearts (scale bar = 300 µm, AVCu: atrioventricular cushions, CA: common atrium, CoM: compact myocardium, CV: common ventricle, EnC: endocardium, EpC: epicardium, TrM: trabeculated myocardium, TW: thoracic wall). **F)** Western blots of whole heart protein extracts from embryonic 10.5 dpc *Raptor*$^{+/+}$, c*Raptor*$^{+/-}$ and c*Raptor*$^{-/-}$ mice revealed significantly decreased phosphorylation of S6 and 4E-BP1 as well as significantly reduced total RAPTOR levels in c*Raptor*$^{+/-}$ hearts and completely undetectable phosphorylation of S6 and 4E-BP1 and RAPTOR protein expression in c*Raptor*$^{-/-}$ hearts.

6.4.3 Cardiac-specific *Raptor* ablation blocks mTORC1 activity in embryonic hearts

To confirm that heart-specific *Raptor* ablation inhibits mTORC1 activity, western blot analyses of 10.5 dpc whole heart protein extracts were performed (Figure 16F). Investigation

of total RAPTOR protein levels as well as of the phosphorylation status of the mTORC1 downstream targets S6 at serine 235 and 236 and 4E-BP1 at serine 65 revealed a significant reduction in 10.5 dpc c*Raptor*$^{+/-}$ hearts and complete absence in 10.5 dpc c*Raptor*$^{-/-}$ hearts (Figure 16F). Quantification of RAPTOR total protein levels normalized to α-ACTININ as well as S6 and 4E-BP1 phosphorylation normalized to total S6 and total 4E-BP1, respectively, confirmed significant reduction (p<0.05/p<0.01) in 10.5 dpc c*Raptor*$^{+/-}$ hearts by 50 % to 65 % and a highly significant reduction (p<0.001) in 10.5 dpc c*Raptor*$^{-/-}$ hearts by 92 % to 98 % compared to 10.5 dpc WT *Raptor*$^{+/+}$ hearts (Figure 16B-D). Taken together, these findings indicate that prenatal cardiac-specific *Raptor* ablation impairs mTORC1 activity resulting in hypoplastic hearts and intrauterine lethality.

6.5 Consequences of pre- and postnatal amino acid restriction on cardiac development, growth and function

Functional annotation analysis of microarray expression data revealed an enrichment of genes involved in amino acid homeostasis in neonatal c*Hccs*$^{+/-}$ hearts (see Chapter 6.1, Table 18 and Supplementary Table S2-S4). These findings together with the upregulation of one of the most important sensors of cellular amino acid availability, MTOR (see Chapter 6.2, Figure 8), gave rise to the question if an increased amino acid demand or biosynthesis is essential for the embryonic regenerative capacity and the postnatal compensatory growth of c*Hccs*$^{+/-}$ hearts. To test this hypothesis and to analyze the role of amino acid homeostasis during cardiac development in general, amino acid availability was restricted during intrauterine and postnatal growth by feeding mice a low protein diet (LPD) containing only 8.8 % crude protein (see Chapter 5.1.5). Female and male mice were put on LPD two weeks prior to mating. Pregnant dams were kept on LPD during pregnancy and offspring were prepared immediately after birth or remained on LPD during lactation and after weaning. In parallel, as controls, mice were treated the same way using normal standard protein diet (SPD) food containing 22 % crude protein.

6.5.1 Mice on LPD do not compensate for the reduced protein content by increased food intake

Mice on LPD might compensate for the reduced amino acid availability by increasing their ingestion. Therefore, the food intake of non-pregnant and pregnant adult female mice on LPD was analyzed in comparison to mice on SPD. The daily food intake of non-pregnant 5 months old females was measured over a time period of 10 days and normalized to BW. While SPD mice ate 0.20±0.014 g food per day and gram BW (4.5±0.327 g per day if not normalized to BW), LPD mice ate 0.17±0.008 g food per day and gram BW (3.7±0.234 g per day if not normalized to BW) (Figure 17A). The difference was not statistically significant. With respect to the amount of crude protein taken up with the food, SPD animals ingested

4.4±0.319 mg crude protein per day and gram BW (99±6.99 mg crude protein per day if not normalized to BW), while LPD animals ingested 1.5±0.070 mg crude protein per day and gram BW (33±2.12 mg crude protein per day if not normalized to BW) (Figure 17A). To measure the food intake during pregnancy, the daily ingestion of 5 months old pregnant mice on LPD in comparison to SPD was analyzed from 13.5 dpc until the end of pregnancy. While pregnant SPD mice ate 0.13±0.003 g food per day and gram BW (4.5±0.238 g per day if not normalized to BW), pregnant LPD mice ate 0.12±0.013 g food per day and gram BW (4.4±0.280 g per day if not normalized to BW) (Figure 17B). The difference was not statistically significant. Regarding the uptake of crude protein, pregnant SPD mice ingested 2.9±0.064 mg crude protein per day and gram BW (99±5.23 mg crude protein per day if not normalized to BW), while pregnant LPD mice ingested 1.1±0.115 mg crude protein per day and gram BW (39±2.46 mg crude protein per day if not normalized to BW) (Figure 17B). In summary, these results indicate that LPD animals do not compensate for the reduced amino acid availability in the food by increasing their ingestion, suggesting that they are indeed exposed to amino acid restriction.

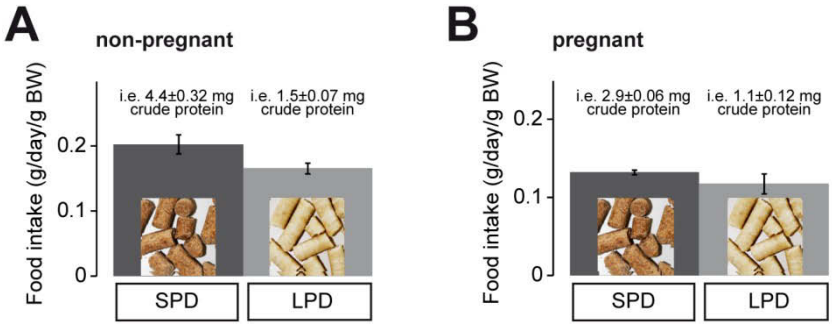

Figure 17. Food intake of non-pregnant and pregnant adult females on SPD and LPD does not differ.
A) The daily food intake of non-pregnant 5 months old female mice on SPD and LPD was measured over a time period of 10 days and normalized to body weight (BW). No significant differences between the diet groups were observed. **B)** The daily food intake of 5 months old pregnant mice on SPD and LPD was measured from 13.5 dpc until the end of pregnancy. No significant differences between the treatment groups were observed. Statistical significance among groups was assessed using unpaired 2-tailed Student *t*-tests. Numbers above the bars correspond to the average amount of crude protein that was taken up per day normalized to BW. Note that LPD animals took up less crude protein than mice on SPD. For **A)**+**B)**: n=3 per group.

6.5.2 Prenatal amino acid restriction neither affects litter size nor genotype distribution

Given that we hypothesized that amino acid availability might be critical for embryonic heart regeneration and compensatory growth in c*Hccs*$^{+/-}$ females, we investigated if amino acid restriction during pregnancy induces prenatal lethality. For this purpose, we compared litter size as well as genotype distribution within SPD and LPD litters (Figure 18). Pregnant dams fed SPD gave birth to 5.1±0.46 offspring per litter, while litter size of LPD fed dams was 4.9±0.55 (Figure 18A). The difference was not statistically significant. Besides, the applied breeding strategy theoretically generates *Hccs*$^{+/Y}$ control males, *Hccs*$^{+/+}$ control females and c*Hccs*$^{+/-}$ females to equal parts (33.33 %, Figure 18B and see Chapter 5.1.2.1, Figure 6). In SPD litters, 34.88±9.16 % control males, 26.79±6.81 % control females, and 38.33±10.48 %

c*Hccs*$^{+/-}$ were identified at P1 (Figure 18B). LPD litters split up in 37.29±7.02 % control males, 27.76±6.66 % control females, and 34.95±10.17 % c*Hccs*$^{+/-}$ mice (Figure 18B). Genotype distribution within SPD as well as LPD fed litters compared to the expected genotype distribution was not significantly different as determined with *chi*-square test (Figure 18B). In line, 2-tailed Student *t*-tests comparing genotype frequency of control males and females as well as of c*Hccs*$^{+/-}$ mice, respectively, between SPD and LPD litters resulted in equal distribution independent of expected frequencies (Figure 18B). In conclusion, amino acid restriction during pregnancy does not cause general or genotype-specific embryonic lethality.

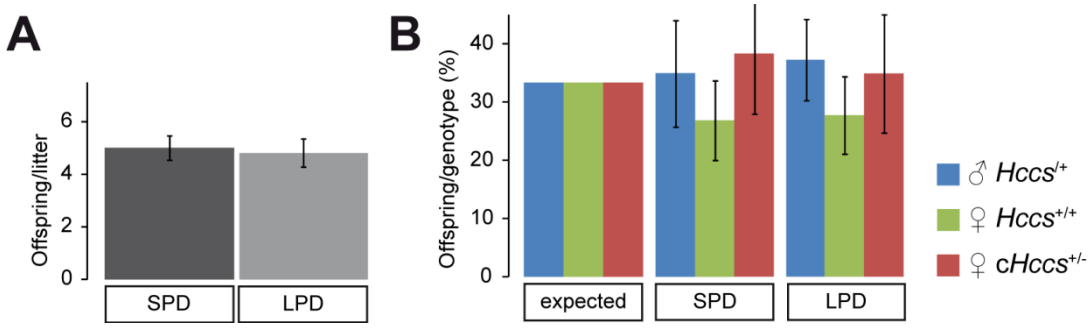

Figure 18. Intrauterine amino acid restriction neither affects litter size nor genotype distribution.
A) Average litter size of dams receiving SPD or LPD food does not differ. Statistical significance among groups was assessed using unpaired 2-tailed Student *t*-tests. **B)** Genotype distribution within litters from SPD and LPD female mice was not significantly different from the expected genotype frequencies. Statistical significance between the groups and the expected genotype distribution was assessed using *chi*-square test. Statistical significance comparing the frequencies of all three genotypes, respectively, between SPD and LPD litters independent of expected frequencies was assessed by unpaired 2-tailed Student *t*-tests. For **A)**+**B)**: n=10 litters for both diet groups.

6.5.3 Consequences of prenatal amino acid restriction for neonatal hearts

6.5.3.1 Prenatal amino acid restriction does not change cardiac morphology but reduces HW/BW ratio in neonatal cHccs$^{+/-}$ mice

To determine the effect of amino acid restriction during pregnancy on cardiac development and growth, H&E-stained longitudinal heart sections from neonatal SPD and LPD P1 offspring were analyzed. No major histological, structural or pathological abnormalities (e.g. thinning of the LV wall or ventricular/atrial septum defects) were observed between the genotypes or the diet groups (Figure 19A). In addition, BW and HW were measured and the HW/BW ratio was determined (Figure 19B+C). BW in newborn mice upon intrauterine amino acid restriction was not significantly different between the genotypes or the diet groups (1.44±0.03 g for SPD *Hccs*$^{+/+}$, 1.42±0.02 g for SPD c*Hccs*$^{+/-}$, 1.44±0.03 g for LPD *Hccs*$^{+/+}$, 1.44±0.04 g for LPD c*Hccs*$^{+/-}$) (Figure 19B). Furthermore, no significant differences in HW were observed between all four groups (7.68±0.26 g for SPD *Hccs*$^{+/+}$, 7.48±0.25 g for SPD c*Hccs*$^{+/-}$, 8.24±0.16 g for LPD *Hccs*$^{+/+}$, 7.52±0.27 g for LPD c*Hccs*$^{+/-}$) (Figure 19C). However, LPD *Hccs*$^{+/+}$ controls demonstrate a clear trend toward increased HW compared to SPD *Hccs*$^{+/+}$ controls (Figure 19C). HW/BW ratio in *Hccs*$^{+/+}$ and c*Hccs*$^{+/-}$ LPD neonates was unchanged compared to their corresponding SPD control groups (5.33±0.15 mg/g for SPD

Hccs$^{+/+}$, 5.25±0.13 mg/g for SPD c*Hccs*$^{+/-}$, 5.77±0.19 mg/g for LPD *Hccs*$^{+/+}$, 5.23±0.10 mg/g for LPD c*Hccs*$^{+/-}$) (Figure 19D). However, interestingly, exposure to LPD during gestation results in a trend toward increased HW/BW ratio in LPD *Hccs*$^{+/+}$ controls compared to SPD *Hccs*$^{+/+}$ mice (probably due to the increase in HW), which results in a significant difference in HW/BW ratio between LPD c*Hccs*$^{+/-}$ females and LPD *Hccs*$^{+/+}$ controls by 10 % (p<0.05) (Figure 19D). Taken together, even though cardiac morphology and LV dimensions at birth were not affected by prenatal LPD, the HW/BW ratio data indicate that restriction of intrauterine amino acid availability causes an increase in HW/BW ratio in *Hccs*$^{+/+}$ controls, which is not obvious in the c*Hccs*$^{+/-}$ neonates. Assuming that the increase in HW and HW/BW ratio in *Hccs*$^{+/+}$ controls represents the normal situation upon prenatal amino acid restriction, these data suggest growth inhibition by prenatal LPD exposure in P1 c*Hccs*$^{+/-}$ hearts.

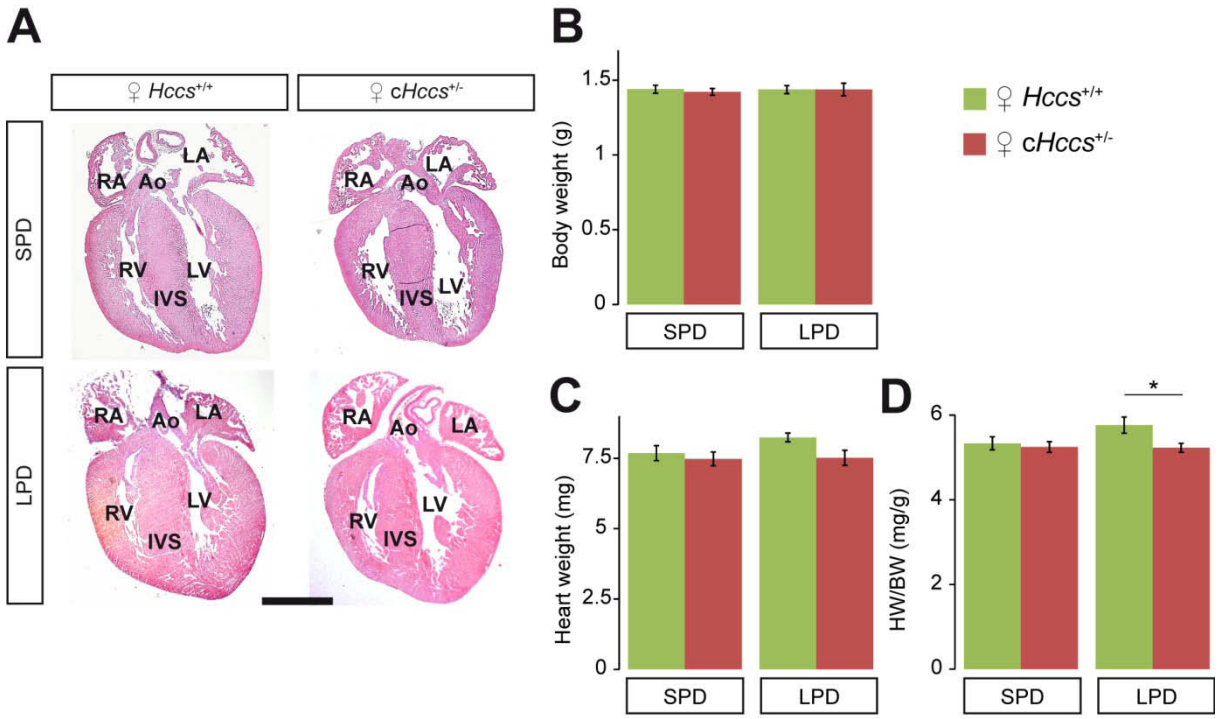

Figure 19. Prenatal LPD exposure does not change cardiac morphology of neonatal hearts but reduces HW/BW ratio in c*Hccs*$^{+/-}$ newborns compared to *Hccs*$^{+/+}$ controls.
A) Longitudinal H&E-stained sections of neonatal control and c*Hccs*$^{+/-}$ hearts after intrauterine amino acid restriction revealed no histological, structural or pathological abnormalities compared to hearts of neonatal SPD offspring (scale bar = 1 mm, Ao: aorta, IVS: interventricular septum, LA: left atrium, LV: left ventricle, RA: right atrium, RV: right ventricle). **B)** No significant differences in body weight (BW) were observed between the genotypes and the diet groups at birth. **C)** No significant differences in heart weight (HW) were observed between diet groups at birth. Neonatal c*Hccs*$^{+/-}$ hearts on LPD demonstrated a trend of reduction in weight compared to LPD *Hccs*$^{+/+}$ hearts, which did not reach statistical significance. **D)** Significant reduction of HW to BW (HW/BW) ratio in c*Hccs*$^{+/-}$ females compared to controls on LPD but not SPD. For **B)**-**D)**: Statistical significance among groups was assessed by one-way ANOVA followed by Bonferroni post-hoc test (*p<0.05, n=18 for SPD *Hccs*$^{+/+}$, SPD c*Hccs*$^{+/-}$ and LPD c*Hccs*$^{+/-}$, n=15 for LPD *Hccs*$^{+/+}$).

6.5.3.2 *Prenatal amino acid restriction increases cardiomyocyte CSA but does not affect proliferation rates in neonatal hearts*

Given that intrauterine amino acid restriction results in slightly increased HW and HW/BW ratio in neonatal *Hccs*$^{+/+}$ controls but not in c*Hccs*$^{+/-}$ newborns, we speculated that this

discrepancy might be mediated by either different cardiomyocyte size or different cardiomyocyte number or a combination of both. Previous studies from our lab already assessed the proliferation rates in LV myocardium of female control (41.75±6.01 %) and c*Hccs*$^{+/-}$ (41.33±11.41 %) neonatal hearts under SPD conditions by KI67 staining and revealed no significant difference between the genotypes (unpublished data). Here, proliferation rates in the LV myocardium of neonatal mice exposed to prenatal amino acid restriction were also similar in *Hccs*$^{+/+}$ control (47.27±2.08 %) and c*Hccs*$^{+/-}$ hearts (48.41±1.19 %) (Figure 20C), as assessed by KI67 staining on longitudinal heart sections (Figure 20A). Moreover, the percentage of KI67-positive cells in neonatal LPD hearts (Figure 20C) closely matches the values determined in neonatal SPD hearts in previous studies (unpublished data). Thus, prenatal amino acid restriction does not impair the proliferative potential of neonatal hearts in general and of neonatal c*Hccs*$^{+/-}$ hearts in particular. To investigate if cell size was affected by prenatal amino acid restriction, cardiomyocyte CSA in the LV myocardium of neonatal hearts after SPD and LPD pregnancies was measured (Figure 20B). Surprisingly, cardiomyocyte CSA of neonatal LPD c*Hccs*$^{+/-}$ hearts (54.76±2.18 µm^2) was significantly increased compared to SPD c*Hccs*$^{+/-}$ hearts (36.71±3.73 µm^2) (p<0.01) (Figure 20D). The same trend was observed for neonatal LPD *Hccs*$^{+/+}$ control hearts (37.30±5.15 µm^2 for SPD *Hccs*$^{+/+}$, 48.28±2.18 µm^2 for LPD *Hccs*$^{+/+}$), even though the difference missed statistical significance (Figure 20D). Besides, neonatal LPD c*Hccs*$^{+/-}$ cardiomyocytes CSA appeared slightly larger than neonatal LPD *Hccs*$^{+/+}$ cardiac cells (Figure 20D). Taken together, these data indicate that prenatal amino acid restriction neither reduced proliferation rates nor cardiomyocyte CSA in neonatal c*Hccs*$^{+/-}$ hearts. Hence, the reason for the reduced HW/BW ratio in neonatal LPD c*Hccs*$^{+/-}$ mice is left unknown at that point. Strikingly, increased cardiomyocyte CSA (Figure 20D) might be responsible for the increased HW in neonatal LPD *Hccs*$^{+/+}$ controls (see Chapter 6.5.3.1, Figure 19C). In contrasts, HW in LPD c*Hccs*$^{+/-}$ neonates was unchanged (see Chapter 6.5.3.1, Figure 19C) despite a significantly increased cell size (Figure 20D). In regard of unaltered proliferation rates (Figure 20C), differences in cell number might underlie these observations.

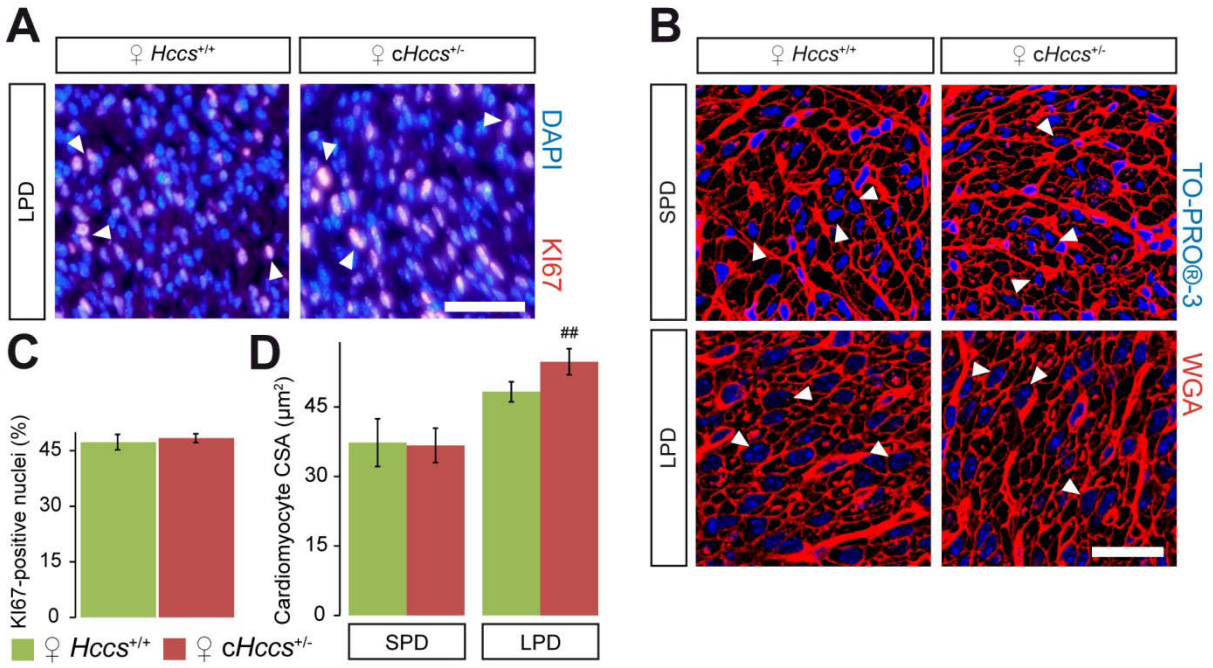

Figure 20. Intrauterine LPD exposure does not alter proliferation rates but increases cardiomyocyte CSA in the LV myocardium of *Hccs*$^{+/+}$ and c*Hccs*$^{+/-}$ neonatal hearts.
A) Immunofluorescence images of KI67-labeled nuclei (red) within the left ventricular (LV) myocardium of neonatal hearts. Nuclei were stained in blue with DAPI. Cycling cardiac cells exhibit colocalization of DAPI and KI67 and hence appear pink (arrowheads) (scale bar = 50 µm). **B)** Fluorescence images of cross-sectioned cardiomyocytes within the LV myocardium of neonatal hearts exposed to SPD or LPD intrauterine conditions. Cardiomyocyte membranes were stained in red with wheat germ agglutinin (WGA) and nuclei in blue with TO-PRO®-3. Only cardiomyocytes that matched the defined measurement criteria were analyzed (arrowheads) (confocal microscopy, scale bar = 25 µm). **C)** Quantification of KI67-positive nuclei revealed unchanged proliferation rates within the LV of hearts from neonatal LPD *Hccs*$^{+/+}$ and c*Hccs*$^{+/-}$ animals, indicating that prenatal amino acid restriction does not affect cardiac proliferation in neonatal mice. Statistical significance among groups was assessed using unpaired 2-tailed Student *t*-tests (n=8 for LPD *Hccs*$^{+/+}$, n=7 for LPD c*Hccs*$^{+/-}$). **D)** Cardiomyocyte cross sectional area (CSA) in neonatal c*Hccs*$^{+/-}$ mice exposed to prenatal amino acid restriction was significantly larger compared to neonatal SPD c*Hccs*$^{+/-}$ cardiomyocytes. The same trend was observed for LPD *Hccs*$^{+/+}$ hearts, but missed statistical significance. Statistical significance among groups was assessed by one-way ANOVA followed by Bonferroni post-hoc test (##p<0.01 vs. SPD c*Hccs*$^{+/-}$, n=4 for SPD *Hccs*$^{+/+}$ and c*Hccs*$^{+/-}$, n=7 for LPD *Hccs*$^{+/+}$, n=8 for LPD c*Hccs*$^{+/-}$).

6.5.4 Consequences of prenatal amino acid restriction for embryonic 13.5 dpc hearts

The lower HW/BW ratio in neonatal LPD c*Hccs*$^{+/-}$ animals (see Chapter 6.5.3.1, Figure 19D) was not attributable to a decrease in cardiomyocyte size or proliferation rate at birth. Thus, it was postulated that the reduction in heart size might be due to a decrease in cell number, caused by cellular events during embryogenesis when amino acids are restricted. To investigate the effect of amino acid restriction on compensatory growth of 13.5 dpc embryonic c*Hccs*$^{+/-}$ hearts as well as on *Hccs*$^{+/+}$ controls, overall cardiac morphology as well as apoptosis and proliferation rates within the embryonic ventricular myocardium were analyzed. Importantly, genes involved in amino acid homeostasis were found to be enriched in 13.5 dpc embryonic c*Hccs*$^{+/-}$ hearts (unpublished data), which provides further evidence that an increased amino acid availability might thus be essential to allow normal cardiac development in c*Hccs*$^{+/-}$ mice. Moreover, cardiomyocyte CSA in LPD neonates was found to be enhanced (see Chapter 6.5.3.2, Figure 20D), while HW was not significantly different (see Chapter 6.5.3.1, Figure 19C). These observations provide further support for a cell number defect in neonatal LPD hearts.

6.5.4.1 Prenatal amino acid restriction does not affect mTOR pathway activity and does not change cardiac morphology in 13.5 dpc embryonic hearts

mTOR pathway activity is highly sensitive to amino acid availability. The pathway is activated if amino acids are abundant and inactivated if they are restricted under conditions of nutrient starvation[144,145]. To analyze mTORC1 activity in our LPD model, western blot analyses were performed with whole heart protein extracts from 13.5 dpc embryos under both normal conditions and prenatal amino acid restriction (Figure 21A). The phosphorylation status of the mTORC1 upstream and mTORC2 downstream target AKT at serine 473 and of the mTORC1 downstream target S6 at serine 240 and 244 was investigated (Figure 21A). After quantification and normalization to total protein levels, the relative phosphorylation was quantified and depicted as fold change in relation to the SPD *Hccs*$^{+/+}$ control group (Figure 21B+C). To further monitor mTOR activity and to additionally evaluate whether LPD induces autophagy, total protein levels of p62 (an important indicator for autophagy that is normally inhibited by mTOR pathway activity[223,224]), were quantified and normalized to GAPDH protein levels (Figure 21D). No significant differences were apparent in any of the analyzed upstream or downstream mTOR pathway mediators when comparing all four groups (Figure 21B-D), indicating that mTOR pathway activity and autophagy in embryonic hearts are not affected by prenatal LPD treatment.

Furthermore, cardiac morphology was analyzed in H&E-stained longitudinal heart sections of 13.5 dpc *Hccs*$^{+/+}$ and c*Hccs*$^{+/-}$ embryos upon intrauterine SPD or LPD exposure (Figure 21E). The extent of trabeculation and ventricular wall thickness was appropriate for LPD embryonic hearts compared to SPD embryos (Figure 21E). The size and thickness of the atrial myocardium was also inconspicuous (Figure 21E). Atrioventricular cushions (AVCu), which can be seen as two thickenings in the lumen of the atrio-ventricular canal and later form the valve leaflets (see Chapter 3.3.1, Figure 3), developed adequately upon amino acid restriction, providing no indication of structural cardiac conditions (Figure 21E). In summary, due to the normal cardiac phenotype in LPD treated embryos, prenatal amino acid restriction does not appear to impair early cardiac development and growth in neither *Hccs*$^{+/+}$ nor c*Hccs*$^{+/-}$ hearts until 13.5 dpc.

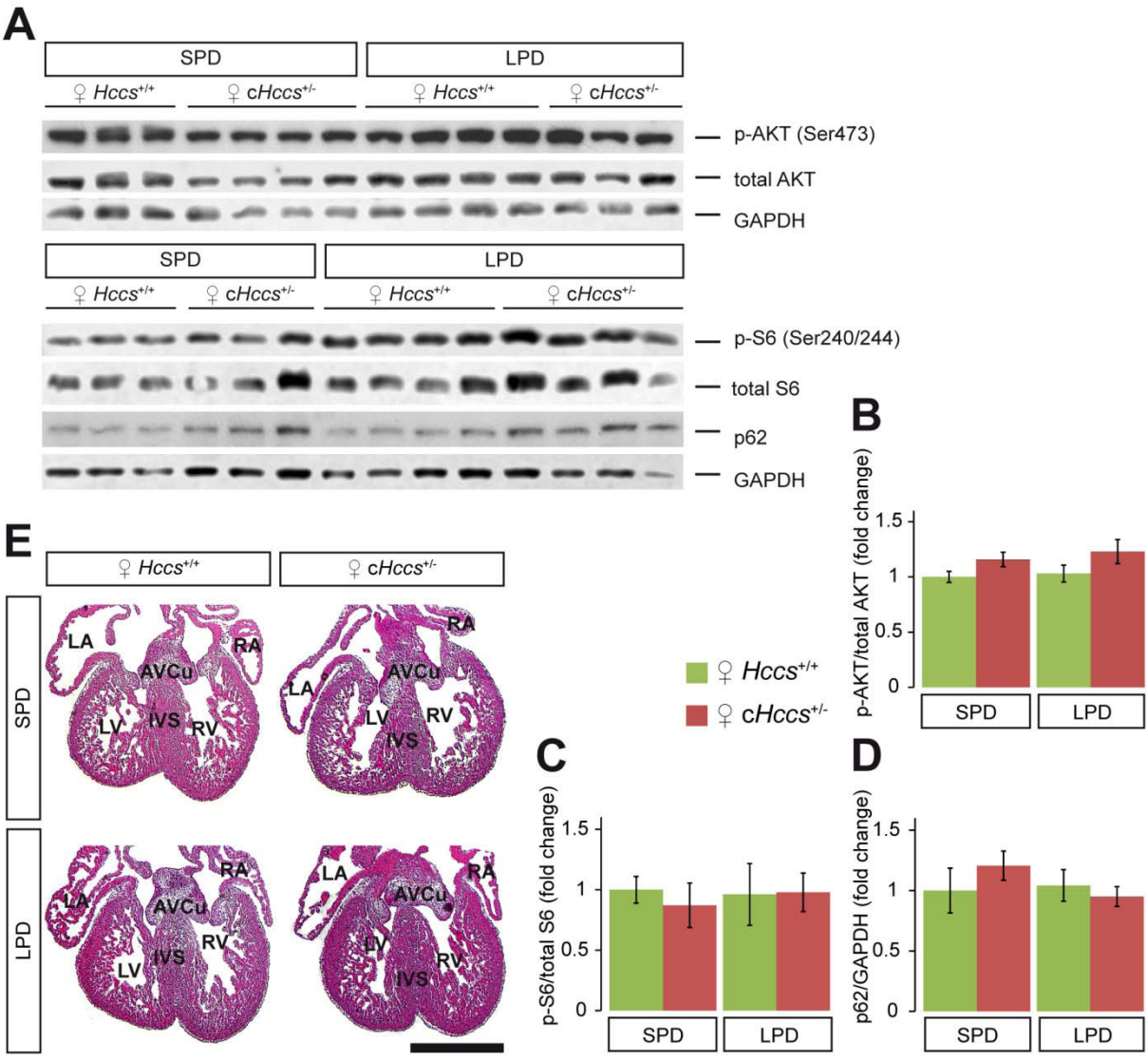

Figure 21. LPD 13.5 dpc hearts demonstrate normal mTOR pathway activity and resemble SPD 13.5 dpc hearts in morphology.
A) Western blots of whole heart protein extracts from 13.5 dpc embryos comparing the phosphorylation status of AKT and S6 as well as total protein levels of p62 between *Hccs*$^{+/+}$ and c*Hccs*$^{+/-}$ mice upon intrauterine SPD or LPD exposure. **B)** Quantification of AKT phosphorylation at serine 473 normalized to total AKT, **C)** S6 phosphorylation at serine 240 and 244 normalized to total S6 and **D)** p62 protein levels normalized to GAPDH revealed no significant differences between the genotypes or the diet groups, indicating that prenatal amino acid restriction neither affects mTOR pathway activity nor the regulation of autophagy in 13.5 dpc embryonic hearts (n=6 for SPD *Hccs*$^{+/+}$, n=6/7 for SPD c*Hccs*$^{+/-}$, n=8 LPD *Hccs*$^{+/+}$, n=7 for LPD c*Hccs*$^{+/-}$). Statistical significance among groups was assessed by one-way ANOVA followed by Bonferroni post-hoc test. **E)** Longitudinal H&E-stained sections of 13.5 dpc embryonic hearts from SPD *Hccs*$^{+/+}$ and c*Hccs*$^{+/-}$ mice were compared with those exposed to intrauterine amino acid restriction. No major morphological changes in overall organ size, atria and ventricular wall thickness, ventricle trabeculation or atrioventricular cushions (AVCu) were observed (scale bar = 600 µM, IVS: interventricular septum, LA: left atrium, LV: left ventricle, RA: right atrium, RV: right ventricle).

6.5.4.2 Prenatal amino acid restriction neither affects apoptosis nor proliferation rates but does alter the expression of cell cycle regulating genes in 13.5 dpc embryonic hearts

It was speculated that the reduced HW/BW ratio in neonatal protein restricted c*Hccs*$^{+/-}$ mice might be caused by a lower cardiomyocyte number due to a reduced proliferative capacity or increased apoptosis rates of cardiomyocytes (and potentially other cell types) during intrauterine development. This hypothesis is in line with studies in newborn LPD rats, which revealed a significantly reduced cardiomyocyte number compared to SPD conditions[23]. Thus,

in the study on hand proliferation in the 13.5 dpc ventricular myocardium was analyzed by immunostaining for histone H3 phosphorylation at serine 10 (p-HH3) (Figure 22A), which marks mitotic cells[218]. Thereby, 13.5 dpc heart sections of *Hccs*$^{+/+}$ and c*Hccs*$^{+/-}$ mice upon intrauterine SPD and LPD exposure were used. At this developmental stage, hyperproliferation of healthy cells is most prominent while at the same time sufficient *Hccs*-deficient cells can be detected[192]. This allows differentiated analyses of proliferation rates in healthy and *Hccs*-deficient cells, respectively.

As described (see Chapter 3.4), under SPD conditions, the functional loss of 50 % cardiac cells in c*Hccs*$^{+/-}$ hearts at mid-gestation (10.5 dpc) is compensated via hyperproliferation of the remaining healthy cardiomyocyte population during the second half of gestation[192]. Thus, for 13.5 dpc c*Hccs*$^{+/-}$ hearts, the proliferation rate was investigated separately for each of the two cell populations within the ventricular myocardium (*Hccs*-positive and *Hccs*-negative) by co-staining for cytochrome (CYT) *c* (Figure 22A). In 13.5 dpc embryonic *Hccs*$^{+/+}$ control hearts, all cardiac cells are normal and hence appear CYT *c*-positive as indicated by the green mitochondrial staining (Figure 22A). In contrast, in 13.5 dpc embryonic c*Hccs*$^{+/-}$ hearts, approximately 30 % cardiac cells are *Hccs*-deficient, thus appear negative for CYT *c* staining, while 70 % cardiac cells are normal and hence appear positive for CYT *c*[192] (Figure 22A). Quantification of p-HH3-positive cells within the ventricular myocardium revealed that the compensatory hyperproliferation of *Hccs*-positive cells in 13.5 dpc embryonic c*Hccs*$^{+/-}$ hearts was still detectable in the corresponding LPD animals (1.25±0.11 % for SPD healthy cells, 0.41±0.05 % for SPD *Hccs*-deficient cells, 1.52±0.16 % for LPD healthy cells, 0.36±0.06 % for LPD *Hccs*-deficient cells) (p<0.01 for all comparisons within one treatment group) (Figure 22B). Importantly, not only is increased proliferation of healthy cells maintained upon intrauterine LPD exposure but also are the absolute values not different between both conditions (Figure 22B). Besides, the decreased proliferative capacity of *Hccs*-deficient cells was also not affected by prenatal amino acid restriction (Figure 22B). Thus, the cell populations contributing to the growth of the embryonic c*Hccs*$^{+/-}$ heart are not changed after exposure to intrauterine amino acid restriction. Proliferation rates in 13.5 dpc LPD *Hccs*$^{+/+}$ control hearts also remain unchanged compared to SPD (0.75±0.06 % for SPD *Hccs*$^{+/+}$, 0.77±0.08 % for LPD *Hccs*$^{+/+}$) (Figure 22B). In summary, no major changes in proliferation at 13.5 dpc can be put forward to explain the reduced HW/BW ratio in neonatal c*Hccs*$^{+/-}$ hearts. Furthermore, our data indicate that LPD does not affect proliferation rates in the embryonic heart, not even if compensatory hyperproliferation is demanded to restore tissue homeostasis.

Even though no differences in proliferation rates were detected in 13.5 dpc embryonic hearts (Figure 22B), intrauterine amino acid restriction might cause changes in the expression pattern of cell cycle regulating genes (e.g. reduced expression of cell cycle

promoting cyclins or increased expression of cell cycle inhibitors), which do not necessarily manifest in proliferation differences at that stage. Hence, the expression of genes involved in cell cycle regulation was investigated by qPCR in 13.5 dpc embryonic hearts. Progression through the different cell cycle phases is tightly controlled by the internal signaling system, which consists of cell cycle promoting cyclins (CCNs), their associated kinases (CDKs) and CDK inhibitors[228-230]. The expression of three cell cycle activators (*Ccnb1* (*cyclin B1*), *Ccnd1* (*cyclin D1*) and *Ccng1* (*cyclin G1*)) as well as of two cell cycle inhibitors (*Cdkn1a* (*p21*) and *Cdkn1b* (*p27*)) was analyzed. CCNB1 is involved in the entry to and transition through M phase of the cell cycle, while D-type cyclins (e.g. CCND1) drive G1/S phase transition[231]. In contrast, CCNG1 has been linked to both positive and negative regulation of cell cycle progression and growth[232] and a putative role in G2/M checkpoint control was suggested[233]. Expression of *Ccng1* is furthermore induced by DNA damage in a p53-dependent manner[234]. The analyzed CDK inhibitors CDKN1A and CDKN1B cause cell cycle arrest in the G1 phase[235-238]. Importantly, CDKN1A and CDKN1B mRNA and protein levels increase in response to amino acid deprivation[239]. In this study, *Ccnb1* expression was not significantly different between the treatment groups or the genotypes (Figure 22C). In *Hccs*$^{+/+}$ hearts the mRNA level of *Ccnd1* was significantly decreased when animals undergo amino acid restriction (p<0.001) (Figure 22C). In addition, for SPD but not LPD animals, there was a slight yet significant decrease in *Ccnd1* expression in c*Hccs*$^{+/-}$ hearts when compared to healthy controls (p<0.05) (Figure 22C). *Ccng1* expression was upregulated by 2.49±0.22-fold in embryonic c*Hccs*$^{+/-}$ hearts and by 1.77±0.64-fold in embryonic *Hccs*$^{+/+}$ control hearts on LPD compared to SPD (p<0.01) (Figure 22C). No significant differences between the genotypes within the treatment groups were observed for *Ccng1* (Figure 22C). Interestingly, CCNG1 fulfills cell cycle inhibitory functions in the heart, where it is involved in prenatal cardiomyocyte cell cycle arrest and binucleation[240]. Hence, it behaves differently compared to the D-type cyclins, such as CCND1, but similar to the cell cycle inhibitor CDKN1B. The expression of the CDK inhibitor *Cdkn1b* remained unchanged between the genotypes (Figure 22C). However, both embryonic c*Hccs*$^{+/-}$ (p<0.05) and *Hccs*$^{+/+}$ hearts (p<0.01) demonstrated increased *Cdkn1b* expression when compared to their respective SPD control groups (Figure 22C). This suggests that whilst *Cdkn1b* expression was not affected by *Hccs*-deficiency, prenatal amino acid restriction resulted in an increased *Cdkn1b* expression in the embryonic 13.5 dpc hearts. Focusing on the CDK inhibitor CDKN1A in SPD 13.5 dpc embryonic hearts, its expression was not affected by prenatal amino acid restriction, but does exhibit an increased expression during embryonic heart regeneration in c*Hccs*$^{+/-}$ embryos (p<0.001) (Figure 22C). This increase was also apparent in the microarray results from previous studies (unpublished data) and might be associated with cell cycle arrest of *Hccs*-deficient cardiomyocytes (see Chapter 3.4).

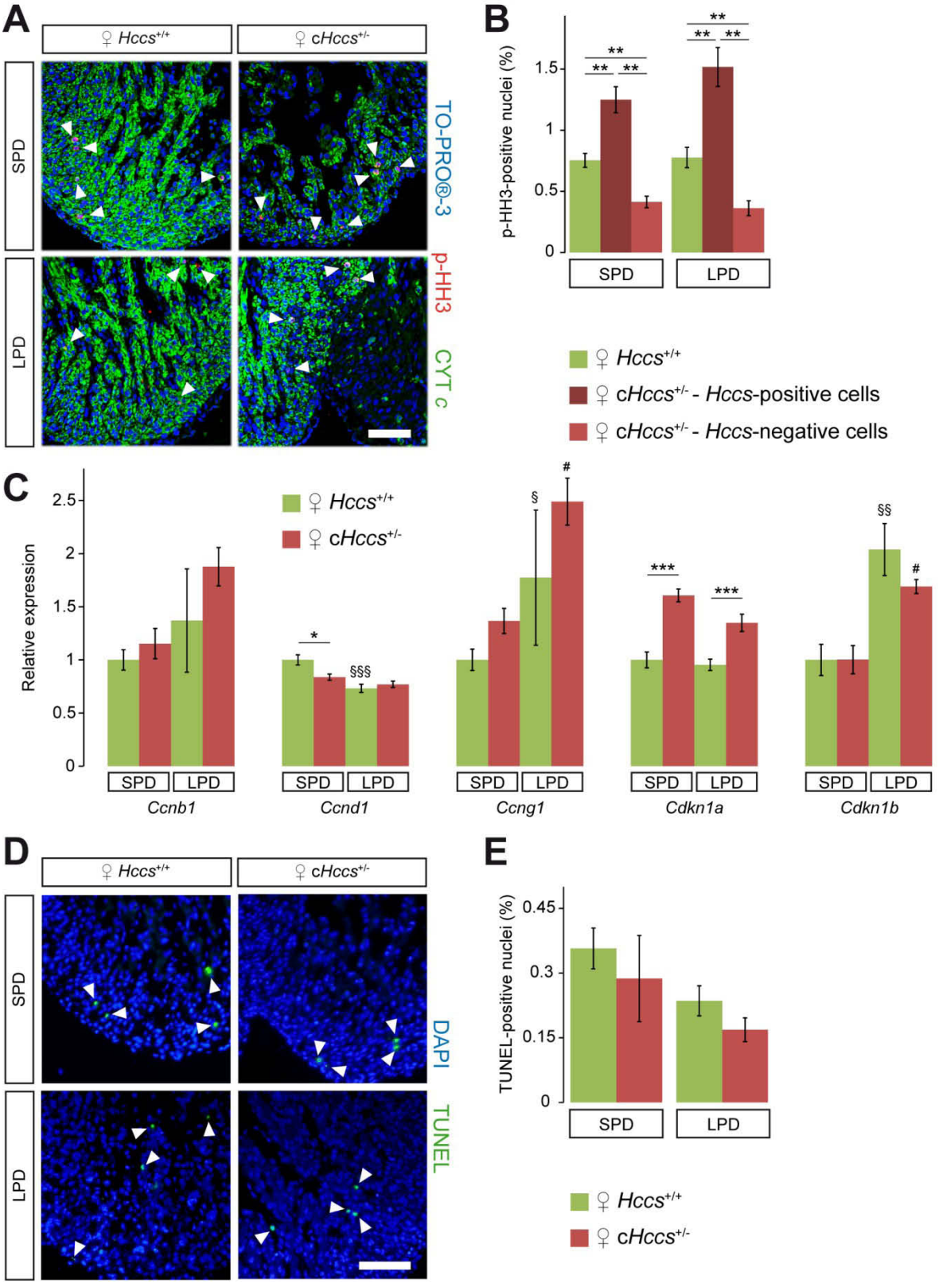

Figure 22. Prenatal amino acid restriction neither induces apoptosis nor reduces proliferation but does affect the expression of cell cycle regulating genes in 13.5 dpc embryonic hearts.
A) Immunofluorescence images of phospho-histone H3 protein (p-HH3)-labeled nuclei (red) within the ventricular myocardium of 13.5 dpc *Hccs*$^{+/+}$ and c*Hccs*$^{+/-}$ hearts exposed to SPD or LPD intrauterine conditions. Co-staining with cytochrome (CYT) *c* allows identification of healthy cells within the c*Hccs*$^{+/-}$ myocardium by green mitochondrial staining. *Hccs*-deficient cells appear negative for CYT *c* staining. Nuclei were stained in blue with TO-PRO®-3. Cycling cardiac cells exhibit colocalization of TO-PRO®-3 and p-HH3 (arrowheads) (confocal microscopy, scale bar = 75 µm). **B)** Quantification of p-HH3-positive nuclei revealed unchanged cell cycle activity within the ventricular myocardium of embryonic SPD and LPD hearts. Note that previously reported hyperproliferation of healthy cells within the embryonic SPD c*Hccs*$^{+/-}$ myocardium persisted in LPD embryonic hearts, indicating that prenatal amino acid restriction neither affects proliferation rates of distinct cell populations within the embryonic c*Hccs*$^{+/-}$ myocardium nor alters cardiac proliferation in *Hccs*$^{+/+}$ controls. Statistical significance among groups was assessed

using Kruskal-Wallis one-way analysis of variance followed by Mann-Whitney post-hoc test (**p<0.01, n=7 for SPD *Hccs*$^{+/+}$, n=6 for SPD and LPD c*Hccs*$^{+/-}$, n=5 for LPD *Hccs*$^{+/+}$). **C)** Relative expression of the cell cycle regulators C*cnb1*, *d1* and *g1* and of the cell cycle inhibitors *Cdkn1a* and *Cdkn1b* in embryonic 13.5 dpc hearts upon intrauterine SPD or LPD exposure were determined by qPCR (n=6 or 7 for SPD *Hccs*$^{+/+}$, n=7 for SPD c*Hccs*$^{+/-}$, n=8 LPD *Hccs*$^{+/+}$, n=6 for LPD c*Hccs*$^{+/-}$). **D)** Fluorescence terminal deoxynucleotidyl transferase dUTP nick end labeling (TUNEL) stainings within the ventricular myocardium of SPD and LPD 13.5 dpc hearts. Nuclei were stained in blue with DAPI. Apoptotic cells were labeled with TUNEL in green. Cells in apoptosis exhibit colocalization of DAPI and TUNEL (arrowheads) (scale bar = 100 µM). **E)** Quantification of TUNEL-positive nuclei revealed no significant differences in programmed cell death between genotypes and treatment groups (n=6 per group). For **C)**+**E)**: Statistical significance among groups was assessed by one-way ANOVA followed by Bonferroni post-hoc test (*p<0.05, ***p<0.001, §p<0.05 vs. SPD *Hccs*$^{+/+}$, §§p<0.01 vs. SPD *Hccs*$^{+/+}$, §§§p<0.001 vs. SPD *Hccs*$^{+/+}$, #p<0.05 vs. SPD c*Hccs*$^{+/-}$). (*Ccnb1*: cyclin B1 gene, *Ccnd1*: cyclin D1 gene, *Ccng1*: cyclin G1 gene, *Cdkn1a*: cyclin-dependent kinase inhibitor 1A gene, *Cdkn1b*: cyclin-dependent kinase inhibitor 1B gene)

Various cyclins and cell cycle inhibitors within embryonic c*Hccs*$^{+/-}$ or *Hccs*$^{+/+}$ control hearts did not show consistent or homogenous expression patterns (Figure 22C), which only allows limited conclusions about cell cycle regulation in impaired or normal cardiac growth after exposure to maternal amino acid restriction. Thus, the initial hypothesis (prenatal amino acid restriction reduces expression of cell cycle promoting cyclins and increases expression of cell cycle inhibitors thereby potentially impairing cardiac proliferation) could certainly not be confirmed. This is in accordance with unchanged proliferation rates in 13.5 dpc embryonic hearts (Figure 22B). Taken together, downregulation of CCND1 as well as upregulation of CCNG1 and CDKN1B could point toward cell cycle delay or inhibition in 13.5 dpc hearts. Considering the complexity of cell cycle regulation and the multitude of control mechanisms, the functional significance of these differentially regulated genes remains yet to be determined.

Given that 13.5 dpc c*Hccs*$^{+/-}$ hearts are still composed of approximately 30 % *Hccs*-deficient cells[192], increased amino acid availability and protein homeostasis might be essential to prevent those cells from undergoing apoptosis. Thus, reduced HW/BW ratio in neonatal LPD c*Hccs*$^{+/-}$ hearts might result from increased apoptosis rates in 13.5 dpc embryonic hearts. Cells undergoing apoptosis were scored by DNA fragmentation evident as positive TUNEL staining (Figure 22D). Quantification of TUNEL-positive cells within the ventricular myocardium of embryonic 13.5 dpc hearts revealed no significant differences between the genotypes or the treatment groups (0.36±0.05 % for SPD *Hccs*$^{+/+}$, 0.29±0.10 % for SPD c*Hccs*$^{+/-}$, 0.24±0.03 % for LPD *Hccs*$^{+/+}$, 0.17±0.03 % for LPD c*Hccs*$^{+/-}$) (Figure 22E). Surprisingly, rather a slight trend toward reduced apoptosis was suggested upon LPD (Figure 22E). Hence, we excluded the possibility that increased apoptosis causes reduced cell number in 13.5 dpc c*Hccs*$^{+/-}$ LPD hearts and thus explains the reduced HW/BW ratio in neonatal c*Hccs*$^{+/-}$ hearts.

In summary, analyses of embryonic 13.5 dpc c*Hccs*$^{+/-}$ hearts upon prenatal amino acid restriction did not confirm our hypothesis regarding cell number reduction. Neither decreased proliferation nor increased apoptosis rates were revealed. Thus, the underlying molecular and cellular mechanisms responsible for the reduced HW/BW ratio in neonatal c*Hccs*$^{+/-}$ hearts upon intrauterine amino acid restriction remain to be investigated and may be found in

later fetal stages. Generally, our data demonstrate for the first time that intrauterine LPD does not impair proliferation or induce apoptosis in 13.5 dpc hearts. Hence, the embryonic murine heart appears to be surprisingly resistant to intrauterine amino acid restriction. These findings suggest that the fetal stage might be the more vulnerable phase during development, which might have major implications in the context of IUGR and developmental programming.

6.5.5 Consequences of combined pre- and postnatal amino acid restriction for adult hearts

In well-established IUGR models (see Chapter 3.2.2), the IUGR insult is normally released at birth, which for instance causes normalization of heart size until weaning in LPD rats[25]. However, postnatal catch-up growth is known to additionally promote the manifestation of adulthood disease following IUGR and developmental programming[15,16]. In this context, we aimed at investigating in which way postnatal conditions that resemble that of *in utero* affect cardiac growth and function in adulthood. Furthermore, we were eager to analyze if c*Hccs*$^{+/-}$ hearts are particularly affected by postnatal amino acid restriction when compared to controls and if the reduced HW/BW ratio seen in newborn LPD c*Hccs*$^{+/-}$ mice can be normalized during adulthood. To address these questions, long-term LPD studies were performed and offspring exposed to intrauterine LPD were postnatally kept on LPD and analyzed at the age of 11 weeks.

6.5.5.1 Pre- and postnatal amino acid restriction does neither affect mTOR pathway activity nor cardiac morphology and size of adult hearts

Analyses of the activity status of the mTOR signaling cascade in embryonic 13.5 dpc hearts revealed no effect of prenatal amino acid restriction (see Chapter 6.5.4.1, Figure 21A-D). However, prolonged amino acid restriction during pre- and postnatal development might impact on mTOR pathway activity in adulthood. To analyze this hypothesis, western blot analyses were performed with heart protein extracts from 11 week old adult animals after both normal and pre- and postnatal SPD or LPD exposure (Figure 23A). To this extend, the phosphorylation status of the mTORC1 upstream and mTORC2 downstream target AKT at serine 473 and of the mTORC1 downstream target S6 at serine 235, 236, 240 and 244 was investigated (Figure 23A-D). Additionally, protein levels of the autophagy marker p62 were quantified and normalized to GAPDH protein levels (Figure 23A+E). No significant differences were apparent in any of the analyzed upstream or downstream mTOR pathway components when comparing all four groups (Figure 23B-E), indicating that mTOR pathway activity in adult hearts was not affected by pre- and postnatal LPD treatment.

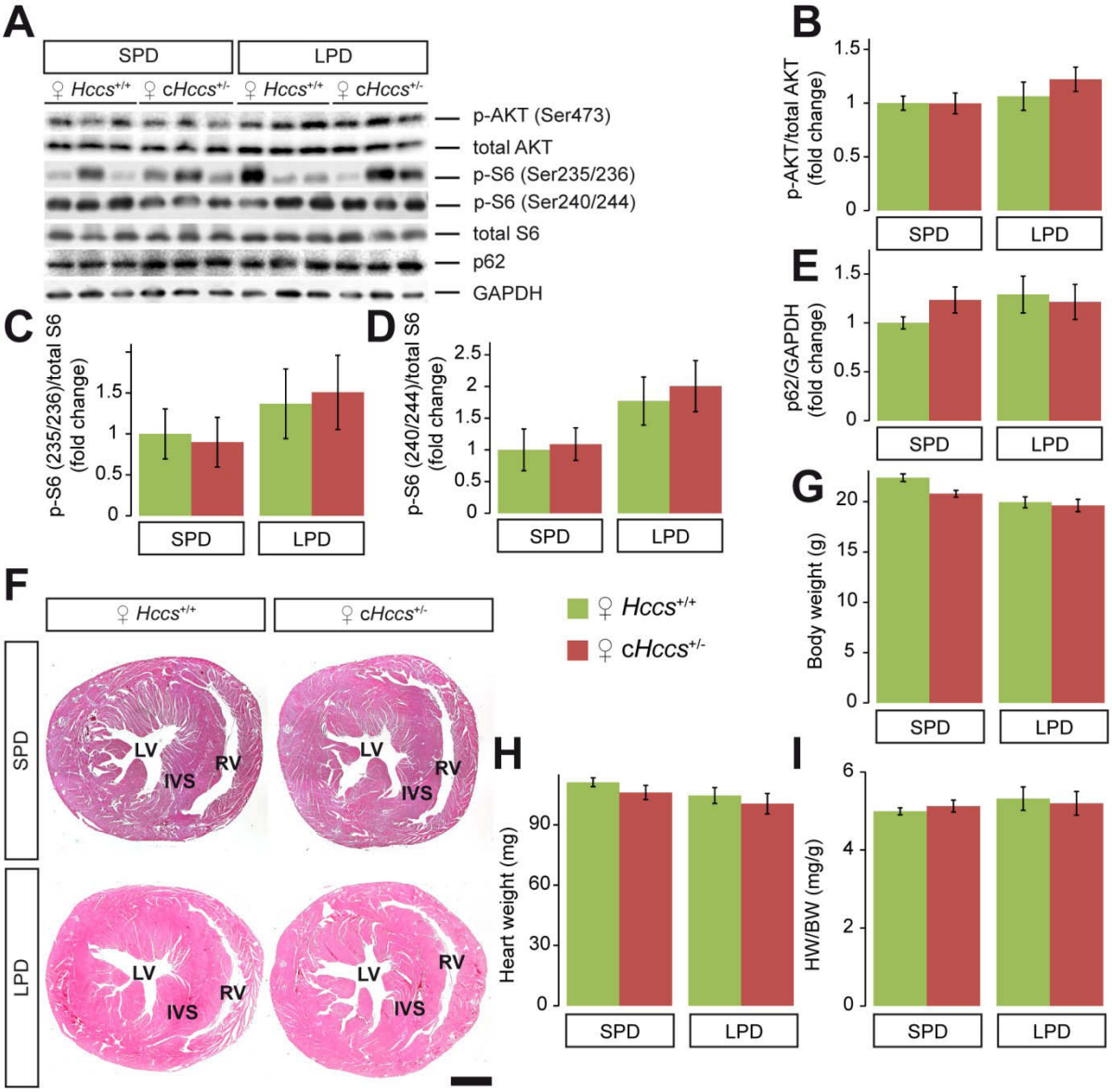

Figure 23. Pre- and postnatal amino acid restriction neither alters mTOR pathway activity nor causes overall growth retardation or heart size reduction in 11 week old adult mice.
A) Western blots of heart protein extracts from adult mice comparing the phosphorylation status of AKT and S6 as well as the total protein level of p62 between *Hccs*$^{+/+}$ and c*Hccs*$^{+/-}$ animals after pre- and postnatal SPD or LPD exposure. **B)** Quantification of AKT phosphorylation at serine 473 normalized to total Akt, **C)**+**D)** S6 phosphorylation at serine 235, 236, 240 and 244 normalized to total S6 and **E)** p62 protein levels normalized to GAPDH revealed no significant differences between the genotypes or the diet groups, indicating that pre- and postnatal amino acid restriction does not affect mTOR pathway activity or the regulation of autophagy in adult hearts. **F)** H&E-stained cross-sections of adult hearts from SPD *Hccs*$^{+/+}$ and c*Hccs*$^{+/-}$ mice were compared with those exposed to pre- and postnatal amino acid restriction. No major morphological changes within the left ventricle (LV), interventricular septum (IVS) or right ventricle (RV) were observed in neither *Hccs*$^{+/+}$ control nor c*Hccs*$^{+/-}$ hearts (scale bar = 1 mm). **G)** No significant differences in body weight (BW) between the genotypes or the treatment groups were determined in adult mice. **H)** Heart weight (HW) was not affected by pre- and postnatal amino acid restriction. **I)** Analysis of the HW to BW (HW/BW) ratio in adult animals revealed no significant differences between the treatment groups or the genotypes. Note that the reduced HW/BW ratio observed in neonatal LPD c*Hccs*$^{+/-}$ mice was no longer obvious in adult c*Hccs*$^{+/-}$ animals. For **G)**-**I)**: n=9 for SPD *Hccs*$^{+/+}$, SPD c*Hccs*$^{+/-}$ and LPD *Hccs*$^{+/+}$, n=13 for LPD c*Hccs*$^{+/-}$. For **B)**-**E)**: n=7 for SPD *Hccs*$^{+/+}$and c*Hccs*$^{+/-}$, n=3 or 6 for LPD *Hccs*$^{+/+}$ and c*Hccs*$^{+/-}$. For **B)**-**E)**+**G)**-**I)**: Statistical significance among groups was assessed by one-way ANOVA followed by Bonferroni post-hoc test.

As described, postnatal cardiac growth in mammals is mainly achieved by cardiomyocyte hypertrophy (see Chapter 3.3.3), a process that requires sufficient protein synthesis and mTOR pathway activity. It is therefore possible that amino acid restriction might negatively impact on protein biosynthesis, consequently impairing postnatal heart growth. H&E-stained heart cross-sections from adult SPD and LPD mice revealed no major histological, structural

or pathological abnormalities between the genotypes or the treatment groups (Figure 23F). Besides, BW, HW as well as HW/BW ratio in adult SPD and LPD mice were measured (Figure 23G-I). Pre- and postnatal LPD neither affects BW (22.29±0.38 g for SPD *Hccs*$^{+/+}$, 20.70±0.33 g for SPD c*Hccs*$^{+/-}$, 19.85±0.54 g for LPD *Hccs*$^{+/+}$, 19.53±0.61 g for LPD c*Hccs*$^{+/-}$), or HW (111.20±2.17 mg for SPD *Hccs*$^{+/+}$, 106.12±3.54 mg for SPD c*Hccs*$^{+/-}$, 104.64±4.00 mg for LPD *Hccs*$^{+/+}$, 100.54±5.07 mg for LPD c*Hccs*$^{+/-}$) nor the HW/BW ratio (4.99±0.09 mg/g for SPD *Hccs*$^{+/+}$, 5.13±0.15 mg/g for SPD c*Hccs*$^{+/-}$, 5.32±0.30 mg/g for LPD *Hccs*$^{+/+}$, 5.20±0.30 mg/g for LPD c*Hccs*$^{+/-}$) in adulthood (Figure 23G-I). This indicates that amino acid restriction does not affect postnatal heart growth on the organ level. Furthermore, the reduced HW/BW ratio observed in neonatal LPD c*Hccs*$^{+/-}$ mice (see Chapter 6.5.3.1, Figure 19D) was no longer obvious in adult LPD animals (Figure 23I). Thus, postnatal compensatory growth of c*Hccs*$^{+/-}$ hearts is not primarily dependent on amino acid availability.

6.5.5.2 Pre- and postnatal amino acid restriction reduces cardiomyocyte size without inducing fibrosis in adult hearts

Although long-term LPD does not seem to affect cardiac organ size in adulthood, we were still interested whether it has an impact on the cellular level or changes tissue composition. Cardiomyocytes in neonatal hearts upon intrauterine amino acid restriction demonstrated increased CSA compared to SPD conditions (see Chapter 6.5.3.2, Figure 20D). To evaluate whether this increased cell size is maintained until adulthood, it was investigated how cardiomyocyte size develops during postnatal life if amino acid restriction persists. Therefore, cardiomyocyte CSA was measured in the LV myocardium of adult hearts after pre- and postnatal SPD and LPD exposure on WGA-stained heart sections (Figure 24A). Interestingly, cardiomyocytes of adult LPD hearts were found to be significantly smaller (213.9±6.50 µm^2 for LPD *Hccs*$^{+/+}$ (p<0.01), 249.2±18.96 µm^2 for LPD c*Hccs*$^{+/-}$ (p<0.05)) compared to their corresponding SPD counterparts (286.0±10.68 µm^2 for SPD *Hccs*$^{+/+}$, 303.8±9.61 µm^2 for SPD c*Hccs*$^{+/-}$) (Figure 24C). However, compensatory postnatal cardiac hypertrophy in c*Hccs*$^{+/-}$ females compared to controls, a major hallmark of the heart conditional *Hccs* KO model (see Chapter 3.4), persists after LPD exposure, even though it missed statistical significance for both diet groups in this study (Figure 24C). These findings indicate that amino acid restriction affects cardiomyocyte size in both genotypes in adulthood but does not specifically impair compensatory postnatal hypertrophy in c*Hccs*$^{+/-}$ mice. Importantly, however, these findings contradict the HW and cardiac organ size data (see Chapter 6.5.5.1, Figure 23F+H), since reduced cardiomyocyte CSA should be represented by a reduced HW.

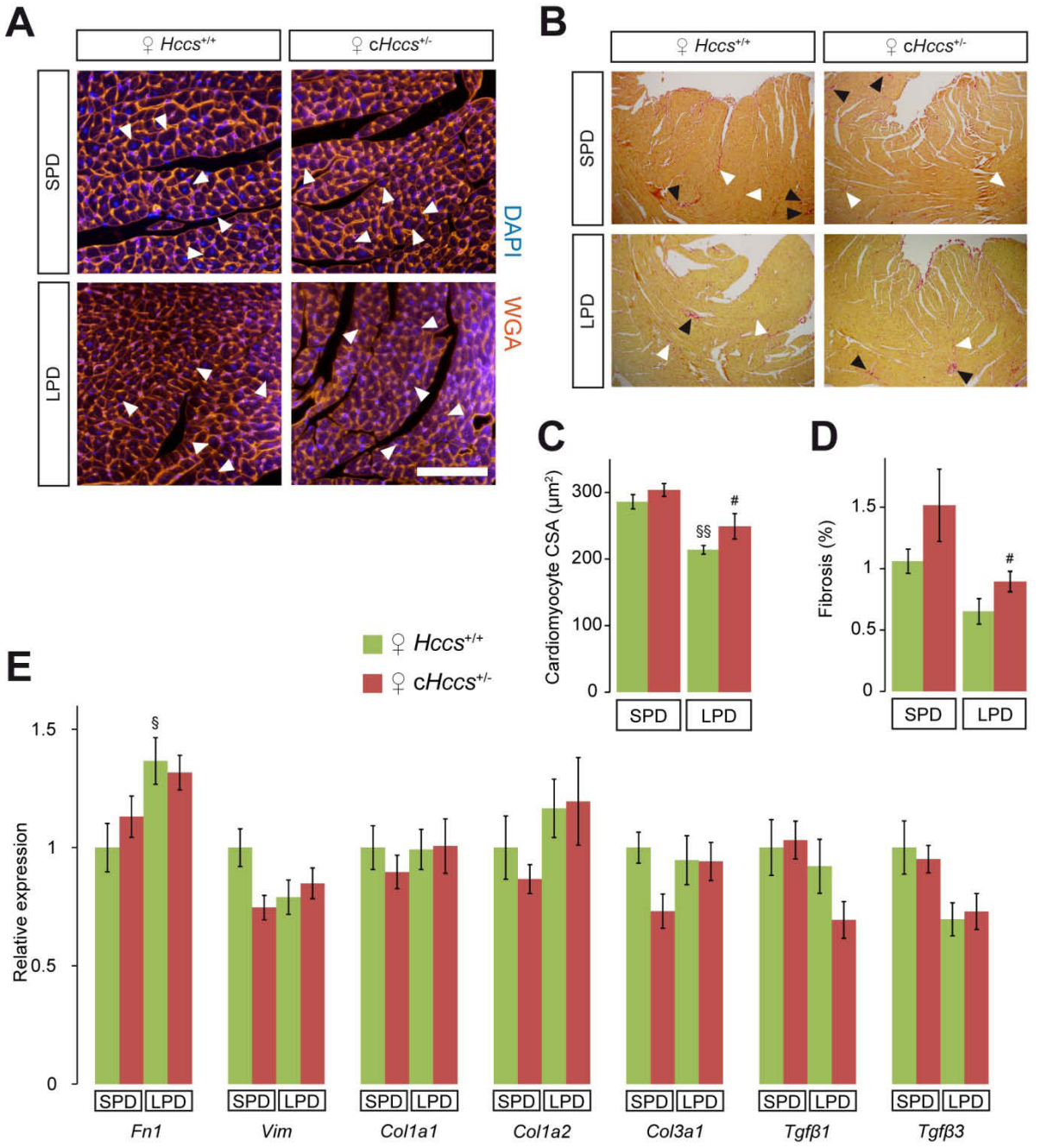

Figure 24. Pre- and postnatal amino acid restriction results in reduced cardiomyocyte size but does not induce compensatory fibrosis in 11 week old adult hearts.
A) Fluorescence images of cross-sectioned cardiomyocytes within the left ventricular (LV) myocardium of hearts from SPD and LPD treated adult animals. Cardiomyocyte membranes were stained in orange with wheat germ agglutinin (WGA) and nuclei in blue with DAPI. Only cardiomyocytes that matched the defined measurement criteria were analyzed (arrowheads) (scale bar = 100 µm). **B)** Random images of the LV myocardium of Sirius red stained heart cross-sections of adult mice after pre- and postnatal SPD or LPD treatment, respectively, demonstrate only minor collagen deposition in all four groups. White arrowheads highlight the red appearance of fine threads of interstitial collagen. Black arrowheads highlight perivascular fibrosis, which was excluded for quantification (scale bar = 300 µm). **C)** Average cardiomyocyte cross sectional area (CSA) revealed significantly smaller cardiomyocytes in mice exposed to pre- and postnatal amino acid restriction. Note that compensatory cardiomyocyte hypertrophy in c*Hccs*$^{+/-}$ compared to *Hccs*$^{+/+}$ mice persists in adult LPD animals, even though it misses statistical significance. Statistical significance among groups was assessed using Kruskal-Wallis one-way analysis of variance followed by Mann-Whitney post-hoc test (§§ p<0.01 vs. SPD *Hccs*$^{+/+}$, #p<0.05 vs. SPD c*Hccs*$^{+/-}$, n=6 for SPD *Hccs*$^{+/+}$, SPD c*Hccs*$^{+/-}$ and LPD c*Hccs*$^{+/-}$, n=4 for LPD *Hccs*$^{+/+}$). **D)** Quantification of fibrotic cardiac tissue within the LV myocardium of SPD and LPD adult mice did not reveal differences in collagen deposition in LPD treated hearts, indicating that pre- and postnatal LPD exposure does not induce LV interstitial fibrosis in adult mice (n=4 per SPD group, n=6 per LPD group). **E)** Relative *fibronectin 1* (*Fn1*), *vimentin* (*Vim*), *collagen type I alpha 1/2* and *type III alpha 1* (*Col1a1*, *Col1a2*, *Col3a1*), *transforming growth factor-β 1* (*Tgfβ1*) and *3* (*Tgfβ3b*) mRNA levels in adult hearts after pre- and postnatal SPD or LPD exposure were determined using qPCR. No differential expression was observed in LPD groups compared to SPD groups or between the genotypes (n=7 for all groups). For **D)**+**E)**: Statistical significance among groups was assessed by one-way ANOVA followed by Bonferroni post-hoc test (§p<0.05 vs. SPD *Hccs*$^{+/+}$, #p<0.05 vs. SPD c*Hccs*$^{+/-}$).

It was speculated that an increase in extracellular matrix deposition within the myocardium after pre- and postnatal amino acid restriction compensates for the reduced cell size in adulthood, thereby resulting in normal HW. The percentage of interstitial fibrosis within the LV myocardium of adult mice was investigated by Sirius red staining (Figure 24B). Quantification of collagen deposition did not reveal differences between the genotypes and no evidence for induction of interstitial fibrosis after pre- and postnatal LPD exposure was obvious (1.06±0.10 % for SPD *Hccs*$^{+/+}$, 1.52±0.30 % for SPD c*Hccs*$^{+/-}$, 0.65±0.10 % for LPD *Hccs*$^{+/+}$, 0.90±0.08 % for LPD c*Hccs*$^{+/-}$) (Figure 24D). Instead, rather a trend toward reduced collagen deposition was demonstrated (Figure 24D). Consequently, accumulation of ECM does not account for the normalization of HW in adult LPD hearts to compensate for the reduced cardiomyocyte size.

Even though Sirius red staining is the standard method to detect fibrosis in pathological settings, it might not be sensitive enough to assess increased ECM deposition in physiological cardiac growth. Hence, cardiac expression of genes that encode for ECM components was investigated in adult hearts after pre- and postnatal LPD exposure compared to SPD treated animals by qPCR analyses (Figure 24E). These ECM components comprised fibronectin 1 (FN1) (a high-molecular weight glycoprotein of the ECM that connects cells with collagen fibers), three different types of collagen (COL1A1, COL1A2, COL3A1) (the most abundant protein of ECM), two different isoforms of the inflammatory mediator transforming growth factor-β (TGFβ1, TGFβ3) as well as vimentin (VIM) (the major cytoskeleton component of mesenchymal cells and a marker for fibroblasts) (Figure 24E). Cardiac expression of all these genes was not significantly different among the genotypes or the different diet groups (Figure 24E), indicating that pre- and postnatal LPD does not change the expression of genes involved in ECM composition, which is in line with the unchanged percentage of fibrotic tissue (Figure 24D). Hence, the molecular and cellular mechanisms that compensate for the reduced cell size and thereby ensure normal HW in LPD adult mice remain to be investigated.

In summary, we revealed that pre- and postnatal LPD exposure reduces cardiomyocyte size but does not alter tissue composition with regard to ECM deposition and fibrosis in adult hearts.

6.5.5.3 Pre- and postnatal amino acid restriction does not cause cardiac dysfunction

Given that cardiac fibrosis is unaltered in adult hearts upon LPD exposure, pathological cardiac remodeling is unlikely. However, investigations on the molecular level might be more sensitive than the detection of fibrosis. Thus, to analyze if pre- and postnatal amino acid restriction causes molecular signs of cardiac stress in adulthood, qPCR expression analysis

of “heart failure marker genes” were performed (Figure 25A) (for gene details see Chapter 6.3.4.2). *Nppb* expression was unchanged between the genotypes and the diet groups (Figure 25A). *Nppa* and *Myh7* expression were slightly increased in adult c*Hccs*$^{+/-}$ SPD hearts compared to SPD controls; even though the difference misses statistical significance (Figure 25A). Besides, the expression of *Nppa* and *Myh7* was significantly decreased comparing adult c*Hccs*$^{+/-}$ LPD with c*Hccs*$^{+/-}$ SPD hearts (p<0.05) (Figure 25A). However, in conclusion, on the molecular level there was no indication for increased cardiac stress imposed by LPD conditions, since the expression of these three “heart failure marker genes” was not significantly increased after pre- and postnatal amino acid restriction compared to SPD.

Cardiomyocyte CSA was found to be reduced in adult hearts (see Chapter 6.5.5.2, Figure 24C), while HW was normal (see Chapter 6.5.5.1, Figure 23H), which represents a contradiction at that point. To investigate overall cardiac morphology in more detail and to measure heart function, echocardiography in adult mice after pre- and postnatal amino acid restriction were performed (Figure 25B-D and Supplementary Table S7). Analysis of end-diastolic LVPW thickness (0.65±0.03 mm for SPD *Hccs*$^{+/+}$, 0.69±0.03 mm for SPD c*Hccs*$^{+/-}$, 0.74±0.02 mm for LPD *Hccs*$^{+/+}$, 0.75±0.05 mm for LPD c*Hccs*$^{+/-}$) (Figure 25B) as well as of end-diastolic LVID (3.96±0.07 mm for SPD *Hccs*$^{+/+}$, 4.01±0.09 mm for SPD c*Hccs*$^{+/-}$, 3.70±0.06 mm for LPD *Hccs*$^{+/+}$, 3.68±0.13 mm for LPD c*Hccs*$^{+/-}$) (Figure 25C) revealed no significant differences between the diet groups and the genotypes, indicating normal overall cardiac morphology and LV wall thickness. These findings are in line with the results obtained from explanted hearts regarding morphology and HW (see Chapter 6.5.5.1, Figure 23F+H). Moreover, analysis of the LV contractile parameters FS (31.03±3.23 % for SPD *Hccs*$^{+/+}$, 27.71±1.90 % for SPD c*Hccs*$^{+/-}$, 29.38±4.56 % for LPD *Hccs*$^{+/+}$, 27.71±4.21 % for LPD c*Hccs*$^{+/-}$) and EF (59.12±4.50 % for SPD *Hccs*$^{+/+}$, 53.09±3.51 % for SPD c*Hccs*$^{+/-}$, 56.23±7.33 % for LPD *Hccs*$^{+/+}$, 53.64±5.31 % for LPD c*Hccs*$^{+/-}$) did not reveal impaired heart function (Figure 25D and Supplementary Table S7). Again, these findings are consistent with unchanged deposition of fibrotic tissue (see Chapter 6.5.5.2, Figure 24D) and normal expression of genes associated with cardiac stress and heart failure (Figure 25E).

In summary, pre- and postnatal amino acid restriction neither induces cardiac stress nor reduces cardiac function in adulthood under baseline conditions, since no indication for pathological responses or remodeling were observed. Furthermore, adult c*Hccs*$^{+/-}$ hearts were not found to be specifically affected by pre- and postnatal amino acid restriction with regard to all the analyzed parameters.

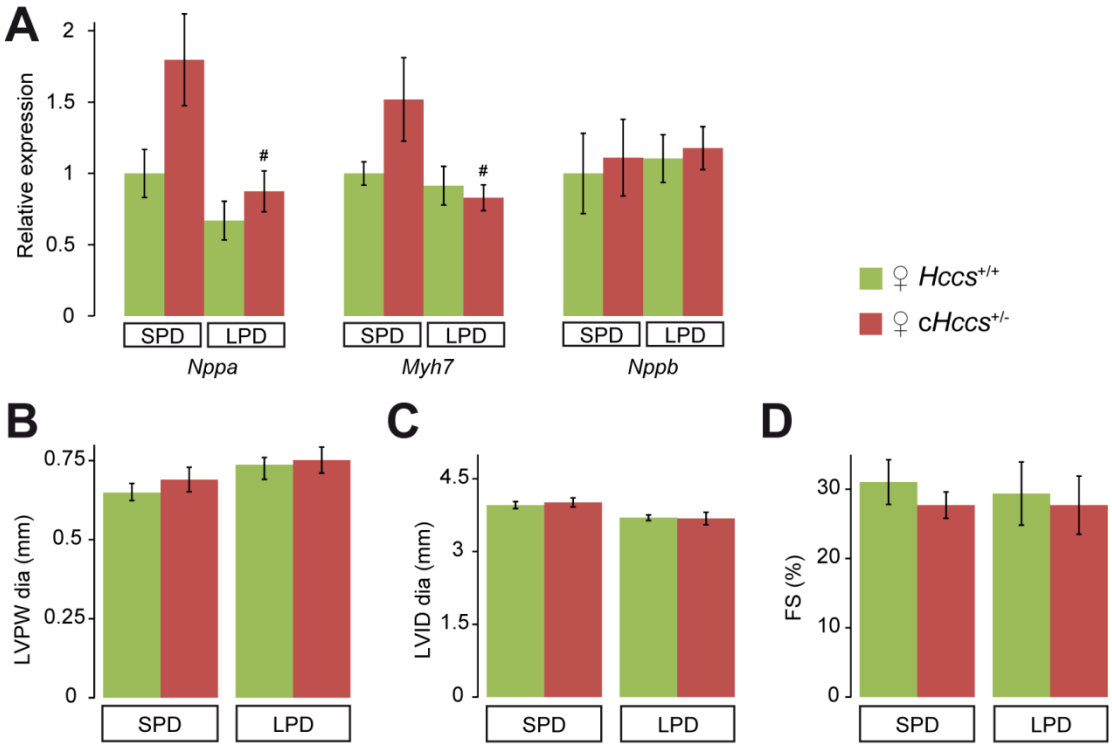

Figure 25. Pre- and postnatal amino acid restriction neither induces the expression of genes associated with cardiac stress nor alters cardiac function in 11 week old adult LPD mice.
A) Relative *natriuretic peptide type A* (*Nppb*), *β-myosin heavy chain 7* (*Myh7*) and *natriuretic peptide type B gene* (*Nppb*) mRNA levels in adult hearts after pre- and postnatal SPD or LPD exposure were determined using qPCR. No significant upregulation of all three heart failure marker genes was observed in LPD groups compared to SPD groups or between the genotypes (n=7 for all groups). **B)** Echocardiographic measurements revealed that left ventricular posterior wall thickness in end-diastole (LVPW dia), **C)** left ventricular internal diameter in end-diastole (LVID dia), as well as **D)** fractional shortening (FS) of the left ventricle are neither different between the genotypes nor the diet groups. Together, these data indicate no difference in overall cardiac morphology and function (n=7 for SPD *Hccs*$^{+/+}$ and LPD c*Hccs*$^{+/-}$, n=6 for SPD c*Hccs*$^{+/-}$ and LPD *Hccs*$^{+/+}$). For **A)**-**D)**: Statistical significance among groups was assessed by one-way ANOVA followed by Bonferroni post-hoc test (#p<0.05 vs. SPD c*Hccs*$^{+/-}$).

7 DISCUSSION

7.1 The role of the mTOR pathway during heart development and consequences of prenatal mTOR pathway inhibition for postnatal health

The mTOR pathway has been implicated in controlling cardiac organ size and regulating physiological and pathological cardiac hypertrophy[58]. On a cellular level, the mTOR signaling cascade is a key sensor of cell nutrition and energy status and acts as master regulator of cell growth, metabolism, proliferation and survival. Even though there is a large body of evidence emphasizing the role of the mTOR pathway in the adult heart, only little is known about its function during prenatal and perinatal cardiac development. Moreover, previous studies suggested that developmental programming affects metabolic processes (reviewed by Barker[18], McMillen and Robinson[19] and Rinaudo and Wang[241]). Given that the mTOR pathway is an important metabolic regulator, it might also be a target of developmental programming mechanisms. Experimental support for this hypothesis comes from studies in fetal lambs, which revealed that intrauterine growth restriction (IUGR) affects the expression of components of the insulin-like growth factor (IGF)-AKT signaling axis (upstream of mTORC1)[242,243]. Interestingly, these changes were proposed to result in cardiac hypertrophy in adulthood[242,243]. However, in these studies it was not analyzed if the observed changes translate into altered mTOR pathway activity at any developmental stage. Importantly, our initial experiments demonstrated increased mTOR pathway activity in neonatal c*Hccs*$^{+/-}$ hearts (see Chapter 6.2, Figure 8). Thus, the aim of the first part of this PhD project was to investigate the role of the mTOR signaling cascade for embryonic cardiac regeneration and postnatal compensatory heart growth of c*Hccs*$^{+/-}$ mice. Furthermore, we aimed at analyzing the general role of the mTOR pathway in the heart during prenatal development as well as in the neonatal period. To address these questions, we successfully inhibited mTORC1 by rapamycin injections in pregnant dams during the last trimester of prenatal development (fetal phase) (see Chapter 6.3.1, Figure 9).

7.1.1 Rapamycin injection in pregnant dams specifically inhibits mTORC1 but not mTORC2 in the offspring heart

The MTOR protein forms the catalytic subunit of the two multiprotein complexes mTORC1 and mTORC2 (see Chapter 3.3.4, Table 1). mTORC1 is a physiological target of the macrolipid rapamycin (see Chapter 3.3.4.1, Figure 5), which induces its inhibition[157,158]. Rapamycin associates with a cellular protein called FKBP12, and this complex binds MTOR adjacent to its kinase domain in the FKBP12-rapamycin-binding (FRB) region leading to allosteric inhibition of MTOR[157,159,244,245]. Although the mechanism by which rapamycin

inhibits mTORC1 remains incompletely understood, rapamycin weakens the interaction between MTOR and RAPTOR[246] and thus reduces mTORC1 intrinsic kinase activity[247].
Despite the fact that rapamycin is generally considered to be a specific inhibitor of mTORC1, cell culture experiments revealed that high-dose and long-term treatment with rapamycin reduces mTORC2 signaling in certain cell types by also impeding mTORC2 assembly[222,248]. Furthermore, recent *in vivo* studies demonstrated that daily rapamycin treatment over a period of 2 to 4 weeks in adult mice (intraperitoneal (i.p.), 2 mg rapamycin/kg BW) disrupts the association of MTOR with the essential mTORC2 component RICTOR in liver, muscle and white adipose tissue[249]. In line, the results of another study revealed that daily rapamycin injections for 4 weeks in adult mice (i.p., 2 mg rapamycin/kg BW) result in reduced AKT phosphorylation at the mTORC2 phosphorylation site serine 473 in the heart, indicating impaired cardiac mTORC2 activity[185].
Importantly, we demonstrated that prenatal rapamycin treatment does not inhibit mTORC2 activity in neonatal hearts, as evident by unchanged phosphorylation of AKT at serine 473 (see Chapter 6.3.1, Figure 9A+C). In our experimental setup, we subcutaneously (s.c.) injected 5 mg rapamycin/kg BW every 12 hours in pregnant dams from 15.5 dpc until birth, which corresponds to a total of only 4 days. Hence, the fetal and neonatal heart appears to be resistant for mTORC2 inhibition by short-term rapamycin treatment (even though a higher daily rapamycin dose was applied), while the adult heart responds to chronic rapamycin treatment with impaired mTORC2 activity. It is important to stress that i.p. rapamycin injections in adult mice and rapamycin treatment of fetal mice by s.c. injections in pregnant dams, which requires passage of the placental barrier, are fundamentally different approaches. This makes it difficult to compare the mTORC2 activity outcomes. In conclusion, methodological differences, especially different treatment durations, might explain the differences in mTORC2 inhibition between neonatal and adult mice.

7.1.2 Prenatal mTORC1 inhibition by rapamycin is a new model for IUGR in mice

Prenatal mTORC1 inhibition by rapamycin treatment from 15.5 dpc until birth induces profound growth retardation in neonatal mice as evident by a significant reduction of BW, HW and KW (see Chapter 6.3.3.1, Figure 11B+E and Supplementary Figure 3C). These findings are in line with conventional IUGR models, which also demonstrated lower BW and HW in neonates after intrauterine low protein diet (LPD)[23] or placental insufficiency[33]. Importantly, prenatal rapamycin treatment impairs heart growth to a larger extend than intrauterine LPD and placental insufficiency do. Intrauterine LPD was shown to reduce BW by ~ 17 % and HW by ~ 10 % at birth compared to newborn standard protein diet (SPD) rats[23]. Placental insufficiency caused BW and HW reduction in neonatal rats by ~ 16 % and ~ 20 %, respectively[33]. In the study presented here, prenatal rapamycin treatment provoked BW reduction in neonatal mice to a similar extend than observed in the well-established IUGR

models (16.4 % for *Hccs*$^{+/+}$ and 14.5 % for c*Hccs*$^{+/-}$) (see Chapter 6.3.3.1, Figure 11B). However, compared with intrauterine LPD and placental insufficiency, the reduction in neonatal HW was more severe after prenatal rapamycin treatment (34.5 % for *Hccs*$^{+/+}$ and 35.3 % for c*Hccs*$^{+/-}$) (see Chapter 6.3.3.1, Figure 11E).

Developmental programming induced by IUGR is a systemic process, in which multiple changes in different organs interact and influence each other. Even though this allows analyses of organ specific adaptations to growth restriction, classical IUGR models can only be used to a limited extend to study developmental programming mechanisms in one particular organ. This makes developmental programming studies quite complex and explains why only few mechanistic insights have been uncovered to date, although the first papers by Barker *et al*. were published more than 25 years ago[250]. Importantly, even though rapamycin treatment is also a systemic approach that affects the entire organism, we provide evidence that prenatal mTORC1 inhibition (in contrast to the well-established IUGR models) more severely affects heart growth than the development of other organ systems. While HW/BW ratio in neonates after intrauterine LPD is unchanged due to BW and HW reduction to a similar extend[23], in our model neonatal HW/BW ratio is reduced (see Chapter 6.3.3.1, Figure 11F), while KW/BW ratio stays the same (see Supplementary Figure 3D).

Hearts of neonatal mice upon intrauterine mTORC1 inhibition (especially c*Hccs*$^{+/-}$ hearts) exhibit a profound morphological phenotype. They are characterized by severe thinning and noncompaction of the ventricular myocardium, developmental delay and immature myocardial morphology (see Chapter 6.3.3.1, Figure 11D). Given that prenatal rapamycin treatment results in severe growth retardation in neonatal mice (especially within the heart), we suggested that this approach serves as a novel model for IUGR and thus for studying developmental programming mechanisms particularly in the fetal and neonatal phase of cardiac development. IUGR is defined as impaired growth of the unborn organism due to an intrauterine insult that is immediately released after birth (see Chapter 3.2.2). We revealed that mTORC1 signaling fully recovers at postnatal day 3 (P3) (see Chapter 6.3.1, Figure 9E), such that an important prerequisite in comparison to IUGR is met. However, the prenatal rapamycin approach displays crucial differences compared to well-established IUGR models. LPD and placental insufficiency normally persist throughout gestation[23,33], whereas rapamycin treatment affects only the final trimester. Hence, every developmental programming occurring before the injection period was initiated (15.5 dpc) will be missed. When we initiated rapamycin treatment from 11.5 dpc onwards, we observed preterm birth and demonstrated severe growth retardation and body malformations (see Chapter 6.3.1 and Supplementary Figure 4). Thus, adjusting the rapamycin treatment protocol, e.g. reducing the dose or the injection intervals, might allow overcoming the fetal lethality when initiating

earlier treatment. Thereby, one could fully assess the usefulness of the rapamycin model to study IUGR and developmental programming.

7.1.3 Reduced cardiomyocyte size and increased apoptosis rates are responsible for cardiac growth retardation in neonates after prenatal mTORC1 inhibition

We were eager to identify the cellular mechanisms that induce the cardiac phenotype in neonates after prenatal mTORC1 inhibition. Postnatal heart growth is primarily achieved by hypertrophy[64]. Interestingly, the mTOR pathway was shown to be of particular importance in the regulation of cardiomyocyte size and hypertrophic growth in adult murine hearts; both under physiological as well as pathological conditions[117]. Exercise training-induced (treadmill running) physiological hypertrophy was demonstrated to be associated with activation of the mTOR signaling pathway in adult mice, as identified by increased phosphorylation of the mTORC1 downstream targets S6K1 and S6[117]. These molecular changes were accompanied by increased cardiomyocyte size[117]. The role of the mTOR signaling cascade in physiological postnatal heart growth was additionally supported by the observation that treatment of 3 week old mice with rapamycin results in smaller hearts at the age of 4 weeks[190]. In contrast, pressure overload-induced pathological hypertrophy after transverse aortic constriction (TAC) was associated with inactivation of the mTOR signaling pathway, as indicated by reduced phosphorylation levels of S6K1 and S6[117]. Additionally, inhibition of mTORC1 by rapamycin as well as cardiac-specific *Mtor* or *Raptor* ablation in adulthood attenuates stress-induced pathological cardiac hypertrophy[182-186]. This is mainly mediated by preventing increased cardiomyocyte growth[182-184].

To date, the role of the mTOR pathway in the regulation of cardiomyocyte size in the perinatal and neonatal period remains obscure. Importantly, we revealed that prenatal rapamycin treatment reduces cardiomyocyte cross sectional area (CSA) in neonates (see Chapter 6.3.3.2, Figure 12F). These data suggest an important role of the mTOR signaling cascade in fetal and neonatal cell size regulation in the heart, similar to adult stages. Reduced cardiomyocyte CSA was also observed in one of the few studies analyzing the effects of mTOR pathway inhibition during heart development. Cardiac-specific *Rheb* KOs (c*Rheb*-KO), the most important upstream regulator of mTORC1, remained inconspicuous until postnatal day 8[189]. Afterwards, they presented signs of dilated cardiomyopathy, such as significantly lower HW, HW/BW ratios, reduced cardiomyocyte CSA and cardiac dysfunction[189]. c*Rheb*-KOs demonstrated unchanged HW and cardiomyocyte CSA at P3 and P5[189]. Unfortunately, neonatal (P1) c*Rheb*-KO mice were not analyzed[189]. Strikingly, we revealed a rather severe phenotype with regard to reduced HW and cardiomyocyte CSA at P1 after prenatal rapamycin treatment (see Chapter 6.3.3.1, Figure 11E and Chapter 6.3.3.2, Figure 12F). The difference might be explained by basic mechanistic differences between the rapamycin approach and c*Rheb*-KO mice. Systematic

rapamycin treatment inhibits mTORC1 in the entire organism from 15.5 dpc onwards. In contrast, *Rheb* deficiency was achieved by *Cre*/*loxP* recombination[189]. For this purpose, an α-myosin heavy chain promoter-driven *Cre* recombinase was used[189], which resulted in inactivation of the floxed *Rheb* gene in cardiomyocytes between 7.5 dpc and 8.0 dpc[251]. Analysis of phosphorylation levels of S6 and 4E-BP1 were not affected in P3 c*Rheb*-KO hearts[189], indicating preservation of mTORC1 signaling. From postnatal day 5 onwards, c*Rheb*-KO mice demonstrated attenuated cardiac mTORC1 activity[189]. Rapamycin treated hearts displayed severely reduced mTORC1 activity already at P1 (see Chapter 6.3.1, Figure 9A). Thus, these data suggest that mTORC1 is essential for fetal and neonatal heart growth, while RHEB is dispensable for the mTORC1 activation during neonatal cardiac development soon after birth. The authors proposed that an isoform of RHEB (e.g. RHEBL1[252]) partially compensates for the loss of RHEB[189]. The results furthermore indicate that RHEB-independent mTORC1 activation might play an important role in cardiac development until postnatal day 3. This might be of major importance with regard to future analyses focusing on upstream signaling pathways that are responsible for the increased mTOR pathway activity in neonatal c*Hccs*$^{+/-}$ hearts. Therefore, attention should be paid on the role of the mTORC1 upstream stimuli AKT and AMPK (see Chapter 3.3.4.1, Figure 5) during fetal and perinatal heart development.

Besides decreased cardiomyocyte CSA, HW reduction in neonatal rapamycin treated mice might additionally be caused by alterations in cell number. Hence, we investigated programmed cell death (autophagy and apoptosis) as well as cell proliferation (see Chapter 6.3.3.2, Figure 12A-D). Importantly, the mTOR signaling cascade is known to inhibit autophagy (see Chapter 3.3.4.1, Figure 5), a highly regulated cellular degradation process important for protein turn-over, recycling of damaged organelles and consequently organismal and cellular adaptation to nutrient starvation[168-173,175]. The protein p62 is one of the best characterized selective autophagy substrates, which targets proteins for autophagy, gets incorporated into autophagosomes and subsequently degraded[223,224]. Interestingly, our results revealed evidence for enhanced autophagy in neonatal hearts after prenatal rapamycin treatment, as indicated by decreased p62 protein levels (see Chapter 6.3.1, Figure 9B+D). Even though autophagy was originally believed to temporary protect cells from apoptosis during times of unfavorable growth conditions[253], recent studies demonstrated that the association between apoptosis and autophagy is by far more complex and that unrestrained autophagy can also promote apoptosis[254,255]. Importantly, studies in adult mice after cardiac-specific *Mtor* or *Raptor* ablation revealed induced apoptosis of cardiomyocytes[182,183]. Thus, it is reasonable to speculate that prenatal mTORC1 inhibition has similar effects in neonatal hearts. Indeed, studies in 10.5 dpc and 12.5 dpc embryonic c*Mtor*-KO mice, though a controversially discussed study due to incomplete cardiac mTOR

pathway inactivation, revealed increased apoptosis of cardiomyocytes[191]. In these mice, cardiac-specific *Mtor* KO was achieved by using a myosin heavy chain-driven *Cre* recombinase[191]. The authors observed mosaic expression of *Cre* recombinase and hence only a subset of cardiomyocytes displays *Mtor* inactivation[191]. Whether the increase in cardiac apoptosis is really due to the cardiac *Mtor* KO or might be a secondary effect resulting from cell competition remains obscure. Unfortunately, autophagy was not analyzed in embryonic c*Mtor*-KO hearts[191]. Strikingly, we observed not only increased autophagy (see Chapter 6.3.1, Figure 9B+D) but also significantly enhanced apoptosis rates in neonatal hearts after prenatal rapamycin treatment (see Chapter 6.3.3.2, Figure 12D). However, further investigations to explore the role of autophagy in our rapamycin model and to elucidate if the increase in cardiomyocyte apoptosis is indeed autophagy-mediated, are required. Analyzing protein levels of LC3B-II, which is essential for the formation of autophagosomes[256], as well as investigating the cellular abundance and localization of LC3B-II by immunohistochemistry stainings might help to uncover the effects of prenatal mTORC1 inhibition on cardiac autophagy. During the time of the study we intensively tried to perform western blot analyses and immunohistochemistry stainings using a LC3B-II antibody. Unfortunately, we experienced serious technical problems, which require special attention in future studies. Assuming that autophagy turns out to be not the main trigger of increased apoptosis, the latter might be a secondary effect maybe due to mechanical left ventricular (LV) wall stress or metabolic alterations.

As stated (see Chapter 3.3.2), fetal cardiac growth mainly occurs through cardiomyocyte proliferation. Thus, the reduced HW in rapamycin treated neonates might furthermore be caused by decreased proliferation rates. However, neonatal cardiomyocyte proliferation rates were found to be unaffected by prenatal mTORC1 inhibition (see Chapter 6.3.3.2, Figure 12C). Though, it remains obscure if rapamycin treatment affects cardiac proliferation in earlier stages.

In summary, we conclude that changes in cardiomyocyte size and apoptosis are part of the cascade of events that cause the profound cardiac phenotype in neonatal hearts after prenatal mTORC1 inhibition.

7.1.4 Prenatal mTORC1 inhibition does not affect cardiac regeneration of c*Hccs*$^{+/-}$ mice but alters apoptosis and cell growth in the neonatal c*Hccs*$^{+/-}$ myocardium

We found increased mTOR pathway activity in neonatal *cHccs*$^{+/-}$ mice (see Chapter 6.2, Figure 8). Hence we hypothesized that this activation is crucial in our model to sustain cardiac regeneration during the second half of gestation. However, prenatal mTORC1 inhibition did not cause embryonic lethality (see Chapter 6.3.2, Figure 10A) and *cHccs*$^{+/-}$ mice were born in expected Mendelian ratios (see Chapter 6.3.2, Figure 10B). Consequently,

enhanced mTOR pathway activity is not essential to ensure survival of *cHccs*$^{+/-}$ mice. Importantly, the period of embryonic heart regeneration in *cHccs*$^{+/-}$ mice, which shows the most dramatic shift in the cell populations, takes place between 10.5 dpc and 13.5 dpc (see Chapter 3.4)[192]. This developmental phase is not affected by the rapamycin treatment, which is initiated at 15.5 dpc. At that stage, the ratio of *Hccs*-deficient versus healthy tissue is already 20:80[192]. Hence, the rapamycin approach is not targeting the actual regenerative phase but rather the "consolidation" phase of fetal compensatory growth in c*Hccs*$^{+/-}$ mice.

Strikingly, HW and HW/BW ratio of neonatal *cHccs*$^{+/-}$ hearts after prenatal mTORC1 inhibition were significantly reduced compared to rapamycin treated *Hccs*$^{+/+}$ neonates (see Chapter 6.3.3.1, Figure 11E+F). The same proves true after prenatal vehicle treatment (see Chapter 6.3.3.1, Figure 11E+F). This is in line with our current understanding of the heart conditional *Hccs* KO model, because formation of the heart from just 50 % of embryonic cardiomyocytes results in a hypoplastic cardiac phenotype at birth evident by a reduced HW/BW ratio, thinner LV walls and significantly reduced cardiomyocyte number (unpublished data, see Chapter 3.4). Thus, the observation that HW and HW/BW ratio in neonatal rapamycin treated *cHccs*$^{+/-}$ mice is reduced might not be a specific effect of prenatal mTORC1 inhibition but instead might reflect the hypoplastic phenotype which is maintained after rapamycin treatment.

Moreover, prenatal mTORC1 inhibition caused cardiac apoptosis in both genotypes with a higher extend in neonatal *cHccs*$^{+/-}$ hearts (6.3.3.2, Figure 12D). It was demonstrated that approximately 10 % *Hccs*-deficient cells remain in the neonatal myocardium[192]. Hence, prenatal rapamycin treatment might more severely affect these *Hccs*-deficient cells, which are normally not actively eliminated[192]. A cardiac protective role of the mTOR pathway was previously reported, since tamoxifen-inducible cardiac-specific *Mtor* as well as *Raptor* deletion in the adult mouse myocardium was demonstrated to cause cardiac dysfunction and heart failure with chamber dilation and wall thinning[182,183]. Furthermore, in a mouse model for ischemia-reperfusion injury the mTOR signaling cascade was found to be activated and its inhibition by rapamycin increased injury[257]. Consistently, mTOR pathway activation was also protective in isolated cardiomyocytes upon oxidative stress[257]. Increased TUNEL-rates in neonatal rapamycin treated *cHccs*$^{+/-}$ hearts might therefore suggest that prenatal mTORC1 inhibition causes apoptosis in general but additionally affects survival of *Hccs*-deficient cells. Unfortunately, the method applied (see Chapter 5.3.4.3.2) does not allow differentiation between healthy and *Hccs*-deficient cells. Thus, immunohistochemistry using antibodies for cytochrome *c* (to differentiate between healthy and *Hccs*-deficient myocardial cells) and cleaved caspase 3 (a marker for apoptotic cells[258]) should be performed.

Neonatal cardiomyocyte CSA was reduced after prenatal mTORC1 inhibition in both genotypes (see Chapter 6.3.3.2, Figure 12F). Strikingly, CSA in rapamycin *cHccs*$^{+/-}$ hearts

was significantly smaller than in rapamycin *Hccs*$^{+/+}$ neonates (see Chapter 6.3.3.2, Figure 12F). In vehicle treated neonatal hearts, cardiomyocyte CSA was not different between the genotypes (see Chapter 6.3.3.2, Figure 12F). These data suggest that in untreated neonatal c*Hccs*$^{+/-}$ hearts elevated mTOR pathway activity is required to achieve normal cell size but is unable to elevate CSA above the control level to e.g. compensate for the reduced cardiomyocyte number. Prevention of elevated cell growth might be beneficial, as it could otherwise be the turning point toward pathological remodeling. Hence, cardiomyocyte growth might have reached its physiological limit and further cell growth might even be restricted by the activity of certain inhibitors. A potential candidate that might be involved in prevention of pathological hypertrophy in response to mTOR pathway hyperactivation is 5´-adenosine monophosphate-activated protein kinase (AMPK), which is closely linked to the mTOR signaling cascade by acting as indirect mTORC1 inhibitor[144,145] (see Chapter 3.3.4.1, Figure 5). Interestingly, we have found elevated AMPK activity in c*Hccs*$^{+/-}$ neonatal hearts in recent pilot experiments (data not shown) and further investigations are currently ongoing. AMPK was shown to contribute to the protection of the heart against hypoxic injury, as demonstrated in neonatal rat cardiomyocytes after exposure to hypoxia[259]. Moreover, increased cardiomyocyte CSA in adult mice was identified in a mouse model for impaired AMPK activity, suggesting restriction of cardiomyocyte growth by AMPK[260]. Taken together, cell size is tightly controlled and kept within a certain range irrespective of cell number in the neonatal heart. Further studies are currently performed to more precisely focus on these cardiac control mechanisms that prevent overshooting cell size upon mTOR pathway hyperactivation in the neonatal stage.

In conclusion, these findings indicate that the mTOR signaling cascade indeed has specific consequences for fetal cardiac growth in the heart conditional *Hccs* KO model but its inhibition still allows survival of *cHccs*$^{+/-}$ offspring until birth. Because apoptosis rates and cardiomyocyte CSA in *cHccs*$^{+/-}$ neonatal hearts after prenatal rapamycin treatment are altered to a larger extend than in *Hccs*$^{+/+}$ neonates, one might expect reduction of HW and HW/BW ratio. However, as discussed above, the degree of reduction between vehicle and rapamycin groups does not differ when comparing the genotypes (see Chapter 6.3.3.1, Figure 11E+F). Importantly, due to the extremely small HW, precise measurement is technically limited even when using highly sensitive laboratory scales. Hence, further reduction of HW and HW/BW ratio in *cHccs*$^{+/-}$ neonates after prenatal mTORC1 inhibition might be below the threshold of detection.

7.1.5 Prenatal mTORC1 inhibition by rapamycin does not severely impair heart function in neonates

The profound morphological phenotype of rapamycin treated neonatal hearts led us to speculate that prenatal mTORC1 inhibition might impair cardiac function at birth. However,

analyses of the left ventricular contractile parameters fractional shortening (FS) and ejection fraction (EF) revealed only slight reductions after prenatal rapamycin treatment in c*Hccs*$^{+/-}$ neonates and no differences in controls (see Chapter 6.3.3.3, Figure 13D+E and Supplementary Table S5). The slightly reduced contractile function in *cHccs*$^{+/-}$ neonates might be explained by the increased apoptosis rates as well as the smaller cardiomyocyte size (see Chapter 6.3.3.2, Figure 12D+F). Support comes from studies that suggested that increased apoptosis, even at low levels, eventually result in heart failure[261]. In this context, adult transgenic mice with inducible cardiomyocyte apoptosis demonstrated lethal, dilated cardiomyopathy[261]. Moreover, pathological hypertrophy is known to go along with increased cell size and transiently increased contractility to maintain cardiac output e.g. during pressure overload[100]. Hence, the decreased cell size after prenatal rapamycin treatment, most prominent in c*Hccs*$^{+/-}$ neonates (see Chapter 6.3.3.2, Figure 12F), might increase the susceptibility to cardiac dysfunction.

Importantly, in adulthood rapamycin treatment as well as cardiac-specific *Mtor* and *Raptor* ablation impair cardiac contractility[182-184,186]. Tamoxifen-inducible cardiac-specific *Raptor* KO mice develop spontaneous cardiomyopathy and die 5 weeks after tamoxifen injection[183]. Tamoxifen-inducible cardiac-specific *Mtor* deletion in the adult mouse myocardium leads to lethal, dilated cardiomyopathy and mice started dying 4 weeks after tamoxifen injection[182]. Hence, it was surprising to assess that prenatal mTORC1 inhibition causes a severe phenotype in neonatal hearts but at the same time only marginally affects heart function. Thus, the fetal and perinatal heart can maintain cardiac contractility upon mTORC1 inhibition while the adult heart cannot. This discrepancy might be explained by the impressive regenerative capacity of the fetal heart[262]. The transition from fetal and perinatal hyperplastic to postnatal hypertrophic growth is accompanied by major changes in cardiac metabolism and substrate utilization[86-88,92], which might also result in different susceptibilities to rapamycin. Hence, differences in the compensatory plasticity might be associated with metabolic adaptations of the fetal and neonatal heart in order to adapt to prenatal mTORC1 inhibition and thus maintain cardiac function (see Chapter 3.3.2). Eventually, the neonatal heart is furthermore subjected to a lower contractile demand and work load than the adult heart, which might also allow better maintenance of cardiac function upon mTORC1 inhibition.

7.1.6 Limitations of the rapamycin approach and suggestions for improvement

Importantly, rapamycin treatment is a systemic approach that does not only affect the heart but also disturbs growth and maturation of other organ systems. This could potentially result in secondary consequences for the myocardium, which cannot be dissected from primary effects of cardiac mTORC1 inhibition. Even though this is in consistence with the classical IUGR models, which also affect the entire organism, it might cause problems regarding the

analysis of the role of mTOR signaling specifically within the heart. Although our rapamycin approach has more severe consequences on cardiac development than on other organ systems and thus allows investigation of the role of mTOR during fetal and neonatal development with special emphasis on the heart to a certain extent, its unspecific effects should be kept in mind.

Furthermore, rapamycin might also affect the mother with respect to placental or mammary gland development. Given that we did not investigate these options, consequences resulting from maternal disturbances cannot be excluded. mTOR is known to be highly expressed in the syncytiotrophoblast of the human placenta[263]. Inhibition of placental mTORC1 decreases the cell surface abundance of amino acid transporters in the trophoblast[264]. Hence, it was suggested that trophoblast mTORC1 signaling links maternal nutrient availability to fetal growth by modulating the flux of amino acids across the placenta[264]. Interestingly, placental mTORC1 activity was demonstrated to be reduced in human IUGR[263]. Moreover, mTOR was shown to be required for trophoblast development by controlling trophoblast cell growth and proliferation[265]. Together, these data indicate that the neonatal phenotype of rapamycin treated mice might at least be partially and additionally mediated by mTORC1 inhibition in the maternal placenta. Furthermore, studies with purified mammary epithelial cells revealed that decreased mTOR pathway activity results in reduced cell proliferation and lactation[266]. Given that the ability of mammary glands to produce milk is determined by the number of cells and their level of viability[266], mTORC1 inhibition by rapamycin might also affect mammary gland development and thereby negatively impacts on development of newborn mice.

We observed mTOR pathway upregulation in neonatal *cHccs*$^{+/-}$ hearts (see Chapter 6.2, Figure 8) and we initially proposed that the mTOR signaling cascade plays an essential role in the *cHccs*$^{+/-}$ myocardium. However, after mTORC1 inhibition, *Hccs*$^{+/+}$ and *cHccs*$^{+/-}$ mice both survived in expected Mendelian ratios (see Chapter 6.3.2, Figure 10B). The rapamycin dose applied (s.c. 5 mg rapamycin/BW every 12 h) might be too high to tease out differences between the genotypes. Completely whipping out mTORC1 activity, as it is the case for the prenatal rapamycin treatment presented here (see Chapter 6.3.1, Figure 9A), might equalize the rather severe phenotype in both genotypes. Studies in adult mice demonstrated that already daily i.p. 2 mg rapamycin/BW injections over a period of one week are sufficient to inhibit cardiac mTORC1 activity[184]. However, i.p. rapamycin injections in adult mice and rapamycin treatment of fetal mice by s.c. injections in pregnant dams are fundamentally different approaches, which makes it difficult to adopt the dose and treatment regime. Ideally, one would aim for a dose that reproducibly reduces mTOR pathway activity but does not cause a phenotype in neonatal *Hccs*$^{+/+}$ controls. This could eventually unmask a specific mTOR function in *cHccs*$^{+/-}$ neonates. Hence, reducing the rapamycin dose or the injection

frequency and at the same time starting the injection period before 15.5 dpc might specifically affect survival of *cHccs*$^{+/-}$ mice. Alternatively, a genetic approach using heterozygous *Raptor* KOs might serve this function as it would allow for inhibiting mTOR pathway activity earlier during heart development. c*Raptor*$^{+/-}$ mice are viable and survive until adulthood (see Chapter 6.4.1, Figure 16A). Moreover, their hearts are morphologically inconspicuous (see Chapter 6.4.2, Figure 16E). However, mTOR pathway activity in 10.5 dpc embryonic (see Chapter 6.4.3, Figure 16B-D+F) and neonatal c*Raptor*$^{+/-}$ hearts (data not shown) as well as HW/BW ratio in neonatal c*Raptor*$^{+/-}$ mice are reduced (data not shown). Thus, c*Raptor*$^{+/-}$ mice comprise an important potential to elucidate the role of the mTOR signaling cascade in the heart conditional *Hccs* KO model in more detail. Generation of double KO mice by crossing c*Raptor*$^{+/-}$ with c*Hccs*$^{+/-}$ mice might help to elucidate open questions that cannot be addressed if the entire organism is affected.

7.1.7 Cardiac-specific *Raptor* ablation revealed that the mTOR pathway is essential during early embryonic cardiac development

To investigate the role of the mTOR signaling pathway during early cardiac development and specifically within the heart excluding secondary effects, we generated mice with cardiac-specific *Raptor* ablation. The RAPTOR protein directly interacts with MTOR and is essential for mTORC1 assembly and function[120,121]. Genetic *Raptor* ablation causes disassembly of the mTORC1 complex, consequently impairing downstream signaling[206].

Cardiac-specific *Raptor* ablated mice died *in utero* between 10.5 dpc and 11.5 dpc (see Chapter 6.4.1, Figure 16A), suggesting that the mTOR pathway is essential during early heart development and thus for survival of the entire organism. Analyses of cardiac morphology revealed a fulminant phenotype at 10.5 dpc with severely reduced ventricular wall thickness, resulting in hypoplastic hearts (see Chapter 6.4.2, Figure 16E). Recent unpublished data from our lab demonstrated a significantly reduced proliferative potential of cardiomyocytes in 10.5 dpc c*Raptor*$^{-/-}$ hearts. Other mouse models with similar phenotypes and proliferation defects support our findings. For instance, mice lacking all three D-type cyclins (*Ccnd1, Ccnd2, Ccnd3*) die around 16.5 dpc due to heart abnormalities and impaired proliferation of myocardial cells[267]. Fetal cardiomyocyte-restricted inactivation of the *yes-associated protein 1* (*Yap1*) gene also causes decreased cardiomyocyte proliferation leading to myocardial hypoplasia and embryonic lethality after 16.5 dpc[59]. Moreover, we argued that in neonatal rapamycin treated hearts increased apoptosis is mediated by unrestricted autophagy (see Chapter 7.1.3). A similar scenario might contribute to hypoplasia in c*Raptor*$^{-/-}$ hearts. We assume that reduced proliferation and potentially increased apoptosis result in a reduced set of cardiac cells in 10.5 dpc c*Raptor*$^{-/-}$ hearts, causing the severe thinning of both the compact as well as the trabeculated myocardium. Hence, future attention should be paid on cellular and molecular mechanisms involved in autophagy and apoptosis in the cardiac-

specific *Raptor* KO model. The trabeculae, which develop between 8.5 dpc and 10.5 dpc, are especially important for proper and powerful contraction as well as for nutrient uptake from the ventricular blood flow by increasing the surface area, as a coronary artery system to supply the myocardium has not been developed at that stage (see Chapter 3.3.1). Consequently, a reduced set of contracting cardiac cells in combination with the almost absent trabeculae in c*Raptor*$^{-/-}$ hearts might result in insufficient nutritional supply of the growing myocardium and in the end cause death of the entire embryo.

Interestingly, embryonic c*Mtor*-KO mice die between 13.5 dpc and the end of gestation[191]. In these mice, cardiac-specific *Mtor* KO was achieved by using a myosin heavy chain-driven *Cre* recombinase[191]. However, only a subset of cardiomyocytes displays *Mtor* inactivation, because mosaic expression of *Cre* recombinase was observed[191]. Therefore, the embryonic day at which c*Mtor*-KO mice die was shown to be dependent on the extent of cardiac *Cre* expression and hence *Mtor* inactivation[191]. Consequently, the reason for the longer survival of c*Mtor*-KO embryos compared to our c*Raptor*$^{-/-}$ mice might be the cardiomyocyte mosaic for the KO of *Mtor*. Interestingly, cardiac proliferation rates in 10.5 dpc and 12.5 dpc c*Mtor*-KO embryos were found to be significantly reduced[191]; a finding that is consistent with our c*Raptor*$^{-/-}$ model.

In line, prenatal rapamycin treatment from 11.5 dpc onwards causes fetal lethality (see Chapter 6.3.1 and Supplementary Figure 4), as demonstrated by a pilot experiment which was terminated after assessing the extensive consequences for the offspring. Importantly, mTORC1 inhibition by rapamycin during late gestation from 15.5 dpc does not result in prenatal lethality (see Chapter 6.3.2, Figure 10), even though neonatal rapamycin treated hearts are hypoplastic (see Chapter 6.3.3.1, Figure 11C-E). Analyses of neonatal cardiac proliferation rates revealed no significant differences between prenatal vehicle and rapamycin treatment (see Chapter 6.3.3.2, Figure 12C). However, proliferation was assessed using immunofluorescence staining for KI67, which labels proliferating cells in all active phases of the cell cycle[217]. Thus, a more specific proliferation marker, such as p-HH3, which is restricted to mitosis and the late G2 phase of the cell cycle[218], might help to uncover subtle differences in proliferation rates in the neonatal stage. Importantly, differences in survival as well as in proliferation rates between the above discussed approaches are most likely due to the different phases of development during which the mTOR pathway was inhibited. Moreover, cell cycle activity in peri- and postnatal cardiomyocytes does not necessarily mean cell division[69]. It is conceivable to speculate that in controls, cardiomyocytes still actively divide, whereas they start to become binucleated in c*Hccs*$^{+/-}$ neonates. In order to focus on potential differences regarding the moment when terminal differentiation occurs, cytokinesis markers, such as aurora B kinase (a chromosomal passenger protein that is involved in chromosome segregation, spindle-checkpoint, and cytokinesis)[268] or determination of the

actual cell number might prove useful. Additionally, analyzing cardiomyocyte proliferation in fetal rapamycin treated hearts shortly before birth (e.g. between 17.5 dpc and 18.5 dpc) might help to reliably elucidate the impact of rapamycin treatment on cardiomyocyte proliferation rates. In this context, the IUGR phenotype of rapamycin treated neonatal hearts might not only be caused by reduced cardiomyocyte size and increased apoptosis rates, as discussed above, but also by reduced proliferation and thus reduced number of cardiac cells. This would again correlate with findings in classical IUGR rat models at birth: less cardiomyocytes[23] as well as a suppressed replicative potential of cardiac cells upon intrauterine LPD[24] and decreased cardiomyocyte number after placental insufficiency[33]. However, one can also speculate that the mTOR pathway plays different roles during different phases of cardiac development. In this context, our results suggest that during embryonic development, the mTOR signaling cascade regulates proliferation; while in later stages it might control cell size. Similar mechanisms have been proposed for cell cycle regulating genes. For instance certain cyclins were shown to be associated with proliferation in embryonic but with hypertrophy in adult cardiomyocytes[76,77,231,269,270]. Moreover, mTOR pathway hyperactivation is often associated with tumor growth, where it certainly promotes proliferation[271-273]. Hence, it appears that the same growth machinery (mTOR pathway) can induce proliferation in one cell type but increases cell size in the other. The latter seems to primarily affect terminally differentiated cardiomyocytes. Thus, for the heart, as long as cardiomyocytes are in principle able to divide, the mTOR pathway might induce proliferation, but as soon as cardiomyocytes withdraw from the cell cycle the mTOR signaling cascade might induce hypertrophy. This consideration would make the mTOR pathway especially interesting with regard to a potential role in the transition from hyperplastic to hypertrophic cardiac growth in the perinatal period, given that until now the molecular players initiating this switch are only insufficiently elucidated (see Chapter 3.3.2).

Strikingly, homozygous cardiac-specific *Raptor* ablation completely abolishes phosphorylation of 4E-BP1 in 10.5 dpc embryonic hearts (see Chapter 6.4.3, Figure 16D+F). This is in line with cardiac-specific *Mtor* or *Raptor* ablation in adulthood as well as with 12.5 dpc embryonic c*Mtor*-KO mice[182,183,191]. In all three models significantly decreased cardiac 4E-BP1 phosphorylation was observed[182,183,191]. In contrast, mTORC1 inhibition by prenatal rapamycin treatment severely inhibited phosphorylation of S6K1 and S6 but not of 4E-BP1 in neonatal hearts (see Chapter 6.3.1, Figure 9A). Differential effects of rapamycin on phosphorylation of various mTORC1 downstream targets have previously been reported in cell culture[274]. In this regard, it was demonstrated that rapamycin potently inhibits S6K1 activity throughout the duration of treatment, while 4E-BP1 phosphorylation recovers within a few hours despite continued rapamycin exposure[274]. Phosphorylated 4E-BP1 dissociates from EIF4E, allowing EIF4E to bind to other translation initiation factors to initiate cap-

dependent translation[162]. Thereby, EIF4E specifically enhances the translation of transcripts, which often encode proteins associated with a proliferative response, such as CYCLIN D1[275]. Moreover, recent studies revealed that the sequence composition of mTORC1 phosphorylation sites is one of the key determinants of whether the site is a good or a poor mTORC1 substrate[276]. In this context, differences in substrate quality were shown to be most important to allow downstream effectors of mTORC1 to respond differentially to temporal and intensity changes in the levels of nutrients and growth factors or pharmaceutical inhibitors such as rapamycin[276]. Furthermore, cell culture experiments demonstrated that *Eif4e* overexpression is associated with significant acceleration of G1 phase progression from G0 phase to S phase, indicating cell cycle control[277]). Thus, it is tempting to speculate that the differences in 4E-BP1 phosphorylation are at least partially responsible (next to the developmental stage as well as differences in the proliferative potential of 10.5 dpc and P1 cardiomyocytes) for the different effects of cardiac-specific *Raptor* ablation and rapamycin treatment, respectively, on cell proliferation.

Taken together, all these findings indicate that regular cardiac mTOR pathway activity is essential during embryonic development, given that mTOR signaling appears to be required for normal cardiomyocyte proliferation and thus for the survival of the entire organism.

7.1.8 Adult mice after prenatal mTORC1 inhibition by rapamycin treatment demonstrate postnatal catch-up growth but no signs of cardiac dysfunction

The concept of developmental programming proposes that IUGR affects cardiac disease in adulthood. For instance, cardiac dysfunction[27] and impaired recovery after ischemia-reperfusion injury[28-30] were observed in adult rat hearts upon intrauterine amino acid restriction. Besides, prenatal hypoxia was shown to result in pathological cardiac remodeling[28] and LV diastolic dysfunction[35] in adulthood.

Analyses of BW and organ weights in adult mice after prenatal rapamycin treatment revealed postnatal catch-up growth, even though the weight parameters of rapamycin treated adult mice remained slightly below vehicle treated adults (see Chapter 6.3.4.1, Figure 14B+C and Supplementary Figure 5A+C+E). Interestingly, similar results were shown for classical IUGR models. BW and HW are reduced in LPD newborn rats, but normalize within the first few weeks of life if the diet is changed to SPD after birth, indicating postnatal compensatory growth[25]. In line, HW, which is reduced after placental insufficiency in pregnant rats, is also restored if postnatal nutrition is normalized[33]. In the context of developmental programming, accelerated postnatal growth is considered to additionally promote the manifestation of cardiovascular disease (CVD) in adulthood following IUGR and developmental programming[14-17]. For instance, in humans a relationship between glucose intolerance, low birth weight and obesity in adulthood was revealed[9]. Thereby, in low- and middle-income

countries, the combination of poor nutrition *in utero* and overnutrition in later life contributes to the increasing incidence of diabetes[20]. As mentioned above, hearts of rapamycin treated animals also demonstrated increased postnatal catch-up growth. HW of 11 week old vehicle treated *Hccs*$^{+/+}$ and *cHccs*$^{+/-}$ mice was 12-fold and 16-fold, respectively, higher compared to P1, while HW of 11 week old rapamycin treated *Hccs*$^{+/+}$ and *cHccs*$^{+/-}$ mice was increased by the factor of 18 and 21, respectively, compared to their neonatal HW (see Chapter 6.3.3.1, Figure 11E and Chapter 6.3.4.1, Figure 14C). In contrast, in both vehicle as well as rapamycin groups, KW of 11 week old mice was approximately 12 times higher than in the neonatal stage (see Chapter 6.3.3.1, Supplementary Figure 3C and Chapter 6.3.4.1, Supplementary Figure 5C). These data indicate that the susceptibility of rapamycin treated hearts for pathological conditions and cardiac dysfunction in adulthood might be increased. However, cardiac function in adult mice after prenatal mTORC1 inhibition was found to be normal (see Chapter 6.3.4.2, Figure 15F+G) and no signs of pathological remodeling or cardiac stress (e.g. cardiac fibrosis or expression of heart failure genes) were observed (see Chapter 6.3.4.2, Figure 15C+D). In contrast, in 12 months old adult rats cardiac dysfunction was observed under baseline conditions upon prenatal hypoxia[35] and intrauterine amino acid restriction[27]. Importantly, in our study 11 week old mice can be considered young adults. In the context of developmental programming, the increased risk for CVD in adulthood manifests if additional stress occurs. Given that we proposed that our approach represents a new IUGR model in mice, it would be interesting to investigate heart function and morphology of *Hccs*$^{+/+}$ and c*Hccs*$^{+/-}$ mice after prenatal rapamycin treatment at older age (for instance after 1 year) or if cardiac stress (such as TAC or chronic angiotensin infusion) is applied. Furthermore, analyses of older rapamycin treated adult mice might also reveal if organ size completely normalizes with ageing.

Cardiomyocyte CSA in adult mice after prenatal rapamycin treatment was significantly increased compared to vehicle treated mice in both genotypes (see Chapter 6.3.4.2, Figure 15B). However, the HW of rapamycin treated adults remained slightly below vehicle treated animals (see Chapter 6.3.4.1, Figure 14C). These findings suggest a reduced cardiomyocyte cell number in adult rapamycin treated hearts, resulting in compensatory increased cardiomyocyte size, which however cannot completely normalize HW by the age of 11 weeks. Indeed, we observed increased apoptosis in neonatal rapamycin treated hearts (see Chapter 6.3.3.2, Figure 12D) and proposed a proliferation defect in the perinatal period (see discussion in Chapter 7.1.3) in both genotypes. It was previously shown that neonatal c*Hccs*$^{+/-}$ hearts have a reduced number of cardiomyocytes and that cardiac hypertrophy in adulthood, as demonstrated in vehicle c*Hccs*$^{+/-}$ hearts (see Chapter 6.3.4.2, Figure 15B), is a major hallmark of the cardiac-specific *Hccs* KO model to compensate for the hypoplastic neonatal phenotype (unpublished data, see Chapter 3.4). Hence, our data

suggest additional reduction of the cardiomyocyte number in both genotypes. Thus, we propose that adult *Hccs*$^{+/+}$ and c*Hccs*$^{+/-}$ rapamycin hearts both respond with cardiomyocyte hypertrophy in addition to baseline compensatory cardiac hypertrophy of vehicle c*Hccs*$^{+/-}$ hearts (see Chapter 6.3.4.2, Figure 15B). This might flatten the difference in cardiomyocyte CSA between adult *Hccs*$^{+/+}$ and c*Hccs*$^{+/-}$ hearts, which is observed under vehicle conditions but no longer obvious after prenatal rapamycin treatment (see Chapter 6.3.4.2, Figure 15B).

7.2 Consequences of pre- and postnatal amino acid restriction

Maternal LPD during pregnancy and lactation is a well-characterized rat model for IUGR, low birth weight and the subsequently increased risk for chronic diseases in the offspring. However, mice have been relatively neglected in this regard and represent a critical resource for investigating the underlying molecular mechanisms of developmental programming.

Amino acids are key players in all life processes and apart from their role as building blocks for protein synthesis, they fulfill further central cellular functions and serve as intermediates in cell metabolism[21]. For instance, tyrosine and phenylalanine are precursors of low molecular weight hormones. Methionine, glycine and serine participate in maintenance of the methyl group pool in cells, which influences, amongst others, the establishment of epigenetic marks such as DNA methylation (reviewed by Kimball and Jefferson[278]). Gluthatione, an important cellular antioxidant, is synthesized *de novo* from glycine, cysteine and glutamic acid (reviewed by Wu *et al.*[279]). Furthermore, and most importantly, amino acid availability is an essential upstream stimulus to activate the mTOR pathway[119]. Consequently, given the importance of amino acids for cell growth and survival, it is not surprising that prenatal amino acid restriction affects the development of various organ systems including the heart, as discussed in the introduction (see Chapter 3.2.2). Moreover, our initial experiments revealed induction of genes involved in amino acid metabolism, biosynthesis and transport in neonatal c*Hccs*$^{+/-}$ hearts (see Chapter 6.1, Table 18 and Supplementary Table S2-4), suggesting dependence of the developing c*Hccs*$^{+/-}$ myocardium on intrauterine amino acid availability. Thus, the aim of the second major part of this PhD project was to understand the implications and involvement of the amino acid metabolism for pre- and postnatal cardiac growth in general and for embryonic cardiac regeneration and postnatal compensatory heart growth of c*Hccs*$^{+/-}$ mice in particular. To address these questions, we fed pregnant dams either a SPD or a LPD during pregnancy and kept offspring on equal diets during lactation and after weaning. Consequences of LPD exposure were analyzed in 13.5 embryos and in neonates as well as in adult 11 week old mice.

7.2.1 Prenatal amino acid restriction does not induce IUGR in neonatal mice

Maternal LPD in the rat is the most commonly used model to study IUGR. LPD newborn rats display significantly lower BW and HW compared to pups from SPD dams[23]. Surprisingly, we did not observe reduced BW or HW in our murine LPD model compared to SPD mice at birth (see Chapter 6.5.3.1, Figure 19B+C), indicating that IUGR was not induced. Consequently, we analyzed the food intake to investigate if the reduced protein content in the food is compensated by increased ingestion. However, we revealed that non-pregnant as well as pregnant mice on SPD and LPD take up the same amount of food (see Chapter 6.5.1, Figure 17). While embryonic and postnatal effects of maternal LPD have been well characterized in rats[280], less is known about how mice respond to *in utero* amino acid restriction. Importantly, we did not exactly determine the gestational age of our newborn LPD mice. We assume that most neonates at P1 were born at 20.5 dpc; however, offspring could also be born at 19.5 dpc or 21.5 dpc. Hence, the precise gestational age might play a role in our investigations. Furthermore, it is obscure whether pups had time to milk feed since this parameter was not monitored in our experiments. Though, this might also impact on neonatal BW. Interspecies differences could furthermore be explained by longer gestation times in rats. While pregnant mice give birth after 19 to 21 days of pregnancy, rats do so after 21 to 23 days. Moreover, newborn rats have generally higher BW compared to newborn mice, such that slight weight differences in mice might be obscured. However, some recent studies suggested LPD-induced IUGR in mice. Mortensen *et al.* provided evidence that LPD results in BW reduction at birth by 40 % compared to murine SPD offspring[281]. Similar to our LPD composition with 8.8 % crude protein, they used 8 % crude protein containing LPD food[281]. LPD was fed to pregnant mice only after a vaginal plug was observed (gestational day 0)[281]. In contrast, we kept male as well as female mice on LPD at least 2 weeks prior to mating (see Chapter 5.1.5). The authors stated that mice gave birth at 19.5 dpc and newborn pups were analyzed immediately[281]. Importantly, Mortensen *et al.* used male as well as female pups to assess IUGR, without differentiating between the genders[281]. By comparison, we only analyzed females. Significant BW reduction in murine LPD offspring by 12 % was confirmed by Whitaker *et al.*[282]. They used isochaloric 8.5 % LPD during breeding, pregnancy and lactation but also did not start LPD treatment before breeding was initiated[282]. Again, the authors did not differentiate between male and female mice at the neonatal stage[282]. IUGR in neonatal mice was furthermore demonstrated by Bhasin *et al.*[283]. On detection of a vaginal plug, they placed females on 9 % LPD and analyzed newborn LPD mice at 19.5 dpc independent of their sex[283]. However, in all three studies the effect of prenatal LPD on neonatal BW but not HW and heart morphology was investigated. Due to the lack of knowledge regarding murine LPD models in general as well as due to the discrepancy between our observations and the well-established rat LPD model, further investigations are

absolutely essential. It might be indispensable to actually prove that the mice in our study are really subjected to amino acid restriction. Even though intake of SPD and LPD food does not differ, the mice might be able to adapt their metabolism in a way that they can extract relatively more protein out of the LPD food. Therefore, analyses of food utilization by measuring the protein amount that is excreted on the respective diet might prove useful. It might also be worth testing, if a further reduction of the dietary protein content causes IUGR in our neonatal mice.

7.2.2 Consequences of prenatal amino acid restriction for neonatal cardiac organ size

Interestingly, we found that the HW/BW ratio in LPD but not SPD *cHccs*$^{+/-}$ neonates was significantly reduced compared to their corresponding *Hccs*$^{+/+}$ controls (see Chapter 6.5.3.1, Figure 19D). The SPD finding is in strong contradiction to the current understanding of the heart conditional *Hccs* KO model. We have previously shown that neonatal *cHccs*$^{+/-}$ mice have a reduced HW/BW ratio and hypoplastic hearts (unpublished data, see Chapter 3.4). The reduced HW/BW ratio in neonatal *cHccs*$^{+/-}$ mice was confirmed in the rapamycin approach both after prenatal vehicle and rapamycin treatment (see Chapter 6.3.3.1, Figure 11F), but was not represented in the SPD group. As a result, a new project was initiated in the lab, which is currently under investigation. Recent data suggest that the difference in HW/BW ratio might be caused by different gestational ages on the day of birth. While neonatal mice in previous experiments as well as in the rapamycin study were born at 19.5 dpc, pregnant dams in the LPD study mainly gave birth at 20.5 dpc (unpublished data). Thus, the intrauterine period seems to be a fundamental factor regarding embryonic cardiac regeneration and growth in *cHccs*$^{+/-}$ mice. We hypothesized that one additional day *in utero* might be able to normalize heart size in the latter, due to the growth permissive environment compared to postnatal conditions. The underlying cellular and molecular mechanisms are currently under investigation and results from this recently initiated project might help to elucidate consequences for preterm birth in humans.

However, LPD *cHccs*$^{+/-}$ neonates, which similar to the SPD pups were also born at 20.5 dpc, revealed a reduced HW/BW ratio compared to LPD *Hccs*$^{+/+}$ controls (see Chapter 6.5.3.1, Figure 19D). Strikingly, comparing HW/BW ratios between neonatal SPD and LPD *Hccs*$^{+/+}$ mice or between SPD and LPD *cHccs*$^{+/-}$ neonates rather indicates a trend toward an increase in the *Hccs*$^{+/+}$ group than toward a decrease in the *cHccs*$^{+/-}$ group upon intrauterine LPD exposure (see Chapter 6.5.3.1, Figure 19D). However, this is in slight contradiction to classical LPD models, which revealed rather unchanged HW/BW ratio in neonatal rats[23]. Though, elevated HW/BW ratio was found in LPD animals after 4 weeks due to reduced BW but unchanged HW[25]. Together, our data indeed provide substantial evidence that maternal dietary changes during development affect the regulation of cardiac organ size in *cHccs*$^{+/-}$

neonates differentially than in *Hccs*$^{+/+}$ controls, irrespective of the contradictory results regarding the SPD animals described above. This raises the question in which way amino acids sustain or promote growth of *cHccs*$^{+/-}$ hearts and how the reduced HW/BW ratio of *cHccs*$^{+/-}$ mice upon intrauterine LPD exposure can be explained. We considered changes in cardiomyocyte size or number (due to altered proliferation or apoptosis rates) as potential underlying mechanisms that might be affected by amino acid restriction and might explain the reduced HW/BW ratio in LPD *cHccs*$^{+/-}$ neonates compared to LPD *Hccs*$^{+/+}$ controls.

7.2.3 Cellular and functional consequences in the heart after pre- and postnatal amino acid restriction

7.2.3.1 Consequences in neonatal hearts

Amino acids play a fundamental role in protein synthesis and cell growth[21]. We analyzed cardiomyocyte size in neonatal hearts upon intrauterine SPD or LPD exposure. We found that the cardiomyocyte CSA was increased in both LPD groups compared to the corresponding vehicle groups, while the difference in CSA was only significant for *cHccs*$^{+/-}$ neonates (see Chapter 6.5.3.2, Figure 20D). Increased CSA but unchanged HW (see Chapter 6.5.3.1, Figure 19C) point toward cell size compensation for a reduced cell number. Evidence that cardiomyocyte CSA and cell number might be inversely correlated and that increased cardiomyocyte size in respect of normal HW can be considered an indirect measure for reduced cell number has recently been published[82]. The authors used a murine model for oxidative damage and revealed unchanged HW/BW ratio but increased cardiomyocyte size at P3[82]. This was accompanied by severely reduced cardiomyocyte proliferation, indicating reduced cardiomyocyte number[82]. Even though cardiomyocyte CSA is increased especially in neonatal LPD *cHccs*$^{+/-}$ hearts (see Chapter 6.5.3.2, Figure 20D), the HW/BW ratio of this group is reduced (see Chapter 6.5.3.1, Figure 19D). This indicates that the increase in cell size might not be sufficient to compensate for the proposed reduction in cardiomyocyte number and that cardiomyocyte number in neonatal LPD *cHccs*$^{+/-}$ hearts might even be further reduced compared to neonatal LPD *Hccs*$^{+/+}$ controls. Importantly, pathological cardiac hypertrophy is primarily achieved by an increase in width resulting in increased CSA, while physiologic cardiac growth is mediated by a combination of increased cardiomyocyte width and length[284]. Thus, the prediction of cardiomyocyte size from only measuring CSA is limited and it might therefore prove helpful to analyze isolated neonatal cardiomyocytes regarding their width, length, surface area and volume to get a precise estimate of their real size. It might be that cardiomyocytes in neonatal LPD hearts have increased CSA but are shorter in length. Hence, the overall cardiomyocyte volume might be unchanged, possibly explaining the unchanged HW.

In the rat model, neonatal LPD hearts had significantly less cardiomyocytes than neonatal SPD hearts[23], which was accompanied by decreased rates of myocardial cell proliferation[24].

We also focused on cardiac proliferation rates in neonatal SPD and LPD hearts and found no significant differences (see Chapter 6.5.3.2, Figure 20C). These observations suggest that the proposed reduction in cell number might be established by a proliferation defect during prenatal development and that altered proliferation rates might no longer be detectable in neonatal hearts. This discrepancy to the rat LPD model might again be explained by interspecies differences between rats and mice as discussed above. Importantly, Aroutiounova *et al*.[24] applied the more specific p-HH3 marker to assess neonatal proliferation rates, while we used KI67 staining, which labels proliferating cells in all active phases of the cell cycle[217]. Given the known issue of cell cycle activity versus cell division in the perinatal heart, as discussed in Chapter 7.1.7, a more specific cell cycle activity marker might help to elucidate this discrepancy. Moreover, precise determination of cardiomyocyte number in neonatal SPD and LPD hearts for instance by stereological approaches (as described by Corstius *et al*.[23] and Lim *et al*.[25]) is certainly of major importance to exclusively address the question of altered cell number in our murine LPD model.

7.2.3.2 Consequences in 13.5 dpc embryonic hearts

We postulated that a possible reduction in cardiomyocyte number might be established by a proliferation defect during prenatal development when amino acids are restricted. Hence, we analyzed 13.5 dpc SPD and LPD hearts; but we neither revealed differences in apoptosis (see Chapter 6.5.4.2, Figure 22E) nor proliferation rates (see Chapter 6.5.4.2, Figure 22B). In detail, we found no significant differences between the diet groups regarding cardiac proliferation in general but also compensatory hyperproliferation of healthy cells in the *cHccs*$^{+/-}$ myocardium was not affected by prenatal LPD exposure (see Chapter 6.5.4.2, Figure 22B). These findings indicate that the demand for increased proliferation of healthy cells in *cHccs*$^{+/-}$ 13.5 dpc embryos does not depend on amino acid availability. Hence survival of *cHccs*$^{+/-}$ mice is ensured (see Chapter 6.5.2, Figure 18B) even if amino acids are restricted. Furthermore, morphology of 13.5 dpc embryonic LPD hearts was inconspicuous (see Chapter 6.5.4.1, Figure 21E), suggesting resistance of murine embryonic hearts against LPD exposure. However, it is conceivable that LPD might affect proliferation in the last trimester of prenatal development, the fetal phase, rather than in the embryonic phase. Previous studies (such as analyzing low oxygen conditions during pregnancy) revealed that IUGR can bring about changes in both embryonic and fetal development. For instance, increased apoptosis rates and premature terminal cardiomyocyte differentiation in fetal rat hearts[34] and ventricular dilation and myocardial hypoplasia in mid-gestation mouse embryos[36] were observed upon hypoxia. Moreover, Louey *et al*. previously showed that IUGR due to placental insufficiency causes decreased cell cycle activity in cardiomyocytes of fetal sheep hearts[285]. In the study on hand, the effects of prenatal LPD exposure on fetal cardiac development were not analyzed. Though, differential expression of cell cycle

regulating genes and accumulating evidence for reduced cell number in murine neonatal LPD hearts supports the general concept that LPD affects cardiomyocyte proliferative capacity. In conclusion, while effects of amino acid restriction in the rat become obvious in offspring at birth, we assume that in mice a reduced amino acid availability results in reduced cardiomyocyte proliferation capacity in fetal stages; a hypothesis that strongly urges for experiments focusing on proliferation rates in fetal hearts.

7.2.3.3 Consequences in adult hearts

In line with the developmental programming concept, studies in the classical LPD rat model (diet changed to SPD after birth) revealed that under baseline conditions prenatal amino acid restriction causes significant changes in heart morphology and function later in life, including interstitial fibrosis[26], hypertrophy[27] and increased stiffening[28] of the LV in adulthood. In these models, the IUGR insult is released at birth and the rats display postnatal catch-up growth. To investigate if cardiac growth and function in adulthood is also affected if postnatal conditions resemble that of *in utero*, we analyzed 11 week old mice after pre- and postnatal amino acid restriction. It is conceivable that maintaining similar conditions during postnatal life prevents CVD caused by developmental programming. Interestingly, we did not observe significant changes regarding BW, HW and HW/BW ratio in adult mice after pre- and postnatal LPD exposure (see Chapter 6.5.5.1, Figure 23G-I). LPD rats also normalized HW until weaning; however they were on SPD after birth[25]. Strikingly, when a SPD was administered to the pups not immediately after birth but after 2 weeks postnatally, LPD rat offspring remained significantly smaller and demonstrated reduced HW, resulting in unchanged HW/BW ratio compared to SPD offspring at 18 weeks of life[286]. However, to the best of our knowledge, our study is the first approach that investigated long-term consequences of LPD treatment without changing the diet to SPD at any time; though that there are no studies we can directly compare our results with.

Given that postnatal growth of the myocardium primarily occurs by cardiomyocyte hypertrophy and deposition of extracellular matrix (ECM)[287], we focused on cardiomyocyte CSA and ECM deposition. According to previous findings in the cardiac-specific *Hccs* KO model (see Chapter 3.4), c*Hccs*$^{+/-}$ hearts compensate the hypoplastic neonatal phenotype by cardiomyocyte hypertrophy in adulthood (unpublished data, see Chapter 3.4). Strikingly, while compensatory hypertrophy is preserved in c*Hccs*$^{+/-}$ females after pre- and postnatal LPD exposure (even though it misses statistical significance in the sample set used in this study), cardiomyocyte CSA in adult *Hccs*$^{+/+}$ as well as c*Hccs*$^{+/-}$ LPD hearts is significantly smaller than in adult SPD hearts (see Chapter 6.5.5.2, Figure 24C). These finding contradicts the adult HW, which was not reduced in LPD compared to SPD hearts in both genotypes (see Chapter 6.5.5.1, Figure 23H). We speculate that other cardiac cell types (e.g. fibroblasts or smooth muscle cells) might be present in a higher number in adult LPD hearts, thus compensating for the

decreased cardiomyocyte CSA resulting in normal HW. Evidence comes from studies showing that upon pathological remodeling following injury dramatic shifts in the various cardiac cell populations and tissue composition occur, such that fibroblasts contribute to a larger extend to the heart tissue[288]. It will be important to investigate this potential mechanism by FACS quantification of non-cardiomyocytes within the LV myocardium of our LPD hearts. Besides, it is tempting to speculate that even though cardiomyocyte CSA is reduced, overall cell volume might be unchanged due to increase in length, as discussed for neonatal hearts above. Analyzing adult cardiomyocyte dimensions after fixation and dissociation of the LV myocardium might prove useful to investigate this alternative. Furthermore, ECM deposition, determined by measuring the percentage of fibrotic tissue, was not increased in adult LPD hearts (see Chapter 6.5.5.2, Figure 24D); excluding the possibility that aggregated ECM deposition is responsible for the normalization of the HW. This finding was also in line with normal expression of genes encoding for ECM components (see Chapter 6.5.5.2, Figure 24E). Moreover, prenatal LPD in the rat was shown to be associated with cardiac dysfunction in the first 2 weeks of life, as obvious by a severe depression in the EF, but recovery of cardiac function in the LPD offspring up to 40 weeks of age[27]. Investigation of heart function in our 11 week old LPD mice revealed normal cardiac contractility (see Chapter 6.5.5.3, Figure 25D and Supplementary Table S7). However, we did not analyze cardiac function in murine LPD offspring during the lactation period. Furthermore, since 11 weeks old mice are rather young adults, investigating heart function and morphology of LPD *Hccs*$^{+/+}$ and c*Hccs*$^{+/-}$ mice at older age (e.g. after 1 year) or if cardiac stress (such as TAC or angiotensin) is applied, might reveal differences compared to adult SPD animals. Importantly, our data are in line with recent data from LPD rats, which revealed that maintaining a poor nutritional environment after birth might not increase the risk for CVD[286]. In this study, LPD rat offspring remained on LPD and were switched to SPD not until 2 weeks postnatally[286]. At 18 weeks of life, heart rate and FS of the cardiac muscle was not different between the treatment groups[286].

In conclusion, we did not find evidence that pre- and postnatal LPD alters postnatal cardiac growth and function in general or in the c*Hccs*$^{+/-}$ myocardium in particular. This is in line with the developmental programming concept stating that postnatal cardiac catch-up growth, which does not occur in our approach, contributes to increased susceptibility for adulthood disease rather than being beneficial[15,16]. However, given that the IUGR insult is not released at birth, our postnatal LPD model might be limited when interpreting the results in regard of developmental programming.

7.2.4 Consequences of pre- and postnatal amino acid restriction on mTOR pathway activity

mTOR pathway activity was shown to be increased in neonatal c*Hccs*$^{+/-}$ hearts (see Chapter 6.2, Figure 8). Due to its dependency on amino acid availability[119], it is assumed that amino

acid restriction downregulates the activity of the mTOR signaling cascade. However, to the best of our knowledge, so far none of the classical IUGR LPD models assessed the molecular consequences of amino acid restriction on mTOR pathway activity. One recent study revealed that maternal LPD, fed exclusively during the preimplantation period of mouse development (until 3.5 dcp), decreases the phosphorylation of S6 in 3.5 dpc murine blastocysts[289]. We also focused on the phosphorylation status of the mTORC1 downstream target S6 in 13.5 dpc embryonic hearts upon intrauterine LPD exposure (see Chapter 6.5.4.1, Figure 21A+C) and in adult hearts after pre- and postnatal LPD treatment (see Chapter 6.5.5.1, Figure 23A+C+D). Interestingly, the phosphorylation status of S6 remained largely unchanged. In a previous study, LPD was successfully used to induce autophagy, which is normally inhibited by the mTOR signaling cascade, in skeletal muscle of adult collagen VI KO mice[290]. When we focused on the autophagy marker p62 in embryonic (see Chapter 6.5.4.1, Figure 21A+D) and adult LPD hearts (see Chapter 6.5.5.1, Figure 23A+E) we did not find evidence for induced autophagy. As discussed before, a solid proof of concept that our mice are indeed amino acid restricted is currently missing. It is possible that the 8 % protein content in the diet is still sufficient to allow normal amino acid levels within the cell, given that certain non-essential amino acids can be synthesized from other metabolic sources. Thereby, normal cardiac mTOR pathway activity might be maintained. However, the mTOR signaling pathway was shown to be specifically sensitive to the essential amino acid leucine[291], which rather suggests a reduction of mTOR pathway activity due to decreased amino acid availability. Though, amino acids are not only essential building blocks for proteins but also serve as important energy source in cellular metabolism[21]. It might therefore be that mice change their metabolism from the very first day of prenatal development when amino acid restriction is applied. This might result in adaptation to amino acid restriction in postnatal development. This might furthermore explain why adult mice that receive LPD for the first time respond with increased autophagy after 4 weeks of LPD, indicating reduced mTOR pathway activity[290]. Moreover, detection of phosphorylation of S6 might be not sensitive enough to determine subtle changes in mTOR pathway activity. Therefore, it is essential to optimize the detection of S6K1 phosphorylation (that did not work out in embryonic and adult heart tissue due to technical limitations), which is a more reliable indicator. As mentioned above, to date none of the well-established classical IUGR LPD models assessed the molecular consequences of amino acid restriction on mTOR pathway activity. However, we have preliminary data indicating that mTOR pathway activity is also unchanged in neonatal LPD rat hearts, which were gratefully provided by Mary Jane Black, Monash University, Australia. Hence, one has to consider that the mTOR signaling pathway might not mediate growth restriction in LPD animal models. Other mechanisms might therefore be responsible for LPD-induced IUGR and amino acid restriction might exert

different cellular effects than protein starvation. In this context, amino acids are known to modulate cell signaling not only via the mTOR signaling cascade but also through protein-coupled receptors and gaseous molecules (e.g. NO)[21]. Moreover, certain non-essential amino acids (e.g. arginine, glutamine, glutamate, glycine and proline) play important roles in regulating gene expression[292-294], micro-RNA levels[295], blood flow[296] and overall metabolism[297-299]. Hence it might not be the function of amino acids as protein building blocks that induces IUGR but their role as energy source or intermediate metabolite in other pathways.

7.3 Conclusions and perspectives

Given the multitude of maternal as well as environmental factors which negatively impact on prenatal heart development as well as the high incidence of preterm birth events in humans, better understanding of molecular and cellular mechanisms adapted by the postnatal heart to compensate for impaired cardiac intrauterine development seems imperative. Elucidation of key processes and factors crucial for the prenatal heart during times of molecular and cellular periods of vulnerability and IUGR might not only reveal important strategies for prevention of congenital and postnatal heart diseases but also identify key mechanisms for cardiac regeneration and cardiac developmental programming. Thus, in respect of developmental programming, we aimed at investigating the role of the mTOR pathway and the impact of amino acid metabolism for prenatal, perinatal and postnatal cardiac growth in general and for embryonic cardiac regeneration and postnatal compensatory heart growth of c*Hccs*$^{+/-}$ mice in particular.

We propose that mTORC1 inhibition by rapamycin represents a new model of IUGR in the mouse, which allows the investigation of developmental programming mechanisms particularly in the fetal and neonatal phase of development. We found that the mTOR pathway has an outstanding role in organ size control of the heart; given that prenatal mTORC1 inhibition more severely affects HW than the size of other organ systems in neonatal mice. In combination with cardiac-specific *Raptor* ablation, we revealed that the mTOR signaling cascade is important for the regulation of cardiomyocyte size in the postnatal heart, while it seems to play an essential role in cardiomyocyte proliferation during embryonic and fetal development. Given these differential regulation of proliferation and hypertrophy during different stages of heart development, the mTOR pathway might not only be a newly discovered target of developmental programming but also a potential factor mediating the transition from proliferative to hypertrophic cardiac growth in the perinatal period. Prenatal impairment of the mTOR signaling cascade does not cause increased risk for CVD in young adulthood under baseline conditions; however, consequences for the adult heart after additional stress is applied in the sense of developmental programming remain

conceivable. This would be in line with our observation that mice respond to IUGR due to prenatal rapamycin treatment with enhanced postnatal cardiac catch-up growth. With respect to our c*Hccs*$^{+/-}$ mice, differential effects regarding apoptosis and cell size regulation were observed upon prenatal mTORC1 inhibition between *Hccs*$^{+/-}$ and c*Hccs*$^{+/-}$ animals. More detailed investigation of the specific role of the mTOR pathway in the c*Hccs*$^{+/-}$ myocardium might be obtained by adjusting the rapamycin injection protocol and by generating c*Hccs*$^{+/-}$/c*Raptor*$^{+/-}$ double KO mice.

Amino acid restriction in the classical LPD rat model is associated with smaller hearts at birth due to a reduced cardiomyocyte number, which potentially might be caused by decreased proliferation rates. We analyzed for the first time cardiac proliferation under LPD conditions in embryonic mice and we were able to demonstrate that amino acid restriction does not affect proliferation in murine embryonic hearts, even if compensatory hyperproliferation is required. Hence, our data suggest that fetal development might depend in a larger extend on a sufficient amount of available protein and thus on an intact amino acid metabolism than embryonic development does. Besides, we did not reveal IUGR in neonatal mice upon intrauterine amino acid restriction. Given that we did not find altered mTOR pathway activity in embryonic or adult LPD animals, further investigations are required to analyze if the mTOR signaling cascade actually mediates growth restriction in LPD animal models. With respect to our c*Hccs*$^{+/-}$ mice, amino acid availability neither seems to be essential for embryonic cardiac regeneration nor for postnatal compensatory hypertrophy. However, after conclusive proof that the mouse is a suitable model to study consequences of amino acid restriction on heart development, we still believe that our c*Hccs*$^{+/-}$ mouse model represents a prime subject to evaluate organ-specific impaired growth and developmental programming at the molecular and cellular level in response to restricted amino acid availability. Moreover, we importantly revealed that amino acid restriction affects postnatal cardiomyocyte hypertrophic growth in general, given that we observed reduced cardiomyocyte CSA in 11 week old *Hccs*$^{+/+}$ and c*Hccs*$^{+/-}$ hearts after prenatal and long-term LPD treatment. Regarding developmental programming of adulthood CVD, pre- and postnatal amino acid restriction in the mouse does not cause an increased risk in young adulthood under baseline conditions. However, consequences for the health of older hearts and after additional stress is applied remain conceivable, a consideration that was not addressed in this study. Most importantly, our LPD results point toward the late fetal period as the vulnerable phase during development that is especially sensitive for maternal malnutrition. These findings might provide new insights for disease prevention in humans and further investigations, e.g. focusing on the mTOR pathway, might help to elucidate underlying mechanisms.

In conclusion, the results anticipated from this study might have major implications for the understanding of developmental programming and furthermore might help to develop new

therapeutic strategies to treat and prevent cardiac disease that have their origin *in utero*. Amino acid supplementation during pregnancy, especially during the last trimester of prenatal development, or determination of mTOR pathway activity as a diagnostic marker for IUGR might represent suitable approaches but require further investigations to evaluate their feasibility as well as their clinical relevance and significance.

SUPPLEMENTAL INFORMATION

Supplementary Table S1. Differentially regulated genes in neonatal c*Hccs*$^{+/-}$ hearts

Affymetrix ID	Gene name	Gene symbol	FC	*p*-value
1422651_at	Adiponectin, C1Q and collagen domain containing	Adipoq	20.80	7.56*10^-09
1456225_x_at	Tribbles homolog 3	Trib3	20.54	1.22*10^-08
1450783_at	Interferon-induced protein with tetratricopeptide repeats 1	Ifit1	13.43	1.19*10^-05
1442026_at	Zinc finger and BTB domain containing 16	Zbtb16	6.78	9.73*10^-08
1417268_at	CD14 antigen	Cd14	6.07	8.62*10^-05
1419665_a_at	Nuclear protein transcription regulator 1	Nupr1	5.86	2.25*10^-05
1417022_at	Solute carrier family 7 (cationic amino acid transporter, y+ system), member 3	Slc7a3	5.61	4.44*10^-06
1426657_s_at	3-phosphoglycerate dehydrogenase	Phdgh	5.53	3.13*10^-06
1451006_at	Xanthine dehydrogenase	Xdh	5.47	1.22*10^-07
1426175_a_at	Tryptase alpha/beta 1	Tpsab1	5.16	1.92*10^-05
1449434_at	Carbonic anhydrase 3	Car3	5.01	3.73*10^-04
1442033_at	C1q and tumor necrosis factor related protein 9	C1qtnf9	4.83	4.68*10^-06
1434202_a_at	Family with sequence similarity 107, member A	Fam107a	4.63	1.46*10^-04
1419254_at	Methylenetetrahydrofolate dehydrogenase (NAD+ dependent), methenyltetrahydrofolate cyclohydrolase	Mthfd2	4.38	3.89*10^-08
1427388_at	Leucine rich repeat containing 2	Lrrc2	4.28	3.59*10^-06
1457666_s_at	Interferon activated gene 202B	Ifi202b	4.26	1.55*10^-03
1451382_at	ChaC, cation transport regulator-like 1	Chac1	4.17	1.22*10^-03
1449025_at	Interferon-induced protein with tetratricopeptide repeats 3	Ifit3	3.95	2.02*10^-04
1433966_x_at	Asparagine synthetase	Asns	3.79	1.45*10^-08
1435477_s_at	Fc receptor, IgG, low affinity IIb	Fcgr2b	3.50	4.09*10^-04
1428834_at	Dual specificity phosphatase 4	Dusp4	3.47	2.07*10^-07
1447927_at	Guanylate binding protein 6	Gbp6	3.33	3.88*10^-06
1454904_at	X-linked myotubular myopathy gene 1	Mtm1	3.07	2.39*10^-03
1427683_at	Early growth response 2	Egr2	2.79	5.64*10^-04
1422905_s_at	Flavin containing monooxygenase 2	Fmo2	2.79	8.33*10^-04
1457117_at	Nuclear factor, erythroid derived 2, like 2	Nfe2l2	2.74	2.88*10^-05
1451171_at	RIKEN cDNA 2310008H04 gene	2310008H04Rik	2.69	1.76*10^-04
1426937_at	mesenteric estrogen dependent adipogenesis	Medag	2.64	2.08*10^-06
1436763_a_at	Kruppel-like factor 9	Klf9	2.61	5.61*10^-05
1436329_at	Early growth response 3	Egr3	2.54	3.42*10^-04
1423259_at	Similar to Id4	LOC100045546	2.52	5.40*10^-05
1419043_a_at	Interferon inducible GTPase 1	Iigp1	2.52	7.52*10^-05
1419456_at	Dicarbonyl L-xylulose reductase	Dcxr	2.51	5.18*10^-04
1424638_at	Cyclin-dependent kinase inhibitor 1A (P21)	Cdkn1a	2.40	3.67*10^-05
1423877_at	Chromatin assembly factor 1, subunit B (p60)	Chaf1b	2.37	3.48*10^-04
1428838_a_at	Deoxycytidine kinase	Dck	2.35	1.30*10^-03
1424948_x_at	Histocompatibility 2, K region locus 1	H2-K1	2.33	1.47*10^-03
1418203_at	Phorbol-12-myristate-13-acetate-induced protein 1	Pmaip1	2.32	4.17*10^-03
1424754_at	Membrane-spanning 4-domains, subfamily A, member 7	Ms4a7	2.30	1.49*10^-04
1419598_at	Membrane-spanning 4-domains, subfamily A, member 6D	Ms4a6d	2.28	3.02*10^-03
1418901_at	CCAAT/enhancer binding protein (C/EBP), beta	Cebpb	2.28	7.81*10^-05
1450886_at	Germ cell-specific gene 2	Gsg2	2.25	3.43*10^-03
1418326_at	Solute carrier family 7 (cationic amino acid transporter, y+ system), member 5	Slc7a5	2.23	7.27*10^-05
1425927_a_at	Activating transcription factor 5	Atf5	2.17	7.07*10^-04
1418248_at	Galactosidase, alpha	Gla	2.16	3.96*10^-03
1453067_at	Apoptosis-inducing, TAF9-like domain 1	Apitd1	2.13	5.01*10^-04
1428942_at	Metallothionein 2	Mt2	2.13	9.47*10^-05
1424942_a_at	Myelocytomatosis oncogene	Myc	2.12	3.17*10^-04
1456653_a_at	Methylenetetrahydrofolate dehydrogenase (NADP+ dependent) 1-like	Mthfd1l	2.09	3.06*10^-04
1423585_at	Insulin-like growth factor binding protein 7	Igfbp7	2.09	2.44*10^-05
1460302_at	similar to thrombospondin 1	LOC640441	2.08	2.01*10^-03
1448842_at	Cysteine dioxygenase 1, cytosolic	Cdo1	2.08	3.30*10^-05
1460251_at	Fas (TNF receptor superfamily member 6)	Fas	2.05	1.54*10^-05
1420401_a_at	Receptor (calcitonin) activity modifying protein 3	Ramp3	2.04	5.05*10^-05

Affymetrix ID	Gene name	Gene symbol	FC	p-value
1452244_at	Mesenteric estrogen dependent adipogenesis	Medag	2.03	3.56*10^-03
1423233_at	CCAAT/enhancer binding protein (C/EBP), delta	Cebpd	2.02	4.59*10^-04
1417516_at	DNA-damage inducible transcript 3	Ddit3	2.01	1.38*10^-04
1453288_at	Activating transcription factor 6	Atf6	2.01	2.47*10^-04
1448749_at	Pleckstrin	Plek	2.01	8.54*10^-04
1427126_at	Heat shock protein 1A, heat shock protein 1B, heat shock protein 1-like	Hspa1a, Hspa1b, Hspa1l	2.01	3.85*10^-03
1420715_a_at	Peroxisome proliferator activated receptor gamma	Pparg	2.01	2.76*10^-05
1431166_at	Chromodomain helicase DNA binding protein 1	Chd1	1.99	1.02*10^-03
1429660_s_at	Structural maintenance of chromosomes 2	Smc2	1.98	7.43*10^-03
1418036_at	DNA primase, p58 subunit	Prim2	1.97	7.19*10^-04
1455679_at	Nucleic acid binding protein 1	Nabp1	1.97	1.41*10^-05
1452115_a_at	Polo-like kinase 4	Plk4	1.95	2.77*10^-04
1435990_at	A disintegrin-like and metallopeptidase (reprolysin type) with thrombospondin type1 motif, 2	Adamts2	1.93	2.00*10^-03
1441111_at	Myosin light chain kinase family, member 4	Mylk4	1.93	1.08*10^-06
1417185_at	Lymphocyte antigen 6 complex, locus A	Ly6a	1.93	1.01*10^-04
1428660_s_at	---	LOC100047963	1.92	1.14*10^-05
1424265_at	N-acetylneuraminate pyruvate lyase	Npl	1.91	3.88*10^-04
1452912_at	Defective in sister chromatid cohesion 1 homolog	Dscc1	1.89	4.92*10^-04
1455899_x_at	Suppressor of cytokine signaling 3	Socs3	1.89	5.00*10^-05
1433479_at	Ubiquitin protein ligase E3 component n-recognin 7 (putative)	Ubr7	1.86	1.39*10^-03
1421009_at	Radical S-adenosyl methionine domain containing 2	Rsad2	1.85	6.50*10^-07
1415859_at	Eukaryotic translation initiation factor 3, subunit C	Eif3c	1.85	2.33*10^-03
1437250_at	Melanoregulin	Mreg	1.84	1.76*10^-04
1424556_at	Pyrroline-5-carboxylate reductase 1	Pycr1	1.84	3.06*10^-05
1425364_a_at	Solute carrier family 3 (activators of dibasic and neutral amino acid transport), member 2	Slc3a2	1.84	3.14*10^-05
1417926_at	Non-SMC condensin II complex, subunit G2	Ncapg2	1.84	1.11*10^-04
1439071_at	RIKEN cDNA 5430416N02 gene	5430416N02Rik	1.82	1.27*10^-03
1423675_at	Ubiquitin specific peptidase 1	Usp1	1.80	7.49*10^-04
1432236_a_at	Suppressor of variegation 3-9 homolog	Suv39h1	1.80	1.48*10^-03
1429778_at	Optineurin	Optn	1.79	2.91*10^-04
1449363_at	Activating transcription factor 3	Atf3	1.79	4.18*10^-05
1448620_at	Fc receptor, IgG, low affinity III	Fcgr3	1.79	1.23*10^-03
1417143_at	Lysophosphatidic acid receptor 1	Lpar1	1.77	1.23*10^-04
1448899_s_at	RAD51 associated protein 1	Rad51ap1	1.76	3.64*10^-04
1429172_a_at	Non-SMC condensin I complex, subunit G	Ncapg	1.75	6.12*10^-03
1430780_a_at	Phosphomannomutase 1	Pmm1	1.75	1.11*10^-04
1438427_at	Family with sequence similarity 120, member B	Fam120b	1.74	8.05*10^-04
1438061_at	RIKEN cDNA 4930523C07 gene	4930523C07Rik	1.74	1.98*10^-04
1460353_at	NDC1 transmembrane nucleoporin	Ndc1	1.72	1.46*10^-04
1422804_at	Serine (or cysteine) peptidase inhibitor, clade B, member 6b	Serpinb6b	1.72	1.57*10^-04
1450350_a_at	Jun dimerization protein 2	Jdp2	1.71	4.63*10^-04
1421182_at	C-type lectin domain family 1, member b	Clec1b	1.71	9.71*10^-04
1448272_at	B-cell translocation gene 2, anti-proliferative	Btg2	1.71	3.12*10^-04
1417636_at	Solute carrier family 6 (neurotransmitter transporter, glycine), member 9	Slc6a9	1.70	1.68*10^-03
1437726_x_at	Complement component 1, q subcomponent, beta polypeptide	C1qb	1.70	6.15*10^-03
1454011_a_at	Replication protein A2	Rpa2	1.70	3.75*10^-05
1418979_at	Aldo-keto reductase family 1, member C14	Akr1c14	1.68	3.11*10^-03
1448183_a_at	Hypoxia inducible factor 1, alpha subunit	Hif1a	1.67	1.20*10^-04
1424211_at	Solute carrier family 25, member 33	Slc25a33	1.67	6.73*10^-04
1418825_at	Immunity-related GTPase family M member 1	Irgm1	1.66	4.51*10^-03
1438619_x_at	Zinc finger, DHHC domain containing 14	Zdhhc14	1.66	1.27*10^-04
1454942_at	Family with sequence similarity 129, member A	Fam129a	1.66	2.94*10^-04
1438556_a_at	Tropomodulin 3	Tmod3	1.65	1.65*10^-04
1433508_at	Kruppel-like factor 6	Klf6	1.65	4.64*10^-05
1438385_s_at	Glutamic pyruvate transaminase (alanine aminotransferase) 2	Gpt2	1.65	3.74*10^-03

Affymetrix ID	Gene name	Gene symbol	FC	p-value
1429775_a_at	Similar to Gpr137b protein	LOC100044979	1.64	4.48*10^-06
1423091_a_at	Glycoprotein m6b	Gpm6b	1.64	5.19*10^-03
1447936_at	RIKEN cDNA 2410006H16 gene	2410006H16Rik	1.64	2.81*10^-04
1452358_at	Retinoic acid induced 2	Rai2	1.64	4.41*10^-03
1448390_a_at	Dehydrogenase/reductase (SDR family) member 3	Dhrs3	1.64	5.48*10^-04
1426519_at	Procollagen-proline, 2-oxoglutarate 4-dioxygenase (proline 4-hydroxylase), alpha 1 polypeptide	P4ha1	1.64	1.64*10^-04
1448135_at	Activating transcription factor 4	Atf4	1.63	1.25*10^-04
1438161_s_at	Replication factor C (activator 1) 4	Rfc4	1.62	8.95*10^-04
1419693_at	Collectin sub-family member 12	Colec12	1.61	5.62*10^-04
1451064_a_at	Phosphoserine aminotransferase 1	Psat1	1.61	3.22*10^-03
1449708_s_at	Checkpoint kinase 1	Chek1	1.61	3.66*10^-03
1418649_at	Egl-9 family hypoxia-inducible factor 3	Egln3	1.61	3.05*10^-04
1439269_x_at	Minichromosome maintenance deficient 7	Mcm7	1.61	8.97*10^-04
1451924_a_at	Endothelin 1	Edn1	1.60	1.27*10^-03
1419029_at	ERO1-like	Ero1l	1.60	5.20*10^-05
1418919_at	Shugoshin-like 1	Sgol1	1.60	6.75*10^-04
1424202_at	SEH1-like	Seh1l	1.59	9.13*10^-03
1437187_at	E2F transcription factor 7	E2f7	1.59	1.73*10^-04
1448226_at	Ribonucleotide reductase M2	Rrm2	1.58	3.29*10^-04
1422535_at	Cyclin E2	Ccne2	1.58	1.37*10^-04
1453228_at	Syntaxin 11	Stx11	1.58	1.27*10^-03
1423918_at	Rhomboid domain containing 1	Rhbdd1	1.57	2.90*10^-03
1418290_a_at	Enhancer of zeste homolog 1	Ezh1	1.57	1.65*10^-03
1452792_at	DAZ interacting protein 1	Dzip1	1.57	1.80*10^-03
1452394_at	Cysteinyl-tRNA synthetase	Cars	1.57	1.40*10^-03
1454968_at	RIKEN cDNA 1110034A24 gene	1110034A24Rik	1.56	1.13*10^-03
1423153_x_at	Complement component factor h	Cfh	1.56	2.07*10^-04
1449155_at	Polymerase (RNA) III (DNA directed) polypeptide G	Polr3g	1.56	3.20*10^-03
1449372_at	DnaJ (Hsp40) homolog, subfamily C, member 3	Dnajc3a	1.55	4.29*10^-03
1416041_at	Serum/glucocorticoid regulated kinase 1	Sgk1	1.55	2.75*10^-04
1448777_at	Minichromosome maintenance deficient 2 mitotin	Mcm2	1.55	1.15*10^-03
1451310_a_at	Cathepsin L	Ctsl	1.55	6.85*10^-04
1424648_at	Intraflagellar transport 27	Ift27	1.54	5.35*10^-03
1449061_a_at	DNA primase, p49 subunit	Prim1	1.54	9.49*10^-04
1431005_at	DNA segment, Chr 10, Wayne State University 102, expressed	D10Wsu102e	1.54	3.48*10^-03
1440866_at	Eukaryotic translation initiation factor 2-alpha kinase 2	Eif2ak2	1.52	9.87*10^-05
1422016_a_at	Centromere protein H	Cenph	1.52	3.46*10^-03
1426995_a_at	Growth factor, erv1-like (augmenter of liver regeneration)	Gfer	1.52	8.05*10^-03
1423620_at	Centromere protein Q	Cenpq	1.52	2.00*10^-04
1416123_at	Cyclin D2	Ccnd2	1.52	6.00*10^-03
1425487_at	SLU7 splicing factor homolog	Slu7	1.52	1.08*10^-03
1426622_a_at	Glutaminyl-peptide cyclotransferase (glutaminyl cyclase)	Qpct	1.52	2.91*10^-03
1438852_x_at	Minichromosome maintenance deficient 6	Mcm6	1.51	1.99*10^-03
1426235_a_at	Glutamate-ammonia ligase (glutamine synthetase)	Glul	1.51	1.24*10^-03
1419292_at	HtrA serine peptidase 3	Htra3	1.51	6.42*10^-05
1418753_at	Glutamine fructose-6-phosphate transaminase 2	Gfpt2	1.50	6.24*10^-05
1451111_at	Nucleoporin 133	Nup133	1.50	1.66*10^-03
1435981_at	Neuron navigator 2	Nav2	-1.51	9.93*10^-03
1436277_at	Ring finger protein 207	Rnf207	-1.52	5.89*10^-03
1435728_at	tRNA-yW synthesizing protein 3 homolog	Tyw3	-1.52	2.51*10^-04
1426832_at	DEAD/H (Asp-Glu-Ala-Asp/His) box polypeptide 26B	Ddx26b	-1.57	5.67*10^-04
1424919_at	v-erb-b2 erythroblastic leukemia viral oncogene homolog 2, neuro/glioblastoma derived oncogene homolog	Erbb2	-1.57	5.09*10^-04
1427251_at	ATPase, Ca++ transporting, cardiac muscle, slow twitch 2	Atp2a2	-1.57	6.12*10^-04
1426032_at	Nuclear factor of activated T-cells, cytoplasmic, calcineurin-dependent 2	Nfatc2	-1.57	6.63*10^-03
1436331_at	Vacuolar protein sorting 13 D	Vps13d	-1.60	9.42*10^-03
1440231_at	Microtubule-associated protein 9	Mtap9	-1.62	9.89*10^-05
1455849_at	Neuron navigator 1	Nav1	-1.63	8.54*10^-03
1440870_at	PR domain containing 16	Prdm16	-1.65	4.70*10^-03

Affymetrix ID	Gene name	Gene symbol	FC	p-value
1456347_at	Leucyl/cystinyl aminopeptidase	Lnpep	-1.69	3.91*10^-03
1457513_at	Striatin interacting protein 1	Strip1	-1.70	4.29*10^-03
1418723_at	Lysophosphatidic acid receptor 3	Lpar3	-1.72	6.69*10^-05
1445517_at	Junction-mediating and regulatory protein	Jmy	-1.73	6.68*10^-03
1447493_at	Phosphoinositide-interacting regulator of transient receptor potential channels	Pirt	-1.73	6.55*10^-03
1454532_at	RIKEN cDNA C030043A13 gene	C030043A13Rik	-1.74	3.28*10^-03
1460028_at	Glutamate receptor interacting protein 2	Grip2	-1.74	6.72*10^-04
1436936_s_at	Inactive X specific transcripts	Xist	-1.77	4.69*10^-03
1452661_at	Transferrin receptor	Tfr	-1.78	1.55*10^-03
1456632_at	B-cell CLL/lymphoma 11A (zinc finger protein)	Bcl11a	-1.78	1.69*10^-03
1451105_at	Vasohibin 2	Vash2	-1.79	1.07*10^-06
1417305_at	SPEG complex locus	Speg	-1.79	2.68*10^-04
1439848_at	Blood vessel epicardial substance	Bves	-1.79	2.83*10^-03
1449566_at	NK2 homeobox 5	Nkx2-5	-1.85	4.15*10^-06
1446965_at	Rho guanine nucleotide exchange factor (GEF) 12	Arhgef12	-1.88	1.57*10^-04
1460628_at	Essential meiotic endonuclease 1 homolog 2	Eme2	-1.94	4.46*10^-03
1446380_at	cAMP responsive element binding protein 5	Creb5	-1.95	5.44*10^-04
1429718_at	SLIT and NTRK-like family, member 5	Slitrk5	-1.97	6.56*10^-04
1440259_at	Mannosidase, alpha, class 1A, member 2	Man1a2	-1.98	4.35*10^-04
1426298_at	Iroquois related homeobox 2	Irx2	-2.02	2.28*10^-04
1443081_at	GATA binding protein 6	Gata6	-2.02	1.43*10^-03
1428117_x_at	Dynein light chain Tctex-type 1, pseudogene 1; Dynein light chain Tctex-type 1B; Dynein light chain Tctex-type 1C; Dynein light chain Tctex-type 1D; Dynein light chain Tctex-type 1E; Dynein light chain Tctex-type 1F	Dynlt1-ps1, Dynlt1b; Dynlt1c, Dynlt1d; Dynlt1e, Dynlt1f	-2.04	5.74*10^-03
1441836_x_at	Gametocyte specific factor 1	Gtsf1	-2.13	8.12*10^-04
1446346_at	A disintegrin-like and metallopeptidase (reprolysin type) with thrombospondin type 1 motif, 9	Adamts9	-2.14	7.76*10^-03
1441573_at	Sex comb on midleg homolog 1	Scmh1	-2.16	6.06*10^-03
1441140_at	Arginine glutamic acid dipeptide (RE) repeats	Rere	-2.23	3.03*10^-03
1435053_s_at	Pleckstrin homology domain containing, family H (with MyTH4 domain) member 1	Plekhh1	-2.32	7.42*10^-05
1441193_at	RIKEN cDNA 5730407M17 gene	5730407M17Rik	-2.37	7.47*10^-03
1439586_at	---	LOC548102	-2.38	4.29*10^-04
1442618_at	Lactate dehydrogenase B	Ldhb	-2.45	6.11*10^-03
1460499_at	RIKEN cDNA 9230110I02 gene	9230110I02Rik	-2.54	6.12*10^-04
1441744_at	Calcium channel, voltage-dependent, L type, alpha 1C subunit	Cacna1c	-2.58	7.10*10^-04
1446014_at	Mitogen-activated protein kinase 8	Mapk8	-2.60	6.79*10^-03
1437431_at	Cut-like homeobox 1	Cux1	-2.61	3.66*10^-04
1443258_at	Forkhead box P1	Foxp1	-2.69	3.01*10^-05
1446954_at	Pyruvate dehydrogenase E1 alpha 1	Pdha1	-2.74	7.85*10^-03
1442632_at	ArfGAP with GTPase domain, ankyrin repeat and PH domain 1	Agap1	-2.83	1.76*10^-03
1441441_at	Proline rich Gla (G-carboxyglutamic acid) 1	Prrg1	-2.94	9.35*10^-04
1442586_at	Suppressor of cytokine signaling 2	Socs2	-2.95	7.96*10^-06
1457642_at	SKI/DACH domain containing 1	Skida1	-3.06	2.10*10^-04
1454395_at	RIKEN cDNA 4632404M16 gene	4632404M16Rik	-3.09	1.03*10^-03
1447043_at	V-erb-a erythroblastic leukemia viral oncogene homolog 4 (avian)	Erbb4	-3.19	1.18*10^-04
1443287_at	Ankyrin repeat domain 63	Ankrd63	-3.20	3.59*10^-04
1446258_at	RIKEN cDNA 9530067D14 gene	9530067D14Rik	-3.28	5.60*10^-07
1457583_at	ST6 (alpha-N-acetyl-neuraminyl-2,3-beta-galactosyl-1,3)-N-acetylgalactosaminide alpha-2,6-sialyltransferase 3	St6galnac3	-3.43	5.12*10^-03
1435984_at	Zinc finger protein 40	Zfp40	-3.53	8.34*10^-03

Listed are differentially regulated genes in neonatal (P1) c*Hccs*$^{+/-}$ hearts compared to *Hccs*$^{+/+}$ controls as determined by Affymetrix microarray analysis. Only genes with a fold change (FC) higher than 1.5 or lower than -1.5 in combination with a highly significant *p*-value ($p<0.001$) are tabulated.

Supplementary Table S2. Neonatal c*Hccs*$^{+/-}$ hearts display enrichment of genes involved in amino acid metabolism

Functional group	*p*-value
Amino acid biosynthesis	1.3*10^-03
Glutamine metabolic process	1.4*10^-03
Glutamine family amino acid metabolic process	1.7*10^-03
Cellular amino acid biosynthetic process	1.9*10^-03
Alanine, aspartate and glutamate metabolism	8.4*10^-03
Amine biosynthetic process	1.1*10^-02

Detailed listing of significantly enriched functional groups involved in amino acid metabolism as determined by DAVID functional annotation microarray analysis of gene class changes in neonatal c*Hccs*$^{+/-}$ hearts.

Supplementary Table S3. Neonatal c*Hccs*$^{+/-}$ hearts display enrichment of genes involved in amino acid transport

Functional group	*p*-value
Amino acid transport	4.8*10^-03
Amino acid transmembrane transporter activity	1.9*10^-02
Amine transport	2.5*10^-02
Carboxylic acid transport	3.1*10^-02
Organic acid transport	3.2*10^-02
Amine transmembrane transporter activity	3.4*10^-02

Detailed listing of significantly enriched functional groups involved in amino acid transport as determined by DAVID functional annotation microarray analysis of gene class changes in neonatal c*Hccs*$^{+/-}$ hearts.

Supplementary Table S4. Neonatal c*Hccs*$^{+/-}$ hearts display enrichment of genes involved in cellular metabolism

Functional group	*p*-value
Hexose metabolic process	4.3*10^-03
Glucose metabolic process	6.8*10^-03
Monosaccharide metabolic process	8.2*10^-03
Hexose biosynthetic process	3.6*10^-02
Monosaccharide biosynthetic process	5.3*10^-02

Detailed listing of significantly enriched functional groups involved in cellular metabolism as determined by DAVID functional annotation microarray analysis of gene class changes in neonatal c*Hccs*$^{+/-}$ hearts.

Supplementary Table S5. Echocardiographic measurements in neonatal mice after prenatal mTORC1 inhibition

	n	IVS dia (mm)	LVPW dia (mm)	IVS sys (mm)	LVPW sys (mm)	LVID dia (mm)	LVID sys (mm)	FS (%)	EF (%)
V									
***Hccs*$^{+/+}$**	7	0.27 ±0.01	0.27 ±0.02	0.43 ±0.02	0.44 ±0.02	1.50 ±0.04	1.02 ±0.04	31.86 ±1.46	63.05 ±1.92
c*Hccs*$^{+/-}$	6	0.26 ±0.01	0.27 ±0.01	0.40 ±0.02	0.40 ±0.02	1.41 ±0.05	0.97 ±0.04	31.08 ±1.42	64.06 ±1.98
R									
***Hccs*$^{+/+}$**	6	0.24 ±0.01	0.26 ±0.01	0.36§ ±0.01	0.38 ±0.02	1.27§§ ±0.05	0.90 ±0.05	29.50 ±1.65	61.38 ±3.00
c*Hccs*$^{+/-}$	7	0.23 ±0.02	0.23 ±0.02	0.34 ±0.02	0.35 ±0.02	1.27 ±0.04	0.04 ±0.23	27.36 ±1.53	55.60$^{\#}$ ±1.77

Echocardiography was performed in neonatal *Hccs*$^{+/+}$ and c*Hccs*$^{+/-}$ mice after prenatal rapamycin treatment. Left ventricular (LV) wall thickness, diameter and contractility were determined in end-systole and end-diastole. Statistical significance among groups was assessed by one-way ANOVA followed by Bonferroni post-hoc test (§p<0.05 vs. vehicle *Hccs*$^{+/+}$, §§p<0.01 vs. vehicle *Hccs*$^{+/+}$, #p<0.05 vs. vehicle c*Hccs*$^{+/-}$). (dia: end-diastole, EF: ejection fraction, FS: fractional shortening, IVS: interventricular septum, LVID: left ventricular internal diameter, LVPW: left ventricular posterior wall, R: rapamycin, sys: end-systole, V: vehicle)

Supplementary Table S6. Echocardiographic measurements in 11 week old adult mice after prenatal mTORC1 inhibition

	n	IVS dia (mm)	LVPW dia (mm)	IVS sys (mm)	LVPW sys (mm)	LVID dia (mm)	LVID sys (mm)	FS (%)	EF (%)
V									
***Hccs*$^{+/+}$**	7	0.74 ±0.02	0.75 ±0.02	0.99 ±0.02	0.94 ±0.05	3.66 ±0.11	2.87 ±0.12	21.66 ±1.53	43.64 ±2.38
c*Hccs*$^{+/-}$	6	0.76 ±0.06	0.76 ±0.04	0.99 ±0.05	0.98 ±0.06	3.96 ±0.18	3.07 ±0.24	23.07 ±2.81	45.18 ±4.64
R									
***Hccs*$^{+/+}$**	9	0.62 ±0.04	0.61 ±0.04	0.83 ±0.06	0.83 ±0.05	3.64 ±0.08	2.84 ±0.14	22.21 ±2.37	45.71 ±3.70
c*Hccs*$^{+/-}$	6	0.63 ±0.04	0.63 ±0.04	0.88 ±0.08	0.88 ±0.05	3.91 ±0.13	3.00 ±0.19	23.58 ±2.45	47.17 ±4.12

Echocardiography was performed in 11 week old adult *Hccs*$^{+/+}$ and c*Hccs*$^{+/-}$ mice after prenatal rapamycin treatment. Left ventricular (LV) wall thickness, diameter and contractility were determined in end-systole and end-diastole. Note that no significant differences between the treatment groups and the genotypes were observed for any of the analyzed parameters. Statistical significance among groups was assessed by one-way ANOVA followed by Bonferroni post-hoc test. (dia: end-diastole, EF: ejection fraction, FS: fractional shortening, IVS: interventricular septum, LVID: left ventricular internal diameter, LVPW: left ventricular posterior wall, R: rapamycin, sys: end-systole, V: vehicle)

Supplementary Table S7. Echocardiographic measurements in 11 week old adult mice after pre- and postnatal amino acid restriction

	n	IVS dia (mm)	LVPW dia (mm)	IVS sys (mm)	LVPW sys (mm)	LVID dia (mm)	LVID sys (mm)	FS (%)	EF (%)
SPD									
***Hccs*$^{+/+}$**	7	0.66 ±0.03	0.65 ±0.03	1.05 ±0.07	1.00 ±0.07	3.96 ±0.07	2.74 ±0.17	31.03 ±3.23	59.12 ±4.50
c*Hccs*$^{+/-}$	6	0.71 ±0.02	0.69 ±0.03	1.06 ±0.04	0.99 ±0.04	4.01 ±0.09	2.91 ±0.13	27.71 ±1.90	53.09 ±3.51
LPD									
***Hccs*$^{+/+}$**	6	0.72 ±0.03	0.74 ±0.02	1.05 ±0.05	1.05 ±0.05	3.70 ±0.06	2.62 ±0.20	29.38 ±4.56	56.23 ±7.33
c*Hccs*$^{+/-}$	7	0.77 ±0.04	0.75 ±0.05	1.05 ±0.04	1.03 ±0.04	3.68 ±0.13	2.69 ±0.23	27.71 ±4.21	53.64 ±5.31

Echocardiography was performed in 11 week old *Hccs*$^{+/+}$ and c*Hccs*$^{+/-}$ mice after pre- and postnatal SPD or LPD exposure. Left ventricular (LV) wall thickness, diameter and contractility were determined in end-systole and end-diastole. Note that no significant differences between the diet groups and the genotypes were observed for any of the analyzed parameters. Statistical significance among groups was assessed by one-way ANOVA followed by Bonferroni post-hoc test. (dia: end-diastole, EF: ejection fraction, FS: fractional shortening, IVS: interventricular septum, LPD: low protein diet, LVID: left ventricular internal diameter, LVPW: left ventricular posterior wall, SPD: standard protein diet, sys: end-systole)

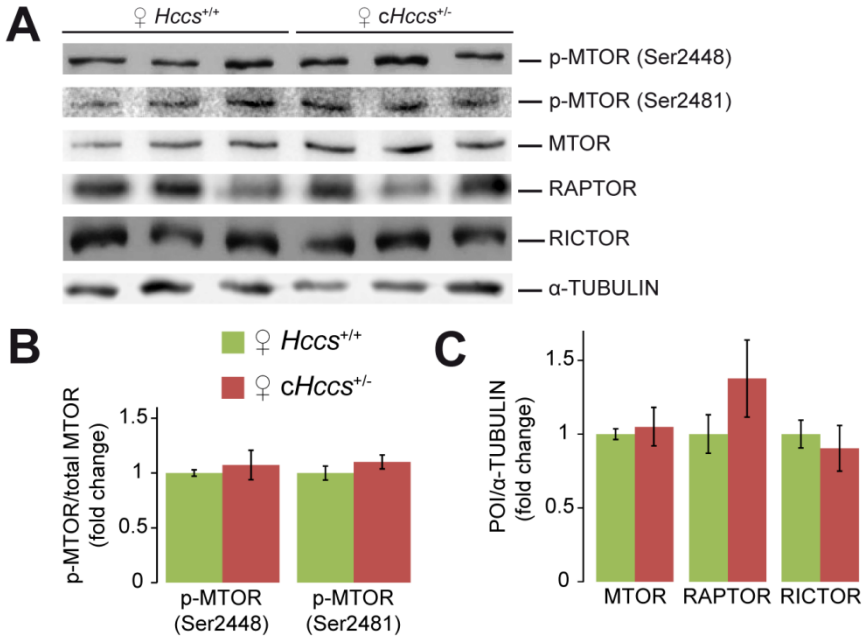

Supplementary Figure 1. Protein levels and phosphorylation status of mTORC1 and mTORC2 core components are unchanged in c*Hccs*$^{+/-}$ neonatal hearts.
A) Western blots of whole heart protein extracts from neonates illustrating total protein levels of MTOR, RAPTOR and RICTOR as well as the phosphorylation status of MTOR at serine 2448 and 2481. **B)** Quantification of MTOR phosphorylation normalized to total MTOR and **C)** of MTOR, RAPTOR and RICTOR total protein levels normalized to α-TUBULIN revealed no significant differences between neonatal *Hccs*$^{+/+}$ and c*Hccs*$^{+/-}$ hearts. Statistical significance among groups was assessed using unpaired 2-tailed Student *t*-test (n=8 per group). (POI: protein of interest)

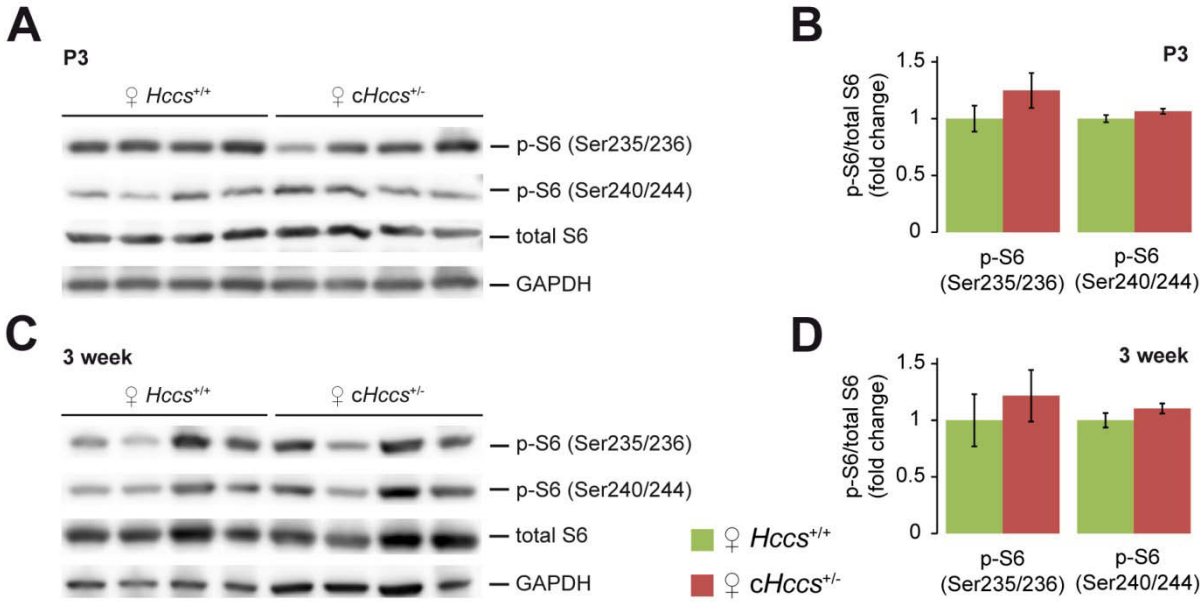

Supplementary Figure 2. Phosphorylation status of mTORC1 downstream targets S6K1 and S6 is unchanged in 3 day and 3 week old c*Hccs*$^{+/-}$ hearts compared to hearts from *Hccs*$^{+/+}$ littermate controls.
A) Western blots of whole heart protein extracts from offspring at postnatal day 3 (P3) illustrating the phosphorylation status of S6 at serine 235, 236, 240 and 244. **B)** Quantification of S6 phosphorylation normalized to total S6 revealed no significant differences between *Hccs*$^{+/+}$ and c*Hccs*$^{+/-}$ P3 hearts. **C)** Western blots of protein extracts from apical heart tissue of 3 week old animals illustrating the phosphorylation status of S6 at serine 235, 236, 240 and 244. **B)** Quantification of S6 phosphorylation normalized to total S6 revealed no significant differences between 3 week old *Hccs*$^{+/+}$ and c*Hccs*$^{+/-}$ hearts. For **B)**+**C)**: Statistical significance among groups was assessed using unpaired 2-tailed Student *t*-test (n=10 per group).

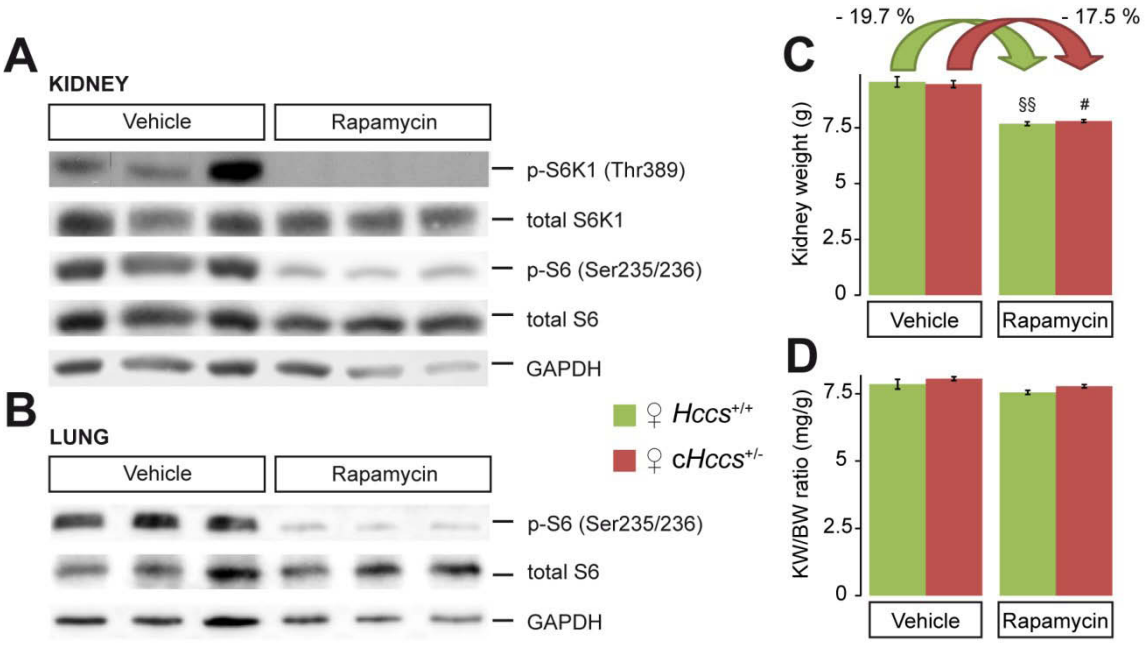

Supplementary Figure 3. Prenatal rapamycin treatment of pregnant mice results in mTORC1 inhibition in neonatal kidney and lung tissue as well as reduced neonatal kidney weight.
A) Western blots of whole kidney protein extracts from neonates after prenatal vehicle or rapamycin treatment displaying the phosphorylation status of S6K1 at threonine 389 and of S6 at serine 235 and 236. In rapamycin treated mice, decreased phosphorylation was obvious at all sites analyzed, indicating mTORC1 inhibition in neonatal kidney tissue. **B)** Western blots of lung protein extracts from neonates after prenatal vehicle or rapamycin treatment displaying the phosphorylation status of S6 at serine 235 and 236. Phosphorylation of S6 was severely reduced in rapamycin treated mice, indicating mTORC1 inhibition in neonatal lung tissue. **C)** Significant reduction of kidney weight in rapamycin treated neonates compared to vehicle treated animals. **D)** Kidney weight to body weight (KW/BW) ratio in neonatal mice was unchanged between the genotypes and the treatment groups. For **C)+D)**: Statistical significance among groups was assessed by one-way ANOVA followed by Bonferroni post-hoc test (§§p<0.01 vs. vehicle *Hccs*$^{+/+}$, #p<0.05 vs. vehicle c*Hccs*$^{+/-}$, n=9 for vehicle *Hccs*$^{+/+}$ and c*Hccs*$^{+/-}$, n=10 for rapamycin *Hccs*$^{+/+}$ and c*Hccs*$^{+/-}$).

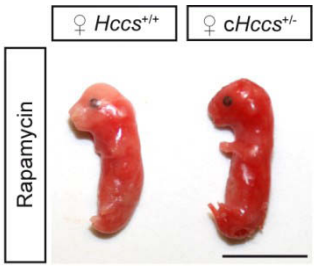

Supplementary Figure 4. Prenatal mTORC1 inhibition from 11.5 dpc onwards results in preterm birth and fetal lethality.
Hccs$^{+/+}$ as well as c*Hccs*$^{+/-}$ embryos were subjected to lethal preterm birth at 16.5 dpc and demonstrated severe growth retardation and body malformations when rapamycin treatment was initiated at 11.5 dpc (scale bar = 1 cm).

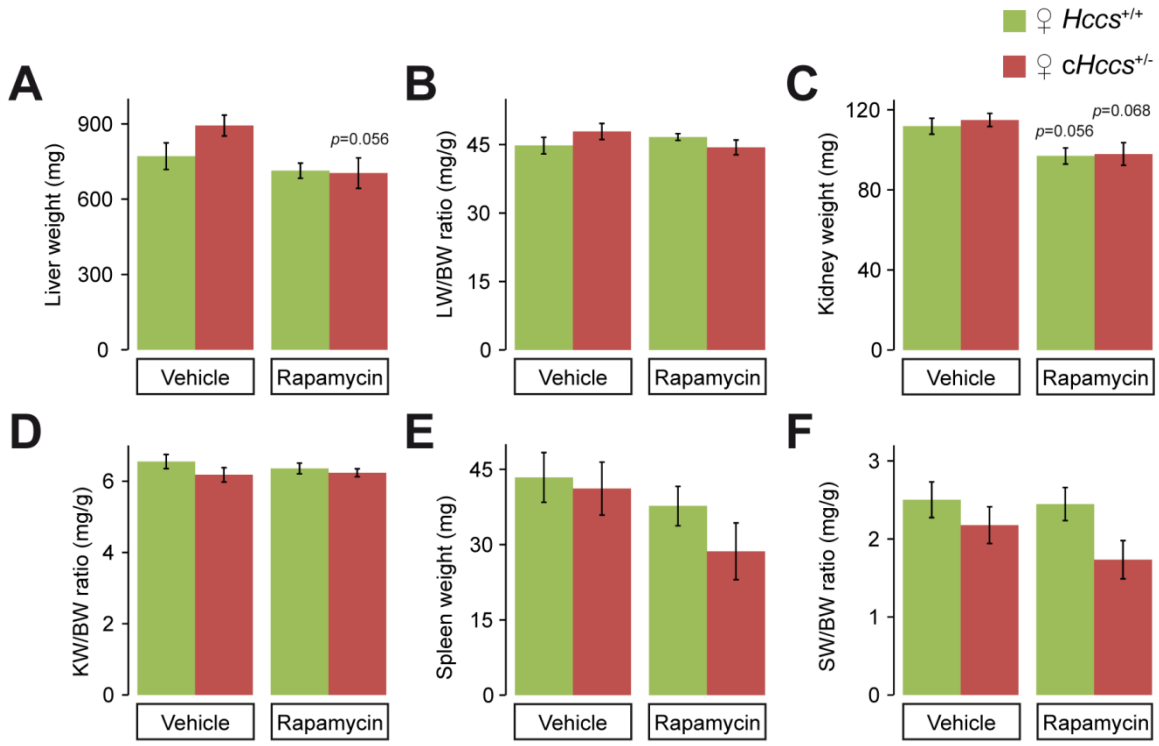

Supplementary Figure 5. Organ weights of liver, kidney and spleen in 11 week old adult mice upon intrauterine mTORC1 inhibition are not significantly different compared to those of vehicle treated animals.
A) Liver weight (LW), **B)** LW to body weight (LW/BW) ratio, **C)** kidney weight (KW), **D)** KW to BW (KW/BW) ratio, **E)** spleen weight (SW) and **F)** SW to BW (SW/BW) ratio in adult mice displayed no significant differences between the treatment groups or the genotypes. Note that absolute LW, KW and SW in adult mice of both genotypes after prenatal mTORC1 inhibition were slightly lower than in vehicle treated animals, indicating only partial organ size normalization during postnatal life. Statistical significance among groups was assessed by one-way ANOVA followed by Bonferroni post-hoc test (n=7 for vehicle *Hccs*$^{+/+}$, n=6 for vehicle and rapamycin c*Hccs*$^{+/-}$, n=9 for rapamycin *Hccs*$^{+/+}$).

BIBLIOGRAPHY

1 Lin, C. J. *et al.* 2012. Partitioning the heart: Mechanisms of cardiac septation and valve development. *Development*. **139:** 3277-3299.

2 Barker, D. J. *et al.* 1989. Weight in infancy and death from ischaemic heart disease. *Lancet*. **2:** 577-580.

3 Barker, D. J. *et al.* 1989. Growth in utero, blood pressure in childhood and adult life, and mortality from cardiovascular disease. *BMJ*. **298:** 564-567.

4 Barker, D. J. *et al.* 1990. Fetal and placental size and risk of hypertension in adult life. *BMJ*. **301:** 259-262.

5 Hales, C. N. *et al.* 1991. Fetal and infant growth and impaired glucose tolerance at age 64. *BMJ*. **303:** 1019-1022.

6 Barker, D. J. *et al.* 1993. Type 2 (non-insulin-dependent) diabetes mellitus, hypertension and hyperlipidaemia (syndrome X): Relation to reduced fetal growth. *Diabetologia*. **36:** 62-67.

7 Hales, C. N. & Barker, D. J. 1992. Type 2 (non-insulin-dependent) diabetes mellitus: The thrifty phenotype hypothesis. *Diabetologia*. **35:** 595-601.

8 Poulsen, P. *et al.* 1997. Low birth weight is associated with NIDDM in discordant monozygotic and dizygotic twin pairs. *Diabetologia*. **40:** 439-446.

9 Ravelli, A. C. *et al.* 1998. Glucose tolerance in adults after prenatal exposure to famine. *Lancet*. **351:** 173-177.

10 Roseboom, T. J. *et al.* 2000. Coronary heart disease after prenatal exposure to the dutch famine, 1944-45. *Heart*. **84:** 595-598.

11 Painter, R. C. *et al.* 2005. Microalbuminuria in adults after prenatal exposure to the dutch famine. *J. Am. Soc. Nephrol.* **16:** 189-194.

12 Fowden, A. L. *et al.* 2006. Intrauterine programming of physiological systems: Causes and consequences. *Physiology (Bethesda)*. **21:** 29-37.

13 Langley-Evans, S. C. & McMullen, S. 2010. Developmental origins of adult disease. *Med. Princ. Pract*. **19:** 87-98.

14 Leon, D. A. *et al.* 1998. Reduced fetal growth rate and increased risk of death from ischaemic heart disease: Cohort study of 15 000 swedish men and women born 1915-29. *BMJ*. **317:** 241-245.

15 Eriksson, J. G. *et al.* 1999. Catch-up growth in childhood and death from coronary heart disease: Longitudinal study. *BMJ*. **318:** 427-431.

16 Singhal, A. *et al.* 2004. Is slower early growth beneficial for long-term cardiovascular health? *Circulation*. **109:** 1108-1113.

17 Singhal, A. *et al.* 2007. Promotion of faster weight gain in infants born small for gestational age: Is there an adverse effect on later blood pressure? *Circulation*. **115:** 213-220.

18 Barker, D. J. 2000. In utero programming of cardiovascular disease. *Theriogenology*. **53:** 555-574.

19 McMillen, I. C. & Robinson, J. S. 2005. Developmental origins of the metabolic syndrome: Prediction, plasticity, and programming. *Physiol. Rev.* **85:** 571-633.

20 Chan, J. C. *et al.* 2009. Diabetes in asia: Epidemiology, risk factors, and pathophysiology. *JAMA*. **301:** 2129-2140.

21 Wu, G. 2013. Functional amino acids in nutrition and health. *Amino Acids*. **45:** 407-411.

22 Snoeck, A. *et al.* 1990. Effect of a low protein diet during pregnancy on the fetal rat endocrine pancreas. *Biol. Neonate*. **57:** 107-118.

23 Corstius, H. B. *et al.* 2005. Effect of intrauterine growth restriction on the number of cardiomyocytes in rat hearts. *Pediatr. Res.* **57:** 796-800.

24 Aroutiounova, N. *et al.* 2009. Prenatal exposure to maternal low protein diet suppresses replicative potential of myocardial cells. *Nutr. Metab. Cardiovasc. Dis*. **19:** 707-712.

25 Lim, K. *et al.* 2010. Effect of maternal protein restriction during pregnancy and lactation on the number of cardiomyocytes in the postproliferative weanling rat heart. *Anat. Rec. (Hoboken)*. **293:** 431-437.

26 Lim, K. *et al.* 2006. Effect of maternal protein restriction in rats on cardiac fibrosis and capillarization in adulthood. *Pediatr. Res.* **60:** 83-87.

27 Cheema, K. K. *et al.* 2005. Prenatal exposure to maternal undernutrition induces adult cardiac dysfunction. *Br. J. Nutr.* **93:** 471-477.

28 Xu, Y. *et al.* 2006. Hypoxia or nutrient restriction during pregnancy in rats leads to progressive cardiac remodeling and impairs postischemic recovery in adult male offspring. *FASEB J.* **20:** 1251-1253.

29 Torrens, C. *et al.* 2006. Folate supplementation during pregnancy improves offspring cardiovascular dysfunction induced by protein restriction. *Hypertension*. **47:** 982-987.

30 Elmes, M. J. *et al.* 2007. Fetal exposure to a maternal low-protein diet is associated with altered left ventricular pressure response to ischaemia-reperfusion injury. *Br. J. Nutr.* **98:** 93-100.

31 Tarry-Adkins, J. L. *et al.* 2013. Poor maternal nutrition followed by accelerated postnatal growth leads to alterations in DNA damage and repair, oxidative and nitrosative stress, and oxidative defense capacity in rat heart. *FASEB J.* **27:** 379-390.

32 Baschat, A. A. & Hecher, K. 2004. Fetal growth restriction due to placental disease. *Semin. Perinatol.* **28:** 67-80.

33 Black, M. J. *et al.* 2012. Normal lactational environment restores cardiomyocyte number after uteroplacental insufficiency: Implications for the preterm neonate. *Am. J. Physiol. Regul. Integr. Comp. Physiol*. **302:** R1101-1110.

34 Bae, S. *et al.* 2003. Effect of maternal chronic hypoxic exposure during gestation on apoptosis in fetal rat heart. *Am. J. Physiol. Heart Circ. Physiol*. **285:** H983-990.

35 Rueda-Clausen, C. F. *et al.* 2009. Effects of hypoxia-induced intrauterine growth restriction on cardiopulmonary structure and function during adulthood. *Cardiovasc. Res.* **81:** 713-722.

36 Ream, M. *et al.* 2008. Early fetal hypoxia leads to growth restriction and myocardial thinning. *Am. J. Physiol. Regul. Integr. Comp. Physiol*. **295:** R583-595.

37 Li, G. *et al.* 2004. Effect of prenatal hypoxia on heat stress-mediated cardioprotection in adult rat heart. *Am. J. Physiol. Heart Circ. Physiol*. **286:** H1712-1719.

38 Li, G. *et al.* 2003. Effect of fetal hypoxia on heart susceptibility to ischemia and reperfusion injury in the adult rat. *J. Soc. Gynecol. Investig.* **10:** 265-274.

39 McMullen, S. *et al.* 2012. A common cause for a common phenotype: The gatekeeper hypothesis in fetal programming. *Med. Hypotheses*. **78:** 88-94.

40 Weaver, I. C. *et al.* 2004. Epigenetic programming by maternal behavior. *Nat. Neurosci.* **7:** 847-854.

41 Dolinoy, D. C. *et al.* 2007. Epigenetic gene regulation: Linking early developmental environment to adult disease. *Reprod. Toxicol.* **23:** 297-307.

42 Morgan, H. D. *et al.* 2005. Epigenetic reprogramming in mammals. *Hum. Mol. Genet.* **14 Spec No 1:** R47-58.

43 Bogdarina, I. *et al.* 2007. Epigenetic modification of the renin-angiotensin system in the fetal programming of hypertension. *Circ. Res.* **100:** 520-526.

44 Ishiwata, T. *et al.* 2003. Developmental changes in ventricular diastolic function correlate with changes in ventricular myoarchitecture in normal mouse embryos. *Circ. Res.* **93:** 857-865.

45 Srivastava, D. & Olson, E. N. 2000. A genetic blueprint for cardiac development. *Nature*. **407:** 221-226.

46 Sedmera, D. *et al.* 2000. Developmental patterning of the myocardium. *Anat. Rec.* **258:** 319-337.

47 Savolainen, S. M. *et al.* 2009. Histology atlas of the developing mouse heart with emphasis on E11.5 to E18.5. *Toxicol. Pathol.* **37:** 395-414.

48 Erokhina, E. L. 1968. Proliferation dynamics of cellular elements in the differentiating mouse myocardium. *Tsitologiia*. **10:** 1391-1409.

49 Erokhina, I. L. 1968. The proliferation and DNA synthesis during early stages of myocardial development. *Tsitologiia*. **10:** 162-172.

50 Rumyantsev, P. P. 1977. Interrelations of the proliferation and differentiation processes during cardiact myogenesis and regeneration. *Int. Rev. Cytol.* **51:** 186-273.

51 Ritter, M. *et al.* 1997. Isolated noncompaction of the myocardium in adults. *Mayo Clin. Proc.* **72:** 26-31.

52 Towbin, J. A. 2010. Left ventricular noncompaction: A new form of heart failure. *Heart Fail. Clin*. **6:** 453-469.

53 Klaassen, S. *et al.* 2008. Mutations in sarcomere protein genes in left ventricular noncompaction. *Circulation*. **117:** 2893-2901.

54 Ichida, F. *et al.* 2001. Novel gene mutations in patients with left ventricular noncompaction or barth syndrome. *Circulation*. **103:** 1256-1263.

55 Hermida-Prieto, M. *et al.* 2004. Familial dilated cardiomyopathy and isolated left ventricular noncompaction associated with lamin A/C gene mutations. *Am. J. Cardiol.* **94:** 50-54.

56 Shou, W. *et al.* 1998. Cardiac defects and altered ryanodine receptor function in mice lacking FKBP12. *Nature*. **391:** 489-492.

57 Arndt, A. K. *et al.* 2013. Fine mapping of the 1p36 deletion syndrome identifies mutation of PRDM16 as a cause of cardiomyopathy. *Am. J. Hum. Genet*. **93:** 67-77.

58 Csibi, A. & Blenis, J. 2012. Hippo-YAP and mTOR pathways collaborate to regulate organ size. *Nat. Cell. Biol*. **14:** 1244-1245.

59 von Gise, A. *et al.* 2012. YAP1, the nuclear target of Hippo signaling, stimulates heart growth through cardiomyocyte proliferation but not hypertrophy. *Proc. Natl. Acad. Sci. U. S. A.* **109:** 2394-2399.

60 Levkau, B. *et al.* 2008. Survivin determines cardiac function by controlling total cardiomyocyte number. *Circulation*. **117:** 1583-1593.

61 Zak, R. 1973. Cell proliferation during cardiac growth. *Am. J. Cardiol.* **31:** 211-219.

62 Zak, R. 1974. Development and proliferative capacity of cardiac muscle cells. *Circ. Res.* **35:** suppl II:17-26.

63 Bugaisky, L. & Zak, R. 1979. Cellular growth of cardiac muscle after birth. *Tex. Rep. Biol. Med*. **39:** 123-138.

64 Li, F. *et al.* 1996. Rapid transition of cardiac myocytes from hyperplasia to hypertrophy during postnatal development. *J. Mol. Cell. Cardiol.* **28:** 1737-1746.

65 Brodsky, W. Y. *et al.* 1980. Mitotic polyploidization of mouse heart myocytes during the first postnatal week. *Cell Tissue. Res.* **210:** 133-144.

66 Oparil, S. *et al.* 1984. Myocardial cell hypertrophy or hyperplasia. *Hypertension*. **6:** III38-43.

67 Korecky, B. *et al.* 1979. Number of nuclei in mammalian cardiac myocytes. *Can. J. Physiol. Pharmacol.* **57:** 1122-1129.

68 Anversa, P. *et al.* 1980. Morphometric study of early postnatal development in the left and right ventricular myocardium of the rat. I. Hypertrophy, hyperplasia, and binucleation of myocytes. *Circ. Res.* **46:** 495-502.

69 Clubb, F. J., Jr. & Bishop, S. P. 1984. Formation of binucleated myocardial cells in the neonatal rat. An index for growth hypertrophy. *Lab. Invest.* **50:** 571-577.

70 Soonpaa, M. H. *et al.* 1996. Cardiomyocyte DNA synthesis and binucleation during murine development. *Am. J. Physiol.* **271:** H2183-2189.

71 Wulfsohn, D. *et al.* 2004. Postnatal growth of cardiomyocytes in the left ventricle of the rat. *Anat. Rec. A Discov. Mol. Cell. Evol. Biol*. **277:** 236-247.

72 Naqvi, N. *et al.* 2014. A proliferative burst during preadolescence establishes the final cardiomyocyte number. *Cell*. **157:** 795-807.

73 Camacho, J. A. *et al.* 1990. Accelerated ribosome formation and growth in neonatal pig hearts. *Am. J. Physiol.* **258:** C86-91.

74 Henglein, B. *et al.* 1994. Structure and cell cycle-regulated transcription of the human cyclin A gene. *Proc. Natl. Acad. Sci. U. S. A.* **91:** 5490-5494.

75 Jahn, L. *et al.* 1994. Cyclins and cyclin-dependent kinases are differentially regulated during terminal differentiation of C2C12 muscle cells. *Exp. Cell Res.* **212:** 297-307.

76 Kang, M. J. *et al.* 1997. Cyclins and cyclin dependent kinases during cardiac development. *Mol. Cells*. **7:** 360-366.

77 Kang, M. J. & Koh, G. Y. 1997. Differential and dramatic changes of cyclin-dependent kinase activities in cardiomyocytes during the neonatal period. *J. Mol. Cell. Cardiol.* **29:** 1767-1777.

78 Soonpaa, M. H. & Field, L. J. 1997. Assessment of cardiomyocyte DNA synthesis in normal and injured adult mouse hearts. *Am. J. Physiol.* **272:** H220-226.

79 Toyoda, M. *et al.* 2003. Jumonji downregulates cardiac cell proliferation by repressing cyclin D1 expression. *Dev. Cell*. **5:** 85-97.

80 Poolman, R. A. *et al.* 1998. Cell cycle profiles and expressions of p21CIP1 and p27KIP1 during myocyte development. *Int. J. Cardiol.* **67:** 133-142.

81 Flink, I. L. *et al.* 1998. Changes in E2F complexes containing retinoblastoma protein family members and increased cyclin-dependent kinase inhibitor activities during terminal differentiation of cardiomyocytes. *J. Mol. Cell. Cardiol.* **30:** 563-578.

82 Puente, B. N. *et al.* 2014. The oxygen-rich postnatal environment induces cardiomyocyte cell-cycle arrest through DNA damage response. *Cell*. **157:** 565-579.

83 Hoerter, J. A. & Opie, L. H. 1978. Perinatal changes in glycolytic function in response to hypoxia in the incubated or perfused rat heart. *Biol. Neonate*. **33:** 144-161.

84 Fisher, D. J. *et al.* 1981. Myocardial consumption of oxygen and carbohydrates in newborn sheep. *Pediatr. Res.* **15:** 843-846.

85 Rolph, T. P. & Jones, C. T. 1983. Regulation of glycolytic flux in the heart of the fetal guinea pig. *J. Dev. Physiol.* **5:** 31-49.

86 Werner, J. C. & Sicard, R. E. 1987. Lactate metabolism of isolated, perfused fetal, and newborn pig hearts. *Pediatr. Res.* **22:** 552-556.

87 Lopaschuk, G. D. *et al.* 1991. Glycolysis is predominant source of myocardial ATP production immediately after birth. *Am. J. Physiol.* **261:** H1698-1705.

88 Wittels, B. & Bressler, R. 1965. Lipid metabolism in the newborn heart. *J. Clin. Invest.* **44:** 1639-1646.

89 Warshaw, J. B. 1972. Cellular energy metabolism during fetal development. IV. Fatty acid activation, acyl transfer and fatty acid oxidation during development of the chick and rat. *Dev. Biol.* **28:** 537-544.

90 Lopaschuk, G. D. & Spafford, M. A. 1990. Energy substrate utilization by isolated working hearts from newborn rabbits. *Am. J. Physiol.* **258:** H1274-1280.

91 Itoi, T. & Lopaschuk, G. D. 1993. The contribution of glycolysis, glucose oxidation, lactate oxidation, and fatty acid oxidation to ATP production in isolated biventricular working hearts from 2-week-old rabbits. *Pediatr. Res.* **34:** 735-741.

92 Stanley, W. C. *et al.* 2005. Myocardial substrate metabolism in the normal and failing heart. *Physiol. Rev.* **85:** 1093-1129.

93 Saddik, M. *et al.* 1993. Acetyl-CoA carboxylase regulation of fatty acid oxidation in the heart. *J. Biol. Chem.* **268:** 25836-25845.

94 Awan, M. M. & Saggerson, E. D. 1993. Malonyl-CoA metabolism in cardiac myocytes and its relevance to the control of fatty acid oxidation. *Biochem. J.* **295:** 61-66.

95 Lopaschuk, G. D. *et al.* 1994. Acetyl-CoA carboxylase involvement in the rapid maturation of fatty acid oxidation in the newborn rabbit heart. *J. Biol. Chem.* **269:** 25871-25878.

96 Makinde, A. O. *et al.* 1997. Upregulation of 5'-AMP-activated protein kinase is responsible for the increase in myocardial fatty acid oxidation rates following birth in the newborn rabbit. *Circ. Res.* **80:** 482-489.

97 Dyck, J. R. *et al.* 1998. Characterization of cardiac malonyl-CoA decarboxylase and its putative role in regulating fatty acid oxidation. *Am. J. Physiol.* **275:** H2122-2129.

98 Eghbali, M. *et al.* 2005. Molecular and functional signature of heart hypertrophy during pregnancy. *Circ. Res.* **96:** 1208-1216.

99 Milliken, M. C. *et al.* 1988. Left ventricular mass as determined by magnetic resonance imaging in male endurance athletes. *Am. J. Cardiol.* **62:** 301-305.

100 Hill, J. A. & Olson, E. N. 2008. Cardiac plasticity. *N. Engl. J. Med.* **358:** 1370-1380.

101 van Berlo, J. H. *et al.* 2013. Signaling effectors underlying pathologic growth and remodeling of the heart. *J. Clin. Invest.* **123:** 37-45.

102 Grossman, W. *et al.* 1975. Wall stress and patterns of hypertrophy in the human left ventricle. *J. Clin. Invest.* **56:** 56-64.

103 Pluim, B. M. *et al.* 2000. The athlete's heart. A meta-analysis of cardiac structure and function. *Circulation*. **101:** 336-344.

104 Kaplan, M. L. *et al.* 1994. Cardiac adaptations to chronic exercise in mice. *Am. J. Physiol.* **267:** H1167-1173.

105 Iemitsu, M. *et al.* 2001. Physiological and pathological cardiac hypertrophy induce different molecular phenotypes in the rat. *Am. J. Physiol. Regul. Integr. Comp. Physiol*. **281:** R2029-2036.

106 McMullen, J. R. *et al.* 2003. Phosphoinositide 3-kinase(p110alpha) plays a critical role for the induction of physiological, but not pathological, cardiac hypertrophy. *Proc. Natl. Acad. Sci. U. S. A.* **100:** 12355-12360.

107 Kim, J. *et al.* 2008. Insulin-like growth factor I receptor signaling is required for exercise-induced cardiac hypertrophy. *Mol. Endocrinol.* **22:** 2531-2543.

108 Bostrom, P. *et al.* 2010. C/EBPbeta controls exercise-induced cardiac growth and protects against pathological cardiac remodeling. *Cell*. **143:** 1072-1083.

109 Brower, G. L. *et al.* 2006. The relationship between myocardial extracellular matrix remodeling and ventricular function. *Eur. J. Cardiothorac. Surg.* **30:** 604-610.

110 Vakili, B. A. *et al.* 2001. Prognostic implications of left ventricular hypertrophy. *Am. Heart J.* **141:** 334-341.

111 Mahdavi, V. *et al.* 1984. Cardiac myosin heavy chain isozymic transitions during development and under pathological conditions are regulated at the level of mRNA availability. *Eur. Heart J.* **5 Suppl F:** 181-191.

112 Nakao, K. *et al.* 1997. Myosin heavy chain gene expression in human heart failure. *J. Clin. Invest.* **100:** 2362-2370.

113 Oliver, P. M. *et al.* 1997. Hypertension, cardiac hypertrophy, and sudden death in mice lacking natriuretic peptide receptor A. *Proc. Natl. Acad. Sci. U. S. A.* **94:** 14730-14735.

114 Ewald, B. *et al.* 2008. Meta-analysis of B type natriuretic peptide and N-terminal pro B natriuretic peptide in the diagnosis of clinical heart failure and population screening for left ventricular systolic dysfunction. *Intern. Med. J*. **38:** 101-113.

115 Fagard, R. H. 1992. Impact of different sports and training on cardiac structure and function. *Cardiol. Clin.* **10:** 241-256.

116 McMullen, J. R. & Jennings, G. L. 2007. Differences between pathological and physiological cardiac hypertrophy: Novel therapeutic strategies to treat heart failure. *Clin. Exp. Pharmacol. Physiol.* **34:** 255-262.

117 Kemi, O. J. *et al.* 2008. Activation or inactivation of cardiac AKT/mTOR signaling diverges physiological from pathological hypertrophy. *J. Cell. Physiol.* **214:** 316-321.

118 Laplante, M. & Sabatini, D. M. 2009. mTOR signaling at a glance. *J. Cell Sci.* **122:** 3589-3594.

119 Hara, K. *et al.* 1998. Amino acid sufficiency and mTOR regulate p70 S6 kinase and eIF-4E BP1 through a common effector mechanism. *J. Biol. Chem.* **273:** 14484-14494.

120 Hara, K. *et al.* 2002. Raptor, a binding partner of target of rapamycin (TOR), mediates TOR action. *Cell*. **110:** 177-189.

121 Kim, D. H. *et al.* 2002. mTOR interacts with raptor to form a nutrient-sensitive complex that signals to the cell growth machinery. *Cell*. **110:** 163-175.

122 Sarbassov, D. D. *et al.* 2004. Rictor, a novel binding partner of mTOR, defines a rapamycin-insensitive and raptor-independent pathway that regulates the cytoskeleton. *Curr. Biol.* **14:** 1296-1302.

123 Sancak, Y. *et al.* 2007. PRAS40 is an insulin-regulated inhibitor of the mTORC1 protein kinase. *Mol. Cell*. **25:** 903-915.

124 Thedieck, K. *et al.* 2007. PRAS40 and PRR5-like protein are new mTOR interactors that regulate apoptosis. *PLoS One*. **2:** e1217.

125 Vander Haar, E. *et al.* 2007. Insulin signalling to mTOR mediated by the Akt/PKB substrate PRAS40. *Nat. Cell Biol*. **9:** 316-323.

126 Wang, L. *et al.* 2007. PRAS40 regulates mTORC1 kinase activity by functioning as a direct inhibitor of substrate binding. *J. Biol. Chem.* **282:** 20036-20044.

127 Frias, M. A. *et al.* 2006. mSin1 is necessary for Akt/PKB phosphorylation, and its isoforms define three distinct mTORC2s. *Curr. Biol.* **16:** 1865-1870.

128 Jacinto, E. *et al.* 2006. SIN1/MIP1 maintains rictor-mTOR complex integrity and regulates Akt phosphorylation and substrate specificity. *Cell*. **127:** 125-137.

129 Peterson, T. R. *et al.* 2009. DEPTOR is an mTOR inhibitor frequently overexpressed in multiple myeloma cells and required for their survival. *Cell*. **137:** 873-886.

130 Pearce, L. R. *et al.* 2007. Identification of protor as a novel rictor-binding component of mTOR complex-2. *Biochem. J.* **405:** 513-522.

131 Woo, S. Y. *et al.* 2007. PRR5, a novel component of mTOR complex 2, regulates platelet-derived growth factor receptor beta expression and signaling. *J. Biol. Chem.* **282:** 25604-25612.

132 Pearce, L. R. *et al.* 2011. Protor-1 is required for efficient mTORC2-mediated activation of SGK1 in the kidney. *Biochem. J.* **436:** 169-179.

133 Kim, D. H. *et al.* 2003. GbetaL, a positive regulator of the rapamycin-sensitive pathway required for the nutrient-sensitive interaction between raptor and mTOR. *Mol. Cell*. **11:** 895-904.

134 Kaizuka, T. *et al.* 2010. Tti1 and Tel2 are critical factors in mammalian target of rapamycin complex assembly. *J. Biol. Chem.* **285:** 20109-20116.

135 Laplante, M. & Sabatini, D. M. 2012. mTOR signaling in growth control and disease. *Cell*. **149:** 274-293.

136 Inoki, K. *et al.* 2002. TSC2 is phosphorylated and inhibited by Akt and suppresses mTOR signalling. *Nat. Cell Biol*. **4:** 648-657.

137 Manning, B. D. *et al.* 2002. Identification of the tuberous sclerosis complex-2 tumor suppressor gene product tuberin as a target of the phosphoinositide 3-kinase/Akt pathway. *Mol. Cell*. **10:** 151-162.

138 Potter, C. J. *et al.* 2002. Akt regulates growth by directly phosphorylating Tsc2. *Nat. Cell. Biol*. **4:** 658-665.

139 Inoki, K. *et al.* 2003. Rheb GTPase is a direct target of TSC2 GAP activity and regulates mTOR signaling. *Genes Dev.* **17:** 1829-1834.

140 Tee, A. R. *et al.* 2003. Tuberous sclerosis complex gene products, tuberin and hamartin, control mTOR signaling by acting as a GTPase-activating protein complex toward Rheb. *Curr. Biol.* **13:** 1259-1268.

141 Sarbassov, D. D. *et al.* 2005. Phosphorylation and regulation of Akt/PKB by the rictor-mTOR complex. *Science*. **307:** 1098-1101.

142 Hardie, D. G. 2007. AMP-activated/SNF1 protein kinases: Conserved guardians of cellular energy. *Nat. Rev. Mol. Cell Biol*. **8:** 774-785.

143 Shaw, R. J. 2009. LKB1 and AMP-activated protein kinase control of mTOR signalling and growth. *Acta Physiol. (Oxf)*. **196:** 65-80.

144 Inoki, K. *et al.* 2003. TSC2 mediates cellular energy response to control cell growth and survival. *Cell*. **115:** 577-590.

145 Gwinn, D. M. *et al.* 2008. AMPK phosphorylation of raptor mediates a metabolic checkpoint. *Mol. Cell*. **30:** 214-226.

146 Nicklin, P. *et al.* 2009. Bidirectional transport of amino acids regulates mTOR and autophagy. *Cell*. **136:** 521-534.

147 Smith, E. M. *et al.* 2005. The tuberous sclerosis protein TSC2 is not required for the regulation of the mammalian target of rapamycin by amino acids and certain cellular stresses. *J. Biol. Chem.* **280:** 18717-18727.

148 Jewell, J. L. *et al.* 2013. Amino acid signalling upstream of mTOR. *Nat. Rev. Mol. Cell Biol*. **14:** 133-139.

149 Shimobayashi, M. & Hall, M. N. 2014. Making new contacts: The mTOR network in metabolism and signalling crosstalk. *Nat. Rev. Mol. Cell Biol*. **15:** 155-162.

150 Kim, E. *et al.* 2008. Regulation of TORC1 by Rag GTPases in nutrient response. *Nat. Cell Biol*. **10:** 935-945.

151 Sancak, Y. *et al.* 2008. The Rag GTPases bind raptor and mediate amino acid signaling to mTORC1. *Science*. **320:** 1496-1501.

152 Sancak, Y. *et al.* 2010. Ragulator-Rag complex targets mTORC1 to the lysosomal surface and is necessary for its activation by amino acids. *Cell*. **141:** 290-303.

153 Bar-Peled, L. *et al.* 2012. Ragulator is a GEF for the Rag GTPases that signal amino acid levels to mTORC1. *Cell*. **150:** 1196-1208.

154 Bar-Peled, L. *et al.* 2013. A tumor suppressor complex with GAP activity for the Rag GTPases that signal amino acid sufficiency to mTORC1. *Science*. **340:** 1100-1106.

155 Efeyan, A. *et al.* 2013. Regulation of mTORC1 by the Rag GTPases is necessary for neonatal autophagy and survival. *Nature*. **493:** 679-683.

156 Shaw, R. J. 2008. mTOR signaling: RAG GTPases transmit the amino acid signal. *Trends Biochem. Sci.* **33:** 565-568.

157 Brown, E. J. *et al.* 1994. A mammalian protein targeted by G1-arresting rapamycin-receptor complex. *Nature*. **369:** 756-758.

158 Sabatini, D. M. *et al.* 1995. The rapamycin and FKBP12 target (RAFT) displays phosphatidylinositol 4-kinase activity. *J. Biol. Chem.* **270:** 20875-20878.

159 Sabatini, D. M. *et al.* 1994. RAFT1: A mammalian protein that binds to FKBP12 in a rapamycin-dependent fashion and is homologous to yeast TORs. *Cell*. **78:** 35-43.

160 Dibble, C. C. & Manning, B. D. 2013. Signal integration by mTORC1 coordinates nutrient input with biosynthetic output. *Nat. Cell Biol*. **15:** 555-564.

161 Ma, X. M. & Blenis, J. 2009. Molecular mechanisms of mTOR-mediated translational control. *Nat. Rev. Mol. Cell Biol*. **10:** 307-318.

162 Richter, J. D. & Sonenberg, N. 2005. Regulation of cap-dependent translation by eIF4E inhibitory proteins. *Nature*. **433:** 477-480.

163 Hudson, C. C. *et al.* 2002. Regulation of hypoxia-inducible factor 1alpha expression and function by the mammalian target of rapamycin. *Mol. Cell. Biol.* **22:** 7004-7014.

164 Duvel, K. *et al.* 2010. Activation of a metabolic gene regulatory network downstream of mTOR complex 1. *Mol. Cell*. **39:** 171-183.

165 Schieke, S. M. *et al.* 2006. The mammalian target of rapamycin (mTOR) pathway regulates mitochondrial oxygen consumption and oxidative capacity. *J. Biol. Chem.* **281:** 27643-27652.

166 Baehrecke, E. H. 2005. Autophagy: Dual roles in life and death? *Nat. Rev. Mol. Cell Biol*. **6:** 505-510.

167 Mizushima, N. & Komatsu, M. 2011. Autophagy: Renovation of cells and tissues. *Cell*. **147:** 728-741.

168 Ganley, I. G. *et al.* 2009. ULK1.ATG13.FIP200 complex mediates mTOR signaling and is essential for autophagy. *J. Biol. Chem.* **284:** 12297-12305.

169 Hosokawa, N. *et al.* 2009. Nutrient-dependent mTORC1 association with the ULK1-Atg13-FIP200 complex required for autophagy. *Mol. Biol. Cell*. **20:** 1981-1991.

170 Jung, C. H. *et al.* 2009. ULK-Atg13-FIP200 complexes mediate mTOR signaling to the autophagy machinery. *Mol. Biol. Cell*. **20:** 1992-2003.

171 Kim, J. *et al.* 2011. AMPK and mTOR regulate autophagy through direct phosphorylation of Ulk1. *Nat. Cell Biol*. **13:** 132-141.

172 Koren, I. *et al.* 2010. DAP1, a novel substrate of mTOR, negatively regulates autophagy. *Curr. Biol.* **20:** 1093-1098.

173 Yu, L. *et al.* 2010. Termination of autophagy and reformation of lysosomes regulated by mTOR. *Nature*. **465:** 942-946.

174 Settembre, C. *et al.* 2011. TFEB links autophagy to lysosomal biogenesis. *Science*. **332:** 1429-1433.

175 Settembre, C. *et al.* 2012. A lysosome-to-nucleus signalling mechanism senses and regulates the lysosome via mTOR and TFEB. *EMBO J.* **31:** 1095-1108.

176 Sciarretta, S. *et al.* 2014. Mammalian target of rapamycin signaling in cardiac physiology and disease. *Circ. Res.* **114:** 549-564.

177 Hentges, K. E. *et al.* 2001. FRAP/mTOR is required for proliferation and patterning during embryonic development in the mouse. *Proc. Natl. Acad. Sci. U. S. A.* **98:** 13796-13801.

178 Murakami, M. *et al.* 2004. mTOR is essential for growth and proliferation in early mouse embryos and embryonic stem cells. *Mol. Cell. Biol.* **24:** 6710-6718.

179 Gangloff, Y. G. *et al.* 2004. Disruption of the mouse mTOR gene leads to early postimplantation lethality and prohibits embryonic stem cell development. *Mol. Cell. Biol.* **24:** 9508-9516.

180 Guertin, D. A. *et al.* 2006. Ablation in mice of the mTORC components raptor, rictor, or mLST8 reveals that mTORC2 is required for signaling to Akt-FOXO and PKCalpha, but not S6K1. *Dev. Cell*. **11:** 859-871.

181 Goorden, S. M. *et al.* 2011. Rheb is essential for murine development. *Mol. Cell. Biol.* **31:** 1672-1678.

182 Zhang, D. H. *et al.* 2010. MTORC1 regulates cardiac function and myocyte survival through 4E-BP1 inhibition in mice. *J. Clin. Invest.* **120:** 2805-2816.

183 Shende, P. *et al.* 2011. Cardiac raptor ablation impairs adaptive hypertrophy, alters metabolic gene expression, and causes heart failure in mice. *Circulation*. **123:** 1073-1082.

184 Shioi, T. *et al.* 2003. Rapamycin attenuates load-induced cardiac hypertrophy in mice. *Circulation*. **107:** 1664-1670.

185 Marin, T. M. *et al.* 2011. Rapamycin reverses hypertrophic cardiomyopathy in a mouse model of LEOPARD syndrome-associated PTPN11 mutation. *J. Clin. Invest.* **121:** 1026-1043.

186 McMullen, J. R. *et al.* 2004. Inhibition of mTOR signaling with rapamycin regresses established cardiac hypertrophy induced by pressure overload. *Circulation*. **109:** 3050-3055.

187 Shen, W. H. *et al.* 2008. Cardiac restricted overexpression of kinase-dead mammalian target of rapamycin (mTOR) mutant impairs the mTOR-mediated signaling and cardiac function. *J. Biol. Chem.* **283:** 13842-13849.

188 Song, X. *et al.* 2010. mTOR attenuates the inflammatory response in cardiomyocytes and prevents cardiac dysfunction in pathological hypertrophy. *Am. J. Physiol. Cell Physiol*. **299:** C1256-1266.

189 Tamai, T. *et al.* 2013. Rheb (ras homologue enriched in brain)-dependent mammalian target of rapamycin complex 1 (mTORC1) activation becomes indispensable for cardiac hypertrophic growth after early postnatal period. *J. Biol. Chem.* **288:** 10176-10187.

190 Shioi, T. *et al.* 2002. Akt/protein kinase B promotes organ growth in transgenic mice. *Mol. Cell. Biol.* **22:** 2799-2809.

191 Zhu, Y. *et al.* 2013. Mechanistic target of rapamycin (Mtor) is essential for murine embryonic heart development and growth. *PLoS One*. **8:** e54221.

192 Drenckhahn, J. D. *et al.* 2008. Compensatory growth of healthy cardiac cells in the presence of diseased cells restores tissue homeostasis during heart development. *Dev. Cell*. **15:** 521-533.

193 Schaefer, L. *et al.* 1996. Cloning and characterization of a putative human holocytochrome c-type synthetase gene (HCCS) isolated from the critical region for microphthalmia with linear skin defects (MLS). *Genomics*. **34:** 166-172.

194 San Francisco, B. *et al.* 2013. Human mitochondrial holocytochrome c synthase's heme binding, maturation determinants, and complex formation with cytochrome c. *Proc. Natl. Acad. Sci. U. S. A.* **110:** E788-797.

195 Saraste, M. 1999. Oxidative phosphorylation at the fin de siecle. *Science*. **283:** 1488-1493.

196 Smeitink, J. *et al.* 2001. The genetics and pathology of oxidative phosphorylation. *Nat. Rev. Genet*. **2:** 342-352.

197 Schwarz, Q. P. & Cox, T. C. 2002. Complementation of a yeast CYC3 deficiency identifies an X-linked mammalian activator of apocytochrome c. *Genomics*. **79:** 51-57.

198 Bernard, D. G. *et al.* 2003. Overlapping specificities of the mitochondrial cytochrome c and c1 heme lyases. *J. Biol. Chem.* **278:** 49732-49742.

199 Hatefi, Y. 1985. The mitochondrial electron transport and oxidative phosphorylation system. *Annu. Rev. Biochem.* **54:** 1015-1069.

200 Gribnau, J. & Grootegoed, J. A. 2012. Origin and evolution of X chromosome inactivation. *Curr. Opin. Cell Biol.* **24:** 397-404.

201 Avner, P. & Heard, E. 2001. X-chromosome inactivation: Counting, choice and initiation. *Nat. Rev. Genet*. **2:** 59-67.

202 Kilkenny, C. *et al.* 2010. Improving bioscience research reporting: The arrive guidelines for reporting animal research. *PLoS Biol*. **8:** e1000412.

203 Stanley, E. G. *et al.* 2002. Efficient Cre-mediated deletion in cardiac progenitor cells conferred by a 3'UTR-ires-Cre allele of the homeobox gene Nkx2-5. *Int. J. Dev. Biol.* **46:** 431-439.

204 Lints, T. J. *et al.* 1993. Nkx-2.5: A novel murine homeobox gene expressed in early heart progenitor cells and their myogenic descendants. *Development*. **119:** 419-431.

205 Moses, K. A. *et al.* 2001. Embryonic expression of an Nkx2-5/Cre gene using ROSA26 reporter mice. *Genesis*. **31:** 176-180.

206 Sengupta, S. *et al.* 2010. mTORC1 controls fasting-induced ketogenesis and its modulation by ageing. *Nature*. **468:** 1100-1104.

207 Theiler, K. 1989. The house mouse: Atlas of mouse development. *New York: Springer-Verlag*.

208 Dennis, G., Jr. *et al.* 2003. DAVID: Database for annotation, visualization, and integrated discovery. *Genome Biol*. **4:** P3.

209 Huang da, W. *et al.* 2007. The DAVID gene functional classification tool: A novel biological module-centric algorithm to functionally analyze large gene lists. *Genome Biol.* **8:** R183.

210 Huang da, W. *et al.* 2009. Systematic and integrative analysis of large gene lists using DAVID bioinformatics resources. *Nat. Protoc*. **4:** 44-57.

211 Mullis, K. *et al.* 1986. Specific enzymatic amplification of DNA in vitro: The polymerase chain reaction. *Cold Spring Harb. Symp. Quant. Biol.* **51:** 263-273.

212 Livak, K. J. & Schmittgen, T. D. 2001. Analysis of relative gene expression data using real-time quantitative pcr and the 2(-delta delta c(t)) method. *Methods*. **25:** 402-408.

213 Lowry, O. H. *et al.* 1951. Protein measurement with the folin phenol reagent. *J. Biol. Chem.* **193:** 265-275.

214 Laemmli, U. K. 1970. Cleavage of structural proteins during the assembly of the head of bacteriophage T4. *Nature*. **227:** 680-685.

215 Wright, C. S. 1984. Structural comparison of the two distinct sugar binding sites in wheat germ agglutinin isolectin II. *J. Mol. Biol.* **178:** 91-104.

216 Gavrieli, Y. *et al.* 1992. Identification of programmed cell death in situ via specific labeling of nuclear DNA fragmentation. *J. Cell Biol.* **119:** 493-501.

217 Scholzen, T. & Gerdes, J. 2000. The KI-67 protein: From the known and the unknown. *J. Cell. Physiol.* **182:** 311-322.

218 Hendzel, M. J. *et al.* 1997. Mitosis-specific phosphorylation of histone H3 initiates primarily within pericentromeric heterochromatin during G2 and spreads in an ordered fashion coincident with mitotic chromosome condensation. *Chromosoma*. **106:** 348-360.

219 Bierer, B. E. *et al.* 1990. Two distinct signal transmission pathways in T lymphocytes are inhibited by complexes formed between an immunophilin and either FK506 or rapamycin. *Proc. Natl. Acad. Sci. U. S. A.* **87:** 9231-9235.

220 Liu, K. J. *et al.* 2007. Chemical rescue of cleft palate and midline defects in conditional GSK-3beta mice. *Nature*. **446:** 79-82.

221 Phung, T. L. *et al.* 2006. Pathological angiogenesis is induced by sustained Akt signaling and inhibited by rapamycin. *Cancer Cell*. **10:** 159-170.

222 Sarbassov, D. D. *et al.* 2006. Prolonged rapamycin treatment inhibits mTORC2 assembly and Akt/PKB. *Mol. Cell*. **22:** 159-168.

223 Bjorkoy, G. *et al.* 2005. p62/SQSTM1 forms protein aggregates degraded by autophagy and has a protective effect on huntingtin-induced cell death. *J. Cell Biol.* **171:** 603-614.

224 Pankiv, S. *et al.* 2007. p62/SQSTM1 binds directly to Atg8/LC3 to facilitate degradation of ubiquitinated protein aggregates by autophagy. *J. Biol. Chem.* **282:** 24131-24145.

225 Tumaneng, K. *et al.* 2012. Organ size control by Hippo and TOR pathways. *Curr. Biol.* **22:** R368-379.

226 Capasso, J. M. *et al.* 1990. Severe myocardial dysfunction induced by ventricular remodeling in aging rat hearts. *Am. J. Physiol.* **259:** H1086-1096.

227 Burlew, B. S. & Weber, K. T. 2002. Cardiac fibrosis as a cause of diastolic dysfunction. *Herz*. **27:** 92-98.

228 Bloom, J. & Cross, F. R. 2007. Multiple levels of cyclin specificity in cell-cycle control. *Nat. Rev. Mol. Cell Biol*. **8:** 149-160.

229 Besson, A. *et al.* 2008. CDK inhibitors: Cell cycle regulators and beyond. *Dev. Cell*. **14:** 159-169.

230 Malumbres, M. *et al.* 2009. Cyclin-dependent kinases: A family portrait. *Nat. Cell. Biol*. **11:** 1275-1276.

231 Ahuja, P. *et al.* 2007. Cardiac myocyte cell cycle control in development, disease, and regeneration. *Physiol. Rev*. **87:** 521-544.

232 Horne, M. C. *et al.* 1996. Cyclin G1 and cyclin G2 comprise a new family of cyclins with contrasting tissue-specific and cell cycle-regulated expression. *J. Biol. Chem.* **271:** 6050-6061.

233 Jensen, M. R. *et al.* 1998. Regulation of cyclin G1 during murine hepatic regeneration following Dipin-induced DNA damage. *Hepatology*. **28:** 537-546.

234 Okamoto, K. & Beach, D. 1994. Cyclin G is a transcriptional target of the p53 tumor suppressor protein. *EMBO J.* **13:** 4816-4822.

235 Harper, J. W. *et al.* 1993. The p21 Cdk-interacting protein Cip1 is a potent inhibitor of G1 cyclin-dependent kinases. *Cell*. **75:** 805-816.

236 Polyak, K. *et al.* 1994. p27Kip1, a cyclin-Cdk inhibitor, links transforming growth factor-beta and contact inhibition to cell cycle arrest. *Genes Dev.* **8:** 9-22.

237 Toyoshima, H. & Hunter, T. 1994. p27, a novel inhibitor of G1 cyclin-cdk protein kinase activity, is related to p21. *Cell*. **78:** 67-74.

238 Harper, J. W. *et al.* 1995. Inhibition of cyclin-dependent kinases by p21. *Mol. Biol. Cell*. **6:** 387-400.

239 Leung-Pineda, V. *et al.* 2004. Induction of p21 and p27 expression by amino acid deprivation of HepG2 human hepatoma cells involves mRNA stabilization. *Biochem. J.* **379:** 79-88.

240 Liu, Z. *et al.* 2010. Regulation of cardiomyocyte polyploidy and multinucleation by cyclinG1. *Circ. Res.* **106:** 1498-1506.

241 Rinaudo, P. & Wang, E. 2012. Fetal programming and metabolic syndrome. *Annu. Rev. Physiol.* **74:** 107-130.

242 Dong, F. *et al.* 2005. Maternal nutrient restriction during early to mid gestation up-regulates cardiac insulin-like growth factor (IGF) receptors associated with enlarged ventricular size in fetal sheep. *Growth Horm. IGF Res.* **15:** 291-299.

243 Wang, K. C. *et al.* 2011. Fetal growth restriction and the programming of heart growth and cardiac insulin-like growth factor 2 expression in the lamb. *J. Physiol*. **589:** 4709-4722.

244 Sabers, C. J. *et al.* 1995. Isolation of a protein target of the FPBP12-rapamycin complex in mammalian cells. *J. Biol. Chem.* **270:** 815-822.

245 Choi, J. *et al.* 1996. Structure of the FKBP12-rapamycin complex interacting with the binding domain of human FRAP. *Science*. **273:** 239-242.

246 Oshiro, N. *et al.* 2004. Dissociation of raptor from mTOR is a mechanism of rapamycin-induced inhibition of mTOR function. *Genes Cells*. **9:** 359-366.

247 Soliman, G. A. *et al.* 2010. mTOR ser-2481 autophosphorylation monitors mTORC-specific catalytic activity and clarifies rapamycin mechanism of action. *J. Biol. Chem.* **285:** 7866-7879.

248 Chen, X. G. *et al.* 2010. Rapamycin regulates Akt and ERK phosphorylation through mTORC1 and mTORC2 signaling pathways. *Mol. Carcinog.* **49:** 603-610.

249 Lamming, D. W. *et al.* 2012. Rapamycin-induced insulin resistance is mediated by mTORC2 loss and uncoupled from longevity. *Science*. **335:** 1638-1643.

250 Barker, D. J. & Osmond, C. 1986. Infant mortality, childhood nutrition, and ischaemic heart disease in england and wales. *Lancet*. **1:** 1077-1081.

251 Lyons, G. E. *et al.* 1990. Developmental regulation of myosin gene expression in mouse cardiac muscle. *J. Cell Biol.* **111:** 2427-2436.

252 Yuan, J. *et al.* 2005. Identification and characterization of RHEBL1, a novel member of Ras family, which activates transcriptional activities of NF-kappa B. *Mol. Biol. Rep.* **32:** 205-214.

253 Boya, P. *et al.* 2005. Inhibition of macroautophagy triggers apoptosis. *Mol. Cell. Biol.* **25:** 1025-1040.

254 Li, W. *et al.* 2012. Autophagy genes function sequentially to promote apoptotic cell corpse degradation in the engulfing cell. *J. Cell Biol.* **197:** 27-35.

255 Joshi, S. & Ryan, K. M. 2014. Autophagy chews Fap to promote apoptosis. *Nat. Cell Biol*. **16:** 23-25.

256 Kabeya, Y. *et al.* 2000. LC3, a mammalian homologue of yeast Apg8p, is localized in autophagosome membranes after processing. *EMBO J.* **19:** 5720-5728.

257 Hernandez, G. *et al.* 2011. A novel cardioprotective p38-MAPK/mTOR pathway. *Exp. Cell Res.* **317:** 2938-2949.

258 Gown, A. M. & Willingham, M. C. 2002. Improved detection of apoptotic cells in archival paraffin sections: Immunohistochemistry using antibodies to cleaved caspase 3. *J. Histochem. Cytochem.* **50:** 449-454.

259 Terai, K. *et al.* 2005. AMP-activated protein kinase protects cardiomyocytes against hypoxic injury through attenuation of endoplasmic reticulum stress. *Mol. Cell. Biol.* **25:** 9554-9575.

260 Kim, M. *et al.* 2014. Mutation in the gamma2-subunit of AMP-activated protein kinase stimulates cardiomyocyte proliferation and hypertrophy independent of glycogen storage. *Circ. Res.* **114:** 966-975.

261 Wencker, D. *et al.* 2003. A mechanistic role for cardiac myocyte apoptosis in heart failure. *J. Clin. Invest.* **111:** 1497-1504.

262 Drenckhahn, J. D. 2009. Growth plasticity of the embryonic and fetal heart. *Bioessays*. **31:** 1288-1298.

263 Roos, S. *et al.* 2007. Mammalian target of rapamycin in the human placenta regulates leucine transport and is down-regulated in restricted fetal growth. *J. Physiol*. **582:** 449-459.

264 Jansson, T. *et al.* 2012. The emerging role of mTORC1 signaling in placental nutrient-sensing. *Placenta*. **33 Suppl 2:** e23-29.

265 Wen, H. Y. *et al.* 2005. mTOR: A placental growth signaling sensor. *Placenta*. **26 Suppl A:** S63-69.

266 Wang, L. *et al.* 2014. Leucyl-tRNA synthetase regulates lactation and cell proliferation via mTOR signaling in dairy cow mammary epithelial cells. *Int. J. Mol. Sci*. **15:** 5952-5969.

267 Kozar, K. *et al.* 2004. Mouse development and cell proliferation in the absence of D-cyclins. *Cell*. **118:** 477-491.

268 Portella, G. *et al.* 2011. Aurora B: A new prognostic marker and therapeutic target in cancer. *Curr. Med. Chem.* **18:** 482-496.

269 Pasumarthi, K. B. & Field, L. J. 2002. Cardiomyocyte cell cycle regulation. *Circ. Res.* **90:** 1044-1054.

270 Evans, S. M. *et al.* 2010. Myocardial lineage development. *Circ. Res.* **107:** 1428-1444.

271 Guertin, D. A. & Sabatini, D. M. 2007. Defining the role of mTOR in cancer. *Cancer Cell*. **12:** 9-22.

272 Hsieh, A. C. *et al.* 2010. Genetic dissection of the oncogenic mTOR pathway reveals druggable addiction to translational control via 4EBP-eIF4E. *Cancer Cell*. **17:** 249-261.

273 Dowling, R. J. *et al.* 2010. mTORC1-mediated cell proliferation, but not cell growth, controlled by the 4E-BPs. *Science*. **328:** 1172-1176.

274 Choo, A. Y. *et al.* 2008. Rapamycin differentially inhibits S6Ks and 4E-BP1 to mediate cell-type-specific repression of mRNA translation. *Proc. Natl. Acad. Sci. U. S. A.* **105:** 17414-17419.

275 Rousseau, D. *et al.* 1996. Translation initiation of ornithine decarboxylase and nucleocytoplasmic transport of cyclin D1 mRNA are increased in cells overexpressing eukaryotic initiation factor 4E. *Proc. Natl. Acad. Sci. U. S. A.* **93:** 1065-1070.

276 Kang, S. A. *et al.* 2013. mTORC1 phosphorylation sites encode their sensitivity to starvation and rapamycin. *Science*. **341:** 1236566.

277 Fingar, D. C. *et al.* 2004. mTOR controls cell cycle progression through its cell growth effectors S6K1 and 4E-BP1/eukaryotic translation initiation factor 4E. *Mol. Cell. Biol.* **24:** 200-216.

278 Kimball, S. R. & Jefferson, L. S. 2006. New functions for amino acids: Effects on gene transcription and translation. *Am. J. Clin. Nutr.* **83:** 500S-507S.

279 Wu, G. *et al.* 2004. Glutathione metabolism and its implications for health. *J. Nutr.* **134:** 489-492.

280 McArdle, H. J. *et al.* 2006. Fetal programming: Causes and consequences as revealed by studies of dietary manipulation in rats - a review. *Placenta*. **27 Suppl A:** S56-60.

281 Mortensen, O. H. *et al.* 2010. A maternal low protein diet has pronounced effects on mitochondrial gene expression in offspring liver and skeletal muscle; protective effect of taurine. *J. Biomed. Sci.* **17 Suppl 1:** S38.

282 Whitaker, K. W. *et al.* 2012. Metabolic adaptations to early life protein restriction differ by offspring sex and post-weaning diet in the mouse. *Nutr. Metab. Cardiovasc. Dis*. **22:** 1067-1074.

283 Bhasin, K. K. *et al.* 2009. Maternal low-protein diet or hypercholesterolemia reduces circulating essential amino acids and leads to intrauterine growth restriction. *Diabetes*. **58:** 559-566.

284 Maillet, M. *et al.* 2013. Molecular basis of physiological heart growth: Fundamental concepts and new players. *Nat. Rev. Mol. Cell Biol*. **14:** 38-48.

285 Louey, S. *et al.* 2007. Placental insufficiency decreases cell cycle activity and terminal maturation in fetal sheep cardiomyocytes. *J. Physiol*. **580:** 639-648.

286 Zohdi, V. *et al.* 2014. When early life growth restriction in rats is followed by attenuated postnatal growth: Effects on cardiac function in adulthood. *Eur. J. Nutr.*

287 Rudolph, A. M. 2000. Myocardial growth before and after birth: Clinical implications. *Acta Paediatr.* **89:** 129-133.

288 Howard, C. M. & Baudino, T. A. 2014. Dynamic cell-cell and cell-ECM interactions in the heart. *J. Mol. Cell. Cardiol.* **70:** 19-26.

289 Eckert, J. J. *et al.* 2012. Metabolic induction and early responses of mouse blastocyst developmental programming following maternal low protein diet affecting life-long health. *PLoS One*. **7:** e52791.

290 Grumati, P. *et al.* 2010. Autophagy is defective in collagen VI muscular dystrophies, and its reactivation rescues myofiber degeneration. *Nat. Med.* **16:** 1313-1320.

291 Han, J. M. *et al.* 2012. Leucyl-tRNA synthetase is an intracellular leucine sensor for the mTORC1-signaling pathway. *Cell*. **149:** 410-424.

292 Kim, J. Y. *et al.* 2011. Select nutrients in the ovine uterine lumen. VII. Effects of arginine, leucine, glutamine, and glucose on trophectoderm cell signaling, proliferation, and migration. *Biol. Reprod.* **84:** 62-69.

293 Kim, J. *et al.* 2011. Select nutrients in the ovine uterine lumen. IX. Differential effects of arginine, leucine, glutamine, and glucose on interferon tau, ornithine decarboxylase, and nitric oxide synthase in the ovine conceptus. *Biol. Reprod.* **84:** 1139-1147.

294 Wu, G. *et al.* 2011. Proline and hydroxyproline metabolism: Implications for animal and human nutrition. *Amino Acids*. **40:** 1053-1063.

295 Liu, X. D. *et al.* 2012. Effects of dietary L-arginine or N-carbamylglutamate supplementation during late gestation of sows on the miR-15b/16, miR-221/222, VEGFA and eNOS expression in umbilical vein. *Amino Acids*. **42:** 2111-2119.

296 Tan, B. *et al.* 2012. Dynamic changes in blood flow and oxygen consumption in the portal-drained viscera of growing pigs receiving acute administration of (L)-arginine. *Amino Acids*. **43:** 2481-2489.

297 Wu, Z. *et al.* 2012. Regulation of brown adipose tissue development and white fat reduction by L-arginine. *Curr. Opin. Clin. Nutr. Metab. Care*. **15:** 529-538.

298 Wang, W. *et al.* 2013. Glycine metabolism in animals and humans: Implications for nutrition and health. *Amino Acids*. **45:** 463-477.

299 Dai, Z. *et al.* 2013. Nitric oxide and energy metabolism in mammals. *Biofactors*. **39:** 383-391.

ERKLÄRUNG

Hiermit versichere ich, die vorliegende Arbeit selbständig erarbeitet und verfasst und gemäß §7 Absatz 3 der Promotionsordnung von 2009 keine anderen als die angegebenen Hilfsmittel und Quellen verwendet zu haben. Diese Dissertation wurde keiner anderen Fakultät oder Universität zur Prüfung vorgelegt. Die Bestimmungen der Promotionsordnung der Mathematisch-Naturwissenschaftlichen Fakultät I der Humboldt-Universität zu Berlin sind mir bekannt.

Berlin, den 28. November 2014

Maria Hennig